2012

An experimental and numerical study of NOx formation mechanisms in NH3-H2-Air flames

Praveen Kumar
Iowa State University

An experimental and numerical study of NO_x formation mechanisms in NH_3-H_2-Air flames

by

Praveen Kumar

A dissertation submitted to the graduate faculty

in partial fulfillment of the requirements for the degree of

DOCTOR OF PHILOSOPHY

Major: Mechanical Engineering

Program of Study Committee:
Terrence R. Meyer, Major Professor
Rodney O. Fox
Song-Charng Kong
Gap-Yong Kim
Hui Hu

Iowa State University

Ames, Iowa

2012

To my parents and my wife

TABLE OF CONTENTS

LIST OF TABLES

LIST OF FIGURES

ACKNOWLEDGEMENTS

This research was funded, in part, by the Iowa Energy Center under Grant 08F-03, with program management provided by Norman Olson, Kevin Nordmeyer, and Dr. Thomas Barton. Technical assistance, guidance, and combustor components used in the current experiments were also provided by Jerry Goeke and the engineers of Goodrich Engine Components, now United Technologies Aerospace Systems.

This work could not be completed without the help from a number of people. First of all, I would like to express my gratitude to my major professor, Dr. Terrence R. Meyer, for his illuminating guidance and persistent encouragement that contributed to the completion of this thesis. Moreover, he is also an expert in stimulating me to achieve a level of independent thinking.

I would like to thank my committee members, Dr. Rodney O. Fox, Dr. Song-Charng, Kong, Dr. Hui Hu and Dr. Gap-Yong Kim. It is a great honor having you in my doctoral committee. Your reviews and constructive comments contributed significantly to this research and thesis.

My special thanks go to Dr. Viswanath R. Katta for his patient and persistent help in my CFD research. His extensive knowledge of combustion and profound understanding of CFD greatly enhanced my perception of current combustion phenomena, my CFD research productivity, and in turn my confidence to complete my thesis.

I also would like to express my appreciation to all of my warmhearted labmates; Mark Johnson, Dr. Arvind Vaidyanathan, Ben Halls, Dr. Derek Wissmiller, Hiep Tran, Daniel Diaz, Kyle Redfren, Dan Stoecklein, Dr. Miao Li, Matthias Veltman, Cuong Huynh

and Sujith Sukumaran for their help and discussion; Special thanks to Dr. Joseph Miller, for helping with the PLIF setup and for consistent support in troubleshooting of the laser diagnostics setup. Special thanks to Jordan Tiarks for his considerate dedication and excellent instrumentation skills in performing experiments. I would like to pay my best regards to Dr. Sumit Ashtekar, Sudheer Tenneti, and Dr. Varun Vikas for motivation and support during my graduate studies. Also, I would like to extend my regards to the ME staff; James Dautremont, Larry couture, Amy Carver, Deb, Carol to assisting with paperwork and ordering parts.

My final thanks go to my wife, Srishti Jaiswal for her sacrifice, persistent love, support, and excellent management of my family throughout my years as a student.

ABSTRACT

The demand for sustainable alternative fuels is ever-increasing in the power generation, transportation, and energy sectors due to the inherent non-sustainable characteristics and political constraints of current energy resources. A number of alternative fuels derived from cellulosic biomass, algae, or waste are being considered, along with the conversion of electricity to non-carbon fuels such as hydrogen or ammonia (NH_3). The latter is receiving attention recently because it is a non-carbon fuel that is readily produced in large quantities, stored and transported with current infrastructure, and is often a byproduct of biomass or waste conversion processes. However, pure or anhydrous ammonia combustion is severely challenging due to its high auto-ignition temperature (650 ºC), low reactivity, and tendency to promote NO_x formation.

As such, the present study focuses on two major aspects of the ammonia combustion. The first is an applied investigation of the potential to achieve pure NH_3 combustion with low levels of emissions in flames of practical interest. In this study, a swirl-stabilized flame typically used in fuel-oil home-heating systems is optimized for NH_3 combustion, and measurements of NO and NH_3 are collected for a wide range of operating conditions. The second major focus of this work is on fundamental investigation of NO_x formation mechanisms in flames with high levels of NH_3 in H_2. For laminar premixed and diffusion jet flames, experimental measurements of flame speeds, exhaust-gas sampling, and *in-situ* NO measurements (NO PLIF) are compared with numerically predicted flames using complex chemical kinetics within CHEMKIN and reacting CFD codes i.e., UNICORN.

From the preliminary testing of the NO_x formation mechanisms, (1) Tian (2) Konnov and (3) GRI-Mech3.0 in laminar premixed H_2/NH_3 flames, the Tian and Konnov mechanisms are found to capture the reduction in measured flame speeds with increasing NH_3 in the fuel mixture, both qualitatively and quantitatively. The NO_x predictions by all the three chemical mechanisms are observed to be in fairly good agreement with the measured NO_x, qualitatively, however predictions are found to be 3 to 4 times higher than the measurements for both lean and rich H_2/NH_3 premixed flames.

For laminar H_2/NH_3 diffusion flames, detailed 2-D comparisons of *in-situ* NO measurements with the 2-D simulated NO using the Tian, GRI-Mech3.0 and modified GRI-Mech chemical mechanisms are performed and found to differ from the measured NO by approximately an order of magnitude. For NH_3 seeded H_2/air diffusion flames, GRI-Mech3.0 seemed to overpredict NO by more than an order of magnitude and failed to capture the fundamental flame characteristics, such asthe flame length variation with increasing NH_3 in the fuel mixture. On the other hand, the predicted NO profiles by the Tian mechanism were not only found to be in better agreement with the measured NO, but they also captured the in-flame NO distribution as well, both qualitatively and quantitatively.

Overall, the Tian mechanism is found to be the superior chemical mechanism to capture the NO_x formation chemistry in NH_3 seeded flames.

CHAPTER 1. BACKGROUND

1.1 General discussions

In general, the primary focus of the present research work encompassed the detailed combustion characterization of NH_3 enriched H_2/air fuel mixtures and effects of NH_3 on NO_x chemistry for both premixed and diffusion flames. This chapter provides a brief background on the types of flames studied in this work and associated emissions; such as CO, CO_2, soot, NO_x etc. Subsequently, details regarding important NO_x formation pathway are provided along with a fair background on parameters and flame conditions that affect NO_x generation and associated reaction pathways. Due to its importance in achieve quantitative flame diagnostics, a detailed theoretical background for planar laser induced fluorescence (PLIF) technique for NO species imaging in flames is provided. This chapter ends with a detailed literature review supporting the motivation of the current research work along with the layout of thesis organization.

1.1.1 Types of flames

In general, the 85% of the energy required to meet the world's energy demand comes from the combustion of fossil fuels like gasoline, diesel etc. Concerning the negative impact of combustion processes, major pollutants such as NO, NO_2, CO, CO_2, unburnt hydrocarbons, soot etc. are produced and cause detrimental effects on the environment. This necessitates the development of sustainable energy resources, advanced pollutants abatement techniques, and improved understanding of the combustion of alternative fuels.

The combustion characterization of a fuel and its detailed chemistry is often performed under two possible extremes, which are present to some degree in most practical combustion systems: 1) premixed flames and 2) non-premixed (diffusion) flames. Under the premixed flame mode, the reactants (typically fuel and air) are mixed at molecular level prior to combustion, whereas in a non-premixed flame, the reactants are separated initially and combustion occurs at the interface of the fuel and air where equivalence ratio (ϕ) is 1. Due to differences in mixing state of the reactants among the two modes; premixed flames are interpreted as kinetically controlled due to dependence of the flame reactions on the reaction kinetics. Whereas, for diffusion flame, the flame reactions are dependent on both the mixing state of the reactants as well as the reaction kinetics. Common examples for premixed and non-premixed flames are gasoline combustion in spark-ignited engines and candle flames, respectively.

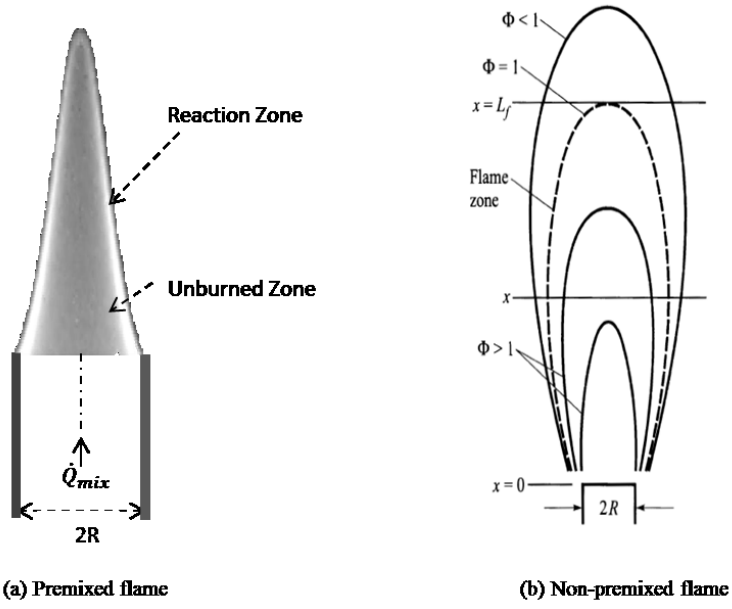

Fig. 1.1. Schematic of (a) premixed and (b) non-premixed flames, courtesy of Turns [Introduction to Combustion, Ed 2, 1996].

Fundamental study of laminar premixed flames allows probing the underlying chemical kinetics of the flame as well as the examination of the factors influencing the laminar flame speed and flame thickness, which are considered critical in comprehensive combustion characterization of premixed flames. The experimentally determined structure, burning speed and thickness of the laminar premixed flames are used to help validate the chemical mechanisms for the combustion reactions. Non-premixed flames, on the other hand, are considered more critical in understanding of the underlying mechanisms of pollutant formation in flames where fuel-air mixing is taking place during the reaction [1–3].

1.1.2 NO formation mechanisms

Nitrogen oxides are a major concern to the environment and are generated by chemical reactions occurring in both premixed and non-premixed flames. Hence, understanding of the underlying kinetics of NO formation and decomposition in flames is imperative for improved NO_x abatement technologies. NO_x chemistry is usually a strong function of the flame temperature as well as the availability of radical concentrations and are exhibited in the following mechanisms [4].

1.1.1.1 Thermal NO

The thermal (Zeldovich) NO mechanism includes the oxidation of N_2 by O and OH radicals at temperatures greater than 1800 K via the following reactions;

$$N_2 + O \leftrightarrow NO + N \qquad \text{(Rxn \# 1.1)}$$

$$N + O_2 \leftrightarrow NO + O \qquad \text{(Rxn \# 1.2)}$$

$$N + OH \leftrightarrow NO + H \quad \text{(Rxn \# 1.3)}$$

Rxn 1.1 is rate limiting among the three pathways, and due to a slower reaction rate compared to fuel oxidation, the radical concentrations of O and OH species are assumed to be at equilibrium yielding NO formation rate as:

$$\frac{\mathrm{d[NO]}}{\mathrm{dt}} = 2k_{1\mathrm{f}} * [\mathrm{O_2}]_{\mathrm{eq}}[\mathrm{N_2}]_{\mathrm{eq}} \quad (1.1)$$

Where $k_{1\mathrm{f}}$ is the forward rate coefficient for Rxn 1.1. Due to very high activation energy (319 kJ/mol), the contribution in NO formation via the thermal route is insignificant below 1500 K, and accurate predictions of temperature and O_2 concentrations are important.

1.1.1.2 Prompt NO

The prompt NO mechanism, also known as the Fennimore mechanism, is related to combustion chemistry of hydrocarbons where the NO production rate is faster even in the low temperature regions, unlike the thermal NO mechanism. In this mechanism, the hydrocarbon radicals react with N_2 to form amines and cyano species, which are then further converted to NO via the following pathways:

$$HCN + O \leftrightarrow NCO + H \quad \text{(Rxn \# 1.4)}$$

$$NCO + H \leftrightarrow NH + CO \quad \text{(Rxn \# 1.5)}$$

$$NH + H \leftrightarrow N + H_2 \quad \text{(Rxn \# 1.6)}$$

$$N + OH \leftrightarrow NO + H \quad \text{(Rxn \# 1.7)}$$

For the prompt NO mechanism, the rate limiting path is the initiation of the N radical from reaction of hydrocarbon radicals with molecular N_2 via:

$$CH + N_2 \leftrightarrow HCN + N \quad \text{(Rxn \# 1.8)}$$

Major differences are reported between the prompt and thermal NO formation pathways, such as temperature range, time scale and chemical kinetics [5,6] . Prompt NO pathways are found to be dominant in premixed flames within an equivalence ratio range from 0.8 to 1.2 just upstream of the flame front. The thermal NO mechanism is most dominant in the post flame regime and has a slower formation rate.

1.1.1.3 Fuel NO

This NO formation route is important for nitrogenous fuel compounds, such as pulverized coal, anhydrous ammonia (NH_3) and heavy distillate fuels, and is generally not important for premixed combustion of natural gas and gasoline. The conversion of fuel-N to NO depends on the local flame temperature, stoichiometry and N-content in the fuel compound. Experimentally, for coal combustion [7], it is shown that fuel-N is converted to the intermediate species HCN and NH_3, which leads to further NO or N_2 formation by branching reactions using free radicals, depending on the local combustion conditions.

1.1.1.4 N_2O pathway

The N_2O pathway, proposed by Pratt and Malte [8], is considered important in lean flames and low temperature conditions. Major steps of the pathway are:

$$O + N_2 + M \Leftrightarrow N_2O + M \qquad \text{(Rxn \# 1.9)}$$

$$N_2O + H \Leftrightarrow NH + NO \qquad \text{(Rxn \# 1.10)}$$

$$N_2O + O \Leftrightarrow NO + NO \qquad \text{(Rxn \# 1.11)}$$

1.1.1.5 NO_2 pathway

The NO_2 formation pathway occurs by the following step:

$$NO + HO_2 \Leftrightarrow NO_2 + OH \qquad \text{(Rxn \# 1.12)}$$

This subsequently leads to NO formation using highly active radicals like CN, OH, H and O via the following reactions:

$$NO_2 + CN \Leftrightarrow NCO + NO \qquad \text{(Rxn \# 1.13)}$$

$$NO_2 + OH \Leftrightarrow HO_2 + NO \qquad \text{(Rxn \# 1.14)}$$

$$NO_2 + H \Leftrightarrow NH + NO \qquad \text{(Rxn \# 1.15)}$$

$$NO_2 + O \Leftrightarrow O_2 + NO \qquad \text{(Rxn \# 1.16)}$$

$$NO_2 + M \Leftrightarrow O + M + NO \qquad \text{(Rxn \# 1.17)}$$

NO_2 pathways contributions towards NO formation are primarily dependent on the local flame temperature and availability of radicals concentrations, mostly in lean fuel-air zones.

1.1.1.6 NNH pathway

In recent studies [9], the contribution of the NNH mechanism towards NO formation, proposed by Bozelli and Dean[10], has been confirmed via the following pathway:

$$O + NNH \Leftrightarrow NH + NO \qquad \text{(Rxn \# 1.18)}$$

where NNH formation occurs via:

$$H + N_2 \Leftrightarrow NNH \qquad \text{(Rxn \# 1.19)}$$

The NNH pathway would be significant in the presence of abundant O radicals, which are mostly encountered in lean-premixed flames like gas-turbine engines.

1.1.2 Planar laser induced fluorescence

The laser induced fluorescence technique has been widely used in fundamental studies of molecular structure, energy transfer, etc., and has been applied in combustion diagnostics widely in recent years. A general background and theoretical overview of the process are discussed briefly in the present section, whereas detailed explanations can be found in references [11,12]. The process of laser induced fluorescence occurs in two stages as illustrated in Fig. 1.2a. In stage 1, the targeted molecule is excited from ground state (X) to an excited state with the absorption of laser energy. The next step consists of spontaneous emission of photons caused due to relaxation of molecules from the excited state back to the ground state. Due to associated energy losses in the process, emission occurs at longer wavelengths than excitation, thus avoiding interference from spurious fluorescence signal caused by laser scattering or Mie scattering.

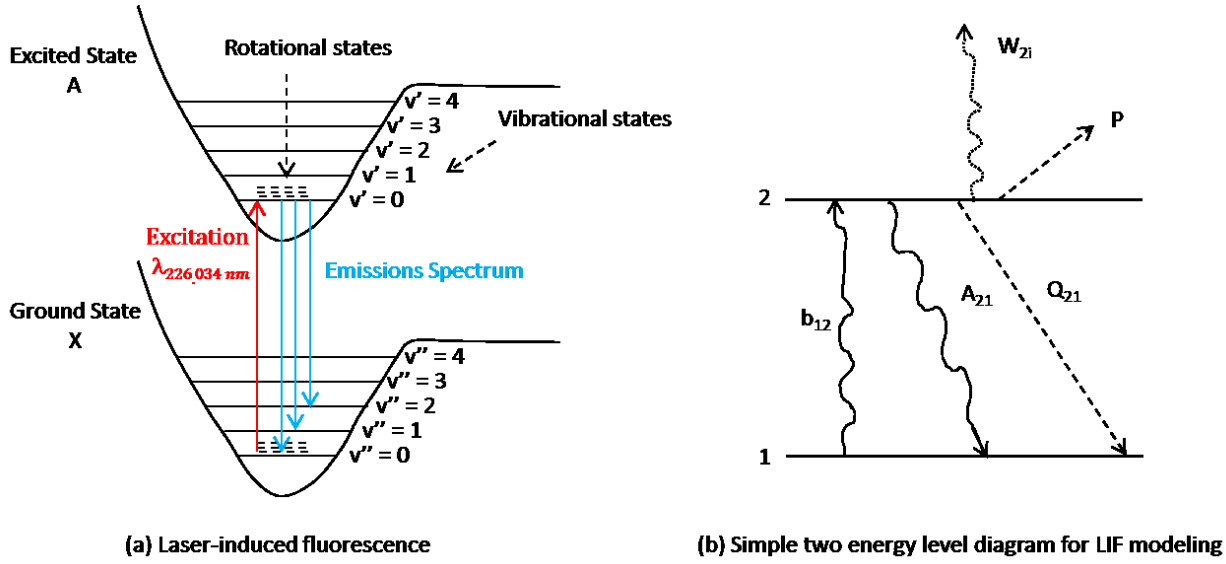

Fig. 1.2. Laser induced fluorescence.

A simple two energy level model of laser induced fluorescence for a molecule is shown in Fig. 1.2b. As can be seen, the excited state losses (from state 2) are caused due to (1) pre-dissociation (P), (2) photo-ionization (W_{2i}) and (3) collisional quenching (Q_{21}) and thus result in weaker fluorescence signal strength. Collisional quenching occurs due to interactions with other molecules, during which the excited state molecules can relax down to the ground state without photon emission. The pre-dissociation and photo-ionization of a molecule are dependent upon specific energy states and thus can be fully eliminated by selecting an appropriate excitation scheme. However, in a combustion environment, the collisional quenching due to the presence of other species is inevitable when using nanosecond (and longer) laser pulses and needs to be accounted for to obtain quantitative measurements of the molecule's concentration.

Typically, in a linear regime, where, fluorescence signal intensity is directly proportional to laser energy, the fluorescence signal intensity can be expressed by eq. 1.2.

$$S_f = E_{laser} * \tau * N_{NO} * f_B * B_{12} * n_{opt} * \left(\frac{A_{21}}{A_{21}+Q_{21}}\right) \quad (1.2)$$

Planar laser induced fluorescence (PLIF) can be utilized easily for the qualitative measurements of species such as OH, HCHO, NO etc.; however, extracting quantitative information from PLIF measurements can be more challenging. For quantitative measurements, the PLIF data need to be corrected for the Boltzmann fraction (f_B) and collisional quenching rate ($\frac{A_{21}}{A_{21}+Q_{21}}$).. The Boltzmann fraction (f_B) represents the population density distribution in the energy states of the target molecule, which has a strong dependence on temperature. On the other hand, the collisional quenching rate represents the quenching of fluorescence signal due to the presence of other species in a combustion environment, which is

dependent on the local temperature and the local species concentrations and their collisional cross sections. Indeed, the quenching of fluorescence signal of species like OH, NO, HCHO etc., by CO, CO_2, CH_4, H_2O, O_2, N_2, OH, H, O species has been studied extensively [13,14] and corresponding quenching correlations have been formulated. This mandates the knowledge of temperature and species concentration distribution in the combustion environment as a pre-requisite. In this challenging situation, often times CFD simulations of flames are used as a complementary tool to obtain the temperature and species concentration mapping.

In addition to Boltzmann fraction and collisional quenching, other corrections related to laser energy, laser beam profile, signal absorption and spectral efficiency of the signal detection system are also needed for accurate quantification of the PLIF signal [15].

1.2 Motivation

In recent years, sustainable energy resources have been developed like H_2, bio-diesel, soy-diesel, pyrolysis oil, bio-fuel. H_2 gained significant attention due to its high energy content, low ignition temperature and practically zero pollutant emissions [16–19]. However due to the lack of H_2 distribution infrastructure, very low volumetric energy density, safety issues and other associated risks due to its low flash point, higher flammability limits, invisible flame, and storage difficulties, implementing a global hydrogen-based economy is a severe challenge, particularly in the transportation sector [20].

Due to the above mentioned challenges with a hydrogen-based economy, anhydrous ammonia (NH_3) is recognized as a potential H_2-carrier and is, therefore, a candidate for being a carbon-free alternative fuel. The recognition of ammonia as a fuel has not only been developed

because of the contemporary research but also from its use during 20th century. The use of ammonia as an alternative combustion fuel dates back well before World War II, when in 1930, an Italy based company obtained a patent for using ammonia as fuel. In Europe, occasionally ammonia was used as a public transportation fuel during WW II. In 1960, the US army tested ammonia extensively and demonstrated successful use of ammonia as fuel in SI engines, slightly modified diesel engines, and gas turbines [21]. Several other recent studies [22–24] analyzed the potential of NH_3 as fuel and concluded that, despite its toxicity, NH_3 is still one of the most attractive carbon-free fuels because it is the second most prevalent chemical in the world and can be synthesized from renewable energy, fossil fuels (via gasification), and from waste heat from nuclear reactors.

There are several advantages to using ammonia as an alternative fuel over hydrogen, which are briefly listed in Table 1.1.

Table 1.1. Anhydrous ammonia (NH_3) fuel advantages over Hydrogen (H_2).

Serial #	H_2	NH_3
1	16 times less volumetric energy density than gasoline at 25 ^{0}C/200 bar pressure.	At 25 ^{0}C /8 bar pressure, volumetric energy density comparable to gasoline [22].
2	Lack in distribution infrastructure.	Already established distribution infrastructure, including pipelines, to deliver in large amounts [23].
3	High flammability limits, low flash points, and invisible flame pose threat of explosions.	Considered non-flammable due to narrow flammability limits. Easily transportable.
4	No characteristic smell. Difficult to detect.	Leaks can be detected easily as low as 5 ppm due to its characteristic odor.
5	Research is onging for IC Engine applications.	High Octane Rating, suitable for IC Engines [25].
6	Not useful as a cooling fluid in vehicles.	Can be used as a refrigerant simultaneously in vehicles, if implemented [22].

Comparison of methanol and liquid hydrogen to anhydrous ammonia was studied by Strickland [24], who showed some remarkable advantages for NH_3 as a transportation fuel in comparison to gasoline. Table 1.2 below shows some characteristics of ammonia fuel compared to other conventional fuels [26–29].

Table 1.2. Properties of NH_3 and other conventional fuels.

Property	Gasoline	Diesel	Natural Gas	H_2	NH_3
Flammability limit, volume % in air	1.4–7.6	0.6–5.5	5–15	4–75	16–25
Auto-ignition temperature, °C	300	230	450	571	651
Peak flame temperature, °C	1977	2053	1884	2000	1850

Anhydrous ammonia (NH_3) has been demonstrated for use in vehicular applications, turbines, engines etc.; however, issues with regard to the lack of understanding of the combustion characteristics, optimized strategies for NO_x abatement in turbulent flames, and inadequate knowledge of NO_x chemistry for NH_3 or NH_3 seeded fuel mixtures, have limited its implementation.

1.3 Objectives

The present research work has the following key objectives:

1) To develop a better understanding of NH_3 through combustion characterization of H_2/NH_3 and CH_4/NH_3 fuel mixtures. In this study, fuel mixtures are characterized in a swirl-stabilized turbulent combustion rig with an approximately 40 kW capacity, and the effects of several parameters like (a) preheated air temperature, (b) equivalence ratio, (c) heat-rate, (d) swirl-plate geometry, (e) nozzle position and geometry and (f) burner

configuration on the flame characteristics like emissions (NO, NO_2, CO, CO_2, UHC, O_2, etc.) and flame temperature are investigated.

2) To develop a detailed chemical mechanism for NH_3-seeded fuel combustion that can predict accurate species concentrations, especially NO. In this study, three contemporary detailed chemical mechanisms are tested by comparing the fundamental flame characteristics, such as flame speed, with the experimental data for laminar H_2 premixed flames with different NH_3 seeding levels.
3) To investigate the performance of the proposed modified GRI-Mech chemical mechanism along with detailed chemical mechanisms (GRI-Mech3.0 and Tian) in predicting the flame structure and species profiles, especially NO formation, in a 2-D laminar diffusion flame by quantitative comparison with the *in-situ* NO concentration measured by NO-PLIF, for H_2/NH_3 fuel mixtures with varying NH_3 seeding level.

1.4 Literature review

The literature review is divided into three sections. The first section starts with discussions of the development of anhydrous ammonia as an alternative fuel for transportation and power generation purposes and elaborates on the challenges associated to bring forth the NH_3 as a fuel.

The second section of the literature review delves into the fundamental studies of the NH_3 seeded flames under both premixed and non-premixed modes. Investigations of NO_x formations chemistry in ammonia seeded flames via flame characterization methods, i.e., flame speed, emissions measurements, reactions kinetics via species measurements, utilizing laser

based diagnostics tools and numerical simulations have been reviewed and discussed. Subsequently, the third section briefly provides an overview of the application of the planar laser induced fluorescence (PLIF) technique for reacting flows.

1.4.1 Anhydrous ammonia (NH_3) combustion

Despite its proven advantages over H_2, anhydrous ammonia (NH_3) has severe challenges associated with achieving clean and stable combustion; it is technically considered non-flammable, has high auto-ignition temperature, low reactivity, toxicity and most important, it is a significant source of NO_x formation if present in the fuel mixture. Use of ammonia as an alternative fuel for vehicular applications has been reported before the WW II era [30]. Later in the mid-60's, the U.S Army probed ammonia characteristics and feasibility for diesel and SI engines with an extensive series of experiments [31–33]. Subsequently, experimental studies were conducted to determine the minimum ignition energy, quenching distance, flame-stability limits, and gas-turbine-burner performance of ammonia-air mixtures [34]. It was concluded that neat ammonia cannot be used as a substitute fuel for hydrocarbons in conventional gas-turbine burners unless the ignition-system energy is increased. The early studies showed that ammonia could provide sustainable combustion when used as a primary fuel or in conjunction with a pilot fuel or spark source in either spark-ignition (SI) or compression-ignition (CI) combustion schemes. In a separate study, Bro & Pederson [35] described the results in terms of engine power output, efficiency, smoke and gaseous emissions of an experimental investigation of methanol, ethanol, methane, and ammonia as primary fuels for a high speed

direct injection diesel engine and noted that although ammonia was applicable, it was least suitable among the four fuels. The idea of using ammonia as a fuel on a global scale couldn't draw much attention due to the then low cost of petroleum based fuels [36]. However, in the last couple decades, the demands of environmentally benign and renewable resources for fuel have increased, and there is an ever increasing interest in ammonia as a fuel for engines, gas turbine combustors and other power generation devices. From the last decades, the research on using NH_3 in engines is increasing; however, limited studies are reported on using ammonia for compression-ignition (CI) and spark-ignition (SI) engines. Saika [37] proposed a clean energy engine-system by using the hydrogen from dissociated ammonia under a catalyst and carried out a fundamental study of the combustion properties of ammonia and dissociated ammonia with air by using a slot burner and a spherical combustion bomb. It was demonstrated that the issues of slow burning speed and the high ignition energy can be solved by adding hydrogen from dissociated ammonia and clearly showed the potential of a partially dissociated ammonia engine system as a promising ammonia fueled system. Later, Mulligan [38] filed a patent for a technology for reducing NO_x in an IC engine fueled by a gaseous hydrocarbon fuel by catalytically producing hydrogen and carbon monoxide fuel gas stream from the gaseous hydrocarbon fuel and a portion of the hot exhaust gas from the internal combustion engine by reacting a portion of the hydrogen produced with ambient nitrogen present in the exhaust gas.

The ammonia produced is used in connection with a selective catalytic reduction reactor to treat the remaining hot exhaust gas produced from the internal combustion engine, resulting in a treated exhaust gas stream having near-zero NO_x emissions. In a separate study, Shawn et al. [39] showed that, with the help of employing an emissions clean up catalyst, engine out

emissions were reasonable at stable combustion conditions for ammonia. However, the authors also pointed out that, lean operation must be absolutely avoided with ammonia for catalytic action with significant quantities of nitrous oxide formed on the catalyst. Later in the same year, a prototype fuel system for producing an emulsion of diesel oil and ammonia was designed and constructed [40] and demonstrated feasibility of combustion of diesel oil/ammonia emulsions in an existing unmodified diesel engine. It also showed that the engine operated successfully on emulsions of fuel oil and ammonia.

In the same time frame, Aaron and Kong [41] tested the feasibility of ammonia combustion by using ammonia seeded diesel as a fuel due to high auto-ignition temperature of ammonia in compression-ignition diesel engines. The results showed that the peak engine torque could be achieved by using different combinations of diesel fuel and ammonia with lower levels of NO_x emissions up to an energy substitution by ammonia under 60%. Subsequently, investigation of the combustion and emissions characteristics of a compression-ignition engine using a dual-fuel approach with ammonia and diesel fuel was performed under the constant engine power operation [42]. Results indicated that in order to achieve favorable fuel efficiency, the preferred operation range was to use 60–40% energy supplied by ammonia. If ammonia accounted for the majority of the fuel energy, NO_x emissions increased significantly due to the fuel-bound nitrogen and pointed to the requirement for the after-treatment of the exhaust. It is recommended that further combustion optimization using direct ammonia/diesel injection strategies be performed to increase the combustion efficiency and reduce exhaust ammonia emissions.

Recently, due to the focus on using metal ammine complexes for ammonia storage, a fuel system for ammonia fuelled internal combustion engines was studied [43]. A series of experiments with varying excess air ratio and different ammonia to hydrogen ratios were conducted in a CFR engine. It was noticed that a fuel mixture with 10 volume% hydrogen outperformed the gasoline counterpart with respect to efficiency and power. It is proposed to reduce the high NO_x emissions using SCR as exhaust after treatment. Based on the current literature review section, the following challenges with NH_3 combustion applications are identified;

1) Ammonia is non-flammable due to its high ignition energy and lower flammability limits.
2) Due to low power output, efficiency, and emissions, NH_3 is a challenging fuel.
3) Lack of conditions and strategies to achieve stable and efficient NH_3 combustion.
4) Since it is established that potential of partially dissociated ammonia engine systems are as promising as conventional fuel engines, the combustion of ammonia and NH_3-H_2 fuel mixtures needs to be well understood.
5) Due to fuel-bound nitrogen, ammonia combustion can lead to high NO_x emissions if not combusted in a controlled environment. However, there is still a need to understand the parameters governing the combustion environment, the NO_x triggering factors, NO_x formation pathways via NH_3, and strategies for ammonia combustion.

1.4.2 Effects of fuel-bound nitrogen on NO_x chemistry

Many conventional fuel options like coal and alternative energy sources like biomass, syngas, etc. have either fuel bound nitrogen or the presence of nitrogenous compounds like

NH_3 and HCN. Both fuel bound nitrogen and nitrogenous compounds may lead to tremendous NO_x formation upon the onset of fuel pyrolysis process in the combustion zone. Thus an improved fundamental understanding of NO_x chemistry in combustion of nitrogenous fuels is imperative for the development of effective NO_x abatement methods and technologies. In this regard, fundamental flame studies of fuel mixture and effects of NH_3, HCN, NO doping on the flame structure as well the NO_x formations has been studied extensively on both premixed and diffusion flames. Lyon [44] and Lyon and Hardy [45] laid the foundation of the thermal De-NO_x process in combustion exhaust gas by investigating high temperature gas-phase NH_3 reactions. Successful numerical simulation of a 2-D axisymmetric, laminar methane-air diffusion flame was demonstrated by Smooke et al. [46], however, investigations related to fuel-N chemistry were not evaluated in this work. In the same year, Sausa et al. [47] performed an experimental and chemical kinetics study of \NH_3 seeded H_2/N_2O/Ar flames at equivalence ratio of 1.1 to understand the fundamental mechanisms for NO formation and destruction, as well to validate the efficacy of NH_3 on the rate of conversion of NO to N_2. Authors utilized the rate and sensitivity analyses to probe the key reaction mechanisms responsible for NO formation and destructions, in a chemical mechanism consisting 20 species and 87 reactions. It was pointed out that adding NH_3 makes chemical rates slow, thus resulting in shifting of the flame away from the fuel nozzle. The numerical model successfully captured the trend of 45% reduction in NO with 4% NH_3 addition.

To understand the kinetics of NO in hydrocarbon fuel mixtures, Rota et al. [48], investigated NO with methane and ethane in an isothermal perfectly stirred reactor within the temperature range 1050 – 1250 K for rich flame conditions with equivalence ratios from 1 to

1.2. The authors used a kinetic model developed by Miller and Bowman [49] for comparison with the experimental data. It was found that at low temperature, effective NO abatement increases with increasing ethane in the fuel mixture; however for higher temperature range the CH_4/C_2H_6 mixture showed larger NO conversion than pure methane. In a similar work, Hasegawa and Sato [50], examined the effects of added NO and O_2 concentration and of CO, H_2 and CH_4 in coal-gasified fuel on NH_3 decomposition characteristics by experiments in a tubular flow reactor and comparison with numerical analysis based on kinetics. Authors concluded that due to the presence of H_2, the reduction of NO to N_2 by ammonia was dominated by the H_2 concentration without any effects from the co-existence of CO.

Later, Zabetta et al. [51], studied the reduction of nitrogen oxides in gas turbine combustors by a detailed chemical kinetics model utilizing a kinetic scheme from Kilpinen et al. [52] and discussed the potential of the chemical kinetics model. They showed that for lower temperatures in the range of 900 -1000 ºC and higher pressure range from 10-20 bar favored fuel-N conversion to N_2. The model also revealed that the conversion efficiency of NH_3 to N_2 enhanced with increasing inlet NH_3, with an important conversion pathway to N_2 via intermediate species, i.e., H_2NO. In a subsequent work, Zabetta and Kilpinen [53] investigated the mechanisms leading to in-cylinder NO_x in compressed ignition engines and developed an improved kinetic model for NO_x prediction using CFD based engine simulations. The developed submodel appeared to be more accurate in predicting NO_x. With an intention to understanding the pathways of fuel-N conversion to NO with and without ammonia seeded CH_4 flames, Sullivan et al. [54] performed a combined experimental and numerical study of NO_x formation in laminar NH_3-seeded, N_2-diluted, methane (surrogate for biomass fuel)

diffusions flames. The GRI-Mech3.0 mechanism and a chemical mechanism developed by Glarborg et al. [55] were used for the numerical modeling. The authors focused on the understanding of the pathways of fuel-N conversion to NO with and without ammonia seeded flames. The model utilizing Glarborg mechanism reported to be in agreement with the measurements over the full range of NH_3 doping, and NO concentration seemed to be reduced with increasing NH_3 due to enhanced conversion rate of NO to N_2. Later, Laurie [56] tested several reduced chemical kinetics schemes, i.e. extended Zeldovich and five schemes involving N_2O pathways and compared NO_x predictions for a slow-speed marine diesel engine utilizing a 0-D model. The model predicted 15% additional NO_x with the addition of nitrous oxide reactions and the N_2O pathways were identified as the most significant contribution to NO_x. Zabetta et al. [57], in a separate study of comparing NO_x abatement methods, i.e. fuel staging (FS), air staging (AS), and selective non-catalytic reduction (SNCR) with a newly developed strategy named, combined staging (CS) by combining FS, AS and SNCR in synergy. It was found that CS is effective in cutting up to 40% NO_x at lower temperatures and within shorter residence time, with limitations in absence of burnout air staging. For diesel NO_x emissions kinetics modeling, Hernandez et al. [58] investigated the role of the kinetics on the local NO formation/destruction paths under diesel engine conditions by utilizing a kinetic scheme with 83 reactions and 38 species. Both NO production and decomposition pathways were identified through a sensitivity analysis on CHEMKIN 4.0. Authors also revealed a coupling between fuel oxidation and the thermal NO mechanism, typically ignored for diesel engine modeling.

Zieba et al. [59], investigated the nitrogen chemistry in an ammonia (NH_3) seeded flameless jet by utilizing a kinetic reactor network model to discuss the primary causes of

differences in ammonia chemistry for methane-free and methane-laden fuel mixtures. They observed that for methane flames, NH_3 reacted relatively late at fuel lean conditions leading to high NO_x formation, and ammonia chemistry was found to be blocked due to consumption of free radicals for the conversion of methane to the methyl radical. For methane-free composition, the reaction rate of NH_3 was reported to be rapid and radicals were generated from H_2 oxidation. Due to important of pathways between NH_2 and OH in the combustion chemistry of nitrogenous fuel mixtures, Mousavipour et al. [60] numerically investigated the fundamental mechanism of the reaction of amidogen with OH radicals. Later, Duynslaegher et al. [61] investigated the effects of initial H_2 content on the structures of diluted NH_3-H_2-O_2-Ar flames at low pressure in near stoichiometric conditions and compared the experimental data with predictions using the Konnov mechanism. The work was focused on the nitric oxide formation pathways at several conditions of ammonia combustion. It was found that a decrease in equivalence ratio strongly increased NO formation, and the Konnov mechanism's predictions showed agreement with experimental data except NH_2 and N_2O species. Subsequently, Shmakov et al. [62], investigated the formation and generation of nitric oxide (NO) in flat premixed burner-stabilized $H_2/O_2/N_2$ flames doped with 300 – 1000 ppm of NO or NH_3 by incorporating numerical modeling. Although, the measured spatial profiles of temperature and major species like H_2, O_2, H_2O, NO, NH_3 were found to be in fairly good agreement with the modeling results for lean and near stoichiometric flames, the model failed to predict the NO concentration for fuel rich conditions. Overall, recommendations for modifications of the model were proposed.

This literature survey reveals that numerous attempts have been made to understand the NO formation pathways in NH_3 seeded flames in both premixed and non-premixed flames. Several detailed chemical mechanisms for NH_3 seeded flames have been developed and validated with partial success, meaning they performed fairly well for some flame conditions but failed to capture the flame chemistry under other flame conditions. Reasonable success has been gained to identify the key NO formation pathways which has contributed towards the development of the reduced chemical mechanisms concepts. Reduced chemical mechanisms for NH_3 flames have also been demonstrated with limited success for some cases but still require more work to be able to capture the key flame chemistry for NH_3 seeded flames.

Despite a number of studies of NO formation pathways in NH_3 seeded flames; understanding of NO chemistry in NH_3 seeded flames requires further improvement, particularly NH_3/H_2/air flames. Several contemporary chemical mechanisms, especially the Tian, Konnov and GRI-Mech3.0 chemical mechanisms have been tested and validated by variety of test conditions and tools. However, the three chemical mechanisms have not yet been compared under identical flame conditions to study the relative performance of the chemical mechanisms as well as to understand the cause of disagreements among them.

Hence, the present work includes a detailed investigation of the chemical pathways of NO formation and detailed comparisons of contemporary chemical mechanisms, i.e., Tian, Konnov and GRI-Mech3.0, for the first time, to gauge not only their individual robustness but also reveal the cause of disagreements among the chemical mechanisms. These mechanisms are employed along with numerical simulations based on computational fluid dynamics with chemistry (CFDC) to study *in situ* NO concentrations. Predictions of flame structure are

compared with flame-speed measurements, and concentrations are compared with laser-based measurements, as described below, as well as exhaust-gas probe sampling methods. This detailed comparison of three key mechanisms, more extensive experimental validation, and analysis of individual reaction steps within the chemical mechanisms all constitute unique contributions of this work.

1.4.3 PLIF diagnostics of reacting systems

A number of imaging diagnostics are utilized for reactive flows, including Mie scattering [63], Rayleigh scattering [64], chemiluminescence or natural light emissions from radicals [65,66], and laser induced fluorescence [67,68], among others.

In early studies [69,70], for a non-direct local heat release measurement in the flame zone, radiations from the free radicals like CH, C_2 are shown to be directly related to the reaction intensity and thus to the heat-release process. Later, it is realized that the identification of the species in the combustion environment can serve as a marker of the flame front and high temperature zone, like OH in H_2 flames and C_2 and CH in hydrocarbon flames. In addition to that, the direct imaging of NO species in flames can be utilized to deduce the dependence of NO_x chemistry on local temperature and surrounding species concentrations, which accelerated the investigations of NO by PLIF in flames. As an application to visualize a hypersonic flow field over a wedge and a hemisphere, planar laser induced fluorescence (PLIF) of NO is employed by Danehy et al. [71] and results were compared with the theoretical PLIF model based on computational fluid dynamics models including ideal-gas and non-equilibrium

chemistry. The technique was reported to be in successful agreement between modeling and experimental results.

Reisel et al. [72] demonstrated the feasibility of quantitative LIF measurements of NO in high pressure ethane-air flames and showed the potential for NO measurements down to ~1 ppm at pressures up to 9 atm. Later, Cooper and Laurendeau [73] reported the influence of air preheating temperature and equivalence ratio on NO concentration in high pressure, swirl-stabilized heptane spray flames using quantitative laser induced fluorescence. It was observed that, for near stoichiometric regions in the flame zone, prompt NO formation and NO concentration increased with increasing preheat temperature. The authors also developed a laser-saturated fluorescence (LSF) technique for quantitative measurements of NO concentration in spray flames [74] and subsequently implemented the LSF technique to study the effects of equivalence ratio on nitric oxide for unconfined liquid heptane flames in LDI burners [75]. It was demonstrated that the entrained excess air reduced NO concentrations at fuel lean flame conditions.

Subsequently, D. Charlston-Goch [76] performed the investigation of the NO_x chemistry by comparing the laser induced fluorescence measurements of NO concentrations in flames of synthesized coal-gas for a pressure range from 1 to 11.9 atm, with the predictions utilizing GRI-Mech2.11 and Kilpinen's chemical mechanisms. On comparison, GRI-Mech2.11 mechanism over-predicted NO concentration, whereas Kilpinen's mechanism captured the NO trend with under prediction in NO concentration. They proposed NNH pathway inclusion to Kilpinen's mechanism improved agreement with the experimental data. Similarly, Thomsen and Laurendeau [77], measured the NO concentration with laser induced fluorescence (LIF) in

a flat, laminar premixed counterflow $CH_4/O_2/N_2$ flame with equivalence ratios from 0.65 to 1.5. This particular flame structure allowed the measurement of nitric oxide in preheat, flame-front, and post-flame zones. The experimental data was compared to the NO predictions by the Sandia opposed diffusion flame code utilizing GRI mechanism 2.11. For lean conditions, agreement between experimental and modeling results was found to be remarkably close, but moderate agreement was found for rich flames with respect to NO concentration and the shape of the NO profiles.

Romain et al. [78] measured in-cylinder qualitative NO concentrations in a diesel compression machine using laser induced fluorescence and corrected it based on the measurements of heat-release rate and flame structure information utilizing OH LIF. It is reported that the NO formation started at the onset of the diffusion flame and fuel lean pockets in diffusion flames were more favorable for NO_x formation.

A literature review reveals that laser diagnostic tools have been applied in a large number of studies related to fundamental flame characteristics, i.e. particle image velocimetry (PIV) for flow field measurements and laser-induced fluorescence for local species concentrations. Planar laser-induced fluorescence has been extensively applied and has been successful in majority of the cases in studying spatial distributions of species concentration. This has helped with understanding the chemical pathways behind the species formation, especially when coupled with computational fluid dynamics (CFD) tools. The coupling of the PLIF technique and CFD has been demonstrated as a powerful tool to study the fundamental flame chemistry and has led to significant contributions toward successful development or improvements in chemical mechanisms for various fuels.

In the present work, the PLIF technique for NO species has been applied for laminar diffusion NH_3/H_2/air flames for the validation of complex chemical mechanisms that are commonly utilized in a variety of current research efforts (i.e. Tian, GRI-Mech3.0, etc.) for NH_3 seeded H_2-air flames. To the best of our knowledge, the application of the PLIF technique for ammonia seeded H_2-air flames has not been investigated yet.

For accurate NO PLIF measurements, the estimation of Boltzmann fraction correction and quenching corrections are critical, which are strongly correlated to the flame temperature and species concentrations. Hence, a state-of-the-art 2-D CFD numerical code i.e. Unsteady Ignition and COmbustion with ReactiOns (UNICORN) [79] is used to predict the flame temperature and species concentrations, which further is incorporated into both the Boltzmann fraction and quenching corrections. The predicted 2-D NO mole fractions profiles are then converted to simulated 2-D NO PLIF signals (arbitrary unit; counts) by incorporating Boltzmann fraction and quenching corrections from the predicted flame temperature and major species concentrations. A lean premixed CH_4-air flame seeded with known NO concentration is used with the identical PLIF setup to estimate the conversion of NO mole fractions into arbitrary units (counts). This method of comparison avoids the discrepancy caused due to flame length adjustment and leads to a direct test of the chemical kinetics within the CFD code (see Chapter 5).

1.5 Thesis organization

Chapter 2 presents the detailed combustion characterization of swirl-stabilized turbulent flames for H_2-NH_3 and CH_4-NH_3 fuel mixtures, in a custom-made 40 kW swirl-stabilized

turbulent combustor. Also, the strategies are presented to achieve 100% anhydrous ammonia (NH_3) combustion with ultra-low NO_x. Chapter 3 discusses the fundamental investigation of flame speeds and validation of chemical mechanisms, e.g. the Konnov, Tian and GRI-Mech3.0 chemical mechanisms, for laminar freely propagating premixed H_2-NH_3 flames.

Subsequently, Chapter 4 summarizes the effects of NH_3 doping on NO_x formation chemistry in H_2-NH_3 laminar premixed flames and compares predictions using the Konnov, Tian and GRI-Mech3.0 chemical mechanisms. Chapter 5 presents detailed descriptions of the NO-PLIF setup and summarizes the results for 2-D quantitative comparison of NO concentration between CFD modeling and *in-situ* NO-PLIF for H_2-NH_3 laminar diffusion flames. Chapter 6 provides the conclusions and recommendations for future work.

1.6 References

[1] Santoro RJ, Semerjian HG, Dobbins RA. Soot particle measurements in diffusion flame. Combustion and Flame 1983;51:203-218.

[2] Santoro RJ, Semerjian HG. Soot formation in diffusion flames: flowrate, fuel species and temperature effects. Twentieth Symposium on Combustion 1984:997-1006.

[3] Santoro RJ, Yeh TT, Horvath JJ. The transport and growth of soot particles in laminar diffusion flames. Combustion Science and Technology 1987;52:89-115.

[4] Bowman CT. Control of combustion-generated nitrogen oxide emission: technology driven by regulations. Twenty-Fourth Symposium on Combustion 1992:859-572.

[5] Fenimore CP. Formation of nitric oxide in premixed hydrocarbon flames. Symposium (International) on Combustion 1971;13(1):373-380.

[6] Drake MC, Ratcliffe JW, Carter RJ, Laurendeau NM. Measurements and modeling of flamefront NO formation and super-equilibrium radical concentrations in laminar high-pressure premixed flames. Symposium (International) on Combustion 1991;23(1).

[7] Glarborg P. Fuel nitrogen conversion in solid fuel fired systems. Progress in Energy and Combustion Science 2003;29(2):89-113.

[8] Pratt DT, Malte PC. Formation of thermal and prompt nitrogen oxide (NO_x) in a jet-stirred combustor. AICHE Journal 1975;71(148):150.

[9] Konnov AA, Colson G, De Ruyck J. The new route forming NO via NNH. Combustion and Flame 2000;121(3):548-550.

[10] Bozzelli JW, Dean AM. O + NNH: a possible new route for NO_x formation in flames. Int. J. Chem. Kinet. 1995;27(11):1097-1109.

[11] Eckbreth AC. Laser diagnostics for combustion temperature and species. Hartford, Connecticut: Gordon and Breach, 1996.

[12] Daily JW. Laser induced fluorescence spectroscopy in flames. Progress in Energy and Combustion Science 1997;23:133-199.

[13] Tamura M, Berg PA, Harrington JE, Luque J, Jeffries JB, Smith GP, Crosley DR. Collisional quenching of CH(a), OH(a), and NO(a) in low pressure hydrocarbon flames. Combustion and Flame 1998;114(3-4):502-514.

[14] Paul PH, Gray JA, Durant JL, Thoman JW. A model for temperature-dependent collisional quenching of NO $A^2 \sum +$. Combustion 1993;259(X):249-259.

[15] Gibaud C, Snyder JA, Sick V, Lindstedt RP. Laser-induced fluorescence measurements and modeling of absolute CH concentrations in strained laminar methane/air diffusion flames. Proceedings of the Combustion Institute 2005;30(1):455-463.

[16] Goltsov VA, Veziroglu TN. From hydrogen economy to hydrogen civilization. World Health 2001;26:909-915.

[17] Veziroglu TN, Momirlan M. Current status of hydrogen energy. Renewable & Sustainable Energy Reviews 2002;6:141-179.

[18] Goltsov V, Veziroglu T, Goltsova L. Hydrogen civilization of the future: a new conception of the IAHE. International Journal of Hydrogen Energy 2006;31(2):153-159.

[19] Veziroglu T, Sahin S. 21^{st} century's energy: hydrogen energy system. Energy Conversion and Management 2008;49(7):1820-1831.

[20] Jensen J, Vestbo A, Li Q, Bjerrum N. The energy efficiency of onboard hydrogen storage. Journal of Alloys and Compounds 2007;446-447:723-728.

[21] Bomelburg HJ. Use of ammonia in energy-related applications, plant/operations progress. Plant/Operations Progress 1982;1(3):175–180.

[22] Zamfirescu C, Dincer I. Using ammonia as a sustainable fuel. Journal of Power Sources 2008;185(1):459-465.

[23] Blarigan PV. Advanced internal combustion engine research. Proceedings of the 2000 DOE Hydrogen Program Review. 2000: 1-19.

[24] G. Strickland. Ammonia as a hydrogen energy storage medium. In: 5th annual thermal storage meeting; paper 8010555-2. McLean, VA, USA.: 1980.

[25] Feibelman PJ, Stumpf R. Comments on "potential roles of ammonia in a hydrogen economy" a study of issues related to the use of ammonia for on-board vehicular hydrogen storage. 2008.

[26] Brandhorst H, Tartachuk B, Cahlea D, Barron T, Baltazar-Lopez M. Ammonia transformation and utilization. In: Proc. of the ammonia – sustainable, emission free fuel conference. San Francisco, CA: Iowa Energy Center. 2007.

[27] McFarlan A. Development of direct ammonia fuel cells for efficient stationary CHP applications. In: Proc. of the ammonia – sustainable, emission free fuel conference. San Francisco, CA: Iowa Energy Center. 2007.

[28] Olson N. Bio-ammonia— a comparison with other biofuels. In: Proc. of the ammonia – sustainable, emission free fuel conference. San Francisco, CA: Iowa Energy Center. 2007.

[29] Lide DR. CRC handbook of chemistry and physics. Boca Raton, Florida: CRC Press, 1991.

[30] Gray J. Dimitroff TE, Meckel NT, Quillian RD. Ammonia fuel – engine compatibility and combustion. In: SAE paper 660156. 1966.

[31] Pearsall TJ, Garabedian CG. Combustion of anhydrous ammonia in diesel engines. In: SAE paper 670947. 1967.

[32] Starkman ES, Newhall HK, Sutton R, Maguire T. Farbar L. Ammonia as a spark ignition engine fuel: theory and application. In: SAE paper 660155. 1966.

[33] Verkamp FJ, Hardin MC, William JR. Ammonia combustion properties and performance in gas-turbine burners. Symposium (International) on Combustion 1967;11(1):985-992.

[34] Bro K, Pederson PS. An experimental investigation of methanol, ethanol, methane and ammonia in a DI diesel engine with pilot injection. In: SAE paper 770794. 1977.

[35] Bro K, Pedersen PS. Alternative diesel engine fuels: an experimental investigation of methanol, ethanol, methane and ammonia in a DI diesel engine with pilot injection. SAE Prog. Technol; (United States) 1980;19.

[36] Cooper JR, Crookes RJ, Mozafari A, Rose JW. Ammonia as a fuel for the IC engine. In: Proceedings of the international conference on environmental pollution. 1991.

[37] Saika T. Study of an ammonia fueled engine as a clean energy system. Journal of the Japan Institute of Energy 2000;79(6):530-539.

[38] Mulligan DN. Internal Combustion Engine with SCR and Integrated Ammonia Production. U.S. Patent US Patent App. 10/293,020, 2002.

[39] Grannell S, Gillespie D, Assanis D, Bohac S. Emissions characterization of an ammonia - gasoline SI engine. In: Ammonia conference – the key to US energy independence. Minneapolis, MN: 2008.

[40] Agosta V, Harbach J. Use of liquid ammonia fuel emulsions in a diesel engine. In: Ammonia conference – the key to us energy independence. Minneapolis, MN: 2008.

[41] Reiter AJ, Kong SC. Demonstration of compression-ignition engine combustion using ammonia in reducing greenhouse gas emissions. Energy & Fuels 2008;22(5):2963-2971.

[42] Reiter AJ, Kong SC. Combustion and emissions characteristics of compression-ignition engine using dual ammonia-diesel fuel. Fuel 2011;90(1):87-97.

[43] Morch CS, Bjerre A, Gottrup MP, Sorenson SC, Schramm J. Ammonia/hydrogen mixtures in a SI-engine: engine performance and analysis of a proposed fuel system. Fuel 2011;90(2):854-864.

[44] Lyon RK. U.S. Patent 3,900,554, 1975.

[45] Lyon RK, Hardy JE. Discovery and development of the thermal DE-NO_x process. Ind. Eng. Chem. Fundamental 1986;25:19-24.

[46] Smooke M. Computational and experimental study of NO in an axisymmetric laminar diffusion flame. Symposium (International) on Combustion 1996;26(2):2161-2170.

[47] Sausa RC, Singh G, Lemire GW, Anderson WR. Molecular beam mass spectrometric and modeling studies of neat and NH_3-doped low-pressure H_2/N_2O/Ar flames : formation and consumption of NO. Combustion 1996:1043-1052.

[48] Rota R, Morbidelli M, Carra S. Combustion kinetics of light hydrocarbons in the presence of nitrogen oxide 1998;(2):4241-4252.

[49] Miller JA, Bowman CT. Mechanism and modeling of nitrogen chemistry in combustion. Progress in Energy and Combustion Science 1989;15(4):287-338.

[50] Hasegawa T, Sato M. Study of ammonia removal from coal-gasified fuel. Combustion and Flame 1998;114(1-2):246-258.

[51] Kilpinen PT, Leppälahti JK, Zabetta EGC, Hupa MM, Kilpinen P. Gas-phase conversion of NH_3 to N_2 in gasification part (I) : a kinetic modeling study on the potential of the method :Combustion 1999;(199901).

[52] Kilpinen P, Hupa M, Aho M, Hämäläinen J. In: 7th international workshop on nitrous oxide emissions. Bergische Universität Gesamthochschule Wuppertal: Cologne, Germany,: 1997.

[53] Zabetta EC, Kilpinen P. Improved NO_x submodel for in-cylinder CFD simulation of low and medium speed compression ignition engines. Energy & Fuels 2001;15:1425-1433.

[54] Sullivan N. Ammonia conversion and NO_x formation in laminar co-flowing nonpremixed methane-air flames. Combustion and Flame 2002;131(3):285-298.

[55] Glarborg P, Jensen AD, Johnsson J. Fuel nitrogen conversion in solid fuel fired systems. Prog. Energy Combust. Sci. 2003;29(2):89-113.

[56] Goldsworthy L. Reduced kinetics schemes for oxides of nitrogen emissions from a slow-speed marine diesel engine. Energy & Fuels 2003;17(2):450-456.

[57] Zabetta EC, Hupa M, Saviharju K. Reducing NO_x emissions using fuel staging, air staging, and selective non-catalytic reduction in synergy. Ind. Eng. Chem. Res. 2005:4552-4561.

[58] Hernández JJ, Collado P, Sanz JA. Role of the chemical kinetics on modeling NO_x emissions in diesel engines. Energy & Fuels 2008;22:262-272.

[59] Zieba M, Brink A, Schuster A, Hupa M, Scheffknecht G. Ammonia chemistry in a flameless jet. Combustion and Flame 2009;156(10):1950-1956.

[60] Mousavipour SH, Pirhadi F, Habibagahi A. A theoretical investigation on the kinetics and mechanism of the reaction of amidogen with hydroxyl radical. The Journal of Physical Chemistry. A 2009;113(46):12961-71.

[61] Duynslaegher C, Jeanmart H, Vandooren J. Flame structure studies of premixed ammonia/hydrogen/oxygen/argon flames: experimental and numerical investigation. Proceedings of the Combustion Institute 2009;32(1):1277-1284.

[62] Shmakov AG, Korobeinichev OP, Rybitskaya IV, Chernov A, Knyazkov DA, Bolshova TA, Konnov AA. Formation and consumption of NO in H_2+O_2+N_2 flames doped with NO or NH_3 at atmospheric pressure. Combustion and Flame 2010;157(3):556-565.

[63] Boyer L. Laser tomographic method for flame front movements studies. Combustion and Flame 1980;39:321-323.

[64] Escoda MC, Long MB. Rayleigh scattering measurements of the gas concentration field in turbulent jets. AIAR 1983;21:81-84.

[65] Darabiha N, Giovangigli V, Trouvé A, Candel S, Eposito E. Coherent flame description of turbulent premixed ducted flames. Proc. France-USA Joint Workshop on Turbulent Combustion 1989:591-637.

[66] Candel S, Veynante D, Lacas F, Maistret E, Darabiha N, Poinsot T. Coherent flamelet model: applications and recent extensions. Recent Advances in Combustion Modeling 1991:19-64.

[67] Hanson RK. Combustion diagnostics: planar imaging techniques. Twenty-first Symposium on Combustion 1986:1677-1691.

[68] Hanson RK. Planar laser-induced fluorescence. J. Quant. Spectrosc. Radiat. Transfer 1988;40:343-362.

[69] John RJ, Wilson ES, Summerfield M. Studies of the mechanism of flame stabilization by a spectral intensity method. Jet Propulsion 1955;25:535.

[70] John RR, Summerfield M. Effect of turbulence on radiation intensity from propane-air flames. Jet Propulsion 1957:169-179.

[71] Danehy PM, Palma PC, Boyce RR, Houwing AFP. Numerical simulation of laser-induced fluorescence imaging in shock-layer flows. AIAA Journal 1999;37:715-722.

[72] Reisel JR, Carter CD, Laurendeau NM. Laser-induced fluorescence measurements of nitric oxide in laminar $C_2H_6/O_2/N_2$ flames at high pressure. Combustion and Flame 1993;92(4):485-489.

[73] Cooper CS, Laurendeau NM. Parametric study of NO production via quantitative laser-induced fluorescence in high-pressure, swirl-stabilized spray flames. Combustion 2000;28:287-293.

[74] Cooper CS, Laurendeau NM. Quantitative laser-saturated fluorescence measurements of nitric oxide in a heptane spray flame. Combustion Science and Technology;127:363–382.

[75] Cooper CS, Laurendeau NM. Quantitative laser-saturated fluorescence measurements of nitric oxide in a heptane-fueled lean direct-injection spray flame at varying global equivalence ratios. Combustion 2000;(x):1993-2000.

[76] Charlston GD, Chadwick B, Morrison RJ, Campisi A, Thomsen D, Laurendeau NM. Laser-induced fluorescence measurements and modeling of nitric oxide in premixed flames of $CO+H_2+CH_4$ and air at high pressures: nitrogen fixation. Combustion and Flame ;125(1):729-743.

[77] Thomsen DD, Laurendeau NM. LIF measurements and modeling of nitric oxide concentration in atmospheric counterflow premixed flames. Combustion and Flame 2001;124(3):350-369.

[78] Demory R, Crua C, Martin RG, Morgan RH. Measuring and processing in-cylinder distributions of NO and OH obtained by laser-induced fluorescence in a diesel rapid

compressions machine. In: 13th int. symp. on applications of laser techniques to fluid mechanics. 2006.

[79] Katta VR, Roquemore WM. Role of flow visualization in the development of unicorn. In: Proceedings of vsj-spie98. 1998. p. 1-16.

CHAPTER 2. EXPERIMENTAL PARAMETRIC STUDIES OF THE EFFECTS OF NH_3 IN LAMINAR AND TURBULENT DIFFUSION FLAMES

A paper to be submitted to *Fuel* Journal

Praveen Kumar and Terrence R. Meyer*

Abstract

In this paper, an extensive combustion characterization of NH_3 % by energy in H_2 ($E\%NH_3$) for H_2/NH_3 and CH_4/NH_3 fuel mixtures are studied for both laminar and turbulent flame regimes in a Hencken burner and a swirl-stabilized turbulent furnace, respectively. For swirl-stabilized turbulent flame, a detailed parametric study of several variables i.e., (1) preheated air temperature, (2) equivalence ratio, (3) heat-rate, (4) swirl geometries, (5) fuel nozzle type and positions and (6) burner configurations was performed at heat-rates from 8-35 kW, typical for a house-hold heating unit. This study is important for practical applications of NH_3-H_2-CH_4 fuel mixtures in both domestic and industrial sectors. At equivalence ratio ~1, the installation of a swirl stabilizer and preheating of co-flow air from 25 to 300 ºC resulted in the significant increase in NH_3 replacement by 30% and 70% for methane-ammonia and hydrogen-ammonia fuel mixtures respectively. However, it also confirmed increased NO_x emissions with increasing preheated air temperature and $E\%NH_3$ for both the fuel mixtures. The nozzle configurations are found to have a significant effect in terms of achieving higher $E\%NH_3$ and the change in fuel nozzle position is shown to have a critical effect on the NO_x emissions and $E\%NH_3$. The effect of the ratio of moles of NH_3 to CH_4 for the CH_4/NH_3/air mixture is also

* Department of Mechanical Engineering, Iowa State University, Ames, IA 50011, USA
* Corresponding author. Tel: +1 515 294 1805.
* E-mail address: trm@iastate.edu

recorded; the data is in reasonable agreement with previous works, and shows gradual reduction in NO concentration and E%NH_3 with decreasing NH_3 to CH_4 mole ratio.

2.1 Introduction

In today's world, the increasing use of fossil fuels has not only driven technological advancements but poses a threat to the environment by continuously generating pollutant emissions. These emissions are also considered to be the major cause behind global warming. Two alternatives for fossil fuels that are attracting many researchers around the globe are H_2 and NH_3. These surrogates, also known as the clean fuel [1], have no fuel bound carbon, and do not produce carbon compounds during combustion .

Initially hydrogen gained researcher's interest with the potential to produce only H_2O as a product. However, due to severe challenges in hydrogen storage technologies, attention has also turned towards NH_3 as hydrogen carrier [2]. Several studies [3,4] have investigated the potential of ammonia as a promising fuel and found that, despite its toxicity and high ignition temperature, there are many remarkable advantages including (i) higher octane rating (ii) easy production and storage (iii) and recyclability, to name a few. Due to continued interest, ammonia combustion has been studied for applications in IC engines, turbine engines, fuel cells, etc. Both theoretical and experimental investigations of ammonia combustion have shown that it has a potential to be combusted in both spark-ignition (SI) and compression-ignition (CI) engines by decomposing the NH_3 into H_2 and N_2 [5]. However, in the SI engine operation, higher NO_x levels were measured with high concentrations of ammonia. Reiter and Kong [6] demonstrated the effect of mixing NH_3 with diesel on greenhouse gas emissions in

compression-ignition (CI) engines. They successfully achieved 95% energy replacement by ammonia in a diesel-ammonia fuel mixture and confirmed attrition in CO_2 emissions as ammonia in the fuel mixture increased. To ensure the safe operation of ammonia or ammonia-blended alternative fuels, it is imperative to study the flammability limit of the fuel mixture. Ciccarelli et al. [7] studied the flammability of the hydrogen and ammonia in air and mixtures of H_2-NH_3-air at initial temperatures ranges from 25 ºC to 600 ºC. They showed widening of flammability limits with an increase in initial temperature for H_2-air and NH_3-air, confirming the Le-Chatelier principle.

Earlier work on flames, with or without ammonia seeding, have studied the NO_x formation mechanisms extensively [8–10]. Several significant NO producing mechanisms are proposed. The nitrogen chemistry modeled by Miller and Bowman [11] predicted the main chemical formation routes of NO_x. It has been established that this pollutant is generated in ammonia seeded flames in two ways: the Zeldovich mechanism and through fuel-bound nitrogen. Sarofim et al. [12] demonstrated experimentally that the conversion efficiency of NH_3 to NO declines with increasing NH_3 seeding in non-premixed flames and validated the measured data by numerical simulations. Likewise, Sullivan et al. [13] reported the experimental and modeling investigation of NH_3 conversion and NO_x formation in laminar methane-air diffusion flames. They found that at low NH_3 concentrations in the fuel mixture, the conversion efficiency of ammonia to NO is 50% less likely to the high NH_3 concentration, where the conversion efficiency is as low as 30%. Subsequently, Tian et al. [14] reported an experimental and kinetic modeling study of premixed $NH_3/CH_4/O_2$/Ar flames and proved that

increases in the ratio of moles of NH_3 to the moles of CH_4 in the fuel mixture (R_{NH3}) results in higher NO formation.

NO measurements performed by Bell et al. [15] with varying NH_3 seeding in methane-air laminar diffusion flames were found to be dominated by the fuel-NO formation mechanism, whereas the prompt NO pathway was dominant for NH_3 absent fuel. Duynslaegher et al. [16] carried out numerical and experimental flame structure studies of premixed ammonia-hydrogen-air flames and showed that in near stoichiometric conditions, a decrease in equivalence ratio strongly accelerates the NO production rate. Duynslaegher et al. also concluded that temperature and equivalence ratio must be well controlled in practical combustors. Later, the properties of laminar premixed H_2 added ammonia-air flames were studied experimentally and computationally by Lee et al. [17] and it was concluded that H_2 substitution results in high burning velocities and NO_x shows a substantial increase at fuel lean conditions. They established that in ammonia seeded flames, the primary mechanism for NO production is through fuel-bound atomic nitrogen. Later, to reduce the inevitable NO generation from the fuel-NO mechanism, Kang et al. [18] demonstrated that a two-step fuel-rich/fuel-lean catalytic combustion is one of the most effective methods to control NO and achieved below 5% conversion efficiency of NH_3 to NO.

This literature review reveals that significant research has been carried out on the understanding of the flame structure and NO_x formation mechanisms for ammonia doped flames. However, the study of energy replacement by ammonia and NO_x formation with respect to several practical parameters such as fuel nozzle geometry, fuel nozzle position, preheated air temperature, and the ratio of ammonia to fuel (R_{NH3}) for CH_4/NH_3 and H_2/NH_3

fuels mixtures at practical flow-rate and heat-rate settings, has not been yet addressed. The comparison of results with laminar flames shows significant differences in characteristics, which provides good insight into NH_3 flame chemistry. Another motivation behind the work is to study combustion with heat rates in the range of 15-30 kW, in contrast to studies in IC engines, with typical heat rates of more than 60 kW.

2.2 Experimental setup and methods

The experimental setup is divided into two sections, (1) Hencken burner setup and (2) Swirl-stabilized turbulent diffusion flame setup.

2.2.1 Hencken burner setup

For laminar non-premixed flame investigations, a Hencken burner was employed. A good detailed elaboration of the Hencken burner is noted in the literature [19], and is briefly discussed here. The Hencken burner produces a flat diffusion flame, uniform, steady and approximately adiabatic. Schematics of the experimental setup and burner cross-section view are shown in Figs. 2.1a and 2.1b, respectively. The commercially available hydrogen and methane gases were employed as fuels for separate studies. The ammonia is mixed with the fuel in a tee-shaped manifold, far ahead of the burner to ensure the homogeneous mixing and fully developed flow at the burner exit. Metered quantities of H_2 or CH_4 and air in standard liter per minute (slpm) are supplied through respective gas cylinders using Alicat mass flow controllers having accuracy of ± (0.8% of reading + 0.2% of full range) operated through the LabView program. NH_3 is metered using an Aalborg rotameter (± 1% full scale). The flames are visualized by using a high resolution charge-coupled device (CCD) camera. Table 2.1

below shows the test conditions in laminar non-premixed flames for both the fuel mixtures. There are a total 4 test conditions for the CH_4/NH_3 fuel mixture. The H_2/NH_3 mixture is tested at only 2 conditions.

Table 2.1. Test runs for CH_4/NH_3 and H_2/NH_3 laminar non-premixed flames (Hencken burner).

	$\dot{Q}_{mix}$	∅	Heat Rate (KW)	E%NH_3 (Range)
CH_4/NH_3	5	0.95	0.275	0 – 47.3
	10	0.95	0.55	0 – 22.4
	16	0.95	0.87	0 – 22.1
	20	0.95	1.1	0 – 19.3
H_2/NH_3	25	0.95	1.18	0 – 74
	26	0.95	1.21	0 – 52.6

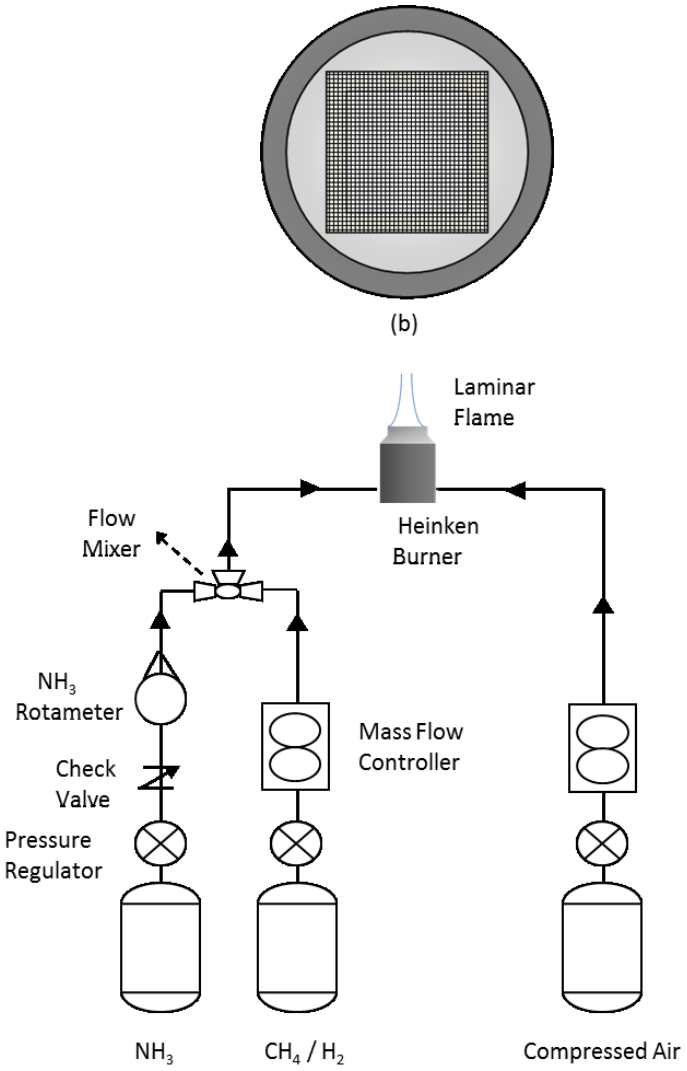

Fig. 2.1. (a) Schematic of Hencken burner setup and (b) burner cross-section.

For each test run, ammonia is added to the CH_4 or H_2 fuel stepwise such that the total flowrate (Q_{Total} = total sum of the flowrates of air and fuel mixture) and the equivalence ratio remain constant at each addition. The NH_3 addition continues until the flame blows off and thus a maximum percent of NH_3 by energy in the fuel mixture at each test run is measured. The percent of NH_3 by energy is designated here as $E\%NH_3$ and is defined as:

$$E\%NH_3 = \left[\frac{(x_{NH3} * LHV_{NH3}) * 100}{(x_{NH3} * LHV_{NH3} + x_{H2} * LHV_{H2})}\right] \quad (2)$$

where, x_i and LHV_i are mole fraction and lower heating value for the ith species. Because of the higher flame speed of the hydrogen, the total flowrates for H_2/NH_3 fuel mixtures are comparatively higher than the CH_4/NH_3, to establish the flames slightly lifted from the burner surface to achieve an adiabatic flame. The heat rate for both the fuel mixtures are kept nearly the same to make the data comparable. Some preliminary experiments showed a change in the flame structure and flow-field with ammonia added to the fuel. To minimize the effects of ammonia addition on flame structure and flow-field, the total flowrate and equivalence ratio are kept constant with each addition of ammonia.

2.2.2 Swirl-stabilized turbulent flame setup

The swirl-stabilized turbulent non-premixed flame investigations were performed on a domestic oil heating furnace about 40 kW capacity. The furnace was equipped with the swirl-stabilizer, air preheating system, furnace control system, and temperature and pressure monitoring devices. The fuel nozzle position is also vertically adjustable. The schematic of the (a) swirl-stabilized turbulent non-premixed flame setup and (b) front view of the combustor are shown in figures 2.2a and 2.2b, respectively. The fuel nozzle used in the current setup is a siphon type SNA air atomizing nozzle, which produces a solid cone spray pattern,(more details can be found on the manufacturer's website [20]).

The flow of combustion air (coflow) to the outer annulus (73 mm) in the combustor is controlled with an Alicat mass flow controller with a range of 0-1500 slpm, and an accuracy of ± (0.8% of reading + 0.2% of full range).

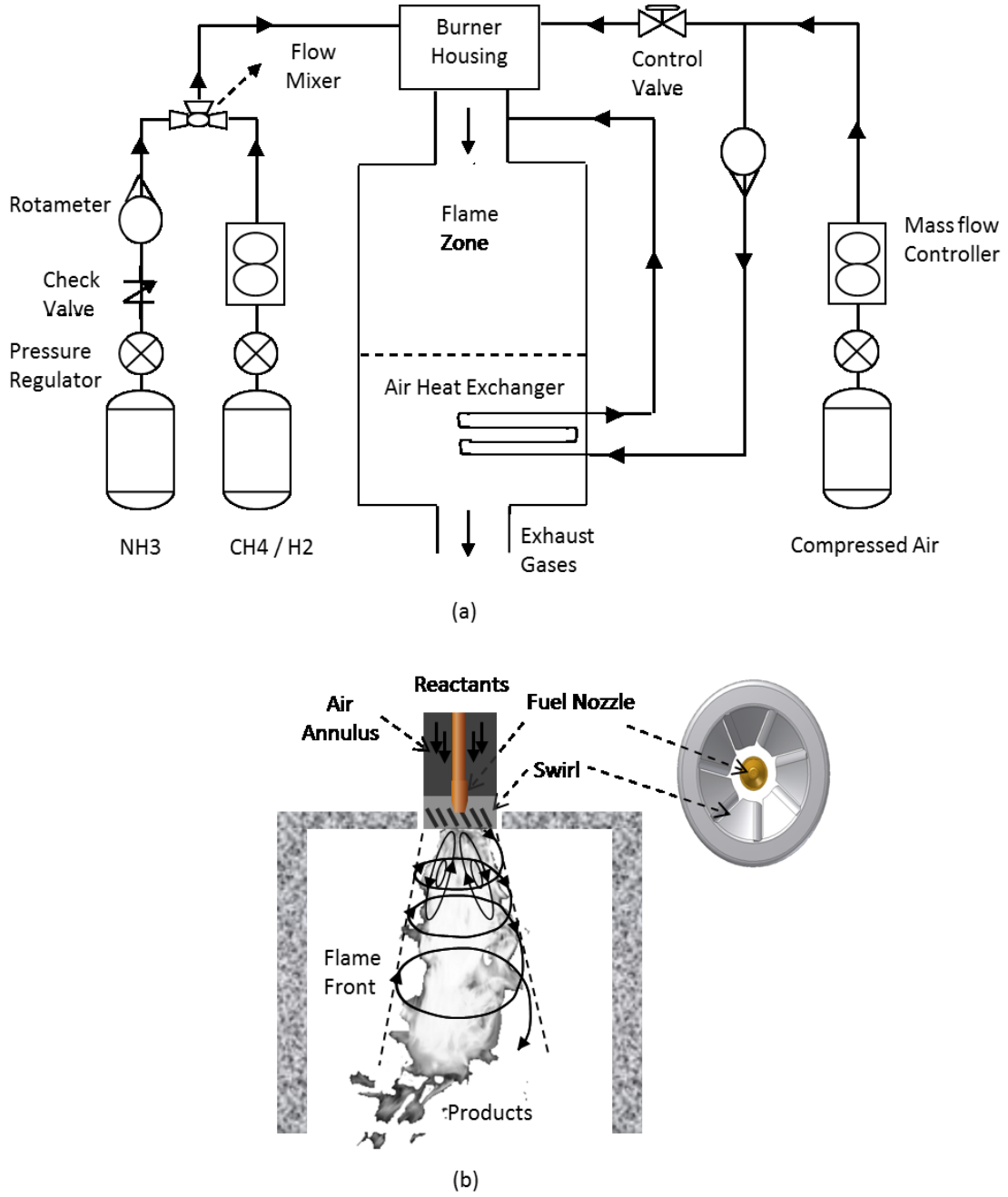

Fig. 2.2. (a) Experimental set-up for the swirl-stabilized turbulent non-premixed flame and (b) front view of combustor.

The Reynolds number range for the fuel mixture is 7000-8000 and for air is 40000-48000, which are well within the turbulent regime. The combustion air flowing to the

chamber is divided before reaching the chamber, with a portion of the flow traveling through the heat exchanger situated in the bottom of the combustion chamber and the remainder of the flow travelling directly to the burner housing. The hot air is introduced slightly downstream of the burner housing, directly into the burner tube as shown in Fig. 2.2a. In order to stabilize the turbulent flame, a swirl stabilizer is employed. The air preheating and swirl has a coupled effect on improving the flame stabilization. By preheating the air, the swirl is also increased because of the lower density of the hot air. A rotameter is installed to observe the flowrate of air through the heat exchanger. This adjustment allows for control over the final combustion air temperature which is measured at the exit of the burner tube directly before the swirl-stabilizer. For exhaust gas sampling, a chemiluminescence analyzer is employed to measure the concentration of NO, NO_2, O_2 and NH_3 slip. All thermocouples and pressure transducers installed in the combustion apparatus are monitored by using a National Instruments DAQ-9172 data acquisition card and LabView software.

Table 2.2. Experimental conditions for swirl-stabilized turbulent diffusion flames.

Items	CH_4/NH_3	H_2/NH_3
Pressure (atm)	1	1
Ambient Temp (C)	25	25
Fuel Temp (C)	25	25
Air Temp (C)	25 – 300	25 – 300
Fuel Flow rate (SLPM)	5 – 50	0 – 85
Air Flow rate (SLPM)	250- 507	139 – 213.7
NH_3 Addition (SLPM)	0 – 57	0 – 57
Heat Rate (KW)	5 – 33	5 – 20
Equivalence Ratio Range	0.5 – 1.0	0.5 – 1.0

Table 2.2 shows the baseline operating conditions for the swirl-stabilized turbulent non-premixed flames. For each fuel mixture, the flame is established at the corresponding starting test run (as shown in Table 2.3). The step-wise ammonia addition to the fuel mixture

continues such that the equivalence ratio and the total flowrate (Q_{mix}) remain unchanged until the flame becomes fully unstable and blows off. The same steps are repeated after changing each parameter, such as nozzle type, nozzle position, preheated air temperature, burner geometry etc., one at a time. Simultaneously, E%NH_3, emissions, and three instantaneous images are recorded at each step of ammonia replacement for each parameter.

Table 2.3. Baseline test runs for swirl-stabilized turbulent non-premixed flames.

$CH_4/NH_3/Air$					
Q_{NH3} (slpm)	Q_{CH4} (slpm)	Q_{Air} (slpm)	Q_{Total} (slpm)	Phi	Heat Rate (KW)
3	49.52	507.5	560	0.95	~31
$H_2/NH_3/Air$					
Q_{NH3} (slpm)	Q_{CH4} (slpm)	Q_{Air} (slpm)	Q_{Total} (slpm)	Phi	Heat Rate (KW)
1	84.23	214.8	300	0.95	~15

The effects of different parameters on NH_3 substitution in H_2/NH_3 and CH_4/NH_3 fuel mixtures and corresponding flame emissions were investigated. These parameters include (1) air preheated temperature, (2) equivalence ratio, (3) heat-rate, (4) fuel nozzle position, (5) swirl geometry and (6) burner configuration. The parametric test matrices for preheated air, equivalence ratio, and heat rate are presented in Tables 2.4, 2.5 and 2.6 respectively. Swirl geometries ranging from F0 to F22 are employed to identify the best swirl plate for flame stabilization. The F0 swirl refers to the case with zero tangential velocity, and the F# goes higher as the tangential velocity increases, thus providing higher residence time for the reactants in the flame zone.

Table 2.4. Pre-heated air temperature test matrix.[1,4]

E%NH_3	25°C	50°C	100°C	200°C	300°C
0	Y	Y	Y	Y	Y
10	Y	Y	Y	Y	Y
20	Y	Y	Y	Y	Y
30	Y	Y	Y	Y	Y
50	Y	Y	Y	Y	Y
60	Y	Y	Y	Y	Y
70	Y	Y	Y	Y	Y
80	Y	Y	Y	Y	Y
90	Y	Y	Y	Y	Y
Max E%NH_3	70	70	75	83.16	90

Table 2.5. Equivalence ratio test matrix.[2,4]

ø	25°C	50°C	100°C	200°C	300°C
0.5	Y	Y	Y	Y	Y
0.6	Y	Y	Y	Y	Y
0.7	Y	Y	Y	Y	Y
0.8	Y	Y	Y	Y	Y
0.9	Y	Y	Y	Y	Y
0.95	Y	Y	Y	Y	Y
1.0	Y	Y	Y	Y	Y

Table 2.6. Heat-rate test matrix.[3,4]

Heat-Rate	300 °C
5	Y
8	Y
10	Y
12	Y
15	Y
16.5	Y
20	Y

[1] Qmix = 560 slpm, Equivalence Ratio = 0.95, Heat-Rate Range = 15 – 35 kW, Swirl F3, nozzle position C
[2] Qmix = 560 slpm, Heat-Rate = 15-19 KW, Swirl F3, nozzle position C
[3] Equivalence Ratio = 0.95, Pre-heated Air temperature = 300 ºC, Swirl F3, nozzle position C
[4] Y represents condition achieved

2.3 Results and discussion

This section is divided into two parts: (1) laminar diffusion flame and (2) swirl-stabilized turbulent diffusion flame. The results of the laminar diffusion flames are discussed first, followed by the swirl-stabilized turbulent non-premixed flame.

2.3.1 Laminar diffusion flame (Hencken burner)

The instantaneous images of the flames at equivalence ratio = 0.95 for CH_4/NH_3/Air and H_2/NH_3/Air fuel mixtures with increasing energy replacement by ammonia ($E\%NH_3$) are shown in Fig. 2.3 and 2.4, respectively. The flame characteristics and flame luminosity both change for both the fuel mixtures with increasing ammonia in the fuel. For the methane-ammonia fuel mixture, the maximum % NH_3 by energy ($E\%NH_3$) achieved is 47% at a total flow rate (Q_{mix}) ~5 slpm (Fig. 2.3), whereas, it is recorded as 74% at Q_{mix} ~25 slpm for hydrogen-ammonia fuel mixtures (see Fig. 2.4). This $E\%NH_3$ reduces with increasing total flowrate for both the fuel mixtures. It is also observed that more $E\%NH_3$ is achievable for the fuel-lean condition compared to fuel-rich for both the fuel mixtures.

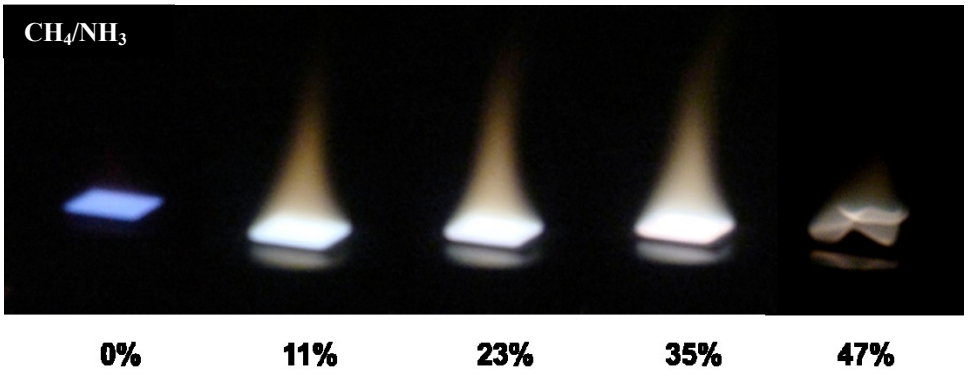

Fig. 2.3. Instantaneous flame images at ∅ = 0.95 with respect to % NH_3 by energy ($E\%NH_3$) for CH_4/NH_3 fuel mixture at Q_{mix} ~5 slpm.

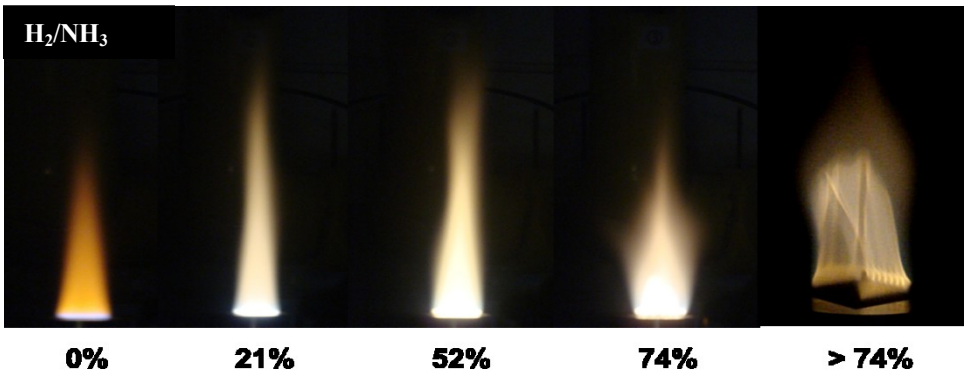

Fig. 2.4. Instantaneous flame images at Ø = 0.95 with respect to % NH_3 by energy (E%NH_3) for H_2/NH_3 fuel mixture at Q_{mix} ~ 25 slpm.

For example, the E%NH_3 increased from 26% to 52% for the change in equivalence ratio from 0.71 to 0.367 for H_2/NH_3/Air at Q_{mix} ~ 26 slpm. Likewise, the E%NH_3 is enhanced from 2.6% to 22.3% when equivalence ratio reduced from 0.768 to 0.748 for CH_4/NH_3/Air at Q_{mix} ~20. It is also noticed that the substitution of NH_3 in the fuel mixture is reduced with increasing heat-rate of the mixture, which can be ascribed to the reduced reactivity of the fuel mixture due to ammonia addition.

2.3.2 Swirl-stabilized turbulent diffusion flame

For the swirl-stabilized turbulent flame, three types of fuel nozzles were tested, including a (a) 4.36 mm (ID) tube, (b) siphon type air atomizing nozzles SNA ~ 0.85 (Delevan part no. 30609-9), and (c) siphon type air atomizing nozzles SNA ~ 1.00 (Delevan part no. 30609-11) for CH_4/NH_3/air at equivalence ratio ~0.95, heat rate ~15 kW and preheated air at 300 °C. More detailed descriptions of the nozzles can be found from the manufacturer's website [20]. For the tube configuration, the peak E%NH_3 recorded is 12 approximately, however, for siphon type air atomizing fuel nozzles the maximum E%NH_3 is considerably higher than the tube type. For example, the maximum NH_3 noted for the SNA ~ 0.85 and 1.0 are E%NH_3 of 13.9%

and 20.1%, respectively. The atomizing nozzles have the capability of producing a very fine spray of fuel mixtures. Higher SNA means finer atomization of the fuel mixture, which results in better mixing of fuel and air. Due to the pronounced atomizing capability of the fuel nozzle SNA ~1.0, the parametric studies for both H_2/NH_3 and CH_4/NH_3 fuel mixtures in the swirl-stabilized turbulent non-premixed flame were conducted on this particular nozzle type. Two different burner configurations were tested, including cases (1) without a flame-holder and (2) with a flame-holder as shown in Figs. 2.5a and 2.5b. The flame holder not only provides higher residence time, it also facilitates better mixing which leads to better flame stability. For ease of discussion, the swirl-stabilized turbulent flame section is further divided into discussions of CH_4/NH_3 and H_2/NH_3, where the parametric studies for both the mixtures are discussed individually.

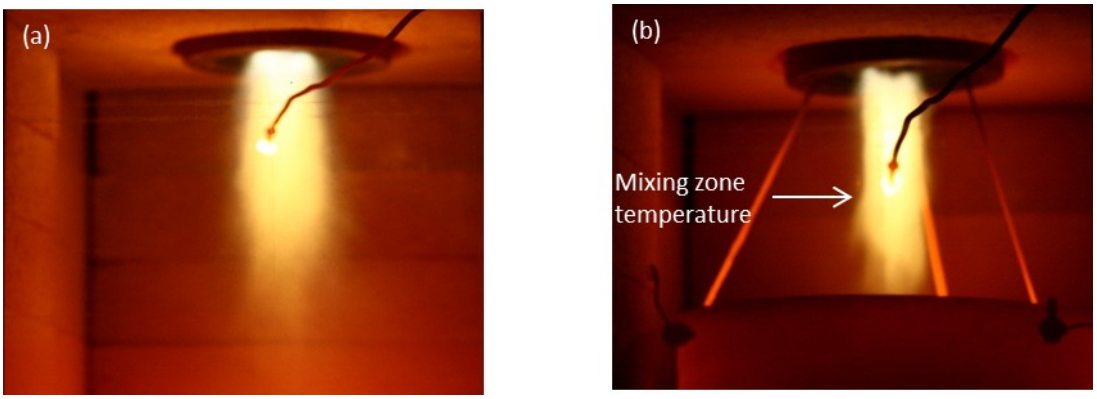

Fig. 2.5. Flame image for (a) without flame-holder (FH) and (b) with flame-holder (FH) for CH_4/NH_3/Air, 300 ºC, Ø = 0.95, heat rate ~10 kW and E%NH_3 = 15.

2.3.2.1 CH_4/NH_3

Figures 2.6a and 2.6b present the effects of the preheated air temperature on the NO_x emissions for cases without a flame-holder and with a flame-holder. For the case without a flame-holder, the NO_x emissions for E%NH_3 = 0 remains in the range of 25 - 40 ppm with

varying preheated air temperature from 25 °C – 300 °C. However for 5% NH_3 by energy in H_2 ($E\%NH_3$ = 5), significant increases in NO_x emissions were observed, which seems to be reducing with increasing air temperature (see Fig. 2.6a). The total attrition in NO_x concentration was recorded as being almost 3 times with air temperature change from 25 °C to 300 °C.

For the case with a flame-holder (Fig. 2.6b), the NO_x emissions for the NH_3-free CH_4/air flame were even further reduced. However, the effect of the flame-holder on NO_x emissions is more pronounced for the case of $E\%NH_3$ = 5. For example, at 25 °C and 300 ºC preheated air temperatures, the NO_x emissions were recorded at approximately 60% and 86%, respectively, lower for the case with a flame-holder compared to the case without a flame-holder. It can also be noted from Figs. 2.6a and 2.6b that increasing the preheated air temperature helps to improve NH_3 energy replacement ($E\%NH_3$) in the fuel mixture for both burner configurations. For the case without a flame-holder , the maximum possible NH_3 energy replacement ($E\%NH_3$) achieved is 20% at 300 °C air temperature (Fig. 2.6a), whereas it is recorded as approximately 70% for the case with a flame-holder (Fig. 2.6b), showing the favorable effects of a flame holder on achieving higher ammonia substitution in the fuel mixture.

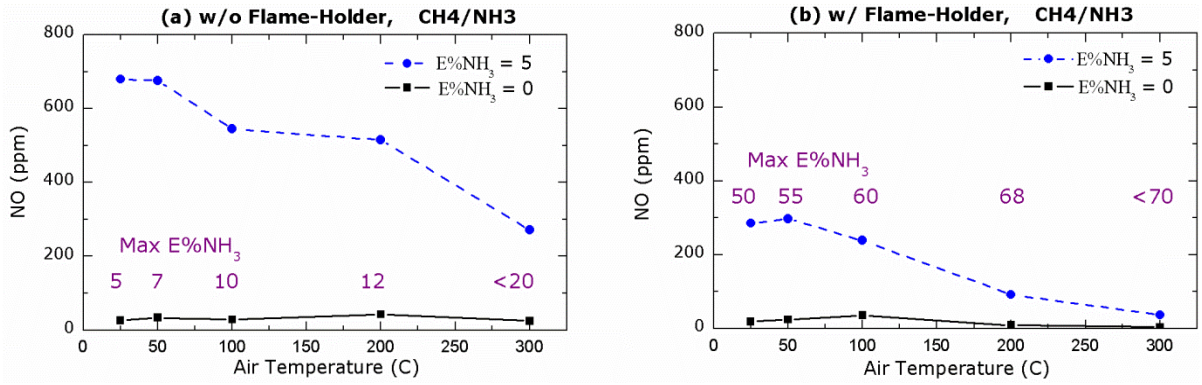

Fig. 2.6. Comparison of NO_x variation with preheated air temperature for $E\%NH_3$ = 0 and 5 for (a) without flame-holder and (b) with flame-holder burner configurations for CH_4/NH_3/Air at Q_{mix} = 560 slpm and Ø = 0.95.

The effects of increasing ammonia energy replacement in the CH_4/NH_3 fuel mixture ($E\%NH_3$) on the NO_x emissions, NH_3 slip, and mixing zone temperature are displayed in Fig. 2.7a and 2.7b for cases without a flame-holder and with a flame-holder, respectively, at 300 °C air temperature. For the case without a flame-holder (Fig. 2.7a), the NO_x is gradually increasing with increasing $E\%NH_3$, and reduction in NH_3 slip indicates higher NH_3 conversion to NO with increasing $E\%NH_3$. For the case with a flame-holder, the NO_x emission profile is recorded as a bell shaped curve with increasing NH_3 in the fuel mixture. NH_3 slip remains fairly constant until $E\%NH_3$ reaches 60%, beyond which a steep increase in NH_3 slip is observed.

It can be conjectured that the NH_3 substitution in the fuel mixture is converted to NO_x formation until $E\%NH_3 = 40$ due to higher mixing zone temperature of 1020 °C – 1105 °C (Fig. 2.7b). Later, further NH_3 addition in the fuel mixture reacts with the NO_x and reduces the NO_x by non-catalytic reduction in the temperature range of 925 °C – 940 °C, as shown in Fig. 2.7b.

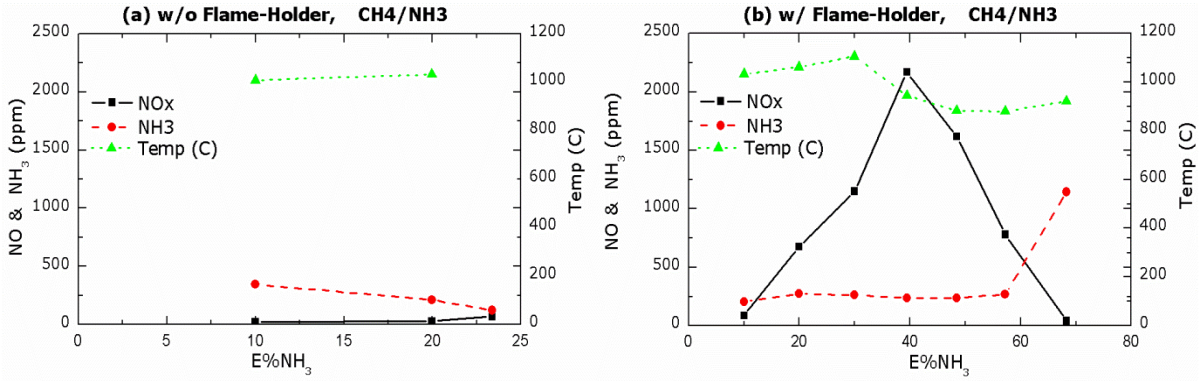

Fig. 2.7. Variation of NO_x, NH_3 slip and mixing zone temperature for (a) w/o Flame-Holder and (b) w/ Flame-Holder burner configurations for CH_4/NH_3/Air at 300C, Qmix = 560 slpm, heat-rate 16 kW and equivalence ratio 0.95.

The profiles of CO and CO_2 emissions with varying E%NH_3 for the case with a flame-holder are also plotted in Fig. 2.8. It is noted that the CO_2 concentration reduces with increasing E%NH_3, corresponding with enhanced CO concentrations because of reduced reactivity leading to incomplete combustion.

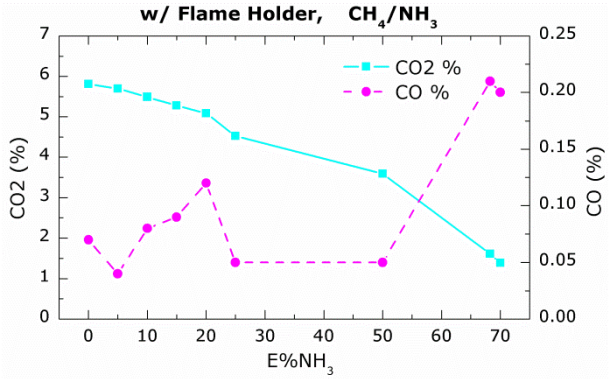

Fig. 2.8. Variation of CO and CO_2 emissions with E%NH_3 for with flame-holder burner configurations for CH_4/NH_3/Air at 300 ºC, Qmix = 560 slpm, heat-rate 16 kW and Ø = 0.95.

The effects of increasing equivalence ratio from 0.5 to 1.0 on the E%NH_3 that can be achieved, on NO_x emissions, and on NH_3 slip are plotted in Fig. 2.9a and 2.9b for cases without a flame-holder and with a flame holder, respectively.

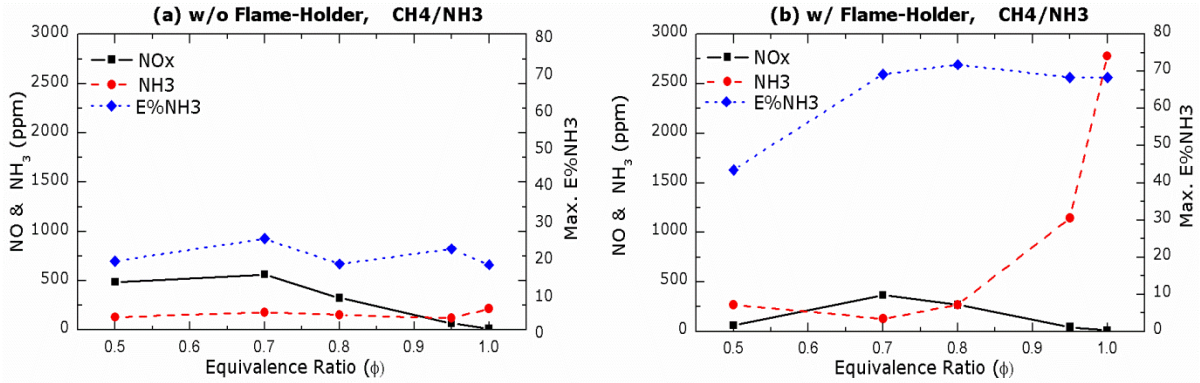

Fig. 2.9. Effects of Ø on NO_x, NH_3 slip and Max. E%NH_3 for (a) without flame-holder and (b) with flame-holder burner configurations for CH_4/NH_3/Air at 300 ºC, Qmix = 560 slpm, heat-rate 16 kW.

For the case without a flame holder, the fuel-rich mixture was much more favorable compared to fuel-lean mixtures not only in increasing the $E\%NH_3$ in the fuel mixture but also in diminishing NO_x emissions. For example, the NO_x emission at $\emptyset = 0.95$ is observed to be $1/9^{th}$ of the NO_x at $\emptyset = 0.5$, whereas $E\%NH_3$ seemed almost unchanged with equivalence ratio. For the case without a flame-holder, near stoichiometric conditions results in significantly lower NO_x and up to 70% NH_3 energy replacement compared to $\emptyset = 0.5$. Unfortunately, there is a correspondingly steep increase in NH_3 slip with enhanced NH_3 substitution ($E\%NH_3$).

In order to investigate the effect of the fuel nozzle positions, the NO variations with $E\%NH_3$ are plotted for three different nozzle positions (1) nozzle C (at the exit plane of the swirl plate, baseline) (2) nozzle B (0.25 inch above the baseline) and (3) nozzle A (0.5 inch above the baseline) in Figs. 2.10a and 2.10b for cases without a flame-holder and with a flame holder, respectively.

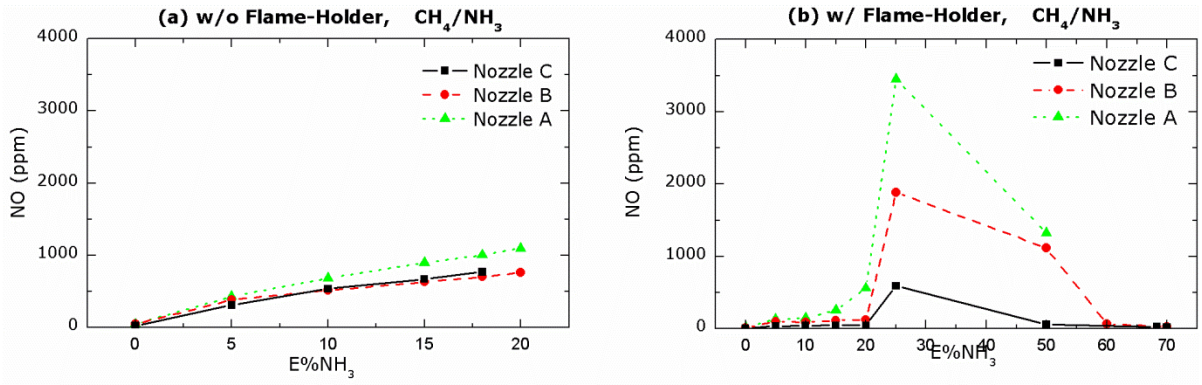

Fig. 2.10. Effects of fuel nozzle positions on NO_x emissions for (a) without flame-holder and (b) with flame-holder burner configurations for CH_4/NH_3/Air at 300 ºC, Qmix = 560 slpm, heat-rate 19 kW.

For the case without a flame-holder, the maximum achieved $E\%NH_3$ is recorded to be same among the three nozzle positions; however, nozzle position C led to the lowest NO_x emissions. The data suggests that the nozzle displacement from the base-line position enhances

the extent of fuel-air mixing by providing higher residence time and thus results in local premix zone in the reaction zone, resulting in higher NO_x emissions. For the case with a flame-holder, again the nozzle C position is found to minimize NO_x emissions, whereas nozzle A position is observed as unfit for efficient combustion; however, due to dominant effect of the flame-holder on mixing, the NO_x emissions are minimized to near zero NO_x emissions for all the three nozzle positions.

2.3.2.2 H_2/NH_3

The effects of the preheated air temperature on NO emissions for cases $E\%NH_3 = 0$ and 50 are plotted in Fig. 2.11a and 2.11b for cases without a flame-holder and with a flame-holder for H_2/NH_3/Air at Q_{mix} = 300 slpm and equivalence ratio 0.95. For the case without a flame-holder, the NO_x emissions for $E\%NH_3 = 0$ increases noticeably from 40 ppm to 90 ppm with an increase in preheated air temperature from 25 °C to 300 °C. Whereas, for $E\%NH_3 = 50$, the NO_x emissions recorded almost 28 times higher than $E\%NH_3 = 0$ at 25 °C room temperature and the NO_x profile is seen to be reducing with enhanced preheated air temperature. For example, the NO_x emissions for case $E\%NH_3$ is reduced by 3 times with the change in air temperature from 25 ºC to 300 °C (Fig. 2.11a). The maximum $E\%NH_3$ achieved for H_2/NH_3 mixtures is almost 70% at 300 °C for the case without a flame-holder (Fig. 2.11a).

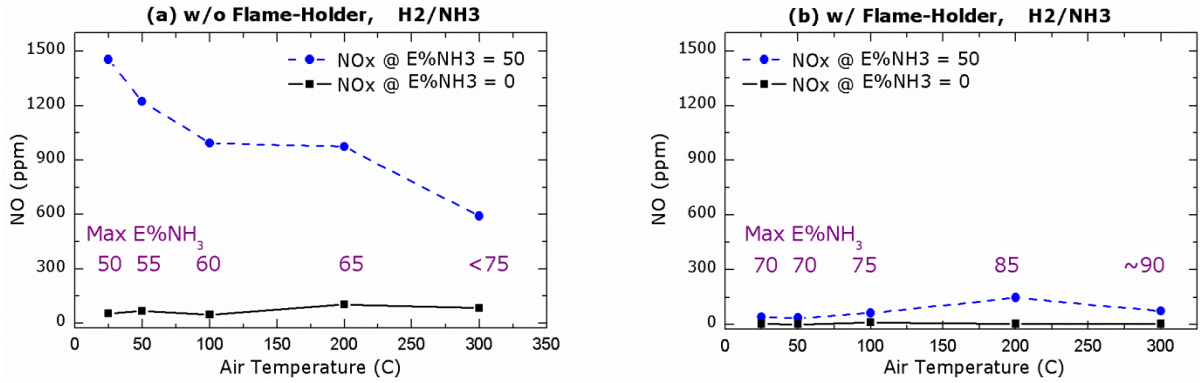

Fig. 2.11. Effects of preheated air temperature on NO emission for cases $E\%NH_3$ = 0 and 50 for (a) without flame-holder and (b) with flame-holder burner configurations for H_2/NH_3/Air at Qmix = 300 slpm and Ø = 0.95.

For the case with a flame-holder (Fig. 2.11b), the NO_x for cases $E\%NH_3$ = 0 and 50 are significantly subdued due to enhanced mixing effects caused by the flameholder compared to the case without a flameholder.

The peak $E\%NH_3$ achieved for the case without a flameholder is noted to be approximately 90% at 300 °C, indicating that the flameholder and preheated air temperature both help to stabilize the combustion and reduce NO_x emissions. The effects of increasing ammonia energy replacement in the H_2/NH_3 fuel mixture ($E\%NH_3$) on the NO_x emissions, NH_3 slip, and mixing zone temperature are plotted in Figs. 2.12a and 2.12b for the cases without a flame-holder and with a flame-holder, respectively, at 300 °C preheated air temperature. It is observed that for the case without a flame-holder (Fig. 2.12a), the NO_x linearly increases with increasing $E\%NH_3$ and reduces in NH_3 slip with increasing $E\%NH_3$, which indicates higher NH_3 conversion. The mixing zone temperature is found to be near 1200 °C (radiation uncorrected) at which the NH_3 can readily convert to NO. For the case with a flameholder (Fig. 2.12b), the NO_x emission profile increases gradually and the magnitudes are subdued to within

100 ppm for the entire range of E%NH_3. The NH_3 slip remains fairly constant in the range of 200 ppm until E%NH_3 = 85 and shoots up to 800 ppm at E%NH_3 = 90.

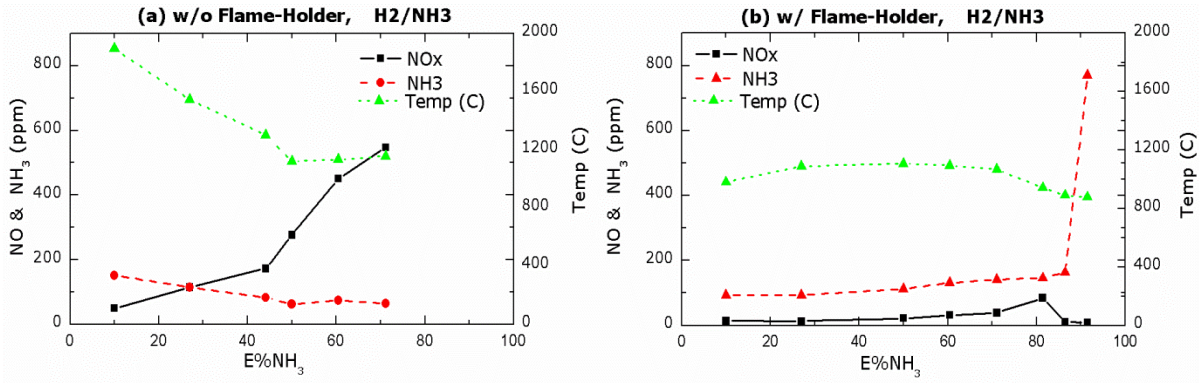

Fig. 2.12. Variation of NO_x, NH_3 slip and mixing zone temperature for (a) without flame-holder and (b) with flame-holder burner configurations for H_2/NH_3/Air at 300 ºC, Qmix = 300 slpm, heat-rate 15 kW and Ø = 0.95.

Due to the presence of the flameholder, the mixing zone temperature is fairly uniform and in the range of 890 - 925 °C at the higher end of E%NH_3 (Fig. 2.12b), which may help with reduction of NH_3 by reaction with NO_x, thus minimizing both species in the exhaust. However, at E%NH_3 = 90, the NH_3 slip gets higher which can be attributed to the lack of sufficient NO_x species to react with.

The effects of increasing equivalence ratio from 0.5 to 1.0 on NO_x emissions and NH_3 slip for the case of E%NH_3 = 50 for the H_2/NH_3 fuel mixture are plotted in Figs. 2.13a and 2.13b for cases without a flame-holder and with a flameholder , respectively. For the case without a flame-holder (Fig. 2.13a), the NO_x linearly increases with equivalence ratio, meaning an adverse effect of near stoichiometric conditions on NO_x emissions for the case of E%NH_3 = 50. For example, the NO_x recorded at Ø = 0.95 is found to be 2 times higher than NO_x at Ø = 0.5. However, the NH_3 slip is found to be approximately independent of equivalence ratio.

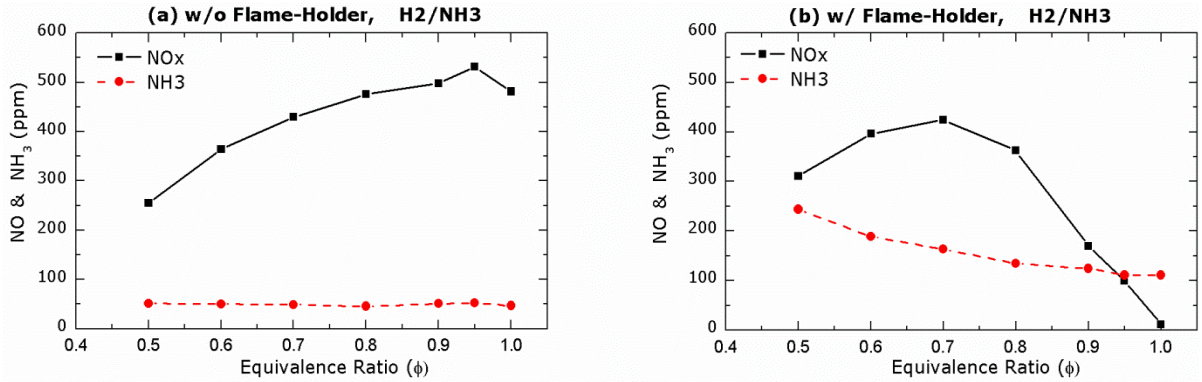

Fig. 2.13. Effects of Ø on NO_x, NH_3 slip at E%NH_3 = 50; for (a) without flame-holder and (b) with flame-holder burner configurations for H_2/NH_3/Air at 300 ºC, Qmix = 300 slpm, heat-rate 16 kW.

Interestingly, the NO_x emissions and NH_3 slip magnitudes are reduced significantly with changes in flame condition from fuel-lean to fuel-rich for the case with a flameholder (Fig. 2.13b). The attrition in NO_x and NH_3 slip was observed to be more than 98% and 56% respectively, indicating that with a flameholder , near stoichiometric conditions are much more favorable for establishing a stable flame with lower emissions.

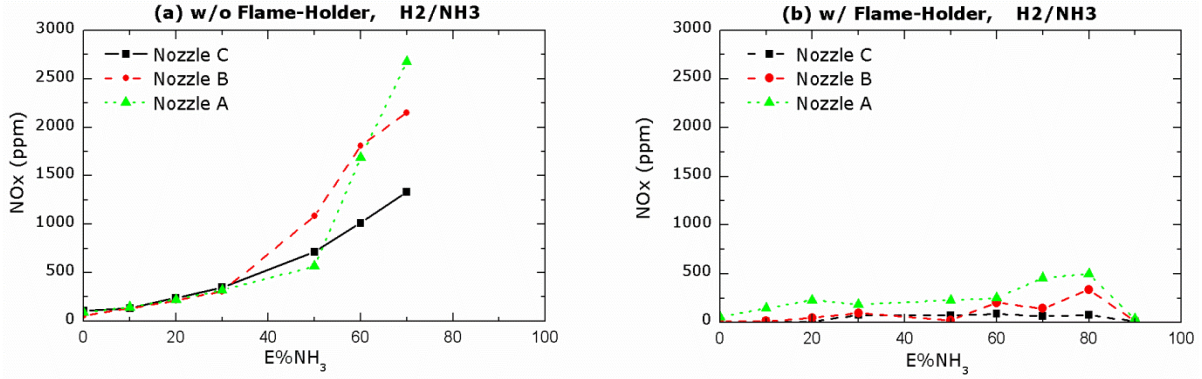

Fig. 2.14. Effects of fuel nozzle positions on NO_x emissions for (a) without flame-holder and (b) with flame-holder burner configurations for H_2/NH_3/Air at 300 ºC, Qmix = 300 slpm, heat-rate 15 kW.

The effects of fuel nozzle position on NO_x emissions for the H_2/NH_3 fuel mixtures are presented in Fig. 2.14. In Figs. 2.14a and 2.14b; the NO variations with E%NH_3 are plotted for three different nozzle positions (1) nozzle C (at the exit plane of the swirl plate, baseline) (2) nozzle B (0.25 inch above the baseline) and (3) nozzle A (0.5 inch above the baseline) for the

cases without a flameholder and with a flameholder, respectively. The maximum achievable $E\%NH_3$ for the three nozzle positions was approximately 70% for the case without a flameholder (Fig. 2.14a) However, nozzle position C was found to be the best location for minimizing NO_x emissions. Overall, nozzle position A results in significantly higher NO_x emissions compared to the nozzle position C (baseline), indicating that enhanced upstream mixing of fuel and air has adverse effects on emissions.

Similarly, for the case without a flame-holder (Fig. 2.14b), the maximum $E\%NH_3$ was determined to be approximately 90, and the NO_x emissions profiles are lowered significantly compared to the case without a flameholder. It can be seen that for the case with a flameholder, all fuel nozzle positions result in ultra-low NO_x emissions at $E\%NH_3 = 90$, indicating the dominant effect of mixing caused by the presence of the flameholder.

In order to further increase the NH_3 substitution levels and reduce emissions in the H_2/NH_3 fuel mixture, a custom-designed fuel nozzle was tested in collaboration with Goodrich Inc. The custom-designed fuel nozzle was verified for an extensive parametric matrix including air temperature, equivalence ratio, burner geometry, flame-holder geometry, swirl geometry, heat-rate etc. Key results from these tests are discussed here.

2.3.2.3 Coaxial swirl Nozzle

A schematic of the custom-designed fuel nozzle is shown in Fig. 2.15. This particular nozzle has two inlet ports: an central inlet 1 and (b) outer inlet 2; the central inlet orifice diameter is 2 mm and inlet 2 is concentric to the center orifice. This specific design is used to enhance the extent of fuel-air mixing with the help of mass diffusion.

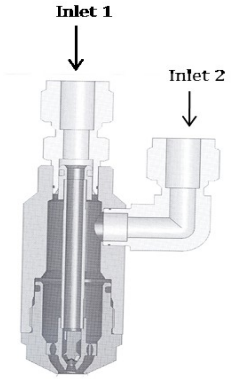

Fig. 2.15. Schematic of custom-designed (Goodrich Inc.) fuel nozzle.

For the case without a flame-holder, it is found that inlet 1 is not favorable for achieving flame stability at high NH_3 substitution because high inlet velocity causes flame blow-off. It is observed that for the case of 30% swirl air passing through inlet 2, the NO_x emissions increased approximately by 10 times compared to the case with no air flow through inlet 2. The use of inlet 2 for the flow of fuel mixture enhanced the NH_3 energy replacement ($E\%NH_3$) in H_2/NH_3 mixture up to 70% without air preheating, compared with 50% for the SNA air atomizing nozzle discussed earlier. The NO_x emissions and NH_3 slip are found to be significantly lower for the custom-designed nozzle compared to SNA air atomizing nozzle.

Figure 2.16 shows the NO_x emissions and NH_3 slip as functions of the percentage of total air flow passing through inlet 1, with the fuel mixture incoming from inlet 2, for H_2/NH_3/Air at 300 °C, Q_{mix} = 300 slpm, heat rate of 15 kW at $E\%NH_3$ = 80 for cases without a flameholder and with a flameholder. Increasing the percentage of total air flow rate through inlet 1 increases the NO_x emissions and reduces the NH_3 slip significantly. For the case without a flameholder, the NO_x emissions are found to be 2 times higher, and NH_3 slip is reduced by 3 times approximately, with a percentage air flow rate from 0% to 5%. This indicates that enhanced NO_x induced by air flow through inlet1 may react with remaining NH_3 in the flame zone and

result in lower NH_3 slip. Similarly, for the case with a flameholder, the NO_x emissions are close to zero. In addition, NH_3 slip is reduced by approximately $1/14^{th}$ times while varying the percentage of total air flow from 0% to 15%. Overall, the use of inlet 2 for the fuel mixture and inlet 1 for passing a percentage of the total air flow rate helps to minimize NH_3 slip by means of non-catalytic reduction in the flame zone.

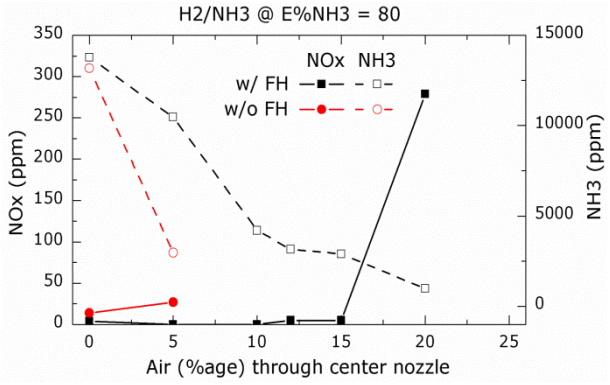

Fig. 2.16. NO_x and NH_3 slip with respect to % air through Inlet 1 at E%NH_3 = 80; for without flame-holder and with flame-holder burner configurations for H_2/NH_3/Air at 300 ºC, Qmix = 300 slpm, heat-rate 15 kW.

An instantaneous flame image of 100% pure anhydrous ammonia (NH_3) is shown in Fig. 2.17 in a swirl-stabilized turbulent flame while using the custom-designed fuel nozzle with a flameholder. The NO_x emissions and NH_3 slip recorded for this flame are 3-5 ppm (ultra- low) and 800-1300 ppm, respectively.

Fig. 2.17. Instantaneous flame image of 100% NH_3 swirl-stabilized turbulent flame.[4]

2.4 Conclusions

An extensive combustion characterization of H_2/NH_3 and CH_4/NH_3 fuel mixtures were studied for both laminar flame (Hencken burner) and turbulent flame (swirl-stabilized turbulent) configurations. For the laminar diffusion flame, flame characteristics such as flame length, luminosity, color etc., changed significantly for both H_2/NH_3 and CH_4/NH_3 fuel mixtures, indicating changes in flame chemistry with increasing NH_3 seeding. The maximum $E\%NH_3$ was recorded as 74% for H_2/NH_3 and 47% for CH_4/NH_3, which can be ascribed to the higher reactivity of H_2 over CH_4.

For swirl-stabilized turbulent flames, a detailed parametric study of NH_3 as a percent of energy replacement ($E\%NH_3$) and corresponding emissions for H_2/NH_3 and CH_4/NH_3 fuel mixtures was conducted with respect to specific variables such as (1) preheated air temperature, (2) equivalence ratio, (3) heat rate, (4) swirl geometries, (5) fuel nozzle type and position, and (6) burner configuration. The effects of increasing air temperature were favorable for increasing NH_3 substitution in both H_2/NH_3 and CH_4/NH_3 fuel mixtures, with significantly

[4] Air Temperature = 25C, F12 swirl, equivalence ratio 0.95, heat-rate 16.15 KW
NO_x ~ 3-5 ppm (ultra low)
NH_3 slip ~ 800 – 1300 ppm

higher NH_3 replacement for H_2 compared to CH_4. The syphon type air-atomizing fuel nozzle was more effective compared to tube type nozzle. However, a custom-designed fuel nozzle exhibited the best performance in achieving higher $E\%NH_3$ as well as lower NO_x emissions and NH_3 slip.

By comparing two different burner configurations (1) without flameholder and (2) with flame-holder, it is observed that the case with a flameholder is far superior in achieving higher $E\%NH_3$, lower NO_x emissions, and lower NH_3 slip. The case with a flame-holder enhances the mixing between fuel and air as well as provides uniform temperature distribution in the mixing zone, thus facilitating non-catalytic reduction of NO by NH_3 in the mixing zone, resulting in lower NO_x and NH_3 slip. Near stoichiometric conditions are found to be better compared to fuel-lean conditions for the case with a flameholder. Based on the analyses, NH_3 replacement is more challenging in CH_4/NH_3 mixtures compared to H_2/NH_3 due to low reactivity of the mixture. For H_2/NH_3 mixtures, an optimized set of parameters were identified, including a custom-designed fuel nozzle, and pure NH_3 flame ($E\%NH_3 = 100$) is achieved with ultra-low NO_x (3-5 ppm) with non-negligible NH_3 slip (800-1300 ppm).. In future work, the waste-exhaust heat can be utilized for thermal NH_3 decomposition to help reduce NH_3 slip.

2.5 References

[1] Zamfirescu C, Dincer I. Using ammonia as a sustainable fuel. Journal of Power Sources 2008;185(1):459-465.

[2] Jensen J, Vestbo a, Li Q, Bjerrum N. The energy efficiency of onboard hydrogen storage. Journal of Alloys and Compounds 2007; 446-447:723-728.

[3] Christensen C, Johannessen T, Sorensen R, Norskov J. Towards an ammonia-mediated hydrogen economy. Catalysis Today 2006; 111(1-2):140-144.

[4] Feibelman P.J., Stumpf R. Coments on "Potential roles of ammonia in a hydrogen economy" a study of issues related to the use of ammonia for on-board vehicular hydrogen storage. 2008.

[5] Gray JT, Dimitroff E, Meckel NT, Quillian Jr. RD. ammonia fuel – engine compatibility and combustion. In: SAE paper 660156. 166.

[6] Reiter AJ, Kong SC. Demonstration of compression-ignition engine combustion using ammonia in reducing greenhouse gas emissions. Energy & Fuels 2008; 22(5):2963-2971.

[7] Ciccarelli G, Jackson D, Verreault J. Flammability limits of NH_3–H_2–N_2–air mixtures at elevated initial temperatures. Combustion and Flame 2006; 144(1-2):53-63.

[8] Glarborg P, Jensen AD, Johnsson J. Fuel nitrogen conversion in solid fuel fired systems. Prog. Energy Combust. Sci. 2003; 29(2):89-113.

[9] Martin R, Brown N. Nitrous oxide formation and destruction in lean, premixed combustion. Combustion and Flame 1990; 80(3-4):238-255.

[10] Bian J. Experimental study of the formation of nitrous and nitric oxides in H_2-O_2-AR flames seeded with NO and/or NH_3. Symposium (International) on Combustion 1991; 23(1):379-386.

[11] Miller JA, Bowman CT. Mechanism and modeling of nitrogen chemistry in combustion. Progress in Energy and Combustion Science 1989; 15(4):287-338.

[12] Sarofim, AF, Williams GC, Modell M, Slater SM. Conversion of fuel nitrogen to nitric oxide in premixed and diffusion flames. AICHE Symp. 1975; 148(71):51–61.

[13] Sullivan N. Ammonia conversion and NO_x formation in laminar coflowing nonpremixed methane-air flames. Combustion and Flame 2002; 131(3):285-298.

[14] Tian Z, Li Y, Zhang L, Glarborg P, Qi F. An experimental and kinetic modeling study of premixed NH_3/CH_4/O_2/AR flames at low pressure. Combustion and Flame 2009; 156(7):1413-1426.

[15] Bell JB, Day MS, Grcar JF, Bessler WG, Schulz C, Glarborg P, Jensen AD. Detailed modeling and laser-induced fluorescence imaging of nitric oxide in a NH_3-seeded non-premixed methane/air flame. Proceedings of the Combustion Institute 2002; 29(2):2195–2202.

[16] Duynslaegher C, Jeanmart H, Vandooren J. Flame structure studies of premixed ammonia/hydrogen/oxygen/argon flames: experimental and numerical investigation. Proceedings of the Combustion Institute 2009; 32(1):1277-1284.

[17] Lee JH, Kim JH, Park JH, Kwon OC. Studies on properties of laminar premixed hydrogen-added ammonia/air flames for hydrogen production. International Journal of Hydrogen Energy 2010; 35(3):1054-1064.

[18] Kang S, Ryu I, Lee S, Shin H, Han H. Characteristics of a stepwise fuel-rich/lean catalytic combustion of natural gas bearing ammonia. Catalysis Today 2006; 117(4):468-474.

[19] Hancock RD, Bertagnolli KE, Lucht RP. Nitrogen and hydrogen cars temperature measurements in a hydrogen/air flame using a near-adiabatic flat-flame burner. Combustion and Flame 1997; 109(3):323-331.

[20] http://www.delavaninc.com/pdf/siphon_catalog_new.pdf.

CHAPTER 3. EXPERIMENTAL AND MODELING STUDY OF CHEMICAL-KINETICS MECHANISMS FOR H_2-NH_3-AIR MIXTURES IN LAMIANR PREMIXED JET FLAMES

A paper accepted to *Fuel* Journal, 2011

Praveen Kumar and Terrence R. Meyer*

Abstract

A combined experimental and modeling study of laminar flame speeds for premixed H_2-NH_3-air jet flames is performed for 0% to 80% NH_3 in H_2 by energy and for equivalence ratios from 0.5 (fuel lean) to 1.1 (fuel rich). Experimental flame speeds in the jet flame configuration compare well with previous data from freely propagating spherical flames after corrections for heat losses. These data are then used to validate flame-speed predictions using CHEMKIN PRO over a wide range of conditions and to evaluate the performance of three detailed chemical kinetic mechanisms. It is found that these mechanisms perform well for H_2-air combustion but begin to deviate substantially (by ~2×) from each other with the addition of NH_3. Differences in flame speeds and associated radical species concentrations (H, O, and OH) are found to be largest for higher levels of NH_3 (50% by energy and greater) and with increasing equivalence ratio. A sensitivity analysis reveals that OH is the key radical leading to NH_3 decomposition from low to high equivalence ratio, and is a likely source of deviation between model predictions. Comparisons with experimental data are used

* Department of Mechanical Engineering, Iowa State University, Ames, IA 50011, USA
* Corresponding author. Tel: +1 515 294 1805.
* E-mail address: trm@iastate.edu

to determine the range of conditions for which each mechanism is capable of providing accurate predictions for H_2-NH_3-air mixtures.

Keywords: NH_3; Ammonia; H_2; Hydrogen; Premixed flames; Flame speed; Chemical kinetics

Nomenclature:

$$E\%NH_3 = \left[\frac{(x_{NH3} * LHV_{NH3}) * 100}{(x_{NH3} * LHV_{NH3} + x_{H2} * LHV_{H2})}\right]$$

$LHV_{fuel} = lower\ Heating\ Value\ of\ the\ fuel\ (kJ/kg)$

$A_{flame} = flame\ Surface\ Area\ (m^2)$

$\dot{Q}_{mix} = volumetric\ flow\ rate\ of\ the\ fuel - air\ mixture\ (m^3/s)$

$S_l = laminar\ flame\ speed\ (m/s)$

$T_\infty = ambient\ temperature\ (K)$

$T = tube\ temperature\ (K)$

$h = conv.heat\ transfer\ coeff\ \left(\frac{W}{\mathrm{m}^2 * K}\right)$

$k = conductivity\ of\ the\ tube\ \left(\frac{W}{m * K}\right)$

$P = inside\ perimeter\ of\ the\ tube$ (m)

A_c = cross sectional area of the tube (m^2)

$\theta = T - T_\infty\ (K)$

$$m^2 = \frac{hP}{kA_c}$$

$L = separation\ distance\ between\ thermocouples\ (m)$

$\dot{Q}_{Total\ Heat\ Trans.} = total\ heat\ transfer\ from\ the\ flame\ to\ the\ tube\ (W)$

$\dot{Q}_{forced\ Conv} = heat\ transfer\ via\ forced\ convection\ (W)$

$\dot{Q}_{free\ Conv} = heat\ transfer\ via\ free\ convection\ (W)$

$\dot{Q}_{Radiation} = heat\ transfer\ via\ radiation\ (W)$

$\dot{Q}_{heatloss} = heat\ loss\ from\ the\ flame\ to\ the\ ambient\ (W)$

3.1 Introduction

The ever-increasing demand for alternative fuels with reduced pollutant and carbon emissions has drawn substantial attention towards hydrogen (H_2) combustion for heating, power, and transportation. However, there are still technical challenges associated with hydrogen storage and distribution, leading to a wide range of research efforts that have suggested ammonia (NH_3) as a potential alternative fuel or H_2 carrier [1,2]. NH_3 can be generated from renewable sources, such as wind or solar energy, during off-peak hours when these resources are underutilized, or from nuclear waste or bio-mass [3]. Once produced, NH_3 is a carbon-free fuel. It has a higher energy density than liquid H_2 and can easily be stored as a liquid at about 8× atmospheric pressure at 21 °C, making it an ideal H_2 carrier [4]. In fact, NH_3 has a well-established distribution infrastructure, with pipelines in the United States, for example, stretching from Louisiana to Minnesota and from Oklahoma to Ohio.

Considering the potential for NH_3 to serve as an alternative fuel or as an H_2 carrier, a number of studies have explored the flame stability and emissions characteristics of NH_3 for combustors or engine applications. This includes the combustion of pure NH_3 as well as NH_3 mixed with conventional fuels such as H_2 and methane (CH_4), among others [5-7]. Reiter & Kong [8], for example, found that NH_3 could replace 95% of the diesel fuel in a conventional

diesel engine and reduce NO_x emissions. Similarly, the effects of NH_3 substitution to improve the safety and performance of H_2 internal combustion engines were investigated and compared with results from computational modeling [9]. In this case, the authors showed that NH_3 substitution increased NO_x and N_2O emissions significantly under lean conditions. While these studies show that NH_3 can potentially act as an alternative fuel, minimizing NH_3 slip (unburned NH_3 in the exhaust), carbon monoxide (in the case of CH_4 and diesel substitution), and NO_x simultaneously remains a difficult challenge. Moreover, achieving efficient operation over a wide range of conditions requires a thorough understanding of NH_3 combustion chemistry.

In an effort to advance this understanding, research work on NH_3 combustion has established N_2 and NO formation and decomposition pathways for NH_3 seeded flames [10]. Detailed kinetic mechanisms describing NO_x formation and re-burning in hydrocarbon/NH_3 and H_2/NH_3 mixtures have been developed by Miller and Bowman [7]. Recently, Mendiara and Glarborg [11] developed a chemical kinetics model involving 97 species and 779 reactions for the oxidation of NH_3 in oxy-fuel combustion of CH_4/NH_3 in a laminar flow reactor with a temperature range from 973 to 1773 K. The updated chemical mechanism captured experimental trends fairly well, focusing particularly on the effects of high CO_2 concentration. Detailed chemical mechanisms for hydrocarbon/NH_3 and H_2/NH_3 reactions have also been developed by Konnov [12], as well as by Tian et al. [13] in a companion work with that of Mendiara and Glarborg [11]. Compared with the Miller and Bowman, these mechanisms have been updated with more extensive reactions for NH_3 chemistry—the full versions containing four-fold the number of species and ten-fold the number of reactions.

The Konnov mechanism was found to be in agreement with the measured NO concentrations in lean CH_4-NH_3-air premixed flames, but NO lean re-burning was not well predicted [12]. Duynslaegher et al. [14] utilized the Konnov mechanism to investigate the effects of initial H_2 content on NH_3-H_2-O_2-Ar flames. They were able to predict the effects of equivalence ratio on NO formation but found disagreement for NH_2 and N_2O species concentrations. Later, Shmakov et al. [15] studied NO- and NH_3-doped H_2-O_2-N_2 flames experimentally and numerically using a derivative of the Konnov detailed reaction mechanism and provided modifications to the reaction chemistry based on the experimental data for better overall agreement. Tian et al. [13] proposed a comprehensive kinetics mechanism based on the experimental and modeling study of 11 premixed $NH_3/CH_4/O_2$/Ar flames at low-pressure (4.0 kPa), stoichiometric conditions. This mechanism has been employed for successfully predicting the structure of CH_4-NH_3 and nitro-methane flames [13]. Because of comprehensive validation with experimental data over a range of conditions, this model is seeing wide use in the recent literature [16] and is being substituted in some instances in place of the GRIMech3.0 mechanism [17].

While the formulations of Konnov and Tian have undergone significant recent development and are being utilized to an increasing extent in the current literature, little or no experimental validation has taken place with regard to laminar flame speeds. Of particular interest in the current work is the laminar flame speed for H_2-NH_3-air mixtures, which is critical for predicting combustor performance parameters, such as fuel consumption rates, wall quenching effects, and NH_3 slip under carbon-free combustion conditions. The combustion characteristics of near-stoichiometric NH_3-air mixtures have previously been

modeled at elevated pressure and temperature conditions using a derivative of the Konnov mechanism in a flat, freely propagating flame model [18]. Results indicate that both equivalence ratio and compression ratio have an important impact on the laminar burning velocity and the adiabatic flame temperature; however the modeling results from Ref. 18 were not compared with experimental data. Hence, there is a gap in the literature regarding the experimental validation of laminar flame speed predictions for H_2-NH_3-air mixtures using the Konnov and Tian mechanisms.

Lee [9,19] evaluated the upstretched laminar burning velocities and stretch effects for laminar, premixed H_2-NH_3-air flames in a freely propagating spherical configuration and compared results with numerical predictions using the Miller and Bowman mechanism [7]. Lee's measurements serve as a baseline for the current study and are used to ensure that the experimental approach described herein is consistent with flame-speed measurements from the published literature. However, for comparisons with the Konnov and Tian mechanisms, we select a different flame configuration (a laminar premixed jet flame) that will be more convenient for a range of subsequent studies. The tube-stabilized jet flame has been adopted as a standard tool for fundamental flame studies and has been used in several cases for characterizing laminar flame speed and flame structure [20,21]. The ability to compare experimental data from a steady laminar flame to results from spherical or planar freely propagating flames will allow rapid assessment of fuel mixtures over a wide range of conditions.

This paper focuses on three main objectives: (i) a more detailed analysis of the methodology for obtaining laminar flame speeds for laminar premixed jet flames, including

corrections for heat transfer effects, (ii) detailed comparisons between the experimental data and models using the Konnov and Tian mechanisms over a wide range of H_2-NH_3-air mixtures and equivalence ratios, and (iii) an analysis of NH_3 decomposition and radical formation rates for the two mechanisms and how these affect model accuracy at the various conditions. Toward these objectives, Experimental laminar flame speeds for premixed H_2-NH_3-air jet flames are compared with numerical predictions using the 1-D, laminar, freely propagating flame code in CHEMKIN Pro 4.0. The primary focus is on the Konnov [12] and Tian [13] mechanisms due to their more detailed treatment of NH_3 chemistry, although limited comparisons are also made with the widely used GRI-Mech3.0 mechanism [22]. The accuracy of the experimental approach as well as each chemical mechanism is evaluated for various conditions, and various sources of disagreement are investigated using sensitivity analyses of species production and decomposition rates.

3.2 Experimental and computational methods

3.2.1 Apparatus and method of measuring flame speed

The laminar jet flame is a well-established configuration that provides a multidimensional combustion zone and has been extensively used by the researchers for premixed flame studies [20,23]. The shape of the flame is a balance between the jet velocity and the laminar flame speed of the fuel-air mixture. It is presumed that the flame front stabilizes at a location for which the average velocity of the unburned fuel-air mixture normal to the conical flame front is equal to the laminar flame speed [24]. In practice, the average flame speed is calculated by dividing the volume flow rate of the mixture by the flame

surface area. This method of estimating the flame speed is very similar to the method adopted by Dong et al. [23].

Figure 3.1a shows the jet-flame configuration on the tube burner setup, as used in the experiments. The reaction zone is the luminous conical edge and the flame surface is area is estimated as the surface area (A_{flame}) confined by the luminous edges. Thus, the laminar flame speed S_l can be calculated from Eq. 3.1:

$$S_l = \frac{\dot{Q}_{mix}}{A_{flame}} \tag{3.1}$$

where $\dot{Q}_{mix}$ is the total volumetric flow rate of the fuel-air mixture.

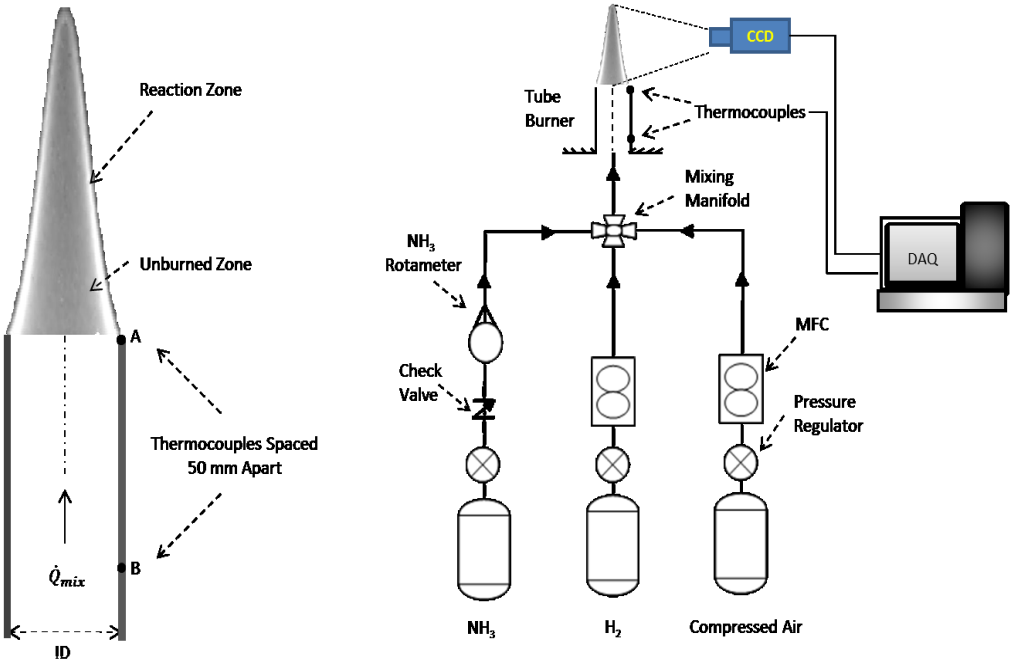

Fig. 3.1. (a) Tube flame configuration and (b) schematic of experimental set-up. MFC – mass-flow controller, CCD – charge-coupled device camera, DAQ – data acquisition system.

A schematic of the experimental setup used for laminar flame speed measurements is shown in Fig. 3.1b. The experimental setup includes a stainless steel tube burner, gas supply

system, control valves, mass flow controllers, mixing manifolds, and a charge-coupled device (CCD) camera to record the flame images. Two K-type thermocouples are attached to the tube burner at different locations to perform heat transfer analysis. The volumetric flow rate of H_2 and air are measured with mass flow controllers (Alicat, ±1.0% full scale), whereas the NH_3 flow rate is controlled by a rotameter (Aalborg, ±5% full scale).

For the present set of experiments, premixed laminar flames are stabilized above two stainless steel tubes with 4.67-mm and 11.11-mm inner diameter (ID). The ID of 4.67 mm ensured a stable flame without flashback or blow-off for the entire range of equivalence ratios for cases of 0%, 20%, 50%, and 80% NH_3 in H_2 by energy. Conditions with $E\%NH_3$ = 0, 20 and 50 used a 4.67-mm tube ID, whereas an 11.11-mm tube ID was used for the case of $E\%NH_3$ = 80. The long straight tubing ensured that the fuel-air mixture was uniformly mixed for each experiment.

3.2.1.1 Method for estimating flame surface area

Flame images at each condition are captured using a 4272 × 2848 pixel CCD camera (Canon EOS DIGITAL REBEL XSi) and an 18–108 mm, *f*/5.6 camera lens. The CCD camera has high light sensitivity, high spatial resolution, and sufficiently large dynamic range. For each experimental condition, 25 flame images are captured and analyzed to capture the flame surface area. Based on the axisymmetric flame structure, each flame image is first split in half along the center axis. Then for one half of the flame image, a Matlab program is executed to identify the luminous conical edge of the flame defined by the local peak in the camera signal. Flame surface area can then be estimated by simple integration of

the area under the luminous conical edge and then multiplied by two for the other half portion of the flame as shown in Eq. 3.2.

$$A_{flame} = 2 * \int_0^r f(x)dx \tag{3.2}$$

For each experimental condition, the flame surface area A_{flame} is determined by the average of 25 surface area measurements. The technique was verified using a premixed CH_4-air flame resulting in a flame speed of 32.9 cm/s at stoichiometric conditions, which is 10% lower than the measured adiabatic flame speed of methane-air flame [25]. For illustration, Fig. 3.2 shows a sample flame image and the corresponding identified luminous conical edge (reaction zone) for pure a CH_4-Air premixed flame at an equivalence ratio ∅ = 1.0.

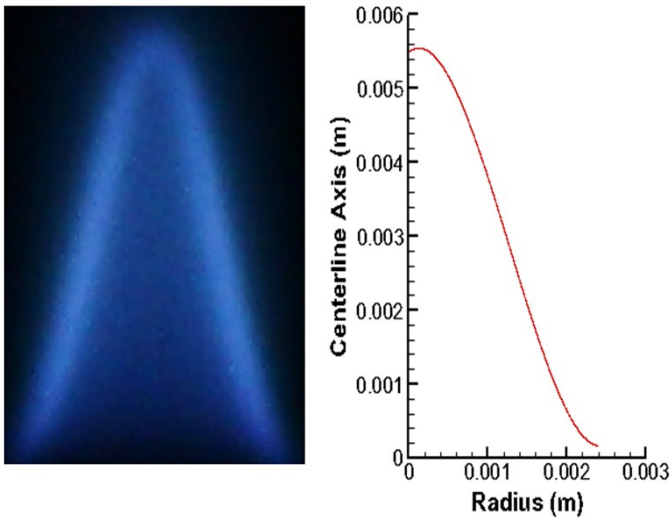

Fig. 3.2. Instantaneous flame image and the identified luminous edge for CH_4-Air at ∅ = 1.0.

3.2.1.2 Experimental inlet conditions

The volumetric flow rates of NH_3, H_2 and air are shown in Tables 3.1, 3.2, 3.3 and 3.4 for cases E%NH_3 = 0, 20, 50 and 80 respectively, for equivalence ratios (∅) ranging from 0.5

to 1.1. All equivalence ratio conditions are calculated based on the following chemical reactions;

$$xNH_3 + yH_2 + a_{stoic}(O_2 + 3.76N_2) \rightarrow bH_2O + cN_2 \quad (3.3)$$

The total volumetric flow rate ($\dot{Q}_{mix}$) for cases E%NH_3 = 20, 50 and 80 is kept constant at 2 standard liters per minute (slpm). Due to higher flame speeds for case E%NH_3 = 0 (pure H_2-air), a total volumetric flow rate $\dot{Q}_{mix}$ = 12 slpm is employed to avoid flame propagation into the fuel tube. Hence, the effects of heat transfer are expected to vary somewhat for cases with and without NH_3, necessitating temperature measurements near the tube exit, as discussed further below.

Table 3.1. Inlet conditions for case E%NH_3 = 0

Tube ID = 4.65 mm				
E%NH_3 = 0				
∅	NH_3 (slpm)	H_2 (slpm)	Air (slpm)	$\dot{Q}_{mix}$ (slpm)
1.1	0	3.79	8.21	12
1.0	0	3.55	8.45	12
0.95	0	3.42	8.58	12
0.9	0	3.29	8.71	12
0.8	0	3.02	8.98	12
0.7	0	2.73	9.27	12
0.6	0	2.42	9.58	12
0.5	0	2.08	9.92	12

Table 3.2. Inlet conditions for case E%NH_3 = 20

Tube ID = 4.65 mm				
E%NH_3 = 20				
∅	NH_3 (slpm)	H_2 (slpm)	Air (slpm)	$\dot{Q}_{mix}$ (slpm)
1.1	0.0819	0.522	1.40	2
1	0.0766	0.488	1.44	2
0.95	0.0738	0.470	1.46	2
0.9	0.0709	0.452	1.48	2
0.8	0.0649	0.414	1.52	2
0.7	0.0585	0.373	1.57	2
0.6	0.0518	0.330	1.62	2
0.5	0.0446	0.284	1.67	2

Table 3.3. Inlet conditions for case E%NH_3 = 50

Tube ID = 4.65 mm				
E%NH_3 = 50				
∅	NH_3 (slpm)	H_2 (slpm)	Air (slpm)	$\dot{Q}_{mix}$ (slpm)
1.1	0.215	0.343	1.44	2
1	0.201	0.320	1.48	2
0.95	0.193	0.308	1.50	2
0.9	0.186	0.296	1.52	2
0.8	0.170	0.270	1.56	2
0.7	0.152	0.243	1.60	2
0.6	0.134	0.214	1.65	2
0.55	0.125	0.211	1.68	2

Table 3.4. Inlet conditions for case E%NH_3 = 80

Tube ID = 11.11 mm				
E%NH_3 = 80				
∅	NH_3 (slpm)	H_2 (slpm)	Air (slpm)	$\dot{Q}_{mix}$ (slpm)
1.1	0.215	0.343	1.44	2
1	0.201	0.320	1.48	2
0.95	0.193	0.308	1.50	2
0.9	0.186	0.296	1.52	2
0.8	0.170	0.270	1.56	2
0.7	0.152	0.243	1.60	2
0.6	0.134	0.214	1.65	2
0.55	0.125	0.211	1.68	2

3.2.2 Computational modeling

A 1-D, laminar, freely propagating flame model is employed in CHEMKIN Pro 4.0 for predicting laminar flame speeds. Such flames, which are assumed to be free from external instabilities and wall effects, represent an idealized model for conducting fundamental

studies. As noted earlier, three reaction mechanisms are used for flame speed predictions: Tian et al. [13], Konnov [12], and GRI-Mech3.0 [22]. While Miller and Bowman [7] used 19 species and 73 reactions, the full Konnov mechanism has over 85 species and 1200 reactions for C, H, N, and O elements [26]. It has been used for a wide range of fuel mixtures, including NH_3, H_2, N_2O, NO, NO_2, and carbon species. However, for the current experiments, all the carbon species and associated reactions are eliminated due to absence of carbon in the fuel mixture. The final mechanism has 31 species and 241 reactions as used by Duynslaegher, et al. [27]. The Tian mechanism includes 84 species with 703 reactions focusing primarily on CH_4-NH_3 flames [13]. GRI-Mech3.0 is the result of considerable research on detailed kinetic mechanisms for NO_x formation and re-burning for natural gas or CH_4 fuel systems. It has been well established for predicting flame structure of pure CH_4 or CH_4 mixtures with other species such as H_2 and CO, among others. The GRI-Mech3.0 mechanism is included in this study for reference, but it has not been updated as recently as the Tian and Konnov mechanisms, especially for NH_3 chemistry in H_2-NH_3-air mixtures [13,26]. Each of the three chemical mechanisms is incorporated into CHEMKIN Pro 4.0 for evaluation of flame speed predictions. However, the GRI-Mech3.0 mechanism failed to converge for a number of conditions, especially with high levels of NH_3. In addition to predictions of flame speed, a study of radical concentrations and a sensitivity analysis of NH_3 decomposition are carried out to help explain differences between model predictions using the Tian and Konnov mechanisms.

3.2.2.1 Heat transfer model and corrected flame speeds

In the present study of flame speed for H_2-NH_3-Air mixtures, heat is not only lost to the ambient via radiation by major species in the flame, but also from the flame base to the burner tube exit. This is observed by monitoring the temperature at the tube exit for each condition. As established from previous work [20,28], flame speed is directly correlated to the flame temperature due to increased reaction rates and thermal and mass diffusivities with increased temperature. Thus, it is important to consider heat losses to ensure the accuracy of CHEMKIN predictions. To determine the heat losses, the tubing is considered to be an extended surface with the following governing equation in Eq. 3.4. The non-dimensional form is shown in Eq. 3.5.

$$\frac{d^2T}{dx^2} - \left(\frac{hP}{kA_c}\right)(T - T_\infty) = 0 \tag{3.4}$$

or

$$\frac{d^2\theta}{dx^2} - (m)\theta = 0 \tag{3.5}$$

Here, T and T_∞ are the tube surface and ambient temperatures (K), respectively, h is the convective heat transfer coefficient (W/m^2·K), k is the conductivity of the tube (W/m·K), P is the inner perimeter of the tube (m), A_c is the cross-sectional area (m^2) of the tube, $\theta = T - T_\infty$, and $m^2 = hp/kA_c$.

To provide the boundary conditions for solving Eq. 3.5, the tube surface temperatures are measured with two K-type thermocouples at Location A (at the tube exit, x = 0 mm) and Location B (x = 50 mm upstream), as shown in Fig. 3.3. Each temperature measurement is time averaged over 60 seconds and care is taken to ensure that the tube surface and the

attached thermocouple are in thermal equilibrium at both locations A and B. The absolute accuracy in the temperature measurement is estimated to be within ± 3 ℃ using a calibrated temperature source, with an uncertainty of $\pm 1\%$. Since the temperature measured at Location B is in close proximity to the ambient temperature, an adiabatic boundary condition is assumed at x = 50 mm which results in the following solution:

$$\frac{\theta}{\theta_b} = \frac{Cosh\, m(L-x)}{(\cosh mL)} \tag{6}$$

where, L is the separation distance between the thermocouples (50 mm).

For each experimental condition, the temperature profile along the tube length is estimated by using Eq. 3.3. Further, the prescribed 50-mm tube length is discretized into 100 sections, each being 0.5 mm in length (Fig. 3.3).

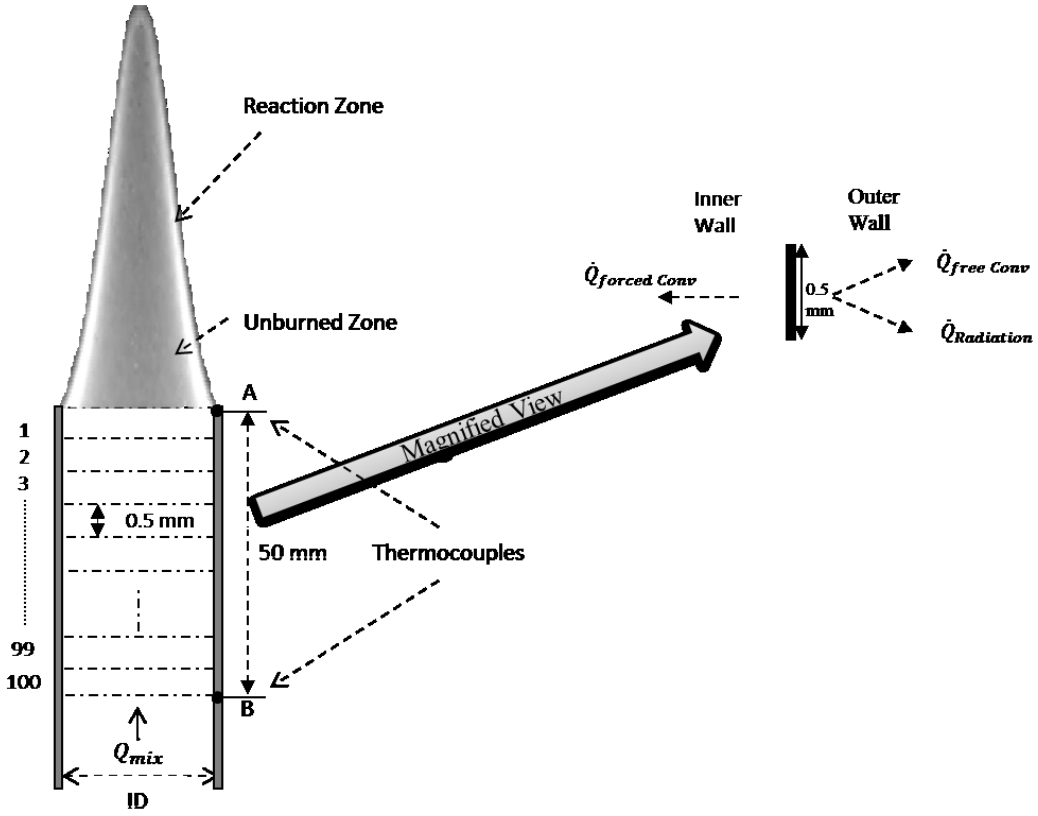

Fig. 3.3. Tube flame and discretization for heat transfer analysis.

For each discretized section, heat from the inner wall is convected back to the unburnt fuel-air mixture by forced convection, whereas heat is lost to the surroundings by free convection and natural convection from the outer wall.

The total heat transfer ($\dot{Q}_{Total}$) from the flame to the tube would be as follows;

$$\dot{Q}_{Total} = \Sigma_1^{100}(\dot{Q}_{forced\ Conv} + \dot{Q}_{free\ Conv} + \dot{Q}_{Radiation}) \quad (3.6)$$

However due to the assumption that $\dot{Q}_{forced\ Conv}$ is transferred back to the unburnt fuel-air mixture, only heat transfer due to $\dot{Q}_{free\ Conv} + \dot{Q}_{Radiation}$ is considered as heat loss from the flame to the ambient, denoted as $\dot{Q}_{heat\ loss}$

$$\dot{Q}_{heat\ loss} = \Sigma_1^{100}\left(\dot{Q}_{free\ Conv} + \dot{Q}_{Radiation}\right) \quad (3.7)$$

Total heat transfer from the flame to the tube ($\dot{Q}_{Total}$) and heat loss to the ambient by free convection and radiation ($\dot{Q}_{heat\ loss}$) are obtained for the entire set of conditions listed in Tables 3.1- 3.4, as shown in Figs. 3.4a and 3.4b respectively.

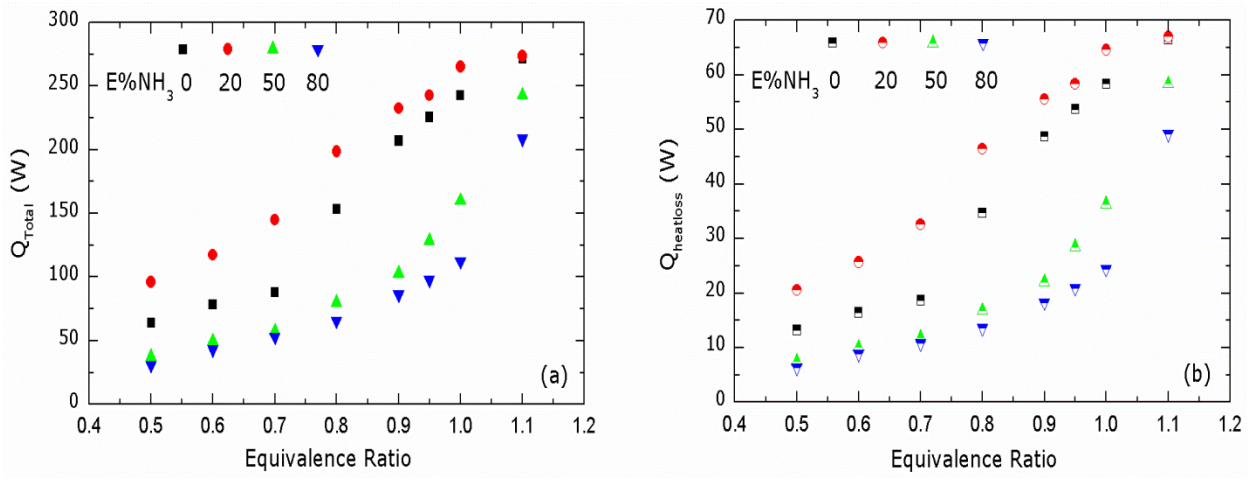

Fig. 3.4. Experimentally determined profiles of (a) $\dot{Q}_{Total}$ and (b) $\dot{Q}_{heatloss}$ with respect to Ø for cases E%NH_3 = 0, 20, 50 and 80.

The heat loss is provided as an input into the PREMIX subroutine module of CHEMKIN Pro 4.0 to adjust the flame speed predictions for both the Konnov and Tian mechanisms. From Fig. 3.4a, it can be easily seen that the total rate of heat transfer from the flame to the burner tube is almost 4 times higher near stoichiometric conditions as compared to fuel lean conditions due to higher flame temperatures. For the same reason, the rate of heat loss increases with equivalence ratio, as shown in Fig. 3.4b. Note that the rate of heat transfer decreases as NH_3 is added for E%NH_3 from 20 to 80. This is expected due to the decrease in flame temperature with NH_3 addition. The case with E%NH_3 = 20 is higher than that for E%NH_3 = 0, likely due, in part, to the higher flowrate needed for the latter.

3.3 Results

Flame speeds are measured for each flame condition with the method explained in section 3.2.1 for equivalence ratios from 0.5 to 1.1. These are compared with flame speed predictions from a 1-D, laminar, freely propagating flame model in CHEMKIN Pro 4.0 with the Konnov [12] and Tian [13] mechanisms. The models are employed under uncorrected (adiabatic) and corrected (non-adiabatic) conditions at standard temperature and pressure. For the uncorrected condition, heat losses are assumed to be zero when computing the theoretical flame speeds. However, for the corrected model, heat loss ($\dot{Q}_{heat\ loss}$) at each condition is estimated based on the heat-transfer analysis as described in section 3.2.2.1 and provided as input to the model. Also, for the adiabatic model, flame speed predictions are evaluated using GRI-Mech3.0 mechanism at each condition and compared with the Tian and

Konnov mechanisms. Subsequently, the effects of reaction rates for specific radicals on the flame speed predictions are analyzed and compared.

3.3.1 H_2-air flames with 0% NH_3 in H_2 by energy($E\%NH_3 = 0$)

To further characterize the laminar flame speed measurements and check the validity of the Matlab code for identifying the luminous conical edge of the flame, pure H_2-Air ($E\%NH_3 = 0$) flames are established for the conditions shown in Table 3.1. Experimental flame speeds are calculated based on the method discussed in the previous section for the equivalence ratio range from 0.5 to 1.1. Figure 3.5a shows the variations of the measured laminar flame speed with increasing equivalence ratio and its comparison for three different mechanisms. The uncorrected (adiabatic) flame speed predictions for Konnov, Tian, and GRI-Mech3.0 mechanisms (Fig. 3.5a) follow similar trends and match closely with measured flame speeds for equivalence ratios from 0.5 to 0.9. However, the experimental data are lower than the predictions at higher equivalence ratios for all three mechanisms. This discrepancy can be attributed to the assumption of an adiabatic flame for the 1-D, laminar, freely propagation flame model. Heat losses could be significant in the experimental arrangement at higher equivalence ratios due to higher flame temperatures. It is notable that the current experimental data agree closely with that of Dong et al. [23], who also used a laminar premixed jet flame for studies of flame speed and who would have been subject to the same effects of heat transfer at higher equivalence ratios. While this agreement gives confidence that the current approach gives repeatable results for a given fuel mixture, it is clearly important to account for heat transfer effects when comparing flame speed data with numerical models [24].

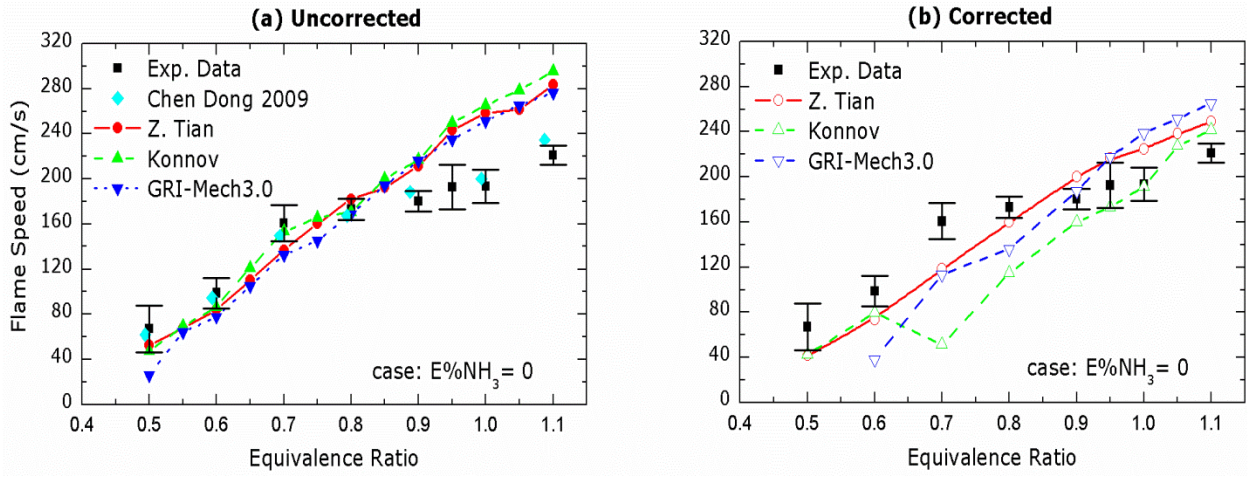

Fig. 3.5. Comparison of measured and predicted laminar flame speeds vs. ∅ for case E%NH_3 = 0, for (a) uncorrected and (b) corrected models. Lines with symbols: predictions, symbols: measured.

Figure 3.5b shows the corrected (non-adiabatic) flame speed predictions by incorporating heat losses ($\dot{Q}_{heat\ loss}$) into the model for the Tian, Konnov and GRI-Mech3.0 mechanisms. It is apparent that the inclusion of heat transfer effects reduces the predicted flame speed at higher equivalence ratios to more closely match that of the experimental data (within ~10%). The main discrepancy is with the Konnov mechanism, which under predicts the experimental flame speeds at equivalence ratios of 0.7 and 0.8. Flame speed predictions for GRI-Mech3.0 mechanism are reasonable, but deviate away from the experimental data for lower equivalence ratios. At $\emptyset = 0.5$, the GRI-Mech3.0 mechanism fails to converge, indicating flame lift-off. The Tian mechanism agrees favorably with the experimental data for the full range of equivalence ratios as well as with the literature [23,29] more so than the predictions using the Konnov or GRI-Mech3.0 mechanisms.

We conclude from these data that laminar flame speed measurements using the premixed jet flame configuration may underestimate the adiabatic flame speed by 25% to 30% at higher equivalence ratios unless they are corrected for heat losses. In comparison to

flame speed measurements from the freely propagating spherical flames of Lee [9], for example, we estimate that corrected flame speed measurements are marginally higher by only 5% and 0.3% at equivalence ratios of 0.6 and 1.0, respectively (see Appendix A). Since many premixed flames used in practice experience some heat losses and are not at the adiabatic flame temperature, these data also indicate that flame speeds measured using spherical or planar freely propagating flames at higher equivalence ratio may overpredict actual flame speeds used in practice if heat transfer effects are significant.

3.3.2 H_2-NH_3-air flames

Instantaneous flame images are shown in Fig. 3.6 for H_2-NH_3-air flames at stoichiometric conditions, including E%NH_3 = 20, 50 and 80. The flame structure and color change significantly with increased ammonia addition to the fuel mixture. The case of E%NH_3 = 20 appears most closely attached to the tube, as evident from the close proximity of the peak signal to the tube exit. This is another potential reason why heat transfer effects are highest for this case, as shown previously in Fig. 3.4.

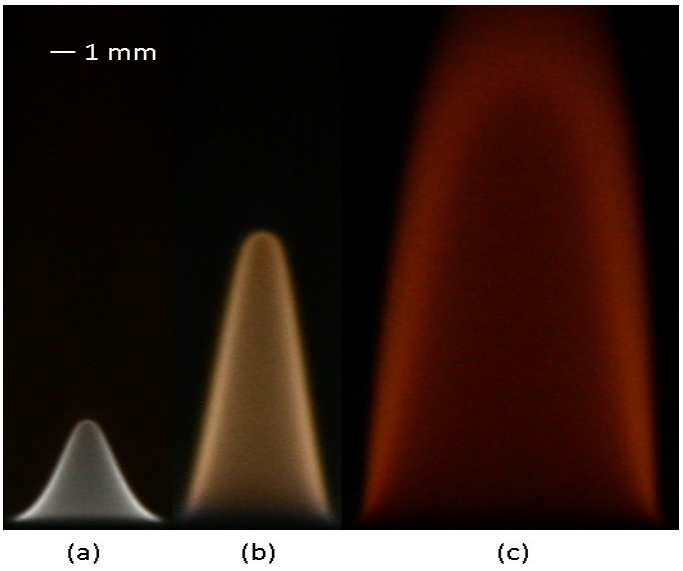

Fig. 3.6. Instantaneous laminar flame images at Ø = 1.0, for E%NH_3 of (a) 20, (b) 50 and (c) 80.

The increase in flame length from 6 mm (for E%NH_3 = 20) to 28 mm for (E%NH_3 = 80) clearly indicates that the reaction zone shifts away from the burner exit with NH_3 addition, which corresponds to a reduction in flame speed. The luminous color change from white to yellow to red for E%NH_3 of 20, 50, and 80, respectively, also confirms a change in flame chemistry with addition of NH_3. The flame-speed data for these conditions are presented and discussed in the following sections.

3.3.2.1 NH_3 addition at 20% by energy in H_2 (E%NH_3 = 20)

Flow rates for achieving E%NH_3 = 20 were shown previously in Table 3.2. For this case, E%NH_3 = 20 and $\dot{Q}_{mix}$ = 2 slpm are kept constant for the entire equivalence ratio range from 0.5 to 1.1. Variations in experimentally measured laminar flame speeds with respect to equivalence ratio are presented in Fig. 3.7a, along with uncorrected theoretical flame speeds for the Konnov, Tian, and GRI-Mech3.0 mechanisms.

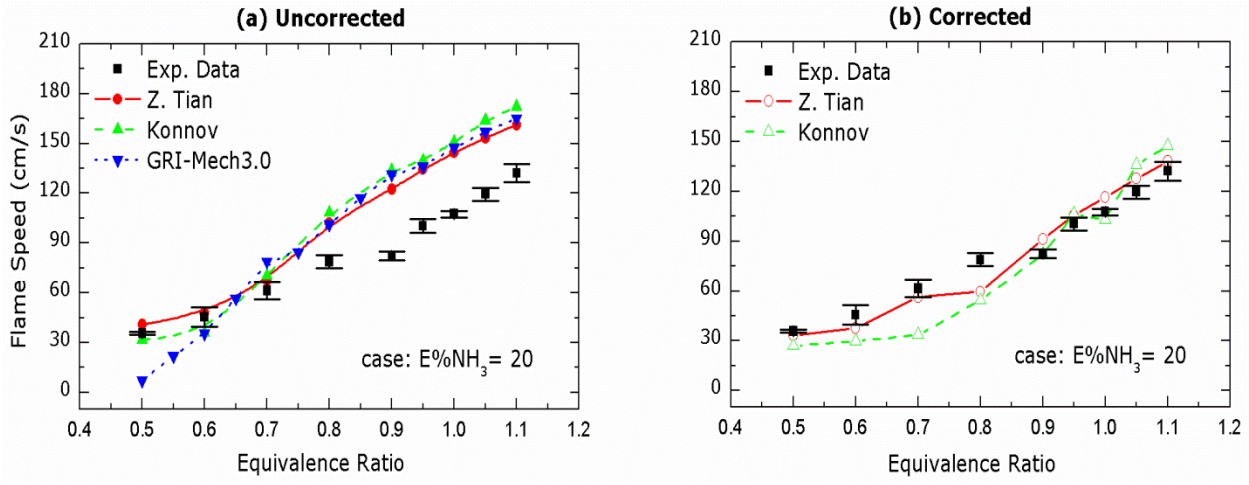

Fig. 3.7. Comparison of measured and predicted laminar flame speeds vs. Ø for case E%NH_3 = 20, for (a) uncorrected and (b) corrected models. Lines with symbols: predictions, symbols: measured.

The measured flame speed for E%NH_3 = 20 rises gradually with increasing equivalence ratio from 35.8 cm/s at $\emptyset = 0.5$ to 132.3 cm/s at $\emptyset = 1.1$. These data are lower by approximately 6% and 15% for $\emptyset = 0.6$ and 1.0, respectively, with heat losses increasing at higher equivalence ratio.

As is the case for H_2-air flames shown in the previous section, the experimental data match closely with the Tian and Konnov model predictions for fuel-lean mixtures, while the GRI-Mech3.0 mechanism seems to under-predict measured flame speeds. At higher equivalence ratios, all three mechanisms agree but predict higher flame speeds than the experimental data if heat losses are not considered.

The corrected (non-adiabatic) flame speed predictions, which incorporate corresponding heat losses ($\dot{Q}_{heatloss}$) into the Konnov and Tian models, are shown in Fig. 3.7b along with the experimental data. Flame speeds after corrections for heat losses are not included for the GRI-Mech3.0 mechanism because the model failed to converge. For fuel lean mixtures (equivalence ratio 0.5 and 0.6), the corrected flame speed predictions using Tian and Konnov

mechanisms reduce only slightly from that shown in Fig. 3.7a due to marginal heat losses from the flame. For equivalence ratios from 0.9 to 1.1, the corrected flame speed predictions are considerably lower due to increased heat losses. From Fig. 3.7b, it can also be observed that the corrected flame speed predictions for the Tian mechanism are in close agreement with the experimental data except at $\emptyset = 0.8$, where the model prediction is 24% lower than the experimental data. Overall, both mechanisms follow the same trend, but the Tian mechanism more closely matches the experimental data. It is notable that the flame speeds drop by nearly a factor of two from E%NH_3 = 0 to 20, and the model and experimental data are capturing this drop with a high degree of accuracy for most equivalence ratios.

3.3.2.2 NH_3 addition at 50% by energy in H_2 (E%NH_3 = 50)

Figures 3.8a and 3.8b illustrate the measurements and predictions of laminar flame speed as a function of equivalence ratio for E%NH_3 = 50 based on operating conditions shown previously in Table 3.3. In Fig. 3.8a, the measured flame speeds increase from 8.4 to 44.9 cm/s as equivalence ratio increases from 0.55 to 1.1. These are somewhat lower than Lee [19], who reported upstretched flame speeds of 19.5, 36.2 and 53.4 cm/s at equivalence ratios 0.6, 0.8 and 1.0 respectively, for E%NH_3 = 50 in a spherical propagating flame. Lee [19] measured flame speeds approximately 25% higher compared to the present work for $\emptyset = 0.6$ and 1.0, and 6% higher for an equivalence ratio of 0.8 (see Appendix). Given the nearly six-fold drop in flame speed from E%NH_3 of 0 to 50 and differences in heat losses between the two flame configurations, this agreement is fairly remarkable.

It is also clear from Fig. 3.8a that theoretical flame speeds begin to deviate significantly when comparing the Tian, Konnov, and GRI-Mech3.0 mechanisms at this condition. The

uncorrected flame speed predictions for the Tian mechanism increase with equivalence ratio at a much higher rate than the Konnov mechanism. For example, the uncorrected flame speed for the Tian mechanism is 41% and 72% higher than the Konnov mechanism at $\emptyset = 0.55$ and 1.1, respectively. The theoretical flame speed for the GRI-Mech3.0 mechanism follows a very similar trend as the Tian mechanism for the full range of equivalence ratios, but consistently predicts a lower flame speed. In fact, the GRI-Mech3.0 mechanism fails to converge at equivalence ratios of 0.5 and 0.6 where flame speeds are lowest, predicting flame lift-off under these conditions.

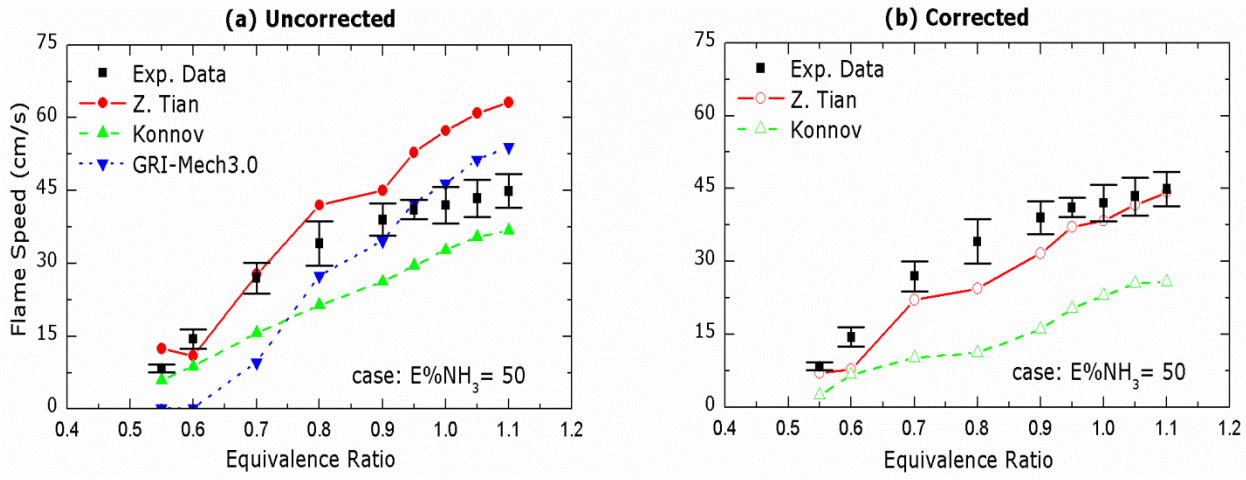

Fig. 3.8. Comparison of experimental flame speeds with predicted laminar flame speeds as a function of $\emptyset$ for $E\%NH_3$ = 50, for (a) uncorrected and (b) corrected models. Lines with symbols: predictions, symbols: measured.

In Fig. 3.8b, it can be seen that incorporating the heat losses in the model for flame speed predictions has a significant impact for both the Tian and Konnov mechanisms. Because the effects of heat losses are greatest at high equivalence ratio, the corrected flame speeds for the Tian mechanism are brought into close agreement with the experimental data, except at $\emptyset \sim 0.8$ where the prediction underestimates the flame speed to a greater degree.

However, the predictions using the Konnov mechanism drop the theoretical flame speeds much below that of the experimental data for the entire range of equivalence ratios.

3.3.2.3 NH_3 addition at 80% by energy in H_2 ($E\%NH_3 = 80$)

For case of $E\%NH_3 = 80$, the measured flame speeds for various equivalence ratios (see Table 4) are displayed in Fig. 3.9. The measured flame speeds increase gradually from 4.9 to 13.2 cm/s for equivalence ratios from 0.5 to 0.95. This is followed by a steep increase from 0.95 to 1.1, reaching a peak flame speed of 21.4 cm/s. These data are approximately a factor of 10 to 15 lower than the case of $E\%NH_3 = 0$ (H_2-air only). The unstretched laminar flame speeds measured by Lee et al. [19] for case $E\%NH_3 = 80$, at equivalence ratios 0.6, 0.8 and 1.0 are 6.3, 14.6 and 22.1 cm/s, respectively, whereas experimental flame speeds for current study at equivalence ratio 0.6, 0.8 and 1.0 are recorded as 6.1, 7.4 and 17.2 cm/s respectively (see Appendix 3.A). Hence, the flame speed data of Lee [19] agree with the current work to within 6% at low equivalence ratio ($\emptyset \sim 0.6$) where heat losses are minimal, but are 48% and 22% lower at equivalence ratios of 0.8 and 1.0 due to increased heat losses.

Unlike the previous cases from $E\%NH_3$ of 0 to 50, the corrected flame speed predictions for $E\%NH_3 = 80$ using the Konnov mechanism capture the experimental trend for the full range of equivalence ratios (see Fig. 3.9b), while the Tian mechanism significantly under predicts the experimental flame speeds. At low equivalence ratio, the Tian mechanism is unable to converge for $E\%NH_3 = 80$, indicating flame lift-off. As usual, the GRI-Mech3.0 mechanism follows a similar trend as the Tian mechanism, but with an even lower predicted flame speed.

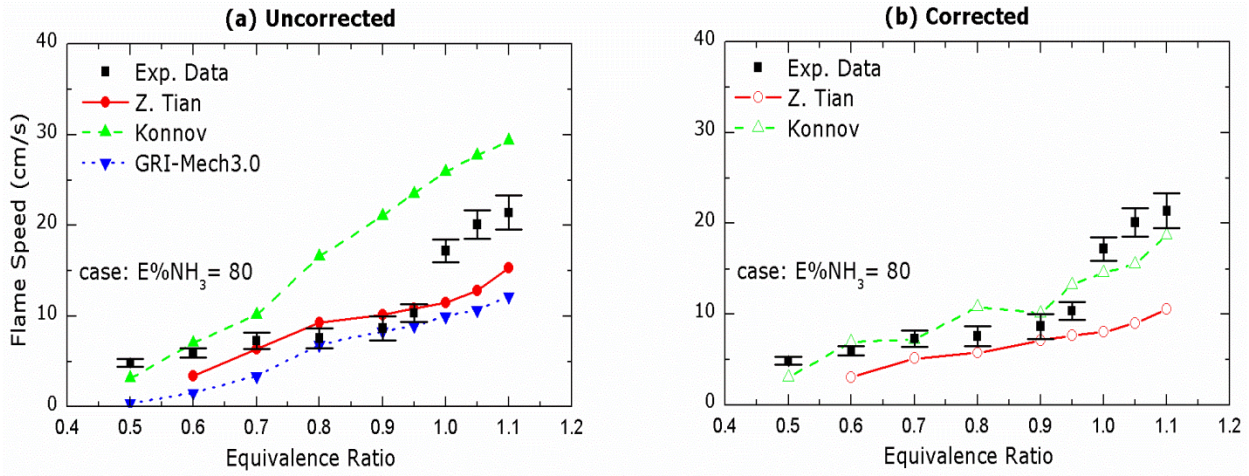

Fig. 3.9. Experimentally measured flame speeds and theoretical laminar flame speeds with respect to Ø for case $E\%NH_3$ = 80, for (a) uncorrected and (b) corrected models. Lines with symbols: predictions, symbols: measured.

Based on these observations, we conclude that the Konnov mechanism is more suitable for estimating theoretical laminar flame speeds when NH_3 content is very high in the fuel mixture. The high level of agreement between the Konnov and Tian mechanisms for $E\%NH_3$ of 0 and 20 and the poor level of agreement at $E\%NH_3$ of 50 and 80 point to fundamental differences in the treatment of NH_3 chemistry between the two mechanisms. Differences are particularly evident at higher equivalence ratio. Furthermore, the high sensitivity of the two mechanisms to heat losses with high NH_3 addition indicates that further investigation of key elementary reactions may shed light on differences between the Tian and Konnov mechanisms, as discussed below.

3.3.3 Effects of radicals on flame speed

From the flame speed analysis in the previous section, it is clear from Figs. 3.7, 3.8 and 3.9 that the heat losses reduce the laminar flame speeds of the fuel-air mixtures. Heat loss from the flame reduces the flame temperature and, thereby, lowers the rate of radical

formation reactions. To investigate the effects of heat loss on radical species and flame speed in the CHEMKIN models, the concentration profiles of H, O and OH radicals are plotted for uncorrected (adiabatic) and corrected (non-adiabatic) models in Fig. 3.10 at an equivalence ratio of 1.0 for E%NH_3 = 50 using the Konnov mechanism.

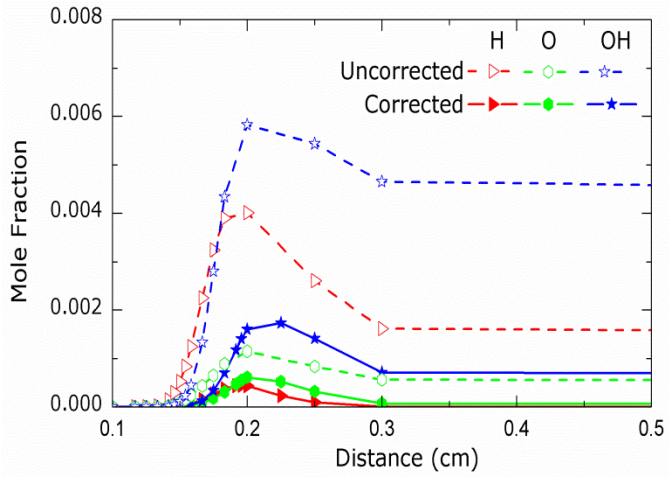

Fig. 3.10. Mole-fraction profiles of H, O, and OH radicals for Konnov mechanism at Ø = 1.0 for E%NH_3 = 50.

From Fig. 3.10, it can be clearly seen that peak H, O and OH concentrations for the corrected (non-adiabatic) model are significantly lower compared to the adiabatic (uncorrected) model. The largest reductions are seen in the H radical, followed by the OH and O radicals. This follows the trend in which flame speed is significantly reduced in the model predictions when heat losses are considered.

To further investigate the effects of reduced radical concentrations on the rate of NH_3 decomposition at different equivalence ratios, the mole fractions of H, O and OH radicals for both the Tian and Konnov mechanisms are plotted in Figs. 3.11a and 3.11b for E%NH_3 = 50 using the uncorrected (adiabatic) model.

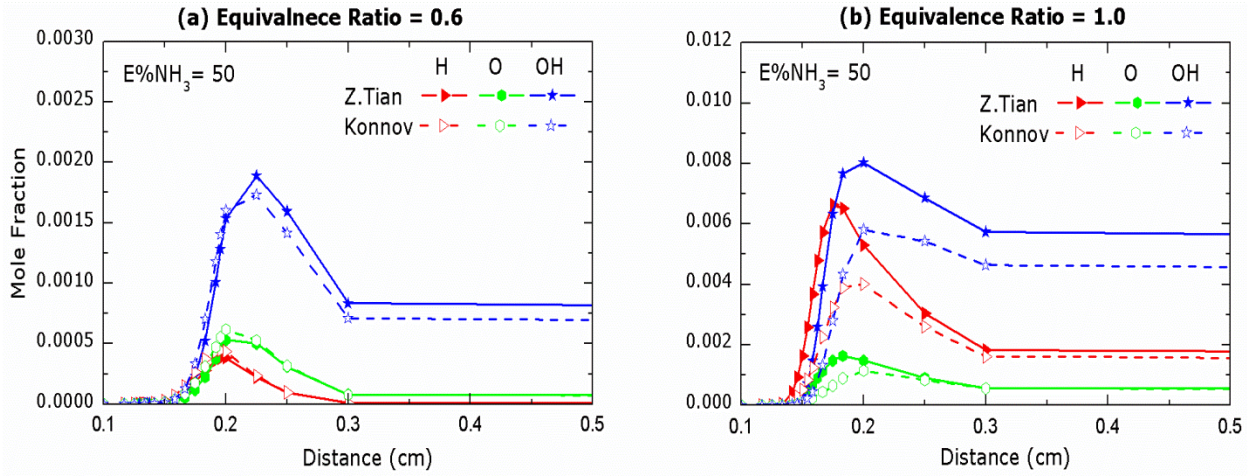

Fig. 3.11. Mole fraction profiles of H, O, and OH for both Tian and Konnov mechanisms at (a) $\emptyset$ = 0.6 and (b) $\emptyset$ = 1.0 for case E%NH_3 = 50 using uncorrected (adiabatic) model.

The data in Fig. 3.11a show that the profiles of H, O and OH are only slightly higher for the Konnov mechanism early in the flame for ϕ = 0.6, with the Tian mechanism having slightly higher OH further downstream. Then, at ϕ = 1.0, the radical mole fractions increase significantly and deviate between the two mechanisms, with the Tian mechanism showing much higher radical mole fractions along the entire length of the fame. These data roughly correspond to the trends in flame speed seen previously in Fig. 3.8.

To assess the relative impact of specific radical species on flame speed and help explain differences in flame speed predictions, a sensitivity analysis of NH_3 decomposition is performed for the Tian and Konnov mechanisms, as shown in Tables 3.5 and 3.6. The location chosen for this analysis is within the reaction zone of the 1-D flame at the location of peak heat release, which varies for each condition but generally occurs along the rising edge shown in Fig. 3.11. It is revealed that the major reaction pathways contributing towards ammonia decomposition include:

$$NH_3 + OH \leftrightarrow NH_2 + H_2O \qquad \text{(Rxn \# 1)}$$

$$NH_3 + H \leftrightarrow NH_2 + H_2 \quad \text{(Rxn \# 2)}$$

$$NH_3 + O \leftrightarrow NH_2 + OH \quad \text{(Rxn \# 3)}$$

At ϕ = 0.6, the sensitivity analysis assigns the greatest significance (~90%) to OH radicals in the decomposition of NH_3, followed by O and H radicals, for both the Tian and Konnov mechanisms. This helps to explain why the Tian mechanism has a slightly higher flame speed at ϕ = 0.6 (see Fig. 3.8). At ϕ = 1.0, reactions involving OH and H radicals are most critical, together accounting for over 90% of NH_3 decomposition. As shown in Figs. 3.10 and 3.11, significant changes in OH and H radicals could lead to significant changes in flame speed with heat losses and changes in equivalence ratio. These data help to explain differences in flame speed between the Tian and Konnov mechanisms. In particular, because OH has the greatest effect on NH_3 decomposition, the relatively high mole fraction of OH radicals for the Tian mechanism leads to a higher flame speed at ϕ = 0.6 and a greater increase in flame speed at higher equivalence ratio.

Table 3.5. Relative contribution of each NH_3 reaction (1-3) to rate of NH_3 decomposition. Relative contributions of Konnov and Tian mechanisms are compared for equivalence ratio of 0.6, E%NH_3 = 50, and uncorrected for heat transfer effects.

Rxn #	Reaction	% Contribution	
		Konnov	Tian
1	$NH_3+OH \leftrightarrow NH_2+H_2O$	91.38	85.59
2	$NH_3+H \leftrightarrow NH_2+H_2$	2.96	2.84
3	$NH_3+O \leftrightarrow NH_2+OH$	5.66	11.58

Table 3.6. Relative contribution of each NH_3 reaction (1-3) to rate of NH_3 decomposition. Relative contributions of Konnov and Tian mechanisms are compared for equivalence ratio of 1.0, E%NH_3 = 50, and, uncorrected for heat transfer effects.

Rxn #	Reaction	% Contribution	
		Konnov	Tian
1	$NH_3+OH \leftrightarrow NH_2+H_2O$	61.8	66.79
2	$NH_3+H \leftrightarrow NH_2+H_2$	31.1	23.57
3	$NH_3+O \leftrightarrow NH_2+OH$	7.02	9.63

To quantify this effect further, the rates of production and decomposition of NH_3 are computed for E%NH_3 = 50 at equivalence ratios of 0.6 and 1.0 for the Konnov and Tian mechanisms. As with the sensitivity analysis discussed above, the location chosen for this analysis is at the peak heat release within the reaction zone. The total rate of production (ROP) and total rate of decomposition (ROD) are shown with positive and negative signs, respectively, in Table 3.7. The rate of decomposition is nearly two orders of magnitude higher than the rate of production and will have the most impact on flame speeds. At an equivalence ratio of 1.0, the higher rate of decomposition for the Tian mechanism is consistent with the higher flame speeds shown in Fig. 3.8. At $\phi = 0.6$, however, the Konnov mechanism displays a higher rate of NH_3 decomposition at the location chosen for sensitivity analysis (near the peak heat release) because of the higher concentrations of OH, H, and O radicals. This is not consistent with the slightly lower flame speeds for the Konnov mechanism, shown previously in Fig. 3.8a.

Table 3.7. Total rates of production (ROP) and decomposition (ROD) of NH_3 at location of peak heat release for Tian and Konnov mechanisms at Ø = 0.6 and 1.0 for case E%NH_3 = 50.

		Total Rate of Decomposition (ROD)		Total Rate of Decomposition (ROD)	
E%NH_3	Ø	Tian	Konnov	Tian	Konnov
50	0.6	2.81E-05	2.29E-5	-1.62E-03	-3.24E-03
	1.0	2.39E-04	1.09E-04	-1.07E-02	-7.38E-03

To explain the higher flame speeds for the Tian mechanism at $\phi = 0.6$, it is necessary to attribute a significant role to the OH radical, which dictates NH_3 decomposition at $\phi = 0.6$ (see Table 3.5) and is higher for the Tian mechanism beyond the location of peak heat release as shown in Fig. 3.11a. These data highlight the role of OH in determining flame speeds at different equivalence ratios, with and without heat losses, and for the different chemical mechanisms.

3.4 Conclusions

Flame speed measurements are performed for H_2-NH_3-Air mixtures in a laminar jet flame configuration. Data are compared with flame speed predictions using the Tian and Konnov chemical mechanisms in a 1-D, laminar, freely propagating flame speed model in CHEMKIN Pro 4.0. Cases include equivalence ratios of 0.5 to 1.1 and NH_3 as a percent of the energy in H_2 of E%NH_3 = 0 (pure H_2-Air), 20, 50 and 80. The heat loss for each condition is determined from thermocouple measurements along the burner tube and incorporated into the theoretical model. Flame speed predictions for the GRI-Mech3.0

mechanism are also computed for the adiabatic model and compared with the Tian and Konnov mechanisms for a limited number of cases.

Results show that for E%NH_3 = 0, the laminar flame speed predictions for all three mechanisms are comparable, with the GRI-Mech3.0 mechanism showing lower flame speeds by a factor of two only at the lowest equivalence ratio of 0.5. With corrections for heat losses, however, only the Tian mechanism showed agreement with experimental date for the full range of equivalence ratios. Similarly, for E%NH_3 of 20 and 50, the Tian mechanism is shown to be more robust than Konnov mechanism in predicting laminar flame speeds for H_2-NH_3-air mixtures. The GRI-Mech3.0 mechanism followed the same trends as the Tian mechanism, but underpredicted flame speeds and had difficulty with model convergence (indicating flame lift-off) at lower equivalence ratios. In contrast, for E%NH_3 = 80, the Tian mechanism failed to predict experimental flame speeds as well as the Konnov mechanism. Hence, the Konnov mechanism is found to more suitable for fuel mixtures having high ammonia content. Similarly, the GRI-Mech3.0 mechanism is not recommended at lean conditions or for fuel-air mixtures having high NH_3 concentrations.

The mole fractions of H, O and OH radicals are used to evaluate possible sources of deviation between the Tian and Konnov mechanisms and are found to differ significantly for $\emptyset$ = 1.0. At this condition, the theoretical flame speeds predicted by the Tian mechanism are found to be higher than Konnov and correspond with higher peak mole fractions of OH, H, and O radicals. From sensitivity analyses of NH_3 decomposition rates, it is verified that the radical pool of OH, H, and O play an important role in controlling the total rate of

decomposition of NH_3 via three primary reaction pathways, with OH having a more significant impact.

From the current study, it is revealed that the radical mole fractions have strong implications on the predicted flame speeds. Therefore it is of future interest to validate these radical concentrations, which is experimentally convenient using the laminar jet flame configuration of the current study. Similarly, these differences in radical mole fractions may be consequential for the NO formation in the flame. Hence, follow-on work will include investigation of the effects of radical species on the NO formation rates in H_2-NH_3-air flames using both the Tian and Konnov mechanisms.

Acknowledgments

This research was funded, in part, by the Iowa Energy Center under Grant 08F-03, with program management provided by Norman Olson, Kevin Nordmeyer, and Thomas Barton. The authors are also grateful to Miao Li, James Dautremont, Matthias Veltman, Cuong Huynh, Christopher Gross, Jordon Tiarks, Sudheer Tenneti, and Song-Charng Kong of Iowa State University for assistance and helpful discussions.

Appendix: Comparisons with spherical freely propagating flames

In comparison to measurements from the freely propagating spherical flames of Lee et al. [9,19], the current data show lower flame speeds primarily due to heat losses to the flame tube. Comparisons at each condition in common with the work of Lee [9,19] are described in the previous sections and are summarized further in Table 3.8 below. As noted earlier, with

no NH_3 addition, the data agree to within 6% from low to high equivalence ratio. With 20% NH_3 addition by energy, the data agree to within 6% at low equivalence ratio and to within 15% at high equivalence ratio. With 50% NH_3 addition by energy, more significant deviations occur potentially due to the low flame speeds involved, with the current measurements being 6% to 25% lower than that of Lee. With 80% NH_3 addition by energy, the data are again comparable but are 5% to 48% lower than that of Lee.

Table 3.8. Comparison of current flame speed data with that of Lee et al. [9, 19].

	Flame speed (cm/s)					
	Ø = 0.6		Ø = 0.8		Ø = 1	
E%NH_3	Lee	Current	Lee	Current	Lee	Current
0	93.8	98.8	na	na	193	193
20	48.3	45.5	na	na	127	108
50	19.5	14.4	36.3	34.1	53.5	42.0
80	6.3	6.1	14.6	7.4	22.1	17.2

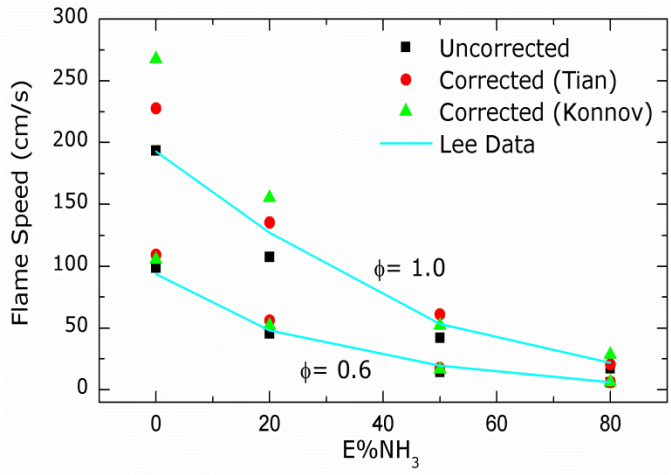

Fig. 3.12. Comparison of current flame speed data with that of Lee et al. [9, 19] at Ø = 0.6 and 1.0 with and without corrections for heat losses.

Despite some differences with the data of Lee [9,19], the current experimental data show excellent agreement when the current CHEMKIN Pro 4.0 model using the Konnov [12] and

Tian [13] chemical mechanisms after the effects of heat losses are considered. Hence it should be possible to use this model to estimate the effects of heat losses to see if the current experimental data would otherwise be close to the adiabatic measurements of Lee [9,19]. Fig. 3.12 shows such a comparison after an approximate correction is applied to the current experimental data using the CHEMKIN model.

3.5 References

[1] Zamfirescu C, Dincer I. Using ammonia as a sustainable fuel. J. Power Sources 2008;185:459-465.

[2] Zamfirescu C, Dincer I. Ammonia as a green fuel and hydrogen source for vehicular applications. Fuel Process Technol 2009;90:729-737.

[3] Brandhorst H, Baltazar-Lopez M, Tatarchuk B, Cahela DR, Barron T. Ammonia – it's transformation and effective utilization. 6th International Energy Conversion Engineering Conference. Cleveland, Ohio; 2008. p. 1-11.

[4] Thomas G, Parks G. Potential roles of ammonia in a hydrogen economy. 2006. <http://www.hydrogen.energy.gov/>.

[5] Fenimore CP, Jones GW. Oxidation of ammonia in flames. J Phys Chem 1961;65:298-303.

[6] Bian J. Experimental study of the formation of nitrous and nitric oxides in H_2-O_2-Ar flames seeded with NO and/or NH_3. Symposium (International) On Combustion 1991;23:379-386.

[7] Miller JA, Bowman CT. Mechanism and modeling of nitrogen chemistry in combustion. Prog Energ Combust 1989;15:287-338.

[8] Reiter AJ, Kong SC. Combustion and emissions characteristics of compression-ignition engine using dual ammonia-diesel fuel. Fuel 2011;90:87-97.

[9] Lee JH, Lee SI, Kwon OC. Effects of ammonia substitution on hydrogen/air flame propagation and emissions. Int J Hydrogen Energ 2010;35:11332-11341.

[10] Glarborg P. Fuel nitrogen conversion in solid fuel fired systems. Prog Energ Combust 2003;29:89-113.

[11] Mendiara T, Glarborg P. Ammonia chemistry in oxy-fuel combustion of methane. Combust Flame 2009;156:1937-1949.

[12] Konnov AA. Implementation of the NCN pathway of prompt-NO formation in the detailed reaction mechanism. Combust Flame 2009;156:2093-2105.

[13] Tian Z, Li Y, Zhang L, Glarborg P, Qi F. An experimental and kinetic modeling study of premixed $NH_3/CH_4/O_2$/Ar flames at low pressure. Combust Flame 2009;156:1413-1426.

[14] Duynslaegher C, Jeanmart H, Vandooren J. Flame structure studies of premixed ammonia/hydrogen/oxygen/argon flames: experimental and numerical investigation. Proc Combust Inst 2009;32:1277-1284.

[15] Shmakov AG, Korobeinichev OP, Rybitskaya IV, Chernov AA, Knyazkov DA, Bolshova TA, Konnov AA. Formation and consumption of NO in $H_2/O_2/N_2$ flames doped with NO or NH_3 at atmospheric pressure. Combust Flame 2010;157:556-565.

[16] Zhang K, Li Y, Yuan T, Cai J, Glarborg P, Qi F. An experimental and kinetic modeling study of premixed nitromethane flames at low pressure. Proc Combust Inst 2011;33:407-414.

[17] Hansen S, Glarborg P. Simplified model for reburning chemistry. Energ Fuel 2010;24:4185-4192.

[18] Duynslaegher C, Jeanmart H, Vandooren J. Use of ammonia as a fuel for SI engine. Combustion.org.uk 2009:1-6.

[19] Lee JH, Kim JH, Park JH, Kwon OC. Studies on properties of laminar premixed hydrogen-added ammonia/air flames for hydrogen production. Int J Hydrogen Energ 2010;35:1054-1064.

[20] Natarajan J, Lieuwen T, Seitzman J. Laminar flame speeds of H_2/CO mixtures: effect of CO_2 dilution, preheat temperature, and pressure. Combust Flame 2007;151:104-119.

[21] Bouvet N, Chauveau C, Gökalp I, Lee SY, Santoro RJ. Characterization of syngas laminar flames using the bunsen burner configuration. Int J Hydrogen Energ 2011;36:992-1005.

[22] Smith GP, Golden DM, Frenklach M, Moriarty NW, Eiteneer B, Goldenberg M, et al. GRI-mech. 3.0. <http://www.me.berkeley.edu/gri_mech/>.

[23] Dong C, Zhou Q, Zhao Q, Zhang Y, Xu T, Hui S. Experimental study on the laminar flame speed of hydrogen/carbon monoxide/air mixtures. Fuel 2009;88:1858-1863.

[24] Turns SR. An introduction to combustion: concepts and applications. New York: McGraw-Hill; 2001.

[25] Coppens F, Deruyck J, Konnov AA. Effects of hydrogen enrichment on adiabatic burning velocity and NO formation in methane-air flames. Exp Therm Fluid Sci 2007;3:437-444.

[26] Konnov A. Development and validation of a detailed reaction mechanism for the combustion of small hydrocarbons. 28th Symposium (Int.) on Combustion, Edinburgh, 2000 [abstract symposium. paper: 317].

[27] Duynslaegher C, Jeanmart H, Vandooren J. Ammonia combustion at elevated pressure and temperature conditions. Fuel 2010;89:3540-3545.

[28] Gu X. Laminar burning velocity and markstein lengths of methane–air mixtures. Combust Flame 2000;121:41-58.

[29] Huang Z, Zhang Y, Zeng K, Liu B, Wang Q, Jiang D. Measurements of laminar burning velocities for natural gas–hydrogen–air mixtures. Combust Flame 2006;146:302-311.

CHAPTER 4. A COMPARISON OF DETAILED CHEMICAL KINETIC MECHANISMS FOR NO FORMATION IN LAMINAR H_2-NH_3-AIR PREMIXED JET FLAMES

A paper to be submitted in *Fuel* Journal, 2012

Praveen Kumar and Terrence R. Meyer*

Abstract

A number of detailed chemical mechanisms have been developed to predict NO and NH_3 reaction kinetics for a variety of fuel mixtures. Despite extensive experimental validation, the chemical pathways and predictions of net NO production can differ substantially. In the current work, a numerical study of premixed H_2-NH_3-air flames is conducted using three detailed chemical mechanisms to compare NO and NH_3 reaction kinetics for the same flow conditions and to identify and resolve key sources of disagreement. As a validation method, NO emission measurements are performed for 0% to 80% NH_3 in H_2 by energy (E%NH_3) laminar premixed flames on an eight port tube burner setup.

The Tian, Konnov and GRI-Mech3.0 detailed mechanisms are employed in a 1-D, laminar freely propagating flame model in CHEMKIN PRO with up to 80% NH_3 in H_2 by energy and for equivalence ratios from 0.7 to 1.1. A sensitivity analysis is performed to determine the relative contributions of various precursors, radical species, and reaction pathways to NO and NH_3 production and destruction in the flame zone. Based on these analyses, significant differences in numerical predictions are identified, and a modified GRI-Mech3.0 mechanism with three additional reactions and updated rate parameters is proposed. The new mechanism

* Department of Mechanical Engineering, Iowa State University, Ames, IA 50011, USA
* Corresponding author. Tel: +1 515 294 1805.
* E-mail address: trm@iastate.edu

verifies the key role of these reactions in net NO production and allows improved agreement for lean and rich conditions.

Keywords: Hydrogen, H_2, Ammonia, NH_3, Nitric Oxide, NO, Premixed flame, Combustion kinetics, Chemical Kinetics, Detailed chemistry, GRI-Mech3.0.

Nomenclature:

$E\%NH_3 = percent\ of\ NH_3\ by\ energy\ in\ H_2/NH_3\ mixture$

$X_i\ =\ mole\ fraction\ of\ i^{th}\ species.$

$\dot{Q}_{mix} = volumetric\ flow\ rate\ of\ the\ fuel - air\ mixture\ (slpm)$

$\emptyset\ =\ equivalence\ ratio$

$\mathrm{ROP}\ =\ total\ rate\ of\ production\ \left(\frac{mole}{cm^3 * s}\right)$

$\mathrm{ROD}\ =\ total\ rate\ of\ decompostion\ \left(\frac{mole}{cm^3 * s}\right)$

$net\ rate\ of\ production = \mathrm{ROP} - \mathrm{ROD}$

4.1 Introduction

Ammonia (NH_3) is a component of fuel gases generated from biomass or waste-to-energy gasification and can be a significant source of flame-generated nitric oxide (NO) emissions. The role of NH_3 as a direct carrier for hydrogen has also increased interest in NH_3 chemistry due to its relatively high energy density and established infrastructure for distribution and storage [1]. A number of studies have focused on the flame structure and combustion characteristics of NH_3-seeded flames using conventional fuels such as H_2, CH_4, diesel, etc. [2-6]. For accurate prediction of emissions due to fuel-bound nitrogen, a comprehensive understanding of NH_3 combustion chemistry and NO formation is required. Miller and

Bowman [7] developed a detailed chemical mechanism for predicting the production of nitrogen species such as NO, N_2O, and NO_2 in hydrocarbon/NH_3 and H_2/NH_3 mixtures. Subsequently, Bian et al. [5] established a simplified kinetics mechanism by proposing several modifications to the NH_2 and NH species rate constants based on investigations of the effects of NH_3 seeding in H_2/O_2/Ar flames under both lean and stoichiometric conditions. Later, Glarborg et al. [8] proposed pathways for the formation of N_2 and NO from NH_3 under fuel-rich conditions. For these flames, it was established that radical concentrations play an important role in determining fuel oxidation rates and thus affect not only the laminar burning velocity but also the flame structure and emissions.

The GRI-Mech3.0 mechanism [9], primarily intended for predicting the flame structure of methane flames, has also been utilized for predicting the combustion chemistry of pure H_2-air and NH_3-seeded methane flames, with limited success. For example, Harrington et al. [10] measured concentrations of NO and OH by using laser-induced fluorescence (LIF) as well as temperature profiles in 38-torr and 78-torr premixed H_2/air flames and showed considerable disagreement between the experiments and modeling results with the simplified GRI-Mech 2.11 mechanism. Subsequently, Sullivan et al. [11] compared the Glarborg and GRI-Mech3.0 mechanisms for NH_3-seeded CH_4-air laminar diffusion flames and showed better agreement for the Glarborg mechanism with the experimental data.

In recent years, a more detailed version of chemical mechanisms for hydrocarbon/NH_3 and H_2/NH_3 mixtures have been developed by Konnov [12] as well as by Glarborg and coworkers in Tian et al. [13]. The Konnov mechanism [12] has been widely used for predicting the flame structures of various NH_3/NO/N_2O-seeded H_2 and hydrocarbon flames. For some flames, it has

shown remarkable agreement with the experimental data. For instance, Konnov et al. [14] measured the concentrations of NO in $CH_4/NH_3/O_2/N_2$ flames and found satisfactory agreement between experiments and predictions in major species concentrations like CO, CO_2, O_2 and NO_x under lean conditions. However, this success was not repeated for CH_4-O_2-N_2 premixed flames doped with NO for lean conditions at standard pressure and temperature [15].

Similarly, the detailed mechanism developed by Tian et al. [13], based on the framework of Skriberg et al. [16], has been successfully demonstrated to predict the flame structure of CH_4-NH_3 and nitro-methane flames in close agreement with the experimental data for 11 premixed $NH_3/CH_4/O_2$/Ar flames at low-pressure (4.0 kPa) and stoichiometric conditions. With comprehensive validation over a range of conditions, the Tian mechanism is increasingly being utilized [17] in place of the GRI-Mech3.0 mechanism for some cases [18].

In addition to work on detailed chemical kinetic mechanisms, the development of simplified chemistry for NH_3 flames has been pursued to reduce the computational cost in combustion modeling. Lindstedt et al. [19] developed a simplified chemical mechanism for NH_3 oxidation having 22 species and 97 reactions with experimental validation in NH_3-seeded H_2/O_2, $H_2/NO/O_2$ and pure NH_3/O_2 premixed laminar flames. Recently, Duynslaegher et al. [20] utilized a reduced version of the Konnov mechanism (by eliminating all carbon species and associated reactions) in predicting the effects of initial H_2 content on NH_3-H_2-O_2-Ar flames. These authors showed good agreement between modeling and experimental data, except for NH_2 and N_2O species, but reported poor performance for the Lindstedt and GRI-Mech3.0 mechanisms in predicting the flame structure compared to the more detailed but "carbon-free" Konnov mechanism. Subsequently, the same reduced version (31 species and

245 reactions) of the Konnov detailed mechanism was further used in simulating the flame structures of NH_3 flames at elevated pressure and temperature conditions by Duynslaegher et al. [21]. Later Shmakov et al. [22] studied NO and NH_3 doped H_2-O_2-N_2 flames experimentally and numerically using another integral part of the Konnov detailed mechanism and employed modifications to the reaction chemistry based on the experimental data for better overall agreement. While their results were promising, we are not aware of their modified mechanism being readily available in the literature.

For NH_3-seeded flames, therefore, a number of possible detailed chemical kinetic mechanisms can be used which have demonstrated some success in predicting flame structure. However, these mechanisms have not been compared directly under the same flame conditions, especially with regard to predicting NO chemistry in NH_3-seeded flames. Hence it is unclear if the level of detail in each mechanism leads to substantial differences in predicted NO emissions, and it is unclear which elementary reactions and sub-mechanisms contribute most significantly to these differences. Recently, for example, Lee et al. [23,24] utilized the Miller and Bowman mechanism [7] to predict NO formation for H_2-NH_3-air mixtures in a spherical, freely propagating flame. This compact mechanism has been validated under certain conditions, but the NH_3 oxidation pathways and NO formation chemistry via NNH are considered incomplete and potentially could predict substantially different NO concentrations as compared with the more detailed mechanisms discussed above.

Thus far, we are not aware of a study that has compared the performance of these different chemical kinetic mechanisms under similar flame conditions and determined the impact of certain reaction pathways on predictions of NO emissions, especially for NH_x chemistry. The

goal of the current work is to compare predictions of NO formation for several detailed chemical mechanisms that have undergone significant development and validation in recent years. This includes the Konnov and Tian mechanisms, which are considered to be the most detailed, as well as GRI-Mech3.0, which is commonly used in commercial numerical models but has not been optimized for NH_x chemistry. We will only briefly compare results with the Miller and Bowman mechanism as the focus here is on the more recently updated, detailed kinetics models. The present study will employ these mechanisms to model premixed H_2-NH_3-air flames with three primary objectives: (1) comparison of the NO predictions with varying NH_3 content in the fuel mixture for lean and rich conditions, (2) sensitivity analyses of NO chemistry to identify the key precursors, radicals, and NO production and decomposition pathways for each mechanism, and (3) modifications of the key NO chemistry pathways to rectify significant differences in NO predictions among the three mechanisms.

4.2 Numerical modeling

A 1-D laminar, adiabatic freely propagating flame model is employed in CHEMKIN PRO for the different chemical mechanisms. The Tian mechanism [13] includes 703 reactions and 84 species, whereas the Konnov mechanism includes 241 reactions and 31 species with carbon species removed based on Duynslaegher et al. [20]. The GRI-Mech3.0 mechanism [9], which is optimized for methane flames, includes 325 reactions and 53 species.

A two-point boundary value solver (TWOPNT) is used within CHEMKIN to calculate equilibrium concentrations on a coarse grid as a starting point to solve the discretized species and energy equations. Subsequently, the grid spacing is refined and the

discretized equations are solved iteratively until the solution converges. A windward differencing discretization scheme is used with initial adaptive grid control using gradient (GRAD) and curvature (CURV) settings as 0.9 each. Mixture-averaged transport properties (e.g., for mass and thermal diffusion) are used.

Table 4.1 displays the operating conditions with given inlet species mole fractions and total flow rates, $\dot{Q}_{mix}$, in standard liters per minute (slpm) for equivalence ratios of 0.7, 1.0 and 1.1.

Table 4.1. Inlet conditions for ∅ = 0.7, 1.0 and 1.1.

Case	X_{NH_3}	X_{H_2}	X_{O_2}	X_{N_2}	$\dot{Q}_{mix}$(slpm)	$E\%NH_3$	Tube ID (OD)
	∅ = 0.7						
1	0.0000	0.2273	0.1623	0.6105	12	0	0.1875 (1/4 in)
2	0.0293	0.1867	0.1646	0.6194	2	20	0.1875 (1/4 in)
3	0.0523	0.1548	0.1665	0.6264	2	35	0.1875 (1/4 in)
4	0.0650	0.1373	0.1676	0.6304	2	43	0.1875 (1/4 in)
5	0.0763	0.1216	0.1684	0.6336	2	50	0.1875 (1/4 in)
6	0.1274	0.0505	0.1726	0.6494	2	80	0.4375 (1/2 in)
	∅ = 1.0						
7	0.0000	0.2958	0.1479	0.5563	12	0	0.1875 (1/4 in)
8	0.0383	0.2441	0.1507	0.5668	2	20	0.1875 (1/4 in)
9	0.0686	0.2031	0.1529	0.5754	2	35	0.1875 (1/4 in)
10	0.0854	0.1805	0.1541	0.5799	2	43	0.1875 (1/4 in)
11	0.1004	0.1601	0.1553	0.5842	2	50	0.1875 (1/4 in)
12	0.1690	0.0674	0.1602	0.6028	2	80	0.4375 (1/2 in)
	∅ = 1.1						
13	0.0000	0.3161	0.1436	0.5403	12	0	0.1875 (1/4 in)
14	0.0410	0.2612	0.1466	0.5514	2	20	0.1875 (1/4 in)
15	0.0735	0.2175	0.1489	0.5601	2	35	0.1875 (1/4 in)
16	0.0915	0.1934	0.1502	0.5649	2	43	0.1875 (1/4 in)
17	0.1077	0.1717	0.1513	0.5692	2	50	0.1875 (1/4 in)
18	0.1816	0.0724	0.1567	0.5893	2	80	0.4375 (1/2 in)

For each equivalence ratio, the flame is simulated for six different amounts of NH_3 varying from 0% to 80% by energy. Equivalence ratios from 0.7 to 1.1 are similar to the conditions encountered in premixed combustion and engine systems and is selected for practical interest.

4.3 Experimental setup

Figures 4.1a and 4.1b shows the schematic of the 8 port tube flame burner and an instantaneous flame image at ∅ = 1.0 for case E%NH_3 = 50, respectively. An eight port circular burner assembled from eight individual similar ¼" tubing (ID = 4.76 mm) is used for the present study. Each individual port of the burner is arranged in a symmetrical fashion so that each port flows an identical amount of incoming reactant mixture resulting in eight identical flame structures (as shown in Fig. 4.1b) for each flame condition. This eight port tube burner geometry is built to accommodate the sampling rate required by the exhaust gas analyzers without significant sample dilution. For the present set of experiments, premixed laminar flames are stabilized over the eight port tube burner; the inner diameter of ~4.67mm ensured a stable flame without flashback or blow-off for the entire range of equivalence ratios for cases of 0%, 20%, 35%, 43%, 50%, 65% and 80% NH_3 in H_2 by energy. The percent of NH_3 by energy is designated here as E%NH_3 and is defined as:

$$E\%NH_3 = \left[\frac{(x_{NH3} * LHV_{NH3}) * 100}{(x_{NH3} * LHV_{NH3} + x_{H2} * LHV_{H2})}\right] \quad (4.1)$$

Conditions for equivalence ratios 0.7, 1.0 and 1.1 are established for cases E%NH_3 = 0, 20, 35, 43, 50, 65 and 80.

To establish identical flames over each port on the eight port tube burner, flowrates of each individual species are specified as eight times (8×) the flowrates shown in Table 4.1.

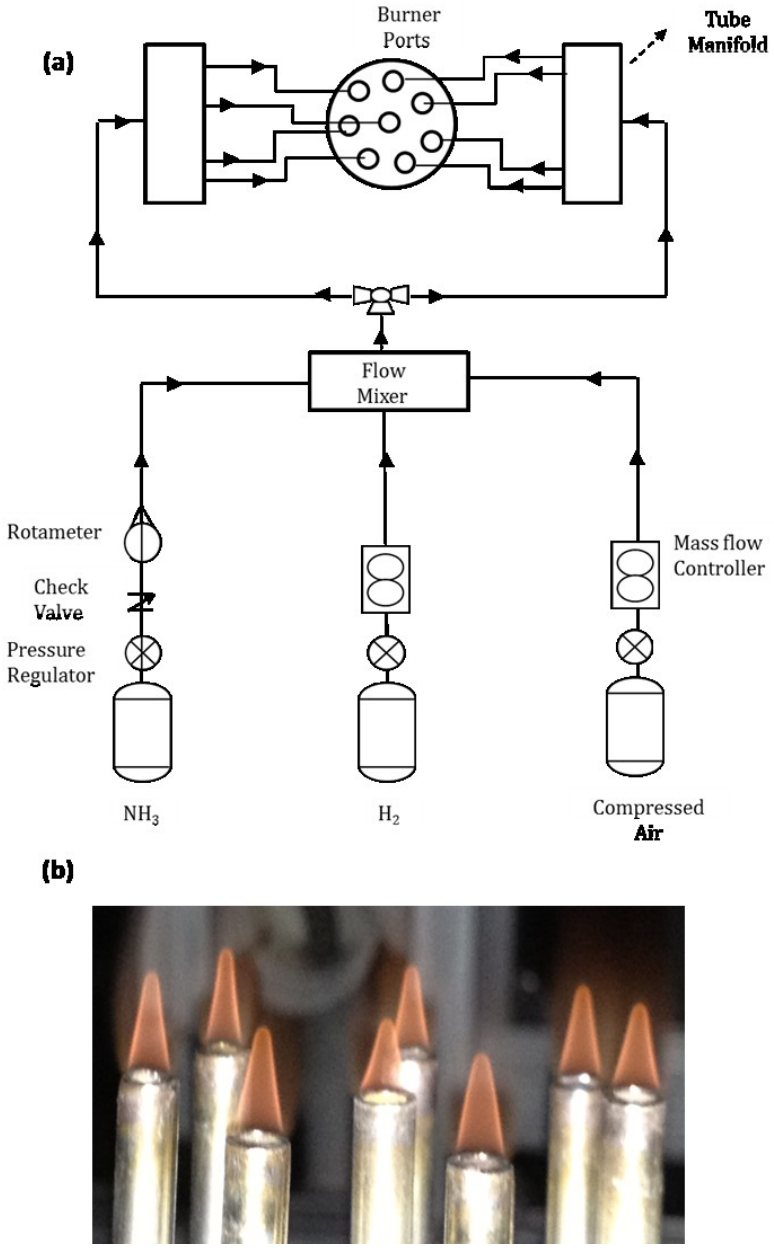

Fig. 4.1. (a) Schematic of eight port tube burner and (b) instantaneous flame image for case E%NH_3 = 50 at Ø = 1.0.

The volumetric flow rate of H_2 and air are measured with mass flow controllers (Alicat, ±1.0% full scale), whereas the NH_3 flow rate is controlled by a rotameter (Aalborg, ±5% full

scale). To ensure uniform mixing of the reactants a flow mixer is utilized along with additional mixing effects provided by the tube manifold on each side of the eight port burner. Sufficiently long tubes are used to ensure laminar fully developed flow at the exit of each port. To keep the flames from surrounding disturbances, flames are established in an enclosed aluminum rectangular duct. For emissions sampling, a sampling probed is placed at the center of the eight port tube burner at 75 mm downstream from the tube exit, from which emission sample is first passed through a gas conditioner to remove any moisture from the sample and then fed to a portable combustion gas analyzer for NO and NO_2 (IMR 1400-PS) with NO measuring range up to 1%.

4.4 Results and discussions

Experimental validation of the chemical mechanisms (Tian and Konnov) has been performed in a companion study of flame speeds for the same laminar H_2-NH_3-air mixtures, which are briefly summarized below. This is followed by a discussion of the comparison of experimentally measured NO emissions with numerically predicted NO mole fractions for the Tian, Konnov and GRI-Mech3.0 mechanisms from lean to rich equivalence ratios and at the operating conditions shown in Table 4.1. Finally, we present sensitivity and rate of production analyses for NO and NH_3 species as well as modification of the GRI-Mech3.0 mechanism and comparisons with the Tian and Konnov mechanisms.

4.4.1 Experimental validation of chemical mechanisms

Previous efforts to validate the detailed chemical kinetic mechanisms discussed in the current work focused on comparisons of experimentally measured and numerically predicted flame speeds in H_2-NH_3-air mixtures. Because the flame speed of NH_3 is an order of magnitude lower than H_2 and is sensitive to the concentrations of O, H, and OH radicals in the flame, this provides a first order test of the accuracy of the chemical mechanisms evaluated here.

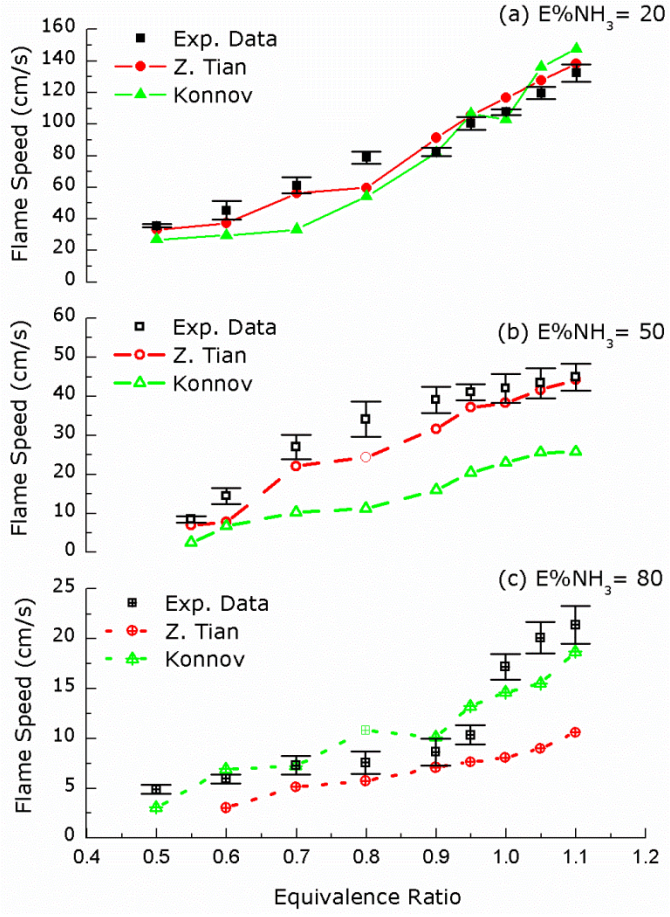

Fig. 4.2. Experimentally measured and numerically predicted laminar flame speeds for Tian and Konnov mechanisms with respect to ∅ for E%NH_3 = (a) 20, (b) 50 and (c) 80. Lines with symbols: predictions, symbols: experimental data.

Figure 4.2 shows a comparison of the theoretically predicted laminar flame speeds for the Tian and Konnov mechanisms with the experimentally determined flame speed data for

$E\%NH_3$ = 20, 50, and 80. For $E\%NH_3$ = 20 (Fig. 4.2a), the flame speed predictions from both the Tian and Konnov mechanisms are nearly equivalent and are in good agreement with the experimental data over the complete range of the equivalence ratios. For $E\%NH_3$ = 50 (Fig. 4.2b), the Tian mechanism appears to capture the correct flame speeds for the full range of equivalence ratios, while the Konnov mechanism appears to be a factor of 2× too slow. For the case of $E\%NH_3$ = 80 (Fig. 4.2c), the Konnov mechanism appears to match the experimentally measured flame speeds and the Tian mechanism is a factor of 2× too slow, especially for equivalence ratios below 0.6 and above 0.95. These data indicate that the validation efforts used to derive the detailed Konnov and Tian mechanisms have led to successful predictions of NH_3 chemistry, but differences in the chemical pathways still persist and can lead to substantial disagreement with increasing levels of NH_3.

4.4.2 Comparison of measured NO emissions with modeling results

It is anticipated that differences in NH_3 oxidation rates may also lead to differences in NO formation chemistry. Predicted NO mole fractions for the case of $\emptyset$ = 0.7 are shown in Fig. 4.3a for varying amounts of NH_3 in H_2 for the Tian, Konnov and GRI-Mech3.0 mechanisms, along with experimental NO emission measurements. The measured NO emission initially increases from 2 ppm to 1830 ppm with $E\%NH_3$ varying from 0 to 50. With higher NH_3 seeding from 50 to 80, NO was reduced to 1/2 of the maximum NO and exhibited approximately 800 ppm of NO.

Figure 4.3b shows a qualitative comparison of the variation of normalized measured NO mole fractions with increasing NH_3 content in the fuel mixture with the three chemical mechanisms. The agreement between the experimental NO data and the numerical predictions

by all three chemical mechanisms are found to be fairly reasonable with a discrepancy for case E%NH_3 = 50. Among the chemical mechanisms, the trends are observed to be approximately similar. For example, the predicted NO mole fractions increase with higher levels of NH_3 in the fuel mixture and peak at nearly identical NO mole fractions at E%NH_3 ~35-43.

For pure H_2/air premixed flames (E%NH_3 = 0), the measured NO is recorded to be 5 ppm with 1% uncertainty of full range (~500 ppm), meaning measured NO is expected to in the range of 0 – 10 ppm, which is found to be in close proximity of NO predictions (~ 7 ppm) by all the three chemical mechanisms. This shows that for a pure H_2/air premixed flame, the agreement between the experimental and numerically predicted NO concentrations is excellent.

The poor agreement of quantitative experimental NO mole fractions with the NO predictions by the chemical mechanisms for all the NH_3 seeded cases (E%NH_3 from 20-80) may result from the possibility of NO reduction by the remaining NH_3 in the exhaust. The heat loss from the flame to the tubing may also impact the NO reductions, but the effects of heat loss are expected to be minimal on the NO concentrations due to minor role of thermal NO pathways in NH_3 seeded flames.

In general, the agreement in predicted NO mole fractions is closer among the three mechanisms at lower levels of NH_3 in the fuel mixture, with the Tian and Konnov mechanisms predicting nearly identical mole fractions from 0-43 E%NH_3. The similar performance of the Tian and Konnov mechanisms in this range is also noted in the flame-speed study discussed earlier [25]. At higher levels of NH_3, there is more substantial disagreement among the

mechanisms. For example, the Tian mechanism predicts higher and lower NO mole fractions than the Konnov mechanism at E%NH_3 = 50 and 80, respectively. This is the same range of E%NH_3 in which the Tian and Konnov mechanisms begin to deviate substantially with regard to predicted flames speeds in Fig. 4.2 [25].

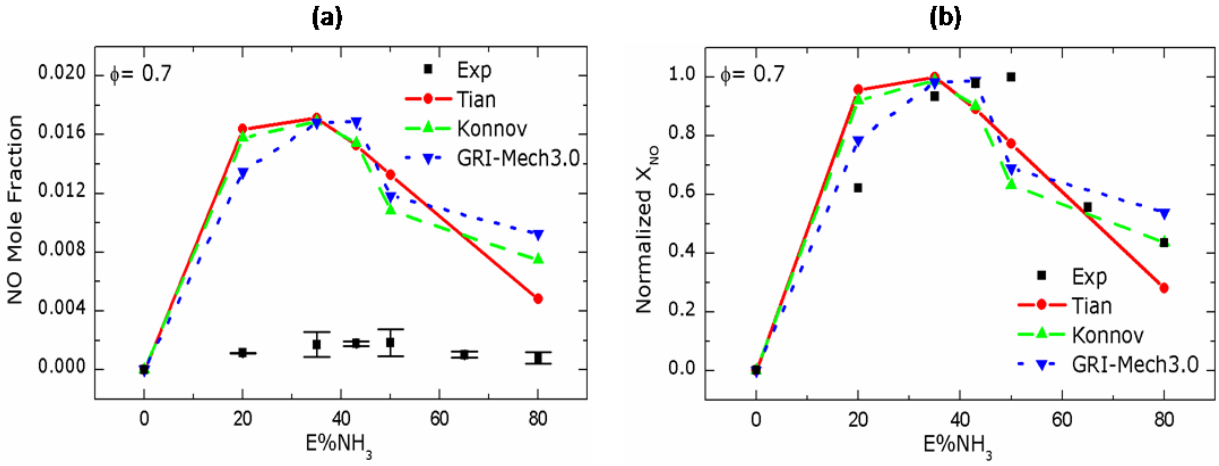

Fig. 4.3. (a) Experimentally measured NO and (b) normalized measured X_{NO} with predicted NO mole fractions versus E%NH_3 for the Tian, Konnov and GRI-Mech3.0 mechanisms at Ø = 0.7.

The predicted NO mole fractions as a function of NH_3 substitution in the fuel mixture are displayed and compared with measured NO emissions in the exhaust both quantitatively and qualitatively in Fig. 4.4a and Fig. 4.4b respectively, for stoichiometric conditions (Ø = 1.0). Although not discussed in great detail in this work, NO mole fractions computed by Lee et al. [23,24] at Ø = 1.0 by using the Miller and Bowman mechanism are also presented for comparison.

The measured NO emission for the stoichiometric flame condition (Ø = 1.0) displays a similar trend with E%NH_3 as noted for Ø = 0.7. The NO increases linearly approximately from 2 ppm to 2300 ppm with an increase in NH_3 seeding level from 0 to 43, with further reduction in NO to 850 ppm with increase in E%NH_3 from 50 to 80. In addition, the measured NO

magnitude for the stoichiometric flame is found to be higher than NO emissions for the lean flames as noticed in Fig. 4.3 ($\emptyset = 0.7$).

Similar to lean flames, the qualitative comparison between the experimental data and the predicted NO mole fractions (Fig.4.4b) for stoichiometric flames appeared to be in excellent agreement supporting the accurate NO trend predictions, however significant discrepancies are observed between the experimental and numerical NO concentrations quantitatively (Fig. 4.4a). The overprediction in NO concentrations by the CHEMKIN modeling utilizing Tian, Konnov and GRI-Mech3.0 chemical mechanisms for the NH_3 seeding cases ($E\%NH_3$ from 20 -80) can be ascribed to the complete NH_3 burn predictions in H_2/NH_3 flame conditions which may not occur in experimental flame conditions.

To determine the effects of incorporating heat loss measurements in the CHEMKIN numerical NO modeling to mimic the experimental flame conditions, NO predictions are evaluated for the Tian and Konnov mechanisms for case $E\%NH_3 = 20$ at $\emptyset = 1.0$, for non-adiabatic numerical modeling. For the Tian mechanism, 25% reduction in temperature is found to reduce the NO prediction by only 15% compared to adiabatic modeling results. Similarly, 22% and 6% reductions are noticed for the temperature and NO mole fraction respectively, for the Konnov mechanism. From the analysis, it is established that due to non-significant differences in NO predictions between adiabatic and non-adiabatic CHEMKIN modeling for the chemical mechanisms, comparisons of experimentally measured NO data with the NO predictions by the adiabatic CHEMKIN PRO model as displayed in Figs. 4.3, 4.4 and 4.5 are fairly reasonable.

For this case (Ø = 1.0), the Tian and Konnov mechanisms are nearly in complete agreement until E%NH_3 = 80, upon which they differ by as much as 40%. It is clear from Fig. 4.4 that the differences with the GRI-Mech3.0 mechanism have increased substantially for this equivalence ratio, both in terms of the general trend and predicted mole fractions. Moreover, differences are most substantial (~2×) with the Miller and Bowman mechanism, as might be expected given the level of detail within the other three mechanisms. However, none of the chemical mechanisms could produce results near that of experimentally measured NO emissions data.

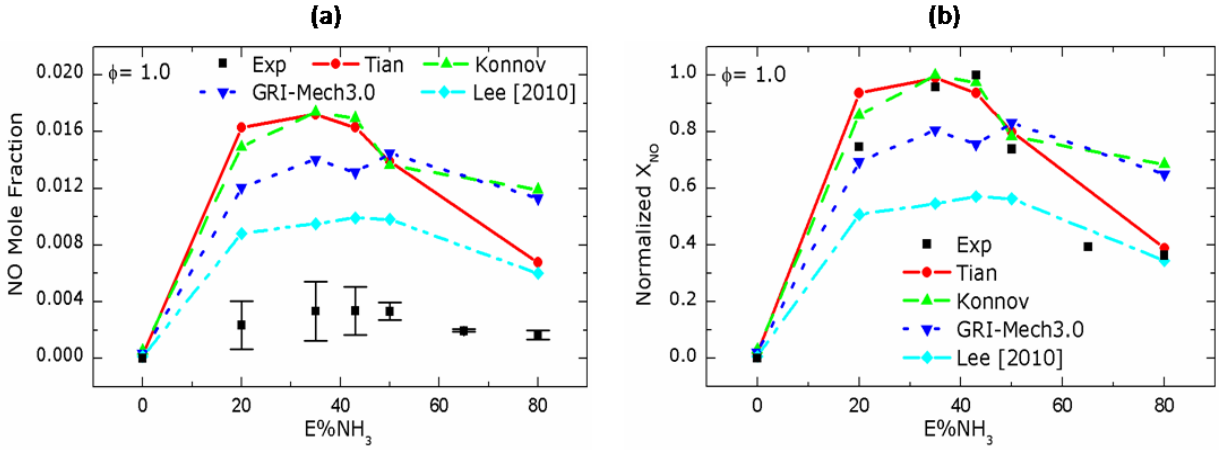

Fig. 4.4. (a) Measured NO emission and (b) normalized NO mole fraction with predicted NO mole fractions for Tian, Konnov, GRI-Mech3.0, and Miller and Bowman (from Lee et al., 2010) mechanisms with respect to E%NH_3 at Ø = 1.0.

The quantitative and qualitative NO mole fraction profiles as a function of NH_3 for slightly fuel rich conditions (Ø = 1.1) predicted using the Tian, Konnov and GRI-Mech3.0 mechanisms along with the measured NO emission profile are displayed in Fig. 4.5a and 4.5b respectively. The quantitative NO concentrations for the Tian, Konnov and GRI-Mech3.0 mechanisms exhibit similar trends for Ø = 1.1 as observed previously for Ø = 0.7 (Fig. 4.3a) and Ø = 1.0 (Fig. 4.4b), although with reduced NO mole fractions overall. A similar qualitative

trend was reported by Lee et al. [24], with reduced NO mole fractions at higher equivalence ratios. For the GRI-Mech3.0 mechanism at Ø = 1.1, the NO concentration profile again shows significant disagreement with the predictions of NO mole fraction from the Tian and Konnov mechanisms. The only exception is at E%NH_3 = 80, where NO predictions using the GRI-Mech3.0 mechanism are in relatively good agreement with the Tian mechanism.

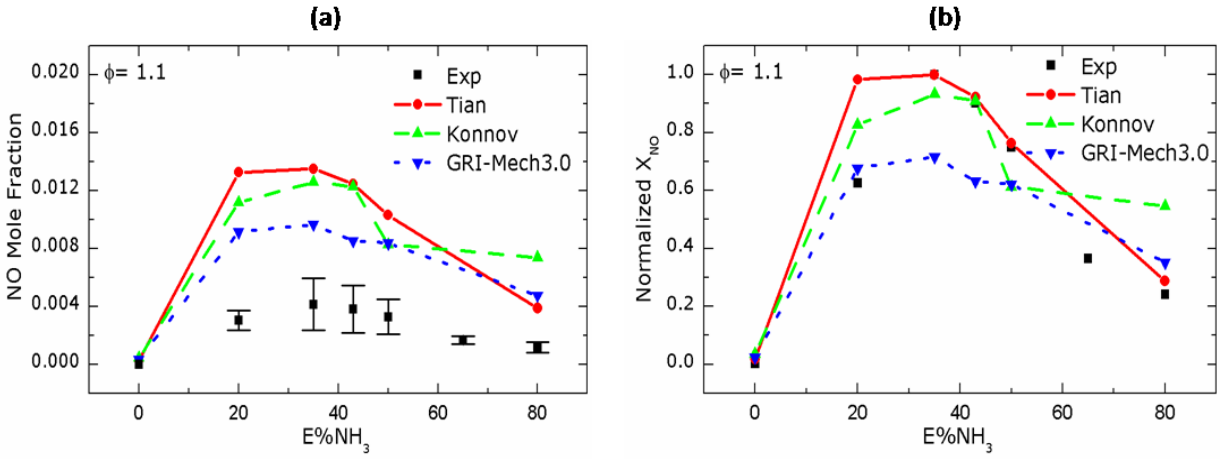

Fig. 4.5. (a) Measured NO emission and (b) normalized X_{NO} with predicted NO mole fractions for Tian, Konnov, GRI-Mech3.0, with respect to E%NH_3 at Ø = 1.1.

The experimentally measured NO profile displayed a similar profile as observed for stoichiometric flame condition with marginal increase in peak NO measurement at E%NH_3 = 43. The qualitative agreement of the measured NO profiles with the predicted NO concentration fits well over the entire range of NH_3 seeding from cases E%NH_3 = 0 to 80 (Fig. 4.5b), indicating model's capability in capturing the trend of the experimental data. Repeatedly, for rich flame conditions, the predicted NO profiles for the chemical mechanisms are found to overshoot the experimental data but with less pronounced effects (Fig. 4.5a) as for lean conditions.

The data from Ø = 0.7 to 1.1 show that there is good agreement between the Tian and Konnov mechanisms at lower levels of NH_3, and that this agreement is less consistent at higher levels of NH_3. In addition, the GRI-Mech3.0 mechanism has substantial disagreement with the Tian and Konnov mechanisms, especially at higher equivalence ratios. In the following section, we analyze sources of disagreement in NO predictions among the three detailed mechanisms (Tian, Konnov, and GRI-Mech3.0) and provide a possible means of improving the performance of the GRI-Mech3.0 mechanism.

4.4.3 Sensitivity and net rate of production analysis

To comprehend the causes of disagreement in NO mole fraction trends among the Tian, Konnov and GRI-Mech3.0 mechanisms with increasing NH_3 substitution in H_2 and from lean to rich flames, a rate of NO production analyses followed by a sensitivity analyses of NH_3 oxidation, NO production and NO decomposition are performed for cases E%NH_3 = 20 and 80 at Ø = 0.7 and 1.0. In addition, NH_3 conversion pathways to NO are examined for two different cases (E%NH_3 = 20 and 80) at equivalence ratios of 0.7 and 1.0. These analyses are carried out at the maximum heat release location in the reaction zone using the CHEMKIN PRO reaction path analyzer module for the 1-D laminar freely propagating flame model. The total rate of production (ROP) and total rate of decomposition (ROD) of species are represented with positive and negative signs, respectively. The net rate of production of species is estimated from the difference of the ROP and ROD magnitudes.

The net NO production rate with E%NH_3 = 20 and 80 for Ø = 0.7 and 1.0 are evaluated and displayed in Table 4.2a and 4.2b respectively, for the Konnov, Tian, and GRI-Mech3.0

mechanisms. It is evident from Table 4.2a that for case E%NH_3 = 20 and ∅ = 0.7, the net NO production rate for Konnov and GRI-Mech3.0 are in close proximity. At E%NH_3 = 80 and ∅ = 0.7, the net NO production rate for the Tian mechanism is noticed to be ~3.5 times higher than the GRI-Mech3.0 mechanism (Table 4.2a), however, the predicted NO mole fraction for GRI-Mech3.0 mechanism is found more than ~2x compared to Tian mechanism (Fig. 4.3).

Similarly at stoichiometric conditions (∅ = 1.0), for case E%NH_3 = 20, the net rate of NO production rate for all the three chemical mechanisms (Table 4.2b) are found in the similar trend of their predicted NO concentrations as displayed in Fig. 4.4. However, the net NO production rate magnitude for Konnov and GRI-Mech3.0 mechanisms are found in close proximity as opposed to the predicted NO mole fraction trend (Fig. 4.4), where Tian and Konnov mechanisms are closer. Likewise, for case E%NH_3 = 80 and ∅ = 1.0 (Table 4.2b), the net NO production rate trend among the three chemical mechanisms are found in contradiction of their corresponding predicted NO trends (Fig 4.4). For example, the GRI-Mech3.0 mechanism displays the lowest net NO rate of production, but the predicted NO concentration is approximately ~2.5x times higher than Tian mechanism (refer Fig. 4.4).

The rate of production analyses for NO molecule revealed that generally at any flame operating conditions, the final predicted NO concentration for a chemical mechanism is not truly reflected by the net NO production rate at the peak heat release location, but seems to be dependent on the NO chemistry over the entire flame zone.

Table 4.2a. Net rate of production $\left(\frac{mole}{cm^3 * s}\right)$ of NO for the Konnov, Tian, and GRI-Mech3.0 mechanisms for E%NH_3 = 20 and 80 at ∅ = 0.7.

Equivalence Ratio 0.7			
E%NH_3	Net NO production rate		
	Konnov	Tian	GRI-Mech3.0
20	2.04E-03	2.98E-03	1.84E-03
80	2.50E-05	5.50E-05	1.50E-05

Table 4.2b. Net rate of production $\left(\frac{mole}{cm^3 * s}\right)$ of NO for the Konnov, Tian, and GRI-Mech3.0 mechanisms for E%NH_3 = 20 and 80 at ∅ = 1.0.

Equivalence Ratio 1.0			
E%NH_3	Net NO production rate		
	Konnov	Tian	GRI-Mech3.0
20	5.54E-03	8.00E-03	4.46E-03
80	2.60E-04	1.46E-04	7.90E-05

To investigate this further, the spatial gradients of NO mole fraction ($\frac{dNO}{dx}$) along the reaction zone (x-axis) are plotted for Konnov, Tian and GRI-Mech3.0 mechanisms for cases E%NH_3 = 20 and 80 for equivalence ratios 0.7 and 1.0 in Figs. 4.6 and 4.7 respectively. At ∅ = 0.7, the spatial gradient of NO mole fraction profiles for Konnov, Tian and GRI-Mech3.0 mechanisms are displayed in Fig. 4.6a and Fig. 4.6b for cases E%NH_3 = 20 and 80, respectively. It is noticed for both cases that the peak NO spatial gradient location coincides with the corresponding peak heat release location for each chemical mechanisms, thus verifying the assumption of highest net NO production rate and supporting the best suitability of peak heat release location for sensitivity analyses. It is also verified that the predicted NO

concentration requires the integral of the spatial gradient of NO over the x-axis (area under the curve, eq. 4.2).

$$NO\ mole\ fraction = \int_0^{x-axis} \left(\frac{dNO}{dx}\right).dx \tag{4.2}$$

In the light of these observations, it is further noted that for case E%NH_3 = 20 and Ø = 0.7 (Fig. 4.6a), the integral (area under the curve) estimated for the Tian and Konnov mechanisms are nearly identical and found lowest for the GRI-Mech3.0 mechanism, which is similar to the predicted NO mole fractions trend as noticed in Fig. 4.3.

For case E%NH_3 = 80 and Ø = 0.7 (Fig. 4.6b), the peak NO spatial gradient for the GRI-Mech3.0 mechanism seemed to be shifted approximately 5 mm downstream compared to the Tian and Konnov mechanisms, suggesting slow flame speed prediction for the GRI-Mech3.0. Interestingly, even though the peak gradient of GRI-Mech3.0 is observed to be the minimum among the three mechanisms, the integral (area under the curve) for the GRI-Mech3.0 mechanisms is found approximately 10% higher than Konnov leading to highest predicted NO mole fraction (shown in Fig. 4.3). It is apparent from the Fig. 4.6b, that due to smallest area under the curve, the Tian mechanism predicted minimum NO concentration (Fig. 4.3).

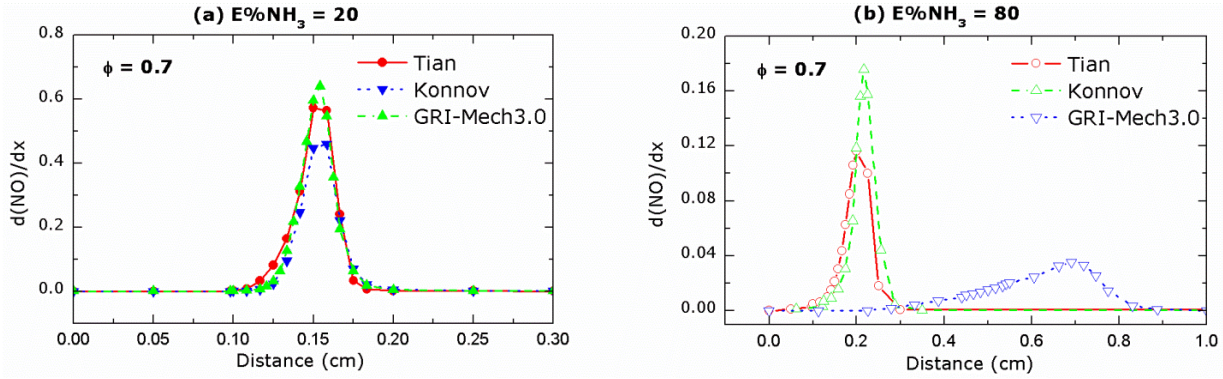

Fig. 4.6. NO concentration gradient along the centerline for cases (a) E%NH_3 = 20 and (b) 80 at for Tian, Konnov, and GRI-Mech3.0 at Ø = 0.7.

Likewise, the spatial gradient NO profile for the Konnov, Tian and GRI-Mech3.0 mechanisms are plotted for case E%NH_3 = 20 and 80 in Fig. 4.7a and 4.7b respectively, at ∅ = 1.0. The integral of NO spatial gradient profiles for the three chemical mechanisms display similar trends as predicted NO mole fractions as observed for both cases E%NH_3 = 20 and 80 at ∅ = 1.0, in Fig. 4.4.

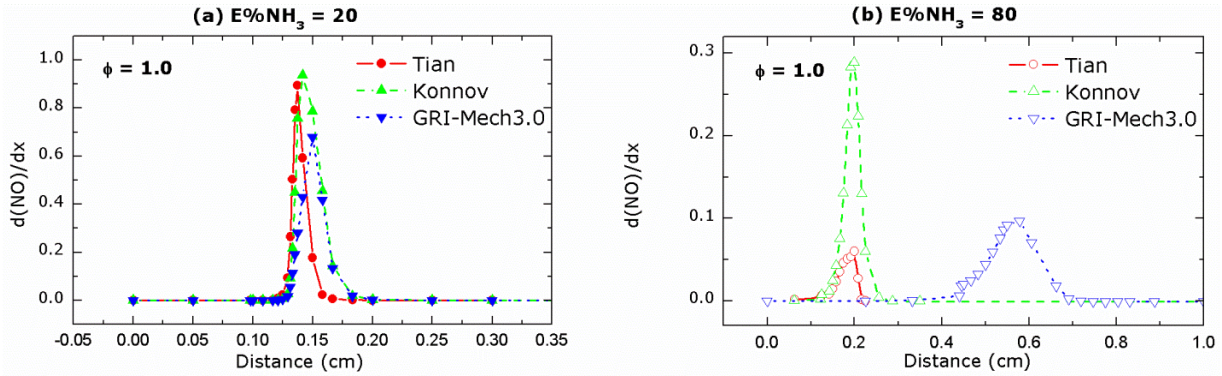

Fig. 4.7. NO concentration gradient along the centerline for cases (a) E%NH_3 = 20 and (b) 80 at for Tian, Konnov, and GRI-Mech3.0 at ∅ = 1.0.

For example, for case E%NH_3 = 20, the Tian and GRI-Mech3.0 mechanisms exhibited maximum and minimum integral (area under the curve) respectively, thus resulting in highest predicted NO concentration and GRI-Mech3.0 leads to minimum NO prediction. Likewise, for similar reasons, the Konnov and Tian mechanisms predict highest and lowest NO concentrations respectively for case E%NH_3 = 80 and ∅ = 1.0.

4.4.3.1 NH_3 oxidation

To identify the key reactions involved in the NH_3 oxidation, a sensitivity analysis of NH_3 oxidation is performed for the Konnov, Tian and GRI-Mech3.0 mechanisms at the prescribed conditions. Figure 4.8 shows the reaction pathways for NH_3 conversion to NO for E%NH_3 = 20 for the Tian, Konnov and GRI-Mech3.0 mechanisms at ∅ = 0.7. For these conditions,

sensitivity analysis reveals that NH_3 oxidation is caused primarily by OH, H and O radicals via the following reactions:

$$NH_3 + OH \leftrightarrow NH_2 + H_2O \quad \text{(Rxn \# 1)}$$

$$NH_3 + H \leftrightarrow NH_2 + H_2 \quad \text{(Rxn \# 2)}$$

$$NH_3 + O \leftrightarrow NH_2 + OH \quad \text{(Rxn \# 3)}$$

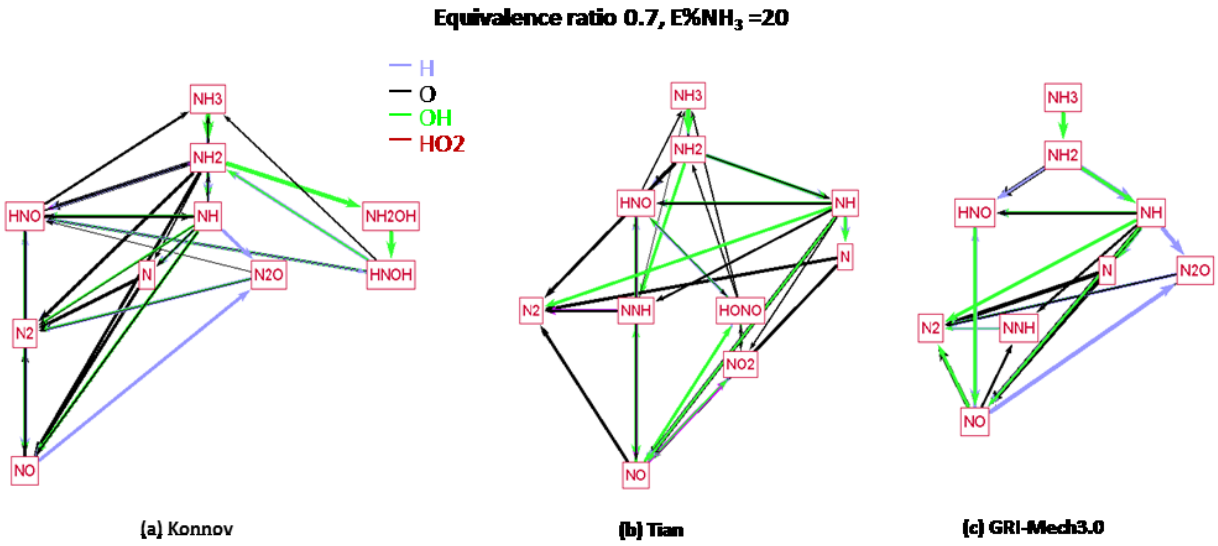

Fig. 4.8. Reaction pathways for NO formation via NH_3 for (a) Konnov, (b) Tian and (c) GRI-Mech3.0 mechanisms for E%NH_3 = 20 and ∅ = 0.7. Colored pathways show the radicals associated with the corresponding reaction path.

The relative contributions of Rxns 1, 2 and 3 towards NH_3 decomposition for E%NH_3 = 20 and (∅ = 0.7) are shown in Table 4.3a and indicate that the OH radical is responsible for at least 65% of NH_3 decomposition for the Tian, Konnov and GRI-Mech3.0 mechanisms. In fact, the initial NH_3 decomposition chemistry is similar and equivalent among the chemical mechanisms, which may cause similar total rates of decomposition of NH_3 among the mechanisms for E%NH_3 = 20 and ∅ = 0.7 (Table 4.4a).

The amine (NH_2) radicals are further reduced to NH and HNO species due to H-abstraction reactions (Rxns # 4-6) via the same key free radicals (OH, H and O), as shown below.

$$NH_2 + OH \leftrightarrow HNO + H_2 \quad \text{(Rxn \# 4)}$$

$$NH_2 + H \leftrightarrow NH + H_2O \quad \text{(Rxn \# 5)}$$

$$NH_2 + O \leftrightarrow HNO + H \quad \text{(Rxn \# 6)}$$

Table 4.3a. Relative contribution of each NH_3 reaction (Rxns # 1-3) to rate of NH_3 decomposition. Relative contributions of Konnov, Tian, and GRI-Mech3.0 mechanisms are compared for E%NH_3 = 20 and 80 for Ø = 0.7.

Ø	E%NH_3	Rxn #	Reaction	% Contribution		
				Konnov	Tian	GRI-Mech3.0
0.7	20	1	$NH_3+OH \leftrightarrow NH_2+H_2O$	70.86	68.09	65.47
		2	$NH_3+H \leftrightarrow NH_2+H_2$	16.6	14.56	18.53
		3	$NH_3+O \leftrightarrow NH_2+OH$	12.5	17.35	16.00
	80	1	$NH_3+OH \leftrightarrow NH_2+H_2O$	91.18	93.61	88.58
		2	$NH_3+H \leftrightarrow NH_2+H_2$	5.17	0.00	0.00
		3	$NH_3+O \leftrightarrow NH_2+OH$	3.65	6.39	11.42

Table 4.3b. Relative contribution of each NH_3 reaction (Rxns # 1-3) to rate of NH_3 decomposition. Relative contributions of Konnov, Tian, and GRI-Mech3.0 mechanisms are compared for E%NH_3 = 20 and 80 for Ø = 1.0.

Ø	E%NH_3	Rxn #	Reaction	% Contribution		
				Konnov	Tian	GRI-Mech3.0
1.0	20	1	$NH_3+OH \leftrightarrow NH_2+H_2O$	55.50	62.91	52.93
		2	$NH_3+H \leftrightarrow NH_2+H_2$	35.17	35.38	31.5
		3	$NH_3+O \leftrightarrow NH_2+OH$	9.31	1.70	15.5
	80	1	$NH_3+OH \leftrightarrow NH_2+H_2O$	72.50	86.46	85.99
		2	$NH_3+H \leftrightarrow NH_2+H_2$	22.13	8.57	14.10

Table 4.4a. Total rate of production $\left(\frac{mole}{cm^3*s}\right)$ (ROP) and rate of decomposition $\left(\frac{mole}{cm^3*s}\right)$ (ROD) of NH_3 for the Konnov, Tian, and GRI-Mech3.0 mechanisms for E%NH_3 = 20 and 80 at ∅ = 0.7.

Equivalence Ratio 0.7							
		Total Rate of Production (ROP)			Total Rate of Decomposition (ROD)		
E%NH_3	Species	Konnov	Tian	GRI-Mech3.0	Konnov	Tian	GRI-Mech3.0
20	NH_3	2.27E-04	1.31E-04	0.0	-4.71E-03	-4.58E-03	-4.12E-03
80	NH_3	4.54E-05	2.02E-05	1.91E-06	-1.07E-03	-4.38E-04	-1.64E-04

Table 4.4b. Total rate of production $\left(\frac{mole}{cm^3*s}\right)$ (ROP) and rate of decomposition $\left(\frac{mole}{cm^3*s}\right)$ (ROD) of NH_3 for the Konnov, Tian, and GRI-Mech3.0 mechanisms for E%NH_3 = 20 and 80 at ∅ = 1.0.

Equivalence Ratio 1.0							
		Total Rate of Production (ROP)			Total Rate of Decomposition (ROD)		
E%NH_3	Species	Konnov	Tian	GRI-Mech3.0	Konnov	Tian	GRI-Mech3.0
20	NH_3	1.14E-03	1.05E-03	0.0	-1.72E-02	-1.39E-02	-1.36E-02
80	NH_3	1.11E-04	9.97E-05	0.0	-5.56E-03	-1.36E-03	-7.64E-04

The HNO and NH species are found as critical NO precursors from the ammonia to nitric oxide conversion pathways (see Fig. 4.8) and lead to several-fold higher NO formation for NH_3 enriched flames, as seen previously in Figs. 4.3–4.5. The NH_3 to NO conversion pathways for the Tian, Konnov and GRI-Mech3.0 mechanisms as displayed in Fig. 4.8 for E%NH_3 = 20 and ∅ = 0.7 reveal that, after the formation of NH_2, the HNO and NH species formed in Rxns 4-6 lead to NO via branching reactions of intermediate species such as NNH, N_2O, NO_2, and HONO with the help of the free radicals H, O, OH, and HO_2. Some differences between the

chemical mechanisms can be observed, such as an NH_2OH sub-mechanism playing a significant role only in the Konnov mechanism, and NNH playing a role only in the Tian and GRI-Mech3.0 mechanisms. In general, the GRI-Mech3.0 mechanism bears greater similarity with the Tian mechanism but exhibits less complex NH_3 conversion pathways to NO as compared to the Tian and Konnov mechanisms.

For $E\%NH_3 = 80$ and $\emptyset = 0.7$, the NH_3 sensitivity analysis (Table 4.3a) reveals that the contribution of Rxn 2 ($NH_3+H \leftrightarrow NH_2+H_2$) to NH_3 oxidation becomes negligible because of reduced H radicals caused by decreased H_2 in the fuel mixture. Hence, for high levels of NH_3 in the fuel, NH_3 decomposition is governed almost entirely by Rxns 1 ($NH_3+OH \leftrightarrow NH_2+H_2O$) and 3 ($NH_3+O \leftrightarrow NH_2+OH$).

The rate sensitivity analyses for case $E\%NH_3 = 20$ at $\emptyset = 1.0$ show similar NH_3 oxidation chemistry (see Table 4.3b) as observed at $\emptyset = 0.7$ (see Table 4.3a) for the Tian, Konnov and GRI-Mech3.0 mechanisms, although with ~2× enhanced contribution by Rxn 2. The increased role of Rxn 2 likely results from an increase in H radicals relative to O or OH radicals near stoichiometric conditions.

For the case of $E\%NH_3 = 80$ and $\emptyset = 1.0$, the relative contribution of major NH_3 decomposition reaction pathways obtained from sensitivity analysis is presented in Table 4.3b. It is noted that the relative contribution of Rxn 1 for $\emptyset = 1.0$ is more dominant for the case of $E\%NH_3 = 80$ than for $E\%NH_3 = 20$ (shown previously in Table 4.3a). For $E\%NH_3 = 80$, the added NH_3 reduces the availability of H radicals and the corresponding contribution of Rxn 2.

4.4.3.2 NO production

The relative contributions of reactions responsible for NO production for cases E%NH_3 = 20 and 80 at Ø = 0.7 and 1.0 are presented in Tables 4.5a and 4.5b, respectively.

Table 4.5a. Relative contribution of each NH_3 reaction to rate of NO production. Relative contributions of Konnov, Tian, and GRI-Mech3.0 mechanisms are compared for E%NH_3 = 20 and 80 for Ø = 0.7.

Ø	E%NH_3	Rxn #	Reaction	% Contribution		
				Konnov	Tian	GRI-Mech3.0
0.7	20	7	HNO+H↔NO+H_2	68.12	59.1	69.49
		8	NO_2+H↔NO+OH	9.39	5.68	8.36
		9	HNO+OH↔NO+H_2O	4.04	14.75	2.23
		10	NH+O↔NO+H	9.36	12.48	9.46
	80	7	HNO+H↔NO+H_2	33.71	12.27	0.00
		9	HNO+OH↔NO+H_2O	18.13	40.21	24.15
		15	HNO(+M)↔H+NO (+M)	0.00	0.00	26.49
		16	HNO+NH_2↔NH_3+NO	13.36	0.00	0.00
		17	HNO+O_2↔NO+HO_2	0.00	17.34	22.02

Table 4.5b. Relative contribution of each NH_3 reaction to rate of NO production. Relative contributions of Konnov, Tian, and GRI-Mech3.0 mechanisms are compared for E%NH_3 = 20 and 80 for Ø = 1.0.

Ø	E%NH_3	Rxn #	Reaction	% Contribution		
				Konnov	Tian	GRI-Mech3.0
1.0	20	7	HNO+H↔NO+H_2	67.36	65.51	64.40
		9	HNO+OH↔NO+H_2O	0.0	6.69	2.23
		10	NH+O↔NO+H	13.91	14.78	12.1
		19	N+O2↔NO+O (thermal NO)	0.0	0.0	10.03
		20	N+OH↔NO+H (thermal NO)	0.0	0.0	10.56
	80	7	HNO+H↔NO+H_2	32.97	29.70	45.18
		9	HNO+OH↔NO+H_2O	0.00	25.86	13.91
		10	NH+O↔NO+H	44.97	0.00	0.00
		15	HNO(+M)↔NO(+M)+H	0.00	17.30	39.34

It appears from Table 4.5a that for case E%NH_3 = 20 and Ø = 0.7, HNO is the dominant pathway for all three chemical mechanisms, accounting for 70–80% of the NO formation via

Rxns 7 and 9. In addition, it appears that the H atom is the most important radical responsible for NO formation under these conditions, with a weighting of 60–80% via Rxns 7 and 8.

Hence, while the OH radical is responsible for NH_3 decomposition initially, the H radical is responsible for the final production of NO under these conditions. Interestingly, the reactions have similar contributions for all the three mechanisms.

For case E%NH_3 = 80 and Ø = 0.7 (Table 4.5a), while HNO contributes to more than 60% of the NO production for all three mechanisms, the Tian and Konnov mechanisms rely primarily on the H and OH radicals to form NO. For the GRI-Mech3.0 mechanism again, due to the reduction of H_2 in the fuel mixture, the role of OH in NO production is increased for flames with high NH_3 content. This is in contrast to the case with E%NH_3 = 20 (Table 4.5a), in which OH played a relatively small role as compared with the H atom. While the GRI-Mech3.0 mechanism differs substantially from the other two mechanisms, it bears the closest resemblance to the Tian mechanism with regard to NO production. The key difference with the Tian mechanism is that GRI-Mech3.0 relies heavily on thermal decomposition of HNO to produce NO and H via Rxn 15 and eliminates reactions requiring H for NO production.

Key reactions involved in NO production for the Tian, Konnov and GRI-Mech3.0 mechanisms at E%NH_3 = 20 and 80 for Ø = 1.0 are shown in Table 4.5b. It can be seen from Table 4.5b that HNO is the dominant NO precursor via Rxn 7 for case E%NH_3 = 20, as was found for lean conditions in Table 4.5a. In fact, the contributions of Rxns 7, 9, 10 are similar for both Ø = 0.7 and 1.0, as shown in Tables 4.5a and 4.5b, respectively. However, the GRI-Mech3.0 mechanism attributes approximately 20% of NO production to the Zeldovich (thermal) mechanism via Rxns 19 and 20, likely due to increased temperatures at Ø = 1.0. This

is in contrast with the Tian and Konnov mechanisms, which do not attribute any NO production to Rxns 19 and 20.

$$N + O_2 \leftrightarrow NO + O \qquad \text{(Rxn \# 19)}$$

$$N + OH \leftrightarrow NO + H \qquad \text{(Rxn \# 20)}$$

For case E%NH_3 = 80 at $\emptyset$ = 1.0, the major reaction pathways for NO production are shown in Tables 4.5b. As is apparent in Table 4.5b, Rxn 7 is no longer the dominant pathway to NO production, as was the case for E%NH_3 = 20 and $\emptyset$ = 1.0 (Table 4.5b), which is consistent with a reduction in H radicals with increased NH_3. All three mechanisms appear to follow similar trends, but no two mechanisms agree on the relative significance of each pathway. The most striking difference is that the Konnov mechanisms predicts a substantial contribution to NO production through reactions of NH and O, whereas the Tian and GRI-Mech3.0 mechanisms rely solely on reactions of HNO, either through thermal decomposition or reactions with H and OH radicals. However, as shown in Fig. 4.4, the predicted NO mole fractions agree most closely between the Konnov and GRI-Mech3.0 mechanisms.

4.4.3.3 NO decomposition

There are substantial differences between the contributions of each reaction pathway to the rate of NO decomposition for all three mechanisms, as shown for cases E%NH_3 = 20 and 80 for $\emptyset$ = 0.7 and 1.0 in Tables 4.6a and 4.6b, respectively.

Table 4.6a. Relative contribution of each NH_3 reaction to rate of NO decomposition. Relative contributions of Konnov, Tian, and GRI-Mech3.0 mechanisms are compared for $E\%NH_3$ = 20 and 80 for Ø = 0.7.

Ø	$E\%NH_3$	Rxn #	Reaction	% Contribution		
				Konnov	Tian	GRI-Mech3.0
0.7	20	11	$NH+NO\leftrightarrow N_2O+H$	18.71	0.00	32.12
		12	$N+NO\leftrightarrow N_2+O$	15.86	29.20	26.78
		13	$NH_2+NO\leftrightarrow N_2+H_2O$	15.19	19.73	0.00
		14	$NH_2+NO\leftrightarrow NNH+OH$	9.97	8.13	0.00
		15	$H+NO(+M)\leftrightarrow HNO(+M)$	9.76	32.9	14.29
	80	11	$NH+NO\leftrightarrow N_2O+H$	22.18	0.00	64.03
		13	$NH_2+NO\leftrightarrow N_2+H_2O$	36.53	37.2	0.00
		14	$NH_2+NO\leftrightarrow NNH+OH$	32.02	41.98	0.00
		18	$NH+NO\leftrightarrow N_2+OH$	0.00	13.85	18.23

Table 4.6b. Relative contribution of each NH_3 reaction to rate of NO decomposition. Relative contributions of Konnov, Tian, and GRI-Mech3.0 mechanisms are compared for $E\%NH_3$ = 20 and 80 for Ø = 1.0.

Ø	$E\%NH_3$	Rxn #	Reaction	% Contribution		
				Konnov	Tian	GRI-Mech3.0
1.0	20	11	$NH+NO\leftrightarrow N_2O+H$	19.89	0.0	50.67
		12	$N+NO\leftrightarrow N_2+O$	61.70	80.0	12.71
		13	$NH_2+NO\leftrightarrow N_2+H_2O$	9.31	20	0.0
		15	$H+NO(+M)\leftrightarrow HNO(+M)$	9.10	0.0	23.2
	80	11	$NH+NO\leftrightarrow N_2O+H$	33.74	0.00	61.52
		12	$N+NO\leftrightarrow N_2+O$	20.5	0.00	0.00
		13	$NH_2+NO\leftrightarrow N_2+H_2O$	0.00	26.01	0.00
		14	$NH_2+NO\leftrightarrow NNH+OH$	23.97	38.46	0.00
		18	$NH+NO\leftrightarrow N_2+OH$	0.00	20.96	19.98

For example for case $E\%NH_3$ =20 at Ø = 0.7 (Table 4.6a), Rxn 11 plays a much more significant role in NO decomposition for GRI-Mech3.0 as compared with the Tian and Konnov mechanisms. At the same time, GRI-Mech3.0 has zero contribution from Rxns 13 and 14, which are important for the Tian and Konnov mechanisms. In fact, the contributions of various

reactions for the Tian and Konnov mechanisms are much closer to each other than to the GRI-Mech3.0 mechanism, which is evident in the net NO production (NO spatial gradient profile) shown previously at E%NH_3 and Ø = 0.7 in Fig. 4.6a. The differences in major NO decomposition reaction pathways with the GRI-Mech3.0 mechanisms are directly related to the differences in the net NO production rate as displayed by spatial gradient of NO profile.

While NO production is dominated by HNO, NO decomposition is dominated by NH_x pathways for the Konnov, Tian and GRI-Mech3.0 mechanisms. As shown in Table 4.6a, for case E%NH_3 = 80 at Ø = 0.7, NH_x radicals play an important role in causing NO reduction to N_2O, N_2 and NNH and are responsible for up to 90% of NO decomposition for all the three chemical mechanisms. From Table 4.6a, the NO decomposition by NH_2 via Rxns 13 and 14 are most critical for the Tian and Konnov mechanisms, accounting for 70-80% of NO decomposition. The other major reactions for the Tian and Konnov mechanisms rely on decomposition of NO via NH, but the Konnov mechanism presumes the products are N_2O and H while the Tian mechanisms presumes that the products are N_2 and OH. This may be a source of deviation between the two mechanisms. In striking contrast to the Tian and Konnov mechanisms, GRI-Mech3.0 relies almost entirely on NH via Rxns 11 and 18 and has no activity via NH_2. However, the GRI-Mech3.0 mechanism bears the most resemblance to the Konnov mechanism for this condition because of the common use of Rxn 11 between the two mechanisms. This explains why the GRI-Mech3.0 mechanism differs most from the Tian mechanism for the case of E%NH_3 = 80 and Ø = 0.7, as shown previously in Fig. 4.3.

From Table 4.6b, it is observed that at stoichiometric conditions for case E%NH_3 = 20, the destruction of NO for the Konnov and Tian mechanisms is dominated by N radicals via Rxn

12, with some contributions from reactions with NH NH_2, NH, and H radicals via Rxns 11, 13, and 15. For the GRI-Mech3.0 mechanism, the NO decomposition chemistry is noted to be significantly different, particularly when compared with the Tian mechanism, and occurs primarily by reaction with NH to produce N_2O. This results in significant differences between the NO mole fractions predicted by GRI-Mech3.0 and that predicted by the Tian and Konnov mechanisms, as shown previously in Fig. 4.4.

For the case of E%NH_3 = 80 and ∅ = 1.0, the NO reformation chemistry among the three chemical mechanisms are significantly different. From Table 4.6b, it is noted that NO reduction by NH radicals via Rxns 11 and 18 carry out more than 80% NO reformation for GRI-Mech3.0 mechanism without any activity of NH_2 radical contribution from Rxns 13 and 14, which played an important role in NO decomposition for Tian and Konnov mechanisms. In addition to that, considerable changes in NO decomposition chemistry are noticed between Tian and Konnov mechanisms. Rxns 11 and 12 showed dominance in Konnov mechanism, whereas Rxns 13 and 18 found important for NO destruction in the Tian mechanism.

4.4.3.4 Comparison between Tian and Modified GRI-Mech3.0 mechanisms

In an effort to improve the overall agreement in NO concentration between Tian and GRI-Mech3.0 mechanisms over the entire range of flame conditions, the rate kinetics parameters (pre-exponential factor (A), pre-factor (b) and activation energy (E_a)) of the key NO formation and destruction pathways in the GRI-Mech3.0 mechanism are modified and three new NO reformation pathways are added: Rxns 11(duplicate), 13 and 14 resulting in a new modified GRI-Mech3.0 (Mod. GRI-Mech) mechanism having 53 species and 328 reactions.

$$NH + NO \leftrightarrow N_2O + H \ \ (duplicate) \qquad \text{(Rxn \# 11)}$$

$$NH_2 + NO \leftrightarrow N_2 + H_2O \qquad \text{(Rxn \# 13)}$$

$$NH_2 + NO \leftrightarrow NNH + OH \qquad \text{(Rxn \# 14)}$$

From the analysis (section 4.4.3), it is anticipated that the rate kinetics of Rxn 11 needs to be reduced and rate constants of Rxns 13 and 14 are required to be increased in order to bring the NO concentration trend for GRI-Mech3.0 closer to Tian's NO profile. The final updated rate kinetics parameters for the modified GRI-Mech3.0 (Mod. GRI-Mech) mechanism is displayed in Tables 4.7a and 4.7b for key NO production and decomposition pathways, respectively.

Table 4.7a. Major NO production pathways with updated kinetics parameters for the new modified GRI-Mech3.0 mechanism. A = pre-exponential factor, b = pre-factor and E_a = activation energy.

Rxn #	Reaction	Rate parameters		
		A	b	E_a
7	$HNO+H \leftrightarrow NO+H_2$	8.80E+11	0.72	650
8	$NO_2+H \leftrightarrow NO+OH$	1.30E+14	0.00	362
9	$HNO+OH \leftrightarrow NO+H_2O$	3.60E+13	0.00	0.00
10	$NH+O \leftrightarrow NO+H$	3.68E+14	0.00	0.00
17	$HNO+O_2 \leftrightarrow HO_2+NO$	2.00E+13	0.00	16000
19	$N+O_2 \leftrightarrow NO+O$	6.40E+09	1.00	6280
20	$N+OH \leftrightarrow NO+H$	3.80E+13	0.00	0.00

Table 4.7b. Major NO decomposition pathways with updated kinetics parameters for the new modified GRI-Mech3.0 mechanism. A = pre-exponential factor, b = pre-factor and E_a = activation energy.

Rxn #	Reaction	Rate parameters		
		A	b	E_a
11	$NH+NO \leftrightarrow N_2O+H$	2.90E+14	-0.400	0.00
	$NH+NO \leftrightarrow N_2O+H$ (dup)	2.20E+13	-0.230	0.00
12	$N+NO \leftrightarrow N_2+O$	1.05E+12	1.50	0.00
13	$NH2+NO \leftrightarrow N_2+H_2O$	2.80E+20	-2.654	1258.0
14	$NH_2+NO \leftrightarrow NNH+OH$	2.30E+10	0.425	-814.0
15	$NO+H(+M) \leftrightarrow HNO(+M)$	1.50E+15	-1.410	0.00
18	$NH+NO \leftrightarrow N_2+OH$	2.20E+13	-0.230	0.00

The NO concentrations profiles for the modified GRI-Mech3.0 and Tian mechanisms are compared for the E%NH_3 range from 0% to 80% for equivalence ratios 0.7, 1.0 and 1.1. In order to assess the improvement in agreement of laminar flame speed predictions between GRI-Mech3.0 and the Mod. GRI-Mech mechanisms, the adiabatic laminar flame speeds using the Mod. GRI-Mech mechanism are evaluated at E%NH_3 = 0%, 20%, 50% and 80% for equivalence ratios 0.7, 1.0 and 1.1, and compared with Tian and GRI-Mech3.0 flame speed data [25].

Figure 4.9a and 4.9b show the variations of the NO mole fractions and adiabatic laminar flame speed profile respectively for the modified GRI-Mech3.0 mechanism compared to Tian mechanism for Ø = 0.7. From Fig. 4.9a, it can be seen that the NO concentration profile for the modified GRI-Mech mechanism has been improved significantly and is in fairly good agreement with the Tian's NO mole fractions, compared to the GRI-Mech3.0 mechanism as shown in Fig. 4.3. The maximum difference in NO prediction between the modified GRI-Mech3.0 and Tian mechanisms is observed to be within 10 % at E%NH_3 = 20. Similarly from Fig. 4.9b, the adiabatic laminar flame speed profile of the modified GRI-Mech3.0 has improved significantly especially at E%NH_3 = 20 and 50 compared to standard GRI-Mech3.0 mechanism and found to be fairly equivalent with Tian's adiabatic flame speed profile.

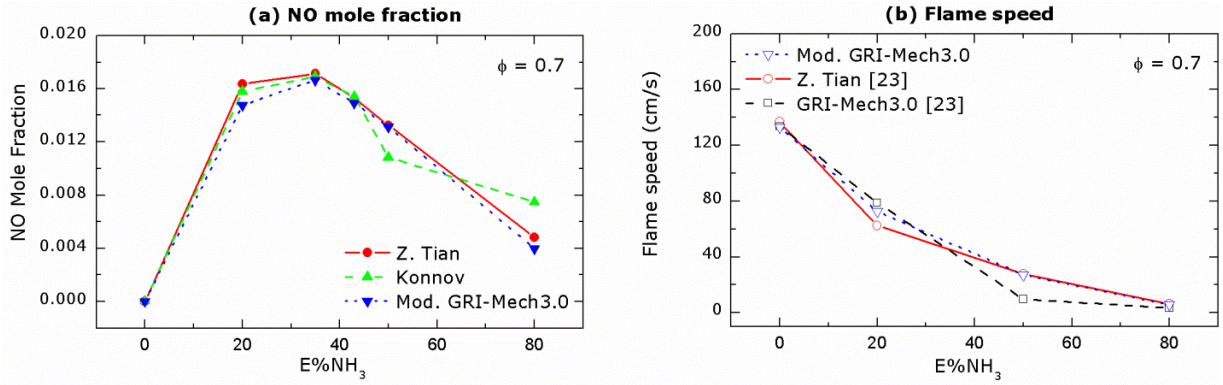

Fig. 4.9. (a) Theoretical NO mole fractions as a function of $E\%NH_3$ for Tian, Konnov and Mod. GRI-Mech3.0 and (b) flame speed variations for modified GRI-Mech3.0, Tian and GRI-Mech3.0 at $\emptyset$ = 0.7. Lines with symbols: predictions.

Likewise, the NO mole fraction and adiabatic laminar flame speed profiles for $\emptyset$ = 1.0 are displayed in Figs. 4.10a and 4.10b respectively for modified GRI-Mech3.0 mechanism and compared with Tian mechanism. From Fig. 4.10a, a significant improvement in NO mole fraction trend for the new modified GRI-Mech3.0 mechanism is observed for lower range of $E\%NH_3$ = 0% to 35% and at $E\%NH_3$ = 80, however for $E\%NH_3$ range from 50 to 80, the modified GRI-Mech3.0 mechanism seemed to over predict NO compared to Tian's NO predictions. The maximum difference in NO mole fraction between modified GRI-Meh3.0 and Tian mechanisms is observed at $E\%NH_3$ = 50, where theoretical NO mole fraction for the modified GRI-Mech3.0 is found to be approximately 25% higher than Tian's NO mole fraction. Similarly, the laminar adiabatic flame speed trend for the modified GRI-Mech3.0 mechanism has improved in agreement with Tian's flame speed data noticeably, as observed in Fig. 4.10b.

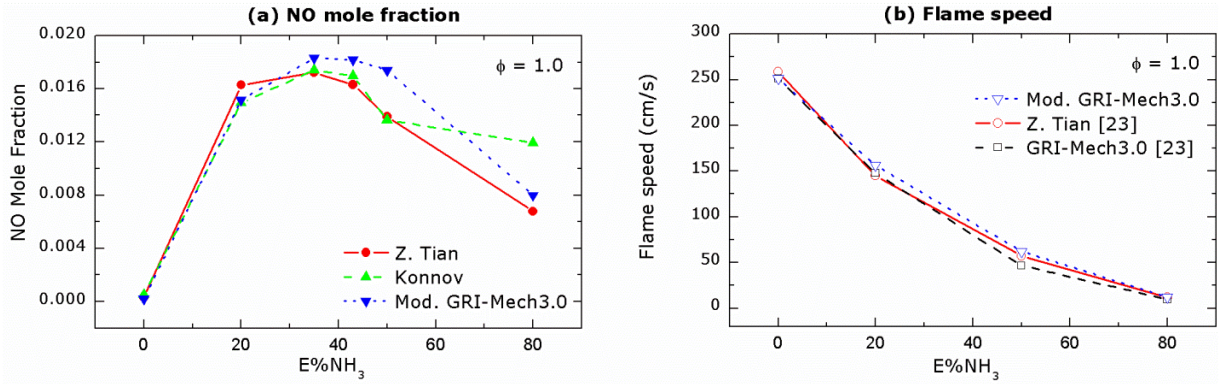

Fig. 4.10. (a) Theoretical NO mole fractions as a function of E%NH_3 for Tian, Konnov and Mod. GRI-Mech3.0 and (b) flame speed variations for modified GRI-Mech3.0, Tian and GRI-Mech3.0 at Ø = 1.0.

For fuel rich conditions (Ø = 1.1), excellent improvement is observed in agreement of the NO mole fraction trend between the modified GRI-Mech3.0 and Tian mechanisms with maximum difference of 7% in NO mole fraction at E%NH_3 = 20, as shown in Fig. 4.11a. Also from Fig. 4.11b, the laminar flame speed trend for the modified GRI-Mech3.0 mechanism is seen to be in close agreement with Tian's laminar flame speed data.

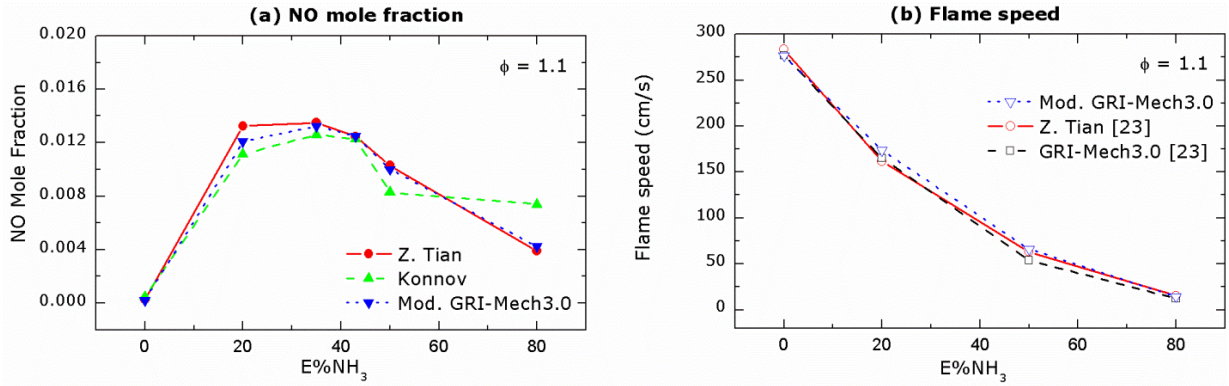

Fig. 4.11. (a) Theoretical NO mole fractions as a function of E%NH_3 for Tian, Konnov and Mod. GRI-Mech3.0 and (b) flame speed variations for modified GRI-Mech3.0, Tian and GRI-Mech3.0 at Ø = 1.1.

The new modified GRI-Mech3.0 (Mod. GRI-Mech) mechanism is also tested for evaluating the laminar flame speed for a non-adiabatic flame speed model by providing experimentally determined heat loss from the flame as an input in the PREMIX code at E%NH_3 = 20 for Ø = 0.7. This method of evaluating non-adiabatic flame speed by calculating

heat loss from the flame is explained more elaborately in the literature [25]. The laminar flame speed calculated for the new modified GRI-Mech3.0 mechanism is found to be within 0.1% of the Tian's laminar flame speed value [25]; whereas for the same condition, the laminar flame speed for GRI-Mech3.0 was noticed to be 39% slower than the flame speed value for Tian mechanism [25].

4.5 Conclusions

The theoretical NO formation is computed in a 1-D, laminar, freely propagating flame speed model in CHEMKIN PRO 4.0 by using three different chemical mechanisms; (1) Tian, (2) Konnov and (3) GRI-Mech3.0. Data are compared with the experimentally measured NO emissions for H_2-NH_3-air premixed flames. Cases include six different ammonia seeding levels in the fuel mixture with a range from E%NH_3 = 0% to 80% for equivalence ratios 0.7, 1.0 and 1.1. Qualitatively, the predicted NO profiles with respect to NH_3 seeding levels are found to be in fairly good agreement with the measured NO, however significant discrepancy is noticed in quantitative comparisons.

Results show that the NO concentration trends with varying E%NH_3 in the fuel mixture among the three mechanisms remain similar for the lower range of ammonia substitution and lean conditions. However, for rich conditions as well as with increasing ammonia substitution, the NO trends for the three mechanisms begin to deviate from each other. This deviation in NO mole fraction from Tian's NO predictions is observed to be much more pronounced for GRI-Mech3.0 mechanism compared to Konnov mechanism.

From the sensitivity and rate of production analysis, HNO and NH species are found to be the key precursors for NO formations in ammonia seeded flames for all three mechanisms, although significant dissimilarities are observed in NO decomposition chemistry between the GRI-Mech3.0 and Tian mechanisms. The discrepancies become wider with increasing ammonia content or the flame temperature. Eventually these differences in the reaction pathways lead to the differences in the net NO production rate among the three mechanisms, resulting in deviations in NO trends at higher ranges of ammonia content in the fuel mixture.

The reaction pathway analyses also allowed identification of the key reactions responsible for the disagreement between the Tian and GRI-Mech3.0 mechanisms. A new modified GRI-Mech3.0 mechanism (53 species and 328 reactions) by adding three extra reactions

$$NH + NO \leftrightarrow N_2O + H \ \ (duplicate) \qquad \text{(Rxn \# 11)}$$

$$NH_2 + NO \leftrightarrow N_2 + H_2O \qquad \text{(Rxn \# 13)}$$

$$NH_2 + NO \leftrightarrow NNH + OH \qquad \text{(Rxn \# 14)}$$

to the GRI-Mech3.0 mechanism with updated rate parameters provided a fairly good agreement of NO concentration trends and laminar flame speed data between Tian and GRI-Mech3.0 mechanisms. The number of non-carbon species in the new modified GRI-Mech3.0 mechanism are 40% less compared to Tian mechanism.

Acknowledgments

This research was funded, in part, by the Iowa Energy Center under Grant 08F-03, with program management provided by Norman Olson, Kevin Nordmeyer, and Thomas Barton. The authors are also grateful to Miao Li, Mark Johnson, James Dautremont, Matthias Veltman,

Cuong Huynh, Christopher Gross, Jordon Tiarks, and Song-Charng Kong of Iowa State University for assistance and helpful discussions.

4.6 References

[1] Zamfirescu C, Dincer I. Using ammonia as a sustainable fuel. Journal of Power Sources 2008;185(1):459-465.

[2] Martin R, Brown N. Nitrous oxide formation and destruction in lean, premixed combustion. Combustion and Flame 1990;80(3-4):238-255.

[3] Vandooren J, Bian J, Vantiggelen P. Comparison of experimental and calculated structures of an ammonia seeded nitric oxide flame. Importance of the NH_2 + NO reaction. Combustion and Flame 1994;98(4):402-410.

[4] Julio SSD, Knuth EL. Direct-sampling studies of NO_x formation from fuel nitrogen. Combustion Science and Technology, 1989;66:149-155.

[5] Bian J. Experimental study of the formation of nitrous and nitric oxides in H_2-O_2-Ar flames seeded with NO and/or NH_3. Symposium (International) on Combustion 1991;23(1):379-386.

[6] Reiter AJ, Kong S-C. Combustion and emissions characteristics of compression-ignition engine using dual ammonia-diesel fuel. Fuel 2011;90(1):87-97.

[7] Miller JA, Bowman CT. Mechanism and modeling of nitrogen chemistry in combustion. Progress in Energy and Combustion Science 1989;15(4):287-338.

[8] Glarborg P. Fuel nitrogen conversion in solid fuel fired systems. Progress in Energy and Combustion Science 2003;29(2):89-113.

[9] Smith GP, Golden DM, Frenklach M, Moriarty NW, Eiteneer B, Goldenberg M, Bowman CT, Hanson RK, Song S, Gardiner JWC, Lissianski VV, Qin Z. GRI-Mech 3.0 1999.

[10] Harrington J. Evidence for a new NO production mechanism in flames. Symposium (International) on Combustion 1996;26(2):2133-2138.

[11] Sullivan N. Ammonia conversion and NO_x formation in laminar co-flowing nonpremixed methane-air flames. Combustion and Flame 2002;131(3):285-298.

[12] Konnov AA. Implementation of the NCN pathway of prompt NO formation in the detailed reaction mechanism. Combustion and Flame 2009;156(11):2093-2105.

[13] Tian Z, Li Y, Zhang L, Glarborg P, Qi F. An experimental and kinetic modeling study of premixed $NH_3/CH_4/O_2/Ar$ flames at low pressure. Combustion and Flame 2009;156(7):1413-1426.

[14] Konnov AA, Dyakov IV, Ruyck JD. Probe sampling measurements of NO in $CH_4+O_2+N_2$ flames doped with NH_3. Combustion Science and Technology 2007;178(6).

[15] Knyazkov D, Shmakov A, Dyakov I, Korobeinichev O, Deruyck J, Konnov A. Formation and destruction of nitric oxide in methane flames doped with NO at atmospheric pressure. Proceedings of the Combustion Institute 2009;32(1):327-334.

[16] Skreiberg O. Ammonia chemistry below 1400 K under fuel-rich conditions in a flow reactor. Combustion and Flame 2004;136(4):501-518.

[17] Zhang K, Li Y, Yuan T, Cai J, Glarborg P, Qi F. An experimental and kinetic modeling study of premixed nitro-methane flames at low pressure. Proceedings of the Combustion Institute 2011;33(1):407-414.

[18] Hansen S, Glarborg P. Simplified model for re-burning chemistry. Energy & Fuels 2010;24(8):4185-4192.

[19] Lindstedt RP, Lockwood FC, Selim MA. A detailed kinetic study of ammonia oxidation. Combustion Science and Technology, 1995;99(4).

[20] Duynslaegher C, Jeanmart H, Vandooren J. Use of ammonia as a fuel for SI engine. Combustion.org.uk 2009:1-6.

[21] Duynslaegher C, Jeanmart H, Vandooren J. Ammonia combustion at elevated pressure and temperature conditions. Fuel 2010;89(11):3540-3545.

[22] Shmakov AG, Korobeinichev OP, Rybitskaya IV, Chernov AA, Knyazkov DA, Bolshova TA, Konnov AA. Formation and consumption of NO in $H_2+O_2+N_2$ flames doped with NO or NH_3 at atmospheric pressure. Combustion and Flame 2010;157(3):556-565.

[23] Lee JH, Kim JH, Park JH, Kwon OC. Studies on properties of laminar premixed hydrogen-added ammonia/air flames for hydrogen production. International Journal of Hydrogen Energy 2010;35(3):1054-1064.

[24] Lee JH, Lee SI, Kwon OC. Effects of ammonia substitution on hydrogen/air flame propagation and emissions. International Journal of Hydrogen Energy 2010;35(20):11332-11341.

[25] Kumar P, Meyer TR. Experimental and modeling study of chemical-kinetics mechanisms for H_2-NH_3-air mixtures in laminar premixed jet flames. Fuel 2011.

CHAPTER 5. INVESTIGATIONS OF NO CHEMISTRY IN LAMINAR H_2/NH_3 DIFFUSION FLAMES BY *IN-SITU* NO-PLIF AND CFD MODELING

A paper to be submitted in *Fuel* Journal, 2012

Praveen Kumar and Terrence R. Meyer*

Abstract

To study the effects of NH_3 seeding on NO_x formation and validation of chemical mechanisms such as, Tian, GRI-Mech3.0, and a proposed modified GRI-Mech3.0 (Mod. GRI-Mech) chemical mechanisms for ammonia seeded H_2/air laminar diffusion flames, *in-situ* NO planar laser induced fluorescence (PLIF) measurements are performed and compared quantitatively with the corresponding 2-D computational NO PLIF, for varying amounts of NH_3 energy percentage in H_2 ($E\%NH_3$) from 0 to 80%. For quantitative comparisons, simulated NO fluorescence signals are generated from predicted NO_x mole fractions via the UNICORN code by incorporating corrections for Boltzmann fraction, quenching corrections and a calibration constant (cc), for all three chemical mechanisms. A calibration flame, CH_4-air laminar premixed flame seeded with NO range from 0 – 600 ppm at equivalence ratio 0.8 is established at identical experimental settings to evaluate the calibration constant (cc) correlated with absorption coefficient, overlap integral and optical efficiency. *In-situ* PLIF signals are corrected for background noise, beam profile and laser energy for each test condition.

Experimentally, with increasing NH_3 addition from 0 to 80% to H_2/air laminar diffusion flames, the flame length and NO concentration distribution seem to grow proportionally, with

* Department of Mechanical Engineering, Iowa State University, Ames, IA 50011, USA
* Corresponding author. Tel: +1 515 294 1805.
* E-mail address: trm@iastate.edu

higher NO concentration near the fuel-oxidizer interface. The predicted NO profiles as well as the flame structure by the Tian mechanism seem to be in reasonable agreement with the experimental NO-PLIF data, with discrepancy within 10 mm from the tube burner exit, where the Tian mechanism produces a local NO peak (bell shape curve), in contrast to gradual increasing experimental NO-PLIF data. Unlike Tian mechanism, the GRI-Mech3.0 mechanism is found to be in complete disagreement with the experimental flame length trend and NO concentration distribution. Interestingly, improved and reasonable agreements of NO mapping as well as flame length are recorded for the modified GRI-Mech3.0 mechanism, supporting the updates applied to standard GRI-Mech3.0 to predict NH_3 seeded flames. Although post flame NO concentration for the modified GRI-Mech3.0 mechanism are in proximity of the Tian mechanism, it failed to capture the in-flame NO concentration trends. Overall, the Tian mechanism is found to be superior in agreement with the NO-PLIF experimental data, among the three chemical mechanisms, with further room of improvement.

5.1 Introduction

Non-intrusive, *in-situ* laser induced fluorescence (LIF) has been proven to be a powerful tool in recent decades [1,2] for probing flame characteristics such as species concentrations, flame temperature. An advanced version of LIF is planar laser-induced fluorescence (PLIF), which is used to make simultaneous measurements over a planar (2-D) field compared to single point measurements [3,4]. The fluorescence signal intensity for a molecule excited by a suitable laser pulse is dependent on many factors such as the molecule's number density, laser

energy, laser profile, population distribution across energy states, and molecular quenching. To perform a quantitative measurement, all these factors need to be considered.

LIF or PLIF has been largely used to diagnose temperature distributions and species concentrations (both qualitative and quantitative) in a wide range of combusting flowfields. For example, Hirano and Tsujishita [5] used planar laser induced fluorescence (PLIF) diagnostics for measurements of NO, CH, CN, NH species to probe the prompt NO formation mechanism. They harnessed the NO rotational spectrum to estimate 2-D flame temperature. They successfully showed the usefulness of this analytical tool for combustion studies. Similarly, to understand the nitric oxide formation in a modern diesel engine combustion chamber, Demory et al. [6] measured qualitative OH and NO concentrations by laser induced fluorescence and compared simulated OH distributions using the KIVA 3V code. Likewise, numerous demonstrations were performed for NO and soot evolution investigations in engine applications [7–10].

Laser induced fluorescence has been proven helpful in improving chemical kinetics of fuel pyrolysis, oxidation, and pollutant formation. For example, Ravikrishna and Laurendeau [11] used LIF for quantitative measurements of NO in CH_4-air and C_2H_6-air counterflow diffusion flames for the validation of flame structure predicted by the Sandia opposed-flow flame code [12] utilizing GRI-Mech2.11 [13]. Based on the comparisons, refinements in rate coefficients were suggested for the prompt-NO initiation reactions in the chemical mechanism. To develop a more thorough understanding of NO kinetics in flames, more accurate *in-situ* NO measurements are required to validate any proposed chemical mechanism. In this effort, Douglas and Laurendeau [14] made quantitative NO measurements in flat, laminar premixed

CH_4-O_2-N_2 flames with equivalence ratio range from 0.65 – 1.5 and compared with the NO predictions using the Sandia opposed flame code with GRI-Mech2.11. They found good agreement between the measured and predicted NO for lean flames, however, predictions failed to match with experimental NO quantitatively as well as qualitatively. Suggestions for refined rate coefficients parameters were made for the key reactions. In another application, LIF was applied to capture quantitative NO production in high-pressure, swirl-stabilized spray flames of liquid heptane [15,16].

In early studies, Hahn and Wendt [17] tested the kinetics of NO formation from fuel nitrogen by introducing anhydrous ammonia with fuel and then with an oxidizer jet. The NO_x kinetics predicted NO_x formation in agreement with experimental data in the case of NH_3 doped with fuel, but agreement was poor when NH_3 was injected in the air side. This indicated deficiencies in the NH_3 pyrolysis kinetic mechanism when it was utilized in the absence of HC fragments. Later, Battles and Hanson [18] presented a method for quantifying OH and NO radicals from PLIF images in high pressure flames utilizing a developed model for quenching cross-sections of OH and NO by Paul and co-workers [19,20]. The model was confirmed in lean CH_4-air flames and the inclusion of interferences from O_2 was recommended for NO fluorescence measurements.

The effects of acoustic forcing at frequencies 22 – 55 Hz on changes in the creation of NO were also studied by facilitating phase-resolved NO planar laser-induced fluorescence measurements [21]. The authors of this study concluded that variations of NO concentrations lead the OH field variations, which were attributed to greater sensitivity of NO to flame temperature. Barlow and co-workers [22,23] investigated the NO formation structure in

turbulent H_2 jet flames with and without N_2 dilution utilizing LIF techniques. Later, Barlow et al. [24], compared major species concentrations such as N_2, O_2, CH_4, CO_2, H_2O, CO, and H_2, OH, and NO measured by LIF in a porous cylindrical burner for different equivalence ratios; they employed numerical calculations using GRI-Mech 2.11, 3.0 [13] and detailed Miller chemical mechanisms [25] . GRI-Mech 2.11 and 3.0 underpredicted and overpredicted, respectively, the NO concentration in fuel-rich conditions. A similar trend was displayed for the Miller mechanism which otherwise seemed to be in fair agreement with the experimental measurements. Data also showed significant dependence of flame structure and NO formations on radiation.

Previous to Barlow's work, Cattolica et al. [26], measured the NO profiles in $H_2/O_2/N_2$ flames using laser induced fluorescence. Driscoll et al. [27], pioneered the application of even lower time resolved (picosecond) laser-induced fluorescence (ps-LIF) and performed NO measurements in a non-premixed, counterflow CH_4/air flame. The authors reported linear ps-LIF was less susceptible to interferences in fuel-rich regions of the flame and less affected by errors resulting from rotational energy transfer (RET). It was also found that the experimental NO concentrations agreed favorably with flame model results within uncertainties of current prompt-NO reaction mechanisms. Hanson and co-workers [28,29] optimized the NO-LIF techniques for high pressure combustion environments by studying different excitation strategies for NO laser induced fluorescence. Utilizing previous results in identifying LIF interference from O_2 and CO_2 in high pressure flames, Lee et al. [30] optimized the LIF detection wavelengths for 2-D imaging of NO in CH_4/air high pressure flames and compared results with model calculations utilizing the GRI-Mech3.0 chemical mechanism. These authors

demonstrated and discussed a practical guideline for 2-D NO-LIF application in high pressure flames.

In a recent study, Powell et al. [31] investigated the NO profiles via saturated LIF for nitrogen diluted H_2/N_2O premixed flames for the equivalence ratio range 0.95 to 1.55 and compared the experimental data with three different chemical mechanisms incorporating $H_2/O_2/N_xH_y$ chemistry. It was found that the model predictions varied by more than 47% for fuel rich conditions, unlike those for the stoichiometric conditions, where disagreement was observed to be approximately 38%. Among the three chemical mechanisms, the Konnov mechanism was found within the range of experimental uncertainty. From the sensitivity and rate-of-production analyses, NH_x/NO chemical interactions, as well as NH_x to N_xH_y recombination reactions under fuel-rich conditions, were reported to be critical to accurately modeling NO profiles in hydrogen-nitrous oxide flames.

In a study of NO formation in laminar, nitrogen-diluted methane diffusion flames seeded with NH_3, Bell et al. [32] compared numerical simulations with detailed chemistry against laser-induced fluorescence (LIF) imaging measurements for a range of ammonia injection rates. Pathways such as prompt NO, followed by the NNH mechanism, thermal NO, and the N_2O mechanism were reported to play important roles in NO formation. In addition, with increasing NH_3 levels, nitrogen levels in the post flame zone were observed to be enhanced and fuel-NO found to be the dominant mechanism. Later, Rahinov et al. [33] studied the formation of the amidogen (NH_2) molecule in a NH_3 doped CH_4/air flame by measuring it via laser absorption spectroscopy and comparing results with 1-D model predictions utilizing several chemical mechanisms. The GRI-Mech3.0 mechanism overpredicted the concentration

significantly in the vicinity of the burner surface. It was reported that the NH_2 radical concentration predicted by all chemical mechanisms were in agreement for NH_3 doped flames and found unaffected by the equivalence ratio, unlike nitrogen oxides doped flames.

Venizelos and Sausa [34] carried out experimental and chemical modeling studies of a 60 torr $NH_3/N_2O/Ar$ flames for the refinement and testing of a detailed chemical mechanism with 87 reactions and 20 species. Spatial profiles of NH_3, N_2O, N_2, H_2O, NO, O_2, NH, O, and OH were recorded using molecular beam mass spectrometry (MB/MS), LIF, or both, and compared with those obtained using both equilibrium and PREMIX flame code calculations. Overall, PREMIX code predictions for majority of the species (like NH_3, N_2O, N_2, H_2O etc.) matched fairly well with the experimental data with a discrepancy in NO concentrations in post flame zone. Hence, the authors recommended a refined version of the chemical mechanism.

In another detailed investigation, Volker [35] studied NO chemistry by quantitative laser spectroscopic measurements of NO in methane-air counterflow diffusion flames and detailed chemical kinetic modeling. Experimental NO profiles for pure CH_4/air as well as NO and NH_3 seeded CH_4/air flames were compared with the detailed modeling results of a chemical mechanism with 74 species and 506 reactions. Acceptable agreement was observed between experiments and modeling, and a recommendation for prompt NO formation in GRI-Mech 2.11 was made.

This literature review reveals that many detailed studies regarding the development of the chemical kinetics of conventional fuel mixtures (H_2, CH_4 etc.) with moderate complex chemistry by adding additives (e.g. NO_2, NO, NH_3) have been conducted. Despite several

investigations on the NO chemistry pathways in NH_3 seeded H_2 flames, NO formations in NH_3 seeded flames are still in the development stage, and no satisfactory chemical mechanism has been found that can predict the combustion characteristics of the NH_3 seeded H_2 flames under most flame conditions.

To better understand the NO formation decomposition pathways in NH_3 seeded H_2-air diffusion flames, detailed quantitative *in-situ* NO PLIF measurements with varying NH_3 seeding levels in H_2 are compared with 2-D NO predictions. The predictions utilize the UNICORN high fidelity CFDC numerical code developed by Katta and Roquemore [36] and employ three different chemical mechanisms: (1) Tian, (2) GRI-Mech3.0, and (3) modified GRI-Mech3.0, a newly proposed chemical mechanism from previous work (Chapter 4). In addition, *in-situ* NO diagnostics in ammonia doped hydrogen-air laminar diffusion flames have been studied and considered as the secondary objective of the present study.

Nomenclature

$S_f = Fluorescence\ signal$

$E_{laser} = Laser\ energy$

$\psi_{overlap} = Overlap\ integral\ between\ excitation\ \ and\ absorption\ spectrums$

$N_{molecule} = Number\ density\ of\ molecule, eg\ (NO)$

$f_B = Boltzmann\ fraction$

$B_{12} = Einstein\ absorption\ coefficient\ of\ ground\ state$

$\eta_{opt} = Optical\ efficiency$

$A_{21} = Einstein\ emission\ coefficient\ of\ excited\ state$

$Q_{21} = Collisional\ quenching\ rate$

5.2 Experimental setup

The NO-PLIF laser diagnostics setup for the current study has been divided into two sections: (a) laminar diffusion jet flame setup and (b) planar laser-induced fluorescence (PLIF) setup including, optics layout, excitation and emissions spectrum, etc., and (c) data collection optics.

5.2.1 Laminar diffusion jet flame setup

A laminar tube-flame setup is employed where open-air laminar diffusion flames at atmospheric pressure are established for H_2/NH_3 fuel mixtures with varying NH_3 seeding level. A schematic of laminar diffusion tube flame setup is shown in Fig. 5.1. The fuel mixtures are metered by using Alicat mass flow controllers (MFCs. Before feeding into the fuel tube, the fuel is ensured to be mixed properly in a mixing manifold and fully developed by using sufficiently long tube length. To keep the flame from the surrounding drifts and maintain flame stability, the entire tube flame setup is surrounded by 4-in × 4-in square aluminum duct with two 15-cm × 0.635-cm slots on the sides of the duct that allow the laser sheets to pass through the flame. For non-corrosive gases, e.g., CH_4 and H_2, a 0-1 standard liter per minute (SLPM) range mass flow controller (MFC) is employed; for corrosive anhydrous NH_3, a relatively smaller flowrate range 0-200 standard cubic per minute (SCCM) is used. All of these MFCs are remotely controlled by a LabView program.

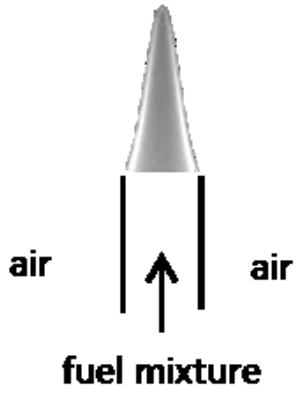

Fig. 5.1. Schematic of laminar diffusion flame

5.2.2 *In-situ* NO measurement setup (NO-PLIF)

Figure 5.2 shows a schematic of the NO planar laser induced fluorescence setup. A general description of each component is summarized in Table 5.1.

Table 5.1. *In-situ* NO measurements setup specifications.

Parts	Specifications
Pump Laser	Nd:YAG Second Harmonic (200mJ @ 532nm)
Dye Laser	Two-Stage Dye Laser and BBO crystal
Camera	Princeton Instrument ® PI-MAX II i1024 ICCD Camera
Lens	UV Lens, focal length f = 45 nm, f/1.8 aperture
Optical Filters	a set of mirrors with a spectrally narrow reflectivity curve,
Gate Time	20 ns
Gain	200×
Gates per Exposure	50 – 300
Laser Sheet	60 mm x 0.5 mm
Laser Pulse Energy	3 mJ
Pulse Width	8ns
Excitation λ	226.034 vacuum nm (online) and 226.042 vacuum nm (offline)
Excitation Scheme	P1(23.5), Q1 + P12(14.5), Q2 + R12(20.5), A – X (0,0) band
Emission Band	A - X (0,1), (0,2) and (0,3) bands

As shown in Fig. 5.2, a Nd:YAG (Neodymium Yttrium Aluminum Garnet) laser (Spectra-Physics PIV400) generates a fundamental 1064 nm wavelength by seeding of an internal diode laser at 1064 nm.

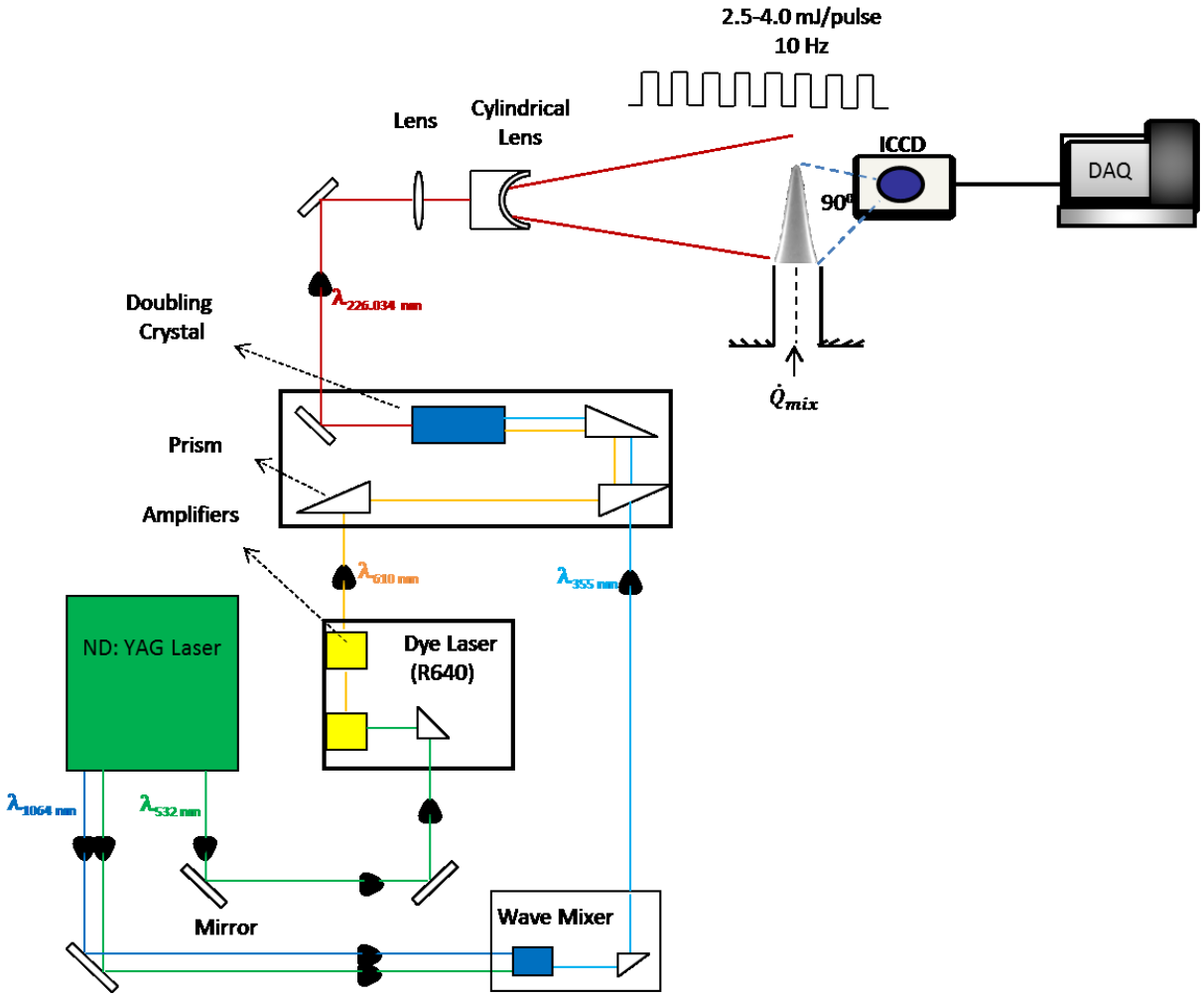

Fig. 5.2. *In-situ* NO diagnostic setup (NO-PLIF).

The fundamental 1064 nm is frequency doubled via a doubling crystal, to generate a second harmonic at 532 nm (from Nd:YAG), as shown in the Fig. 5.2.

$$\lambda_{1064\ nm} \xrightarrow{frequency\ doubled} \lambda_{532\ nm}$$

The 532 nm is further used to pump the dye laser containing Rhodamine (R590) dye to produce output at 610 nm (Fig. 5.2).

$$\lambda_{532\,nm} \xrightarrow{fluorescence\ R590\ Dye} \lambda_{610\,nm}$$

From the Nd:YAG laser, 1064 nm and 532 nm are brought to a wave mixer from a separate route to produce a UV beam at 355 nm.

$$\lambda_{1064\,nm} + \lambda_{532\,nm} \xrightarrow{wavemixer} \lambda_{355\,nm}$$

Subsequently, the 610 nm from the dye laser and 355 nm from the wave mixer are routed to a wave mixing crystal and generate 226.034 nm. The 226.034 nm beam is further passed through a focusing lens and cylindrical (diverging) lens to produce a planar laser sheet 60 mm high and 0.2 mm thick (approximately) that is made passed through the center of the laminar diffusion jet flame (see Fig. 5.2).

$$\lambda_{610\,nm} + \lambda_{355\,nm} \xrightarrow{mixing\ crystal} \lambda_{226.034\,nm}$$

The final output laser at 226.034 nm has a frequency of 10 pulse/sec and energy density range from 2.5 – 4.0 mJ/pulse with pulse width of approximately 7 ns ($7\ x\ 10^{-9}$ sec).

5.2.3 Data collection system

For signal collection optics, a 45 mm focal length Cerco UV objective lens with f/1.8 is placed before the ICCD chip at 90 degrees to the planar laser sheet. The fluorescence signal comprised a spectral width of 11 nm detected over a spectral region centered at 248 nm, which corresponds to the A-X (0, 2) band of NO. Prior to detection, the PLIF signal is filtered to eliminate Rayleigh scattering from the surrounding surfaces using a set of reflecting mirrors with reflectivity band 248 $\pm$ 11 nm. This configuration allows only the PLIF signal to pass

through and thus spurious signals are eliminated. For 2-D PLIF image acquisition, an ICCD camera (Princeton Instruments, PI-MAX II i1024) is used. With 2×2 pixel binning, the camera records images with a 512×512 pixels at a frame rate of 10 frames per second (fps). A built-in image intensifier is used to enhance the signal-to-noise ratio. Due to varying PLIF signal strengths among the flame conditions, the gates per exposure for image acquisitions are kept in the range from 50 – 300, 50 for highest and 300 for lowest NO-PLIF signal flame conditions. However, to maintain the consistency and comparability among PLIF signals of the flame conditions, the average PLIF signal is obtained from the average of 300 shots for each condition. Fig. 5.3 shows the variation of PLIF signal intensity with respect to gates per exposure, with fixed 300-shot accumulations. It is confirmed that the PLIF signal intensity is fairly independent of gates per exposure as long as number of shots accumulated are the same (Fig. 5.3); thus, images at different flame conditions with different gates per exposure rates are still comparable. The detection system utilizes Winview 32 (Princeton Instruments) software to monitor and control the data acquisition process.

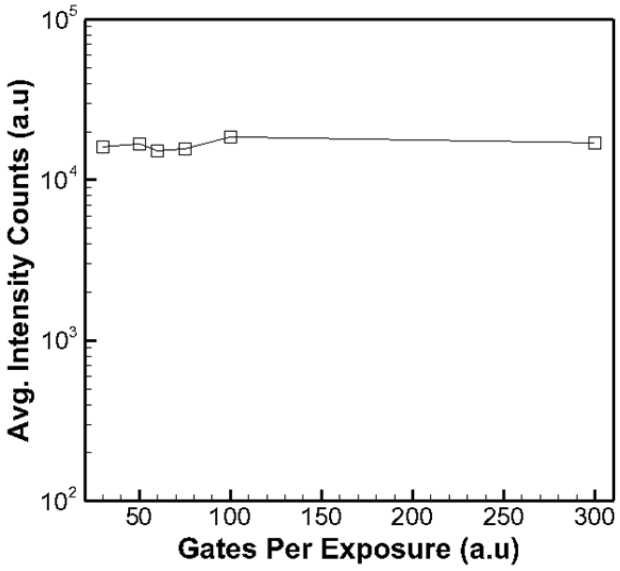

Fig. 5.3. Variation of PLIF signal intensity with respect to gates per exposure

5.3 Numerical modeling

A time-dependent 2-D computational fluid dynamics code with chemistry, known as UNICORN (UNsteady Ignition and COmbustion with ReactioNs), has been used in the present numerical studies. The UNICORN code has been developed to better comprehend the flame dynamics of hydrocarbon flames, i.e., ignition, blow-out, instabilities and species compositions with sufficient accuracy [34]. UNICORN, that solves full PDEs of continuity/mass, u- and v-momentum, species and enthalpy conservation equations in both radial (r) and axial (z) directions, has been methodically developed and validated over a number of years. For numerous complex combustion phenomena, UNICORN has successfully predicted flame dynamics (mixing, velocity field) and species concentrations for major, minor, and intermediate species when coupled with detailed chemical mechanisms. For example, predictions of recirculation zone and soot structures for a laminar ethylene-air flame by UNICORN were confirmed by experimental measurements of flow-field and soot using Mie scattering and laser induced incandescence (LII), respectively [35]. In another study, for low-speed buoyant H_2/air non-premixed flames, the local temperature and NO concentrations were predicted to be higher in the compressed region of the flame and lower in the stretch regions due to the effects of curvature and non-unity Lewis number [36]. Later, Carter and Barlow [37] made time-resolved measurements of NO and OH using PLIF and temperature with thin-filament pyrometry. The time evolution of temperature, OH and NO concentration for both experiments and simulations seemed to be in excellent agreement. Thus, it is established that the UNICORN predictions combined with PLIF measurements is a powerful research tool to study flame structure in both laminar and turbulent flames.

5.3.1 Numerical procedure

For the present work, a CFL number of 0.5 is used on grid system of (201x64) with time step, $\Delta t = 0.137\ msec$. The procedure for each time of iteration is as follows:

1. Estimate transport properties, i.e., kinematic viscosity (ν), thermal diffusivity (α), mass diffusion coefficient (D_{ij}), etc. for each species first, followed by the mixture.
2. Solve species and energy equations to calculate Y_i and sensible enthalpy (h_{mix})
3. Solve for temperature (T) of mixture from ideal gas law.
4. Estimate density (ρ) from ideal gas law.
5. Solve u-velocity, v-velocity momentum equations
6. Solve pressure (p) from Poisson equation.

$$\nabla(momentum\ eq)\ \&\ apply\ \nabla.V = 0 \Rightarrow\ \nabla^2 p = f(\vartheta,\ V)$$

7. Velocity field, u- and v- velocity are corrected based on pressure gradients.

5.3.2 Computational domain

To eliminate the uncertainty from the numerical simulations due to the grid domain, a grid independence test is performed. Four different grid sizes (1) 128x 64, (2) 201x64, (3) 251x90 and (4) 301x161 are used to study the flame structure of a standard 2-D laminar CH_4-air flame. For each grid system, the input parameters, chemical mechanism, boundary, and initial conditions are kept identical. Figure 5.4 shows the temperature contours for different grid systems. It is apparent that choosing an appropriate grid system is also critical for numerical simulations, where the grid of 128x64 is significantly off from the other three grid systems.

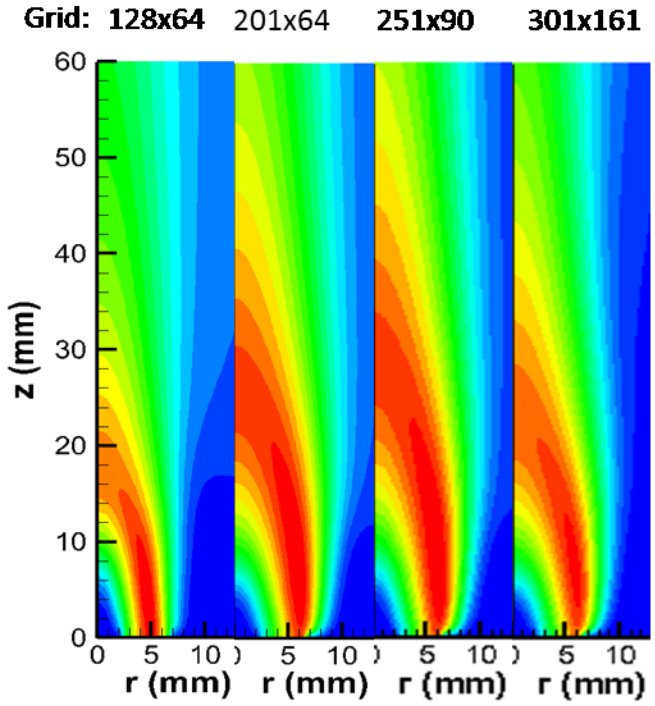

Fig. 5.4. Temperature contours of CH_4-air diffusion flame for different grid sizes. Simulations with GRI-Mech3.0

From the comparisons of centerline temperature profiles among the grid systems in Fig. 5.5, it can be observed that temperature profile for grid 201x64 is in close proximity of both 251x90 and 301x161 in region of interests (0 – 60 mm). Thus, a grid system of 201x64 is selected as a final computational domain for all further numerical modeling.

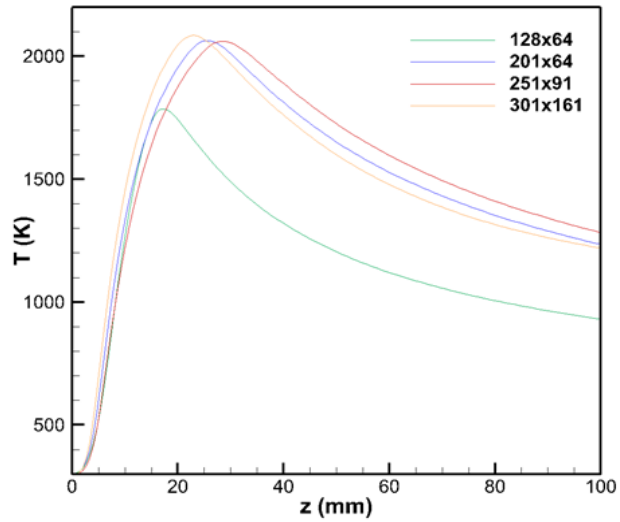

Fig. 5.5. Axial centerline temperature (K) profile for different grid sizes.

5.4 Methodology of quantitative comparison

For a quantitative comparison between the experimental 2-D PLIF images and the 2-D NO computational results for each test condition, the following methodology is employed.

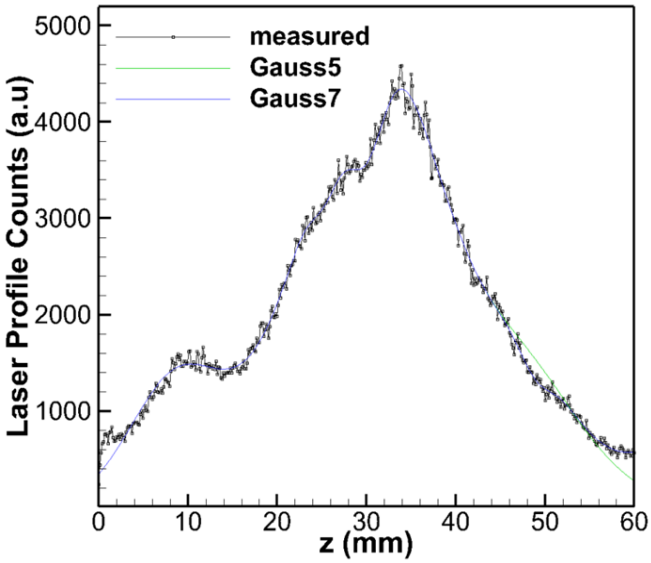

Fig. 5.6. Laser beam (E_{laser}) profile with Gauss 5 and 7 curve fit in axial direction.

The experimental 2-D NO-PLIF image is normalized by the corresponding laser beam profile and laser pulse energy (E_{laser}) for each test run. The result is referred to as the normalized NO signal represented as $S_{f,Experimental}$, where $S_{f,Experimental} = \frac{NO-PLIF}{E_{laser}}$, in arbitrary units (counts). The laser pulse energy (E_{laser}) is evaluated by averaging the pulse energy recorded at the beginning and ending of each test run. A typical laser beam profile is shown in Fig. 5.6.

However, for computational modeling results, the predicted 2-D NO mole fraction (X_{NO}) image is converted back to a simulated PLIF signal represented as $S_{f,Computational}$ in arbitrary units (counts), by incorporating the effects of (1) the overlap-integral (τ), (2) Einstein absorption coefficient (B_{12}), (3) optical efficiency, (4) NO number density (5) Boltzmann fraction, and (6) fluorescence efficiency. Overall, for a computational test run, the NO intensity counts $S_{f,Computational}$ can be represented by the following eq. 5.1.

$$S_{f,Computational} = E_{laser} * \tau * B_{12} * n_{opt} * N_{NO} * f_B * \left(\frac{A_{21}}{A_{21}+Q_{21}}\right) \quad (5.1)$$

The laser energy (E_{laser}) corrections are not required for the computational PLIF signal, as the experimental NO-PLIF images are already normalized by laser beam profile (E_{laser}), so equation 5.2 is utilized;

$$S_{f,Computational} = \tau * B_{12} * n_{opt} * N_{NO} * f_B * \left(\frac{A_{21}}{A_{21}+Q_{21}}\right) \quad (5.2)$$

Also, the overlap-integral (τ), Einstein absorption coefficient (B_{12}) and optical efficiency (n_{opt}) are kept identical among all the test runs due to same excitation scheme and NO-PLIF setup, which simplifies the eq. 5.2 to 5.3

$$S_{f,Computational} = cc * N_{NO} * f_B * \left(\frac{A_{21}}{A_{21}+Q_{21}}\right) \quad (5.3)$$

where cc is a calibration constant:

$$cc = \tau * B_{12} * n_{opt} \tag{5.4}$$

5.4.1 NO number density (N_{NO})

The NO number density (N_{NO}) can be expressed in terms of NO mole fraction (X_{NO}), as follows:

$$N_{NO} = X_{NO} * \left(\frac{p}{kT}\right) \tag{5.5}$$

where, the Boltzmann constant, $k = 1.3806503e^{-23}\ \frac{m^2.kg}{s^2.K}$. From the knowledge of temperature and species concentrations from CFD modeling, N_{NO} can be easily estimated by using eq. 5.5.

5.4.2 Boltzmann fraction (f_B)

The Boltzmann fraction f_B as a function of temperature (shown in Fig. 5.7) is estimated by convolution of the Boltzmann fraction for the NO excitation scheme P1(23.5), Q1 + P12(14.5), Q2 + R12(20.5), in the A – X (0,0) band identified using LIFBASE [38].

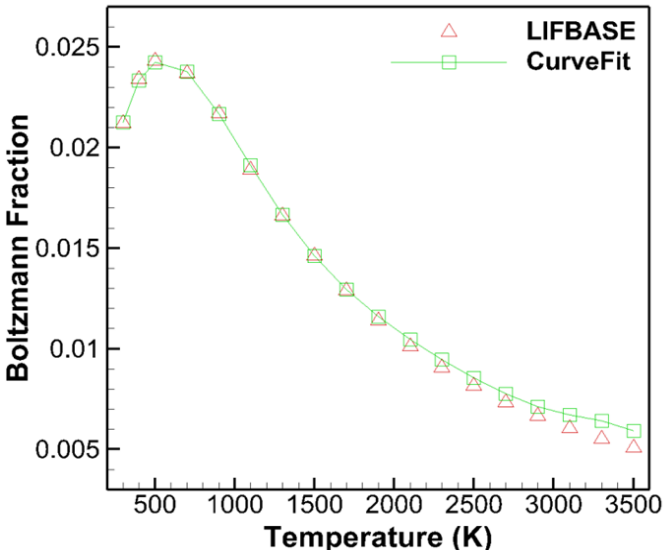

Fig. 5.7. Boltzmann fraction vs. temperature for NO molecule. Excitation band A – X (0,0).

A curve fit for the Boltzmann fraction is estimated from the LIFBASE database and used for Boltzmann fraction corrections. Based on the comparison in Fig. 5.7, the curve fit exhibits excellent agreement with the LIFBASE database within the temperature range 300 K to 2200 K, which is a typical temperature range for the current flame conditions.

5.4.3 Fluorescence efficiency ($n_{fluorescence}$)

The fluorescence efficiency, sometimes known as fluorescence yield, is defined as the ratio of Einstein spontaneous emissions to the total emission:

$$n_{fluorescence} = \frac{A_{21}}{A_{21}+Q_{21}} \tag{5.6}$$

For the fluorescence efficiency ($n_{fluorescence}$), the spontaneous Einstein coefficient for A-X (0, 0) band for NO is $A_{21} = 4.55e^{6}\ s^{-1}$ [39] and the collisional quenching rate is expressed as [17]:

$$Q_{21} = \frac{P}{k.T} * \sum_i X_i * \sigma_i * \sqrt{\frac{8kT}{\pi \mu_i}} \quad (5.7)$$

where X_i, σ_i and μ_i are mole fraction, collisional cross-section and reduced mass of the i[th] colliding species, respectively. However, a more direct expression for NO quenching rate by major colliding species, Q_i, like CO_2, N_2, H_2, CH_4, H_2O, CO_2, O_2, H and OH are used from Tamura et al. [40]. The present flames have significant concentration of NO and NH_3 as well and both species have been proven to be a significant NO quenchers. However, the NO quenching rate for both NO and NH_3 species was unknown until now. The total quenching rate (Q_{21}) is evaluated as:

$$Q_{21} = \sum_{maj.\ speci.} Q_i \quad (5.8)$$

and fluorescence efficiency is estimated using eq. 5.6.

5.4.4 Calibration constant (cc)

To determine the calibration constant (cc) comprised of the overlap-integral (τ), Einstein absorption coefficient (B_{12}), and optical efficiency(n_{opt}), as shown in eq. 5.4, a laminar premixed CH_4-air flame is established as the calibration flame. In past work [41,42], a standard lean premixed CH_4-air flame has been widely used as a standard calibration flame to correlate the PLIF intensity counts to the NO mole fractions concentration in the flame. This premixed flame is preferred because the low flame temperature inhibits in-flame NO generation, leading to a known NO concentration in the exhaust region. This is advantageous over the use of a diffusion flame, where the combustion occurs in the stoichiometric region and NO generation in the flame is inevitable, leading to unknown NO concentration in the far flame zone. In this type of *in-situ* calibration, the standard flame is seeded with a known amount of NO and the NO-PLIF intensity is recorded.

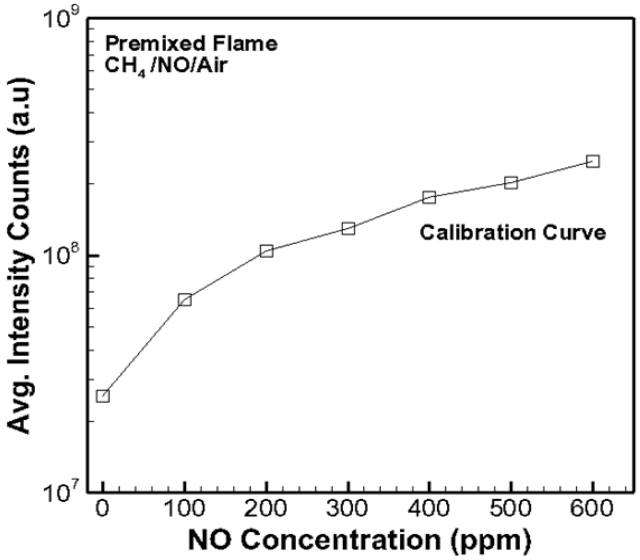

Fig. 5.8. NO-PLIF intensity counts vs. NO seeding for calibration flame.

Previous studies [43] have shown that for lean premixed flames, the effects of NO seeding from the range 0 – 600 ppm on the flame characteristics such as species concentrations, flame length and temperature, etc. are insignificant. Thus, *in-situ* calibration in lean premixed flames with NO seeding range 0 – 600 ppm are considered more accurate than the calibration cell method [44]. For the present experiments, the calibration data is obtained from a lean premixed $CH_4/O_2/N_2/NO$ flame at an equivalence ratio of 0.8 with NO seeding in range of 0 – 600 ppm [45] as the NO-PLIF setup is kept identical. The variation of NO-PLIF intensity counts with NO seeding is shown in Fig. 5.8.

The calibration is accomplished using Eq. 5.9, where NO-PLIF intensity counts ($S_{f,Calibration}$), NO number density (N_{NO}), Einstein emission coefficient (A_{21}), and boltzmann fraction (f_B) for the calibration flames are known. Also, quenching rate of NO by major species (Q_{21}) is estimated based on the known concentrations of major species and NO-PLIF intensity counts for the calibration flame.

$$S_{f,Calibration} = cc * N_{NO} * f_B * \left(\frac{A_{21}}{A_{21}+Q_{21}}\right) \quad (5.9)$$

Based on these known parameters, a calibration constant cc is estimated from Eq. 5.10 as:

$$cc = \frac{S_{f,Calibration}}{N_{NO} * f_B * \left(\frac{A_{21}}{A_{21}+Q_{21}}\right)} \quad (5.10)$$

and recorded to be as $cc = 1.670337e^{-9}\ counts.m^3$. This calibration constant (cc) is used to convert the 2-D simulated NO mole fraction images into a simulated NO-PLIF signal ($S_{f,Computational}$) with arbitrary units (counts) for all the flame conditions.

5.5 Results and discussions

As described in previous sections, calculating absolute NO concentration with NO-PLIF images requires corrections for quenching by other species and local temperature distribution. Simulated NO-PLIF signals ($S_{f,Computational}$) are obtained by using the 2-D CFD modeling results of laminar H_2/NH_3 diffusion flames utilizing the Tian, GRI-Mech3.0 and the modified GRI-Mech3.0 chemical mechanisms. Data from calibration flames (*in-situ* NO measurements in laminar CH_4/air premixed flames) are used to convert the NO mole fractions into signal intensity counts, as described in previous section. For ease of qualitative comparison, both experimental ($S_{f,Experimental}$) and simulated ($S_{f,Computational}$) NO fluorescence 2-D maps are normalized by the peak NO value among NH_3 seeding flames from E%NH_3 = 0% to 80%.

Figure 5.9 shows the normalized 2-D *in-situ* NO contours for H_2/NH_3 laminar diffusion flame with varying NH_3 seeding level in the fuel mixture. The flame length increases with increasing NH_3 in the fuel mixture, which can be attributed to the change in stoichiometric

mass fraction of fuel ($Y_{F,stoic}$). Theories on predicting flame length for laminar non-premixed flames, such as Burke-Schumann [46] for constant density flow and Fay [47] for variable density flow, have established that flame length is inversely proportional to the stoichiometric nozzle-fluid mass fraction, expressed as:

$$L_f \sim \frac{Q_F}{Y_{F,stoic}} \tag{5.11}$$

For example, for pure H_2-air flames, one mole of H_2 requires half moles of O_2 or $0.5 \times (1 + 3.76)$ moles of air to achieve the stoichiometry ($\emptyset = 1$). Whereas, for NH_3, the required moles of air to achieve complete combustion is $1.5 \times (1 + 3.76)$. Thus with the ammonia addition in H_2, the required amount of air to achieve stoichiometric condtion increases, leading to an overall increase in flame height (Fig. 5.9).

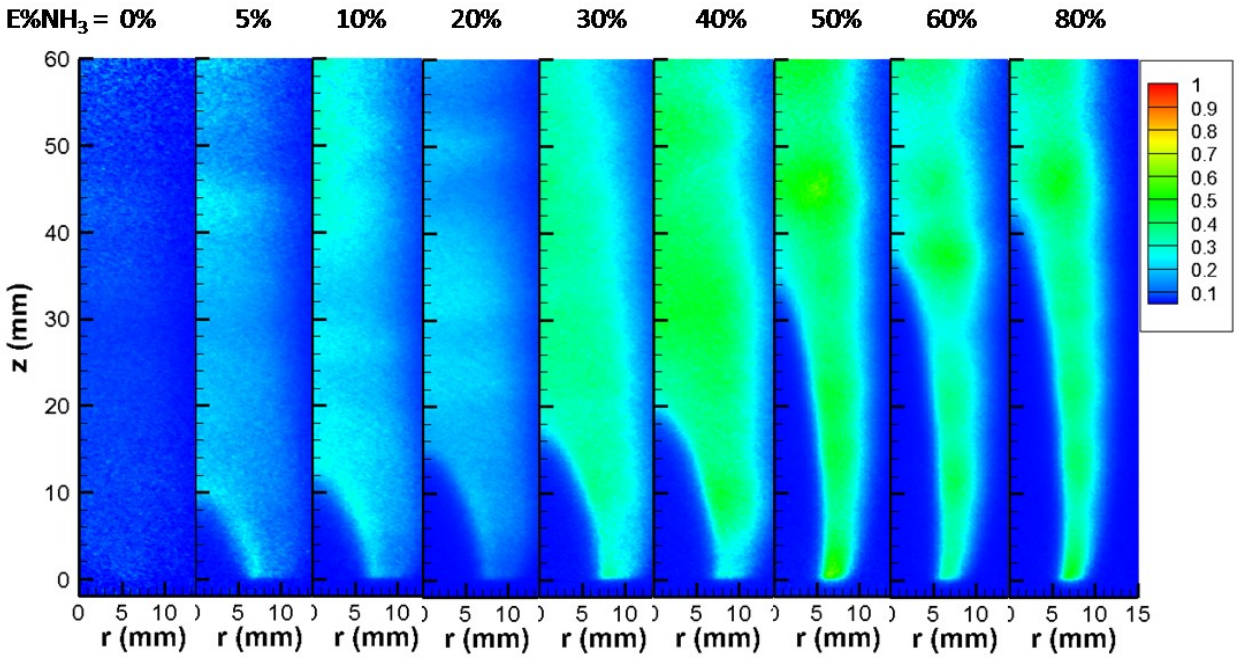

Fig. 5.9. Experimental *in-situ* NO images for H_2/NH_3 laminar diffusion flame with NH_3 seeding levels from 0% to 80%.

Also from Fig. 5.9, the measured 2-D *in-situ* NO contours for H_2/NH_3 laminar diffusion flames are observed to be increasing monotonically with increasing NH_3 doping level. Although the NO-PLIF signal distributions in NH_3 seeded H_2/NH_3 flames are not uniform, significant NO formation is observed to be occring in a region between the high temperature and fuel-lean region of the flames. This is unlike methane-ammonia fuel mixtures, where significant NO is formed in the central region of the flame near tube exit [45]. Due to random background signal caused by inherently low signal-to-noise ratio, the experimental *in-situ* NO measurements display non-smooth spatial distributions.

Figure 5.10 shows the 2-D simulated NO-PLIF signal ($S_{f,Computational}$) contours by the Tian mechanism for NH_3 seeding levels from 0% to 80% for H_2/NH_3 laminar diffusion flames. The flame length predictions by the Tian mechanism, as shown in Fig. 5.10, are in a good agreement with the experimental data (Fig. 5.9). Simulated 2-D, NO-PLIF signal contours (Fig. 5.10) display not only a linear increase in NO with increasing NH_3 doping level, but also significant NO formation occuring in fuel-lean region, as observed in the experimental data (Fig. 5.9). Similarly, the growth of NO signal in the post flame zone region is noticed for both experimental and CFD data. Overall, for model validation, the internal flame structures are comparable between the experiments and Tian mechanism simulations.

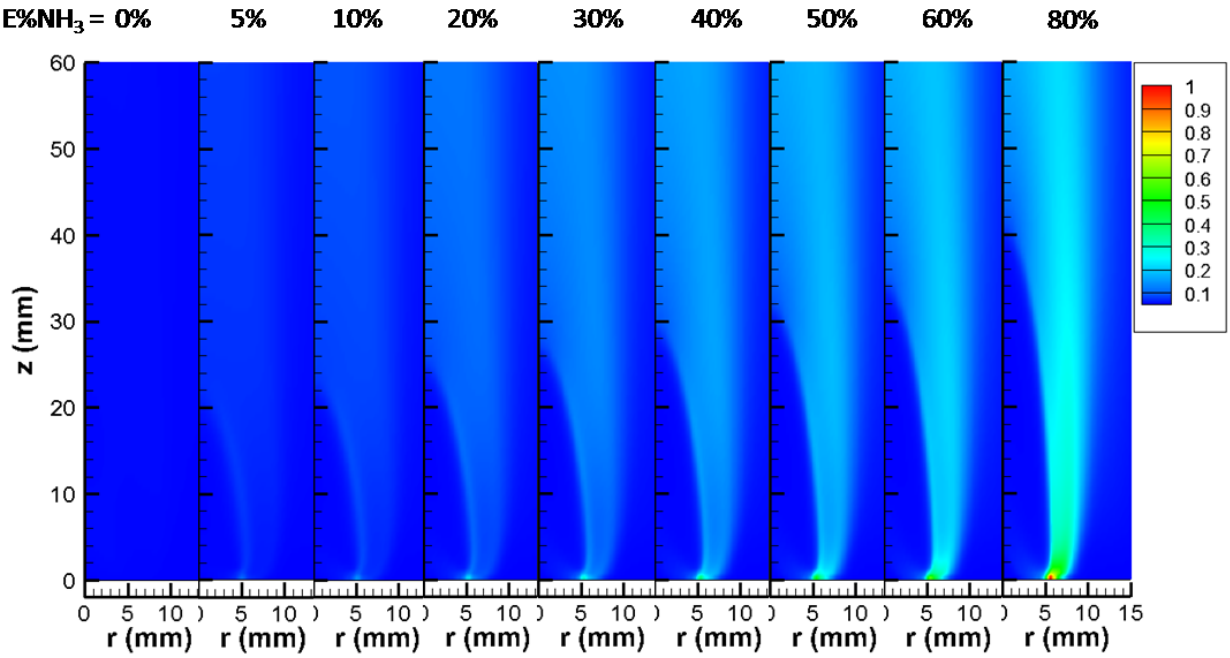

Fig. 5.10. Simulated NO-PLIF signal contours for NH_3 seeding level from 0% to 80% for H_2/NH_3 laminar diffusion flame by the Tian mechanism.

Similarly, 2-D simulated NO-PLIF signal ($S_{f,Computational}$) contours by the GRI-Mech3.0 mechanism are displayed in Fig. 5.11 with varying NH_3 levels in the H_2/NH_3 fuel mixture. On comparison with *in-situ* NO distributions (Fig. 5.9), the flame structure and NO distribution predictions by GRI-Mech3.0 diplay inaccurate trends and significant discrepancies in flame length predictions as well as in NO distribution, especially for higher levels of NH_3 seeding in H_2/NH_3 laminar diffusion flames.

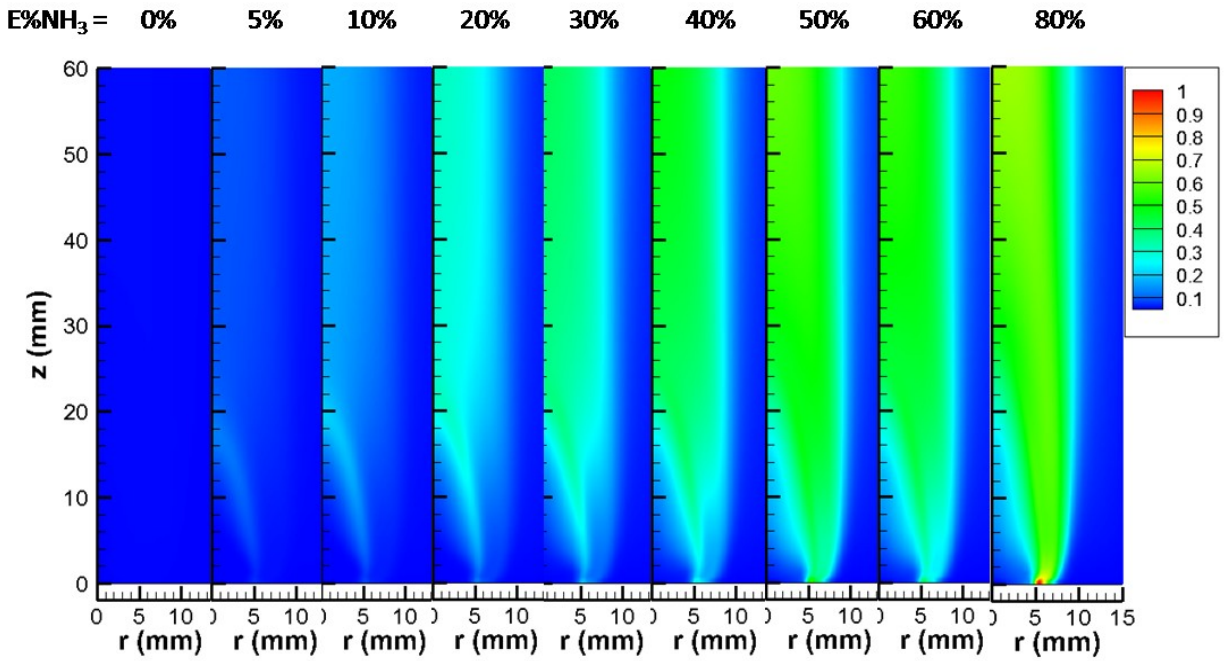

Fig. 5.11. Simulated NO-PLIF signal contours for NH_3 seeding level from 0% to 80% for H_2/NH_3 laminar diffusion flame by the GRI-Mech3.0 mechanism.

Figure 5.12 shows the simulated 2-D NO PLIF signal ($S_{f,Computational}$) contours generated by the newly proposed modified GRI-Mech3.0 based on the recommendations from the previous work (Chapter 4). Unlike the GRI-Mech3.0 mechanism, the apparent flame length variation, as well as the NO distribtion (Fig. 5.12), are improved and compare well with the experimental NO fluorescence signal ($S_{f,Experimental}$) contours (Fig. 5.9), indicating the capability of the newly developed chemical mechanism in predicting flame structures for NH_3 seeded H_2 flames.

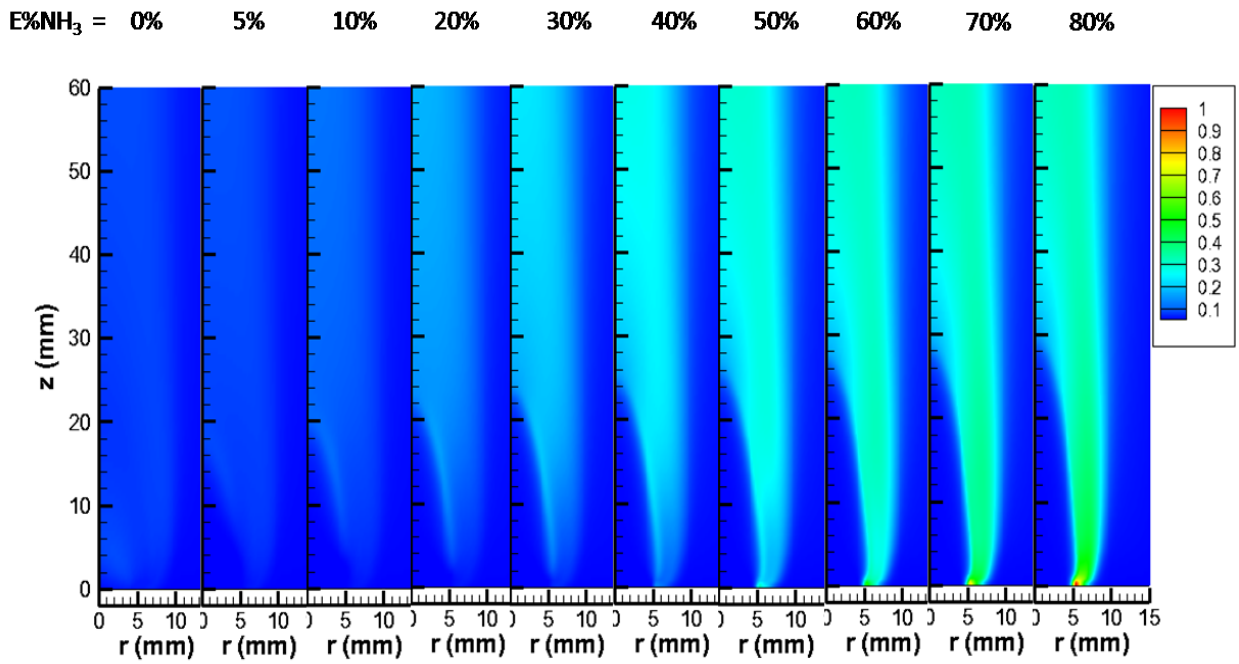

Fig. 5.12. Simulated NO-PLIF signal contours for NH_3 seeding level from 0% to 80% for H_2/NH_3 laminar diffusion flame by the modified GRI-Mech3.0 mechanism.

5.5.1 Comparison of measured NO emissions with predictions

As a preliminary validation method, NO predictions by the Tian, GRI-Mech3.0 and modified GRI-Mech3.0 chemical mechanisms are compared with the experimentally measured NO emissions (as shown in Fig. 5.13) at a location 60 mm downstream along the centerline axis with varying NH_3 seeding level, i.e. E%NH_3 from 0 to 80. In Fig. 5.13, the measured NO exhibited NO mole fractions in the range of 5-7 ppm for pure H_2/air diffusion flame and increase steeply with increase in E%NH_3 from 0 to 20. With further increases in E%NH_3 in the range from 20 to 80, the NO trend seems to increase gradually with increasing NH_3 seeding level, and peak NO emission is measured as 407 ppm for case E%NH_3 = 80.

Qualitatively, the trend captured by the Tian and the GRI-Mech3.0 chemical mechanisms are in fairly reasonable agreement over the entire range of E%NH_3 from 0 to 80. For the

modified GRI-Mech3.0 mechanism, noticeable discrepancy is observed in the NH_3 seeding range from 0 to 20 where minor enhancement in predicted NO is noticed. For all three chemical mechanisms, the predicted NO concentrations are found approximately one order magnitude higher in comparison to the measured NO emissions for the entire range of ammonia seeding levels. Overall, the Tian mechanism was observed to be the closest in agreement with the experimental NO emission data, followed by the modified GRI-Mech3.0 mechanism.

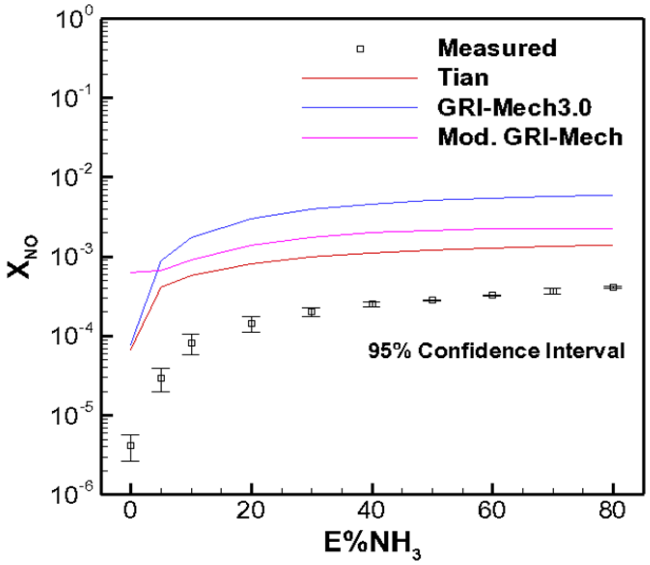

Fig. 5.13. Measured NO emission profile with predicted NO mole fractions by the Tian, GRI-Mech3.0 and modified GRI-Mech mechanisms for range of NH_3 seeding level from 0 to 80.

Figure 5.14 shows the comparison of measured NO emission data, at 60 mm downstream by using a NO-analyzer (IMR 1400-PS) with the calculated NO mole fractions from the *in-situ* NO measurements for H_2/NH_3 diffusion flames with E%NH_3 varying from 0 to 80. To convert the NO-PLIF signals (unit; counts) into NO mole fractions for each E%NH_3 case, major species concentrations including O_2, OH, H, H_2O, N_2, H_2 etc., and temperature from the Tian mechanism's predictions at 60 mm are utilized to incorporate the Boltzmann fraction f_B

corrections (Fig. 5.7) and quenching Q_{21}corrections (Eq. 5.6). It is argued that the CFD model is sufficiently accurate to predict the major species concentrations and temperature.

The calibration constant cc (Eq. 5.10) obtained from the premixed $CH_4/N_2/O_2/NO$ calibration flame is used to finally convert the NO-PLIF signal (unit; counts) to NO mole fractions.

The vertical uncertainty contributions in X_{NO} (PLIF) as shown in Fig. 5.14 are estimated from uncertainties in 1) beam profile and fluctuation, 2) Boltzmann fraction, 3) quenching correction, 4) temperature and, 5) major species concentrations. The horizontal uncertainties bar are evaluated from the uncertainties in species mass flow rates. The uncertainty analysis of NO mole fractions via *in-situ* measurements are discussed in detail in appendix section A.6. The measured NO emission data sampled from the exhaust with the NO analyzer is displayed with a 95% confidence interval in Fig. 5.14

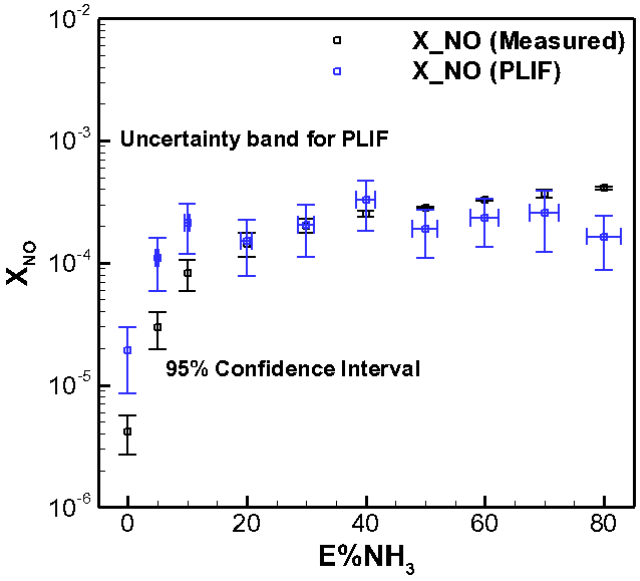

Fig. 5.14. Comparison of measured NO mole fractions by the NO sensor with the converted NO mole fractions by NO-PLIF measurements for range of NH_3 seeding level from 0 to 80 at 60 mm downstream.

From Fig. 5.14, it can be observed that the agreement between the NO mole fractions by *in-situ* technique (PLIF) and NO-analyzer at 60 mm downstream location is excellent for the mid-range of the NH_3 seeding i.e., $E\%NH_3$ from 20 -40, with increasing disagreement between the two on both extreme ranges of $E\%NH_3$. For the lower range of $E\%NH_3$ (0 to 10), relatively higher *in-situ* NO mole fraction magnitude can be ascribed to the assumption of neglecting NO PLIF signal quenching via NO self-quenching and NH_3 while incorporating quenching corrections. In contrast, for the higher range of $E\%NH_3$ (50-80) (Fig. 5.14), relatively lower magnitude for the NO mole fractions by PLIF compared to the measured NO emissions in the exhaust may have been due to discrepancies in temperature and major species concentration predictions by the Tian mechanism compared to actual flames, thus leading to over quenching of NO signal resulting in lower NO mole fraction.

5.5.2 Centerline NO profiles

As apparent from Figs. 5.9 to 5.12, discrepencies are observed in qualitative comparison of 2-D *in-situ* NO profiles with the simulated NO-PLIF signal by the Tian, GRI-Mech3.0 and modified GRI-Mech3.0 (Mod. GRI-Mech) chemical mechanisms, which are further analysed in the following sections.

Centerline ($r = 0$) profiles of *in-situ* NO measurements and simulated NO-PLIF by the Tian, GRI-Mech3.0, and the modified GRI-Mech3.0 mechanisms are compared for the lower range of NH_3 seeding from $E\%NH_3$ = 0% to 30% and for the higher range of NH_3 doping from $E\%NH_3$ = 40% to 80%, as shown in Figs. 5.15 and 5.16, respectively, for laminar H_2/NH_3 diffusion flames.

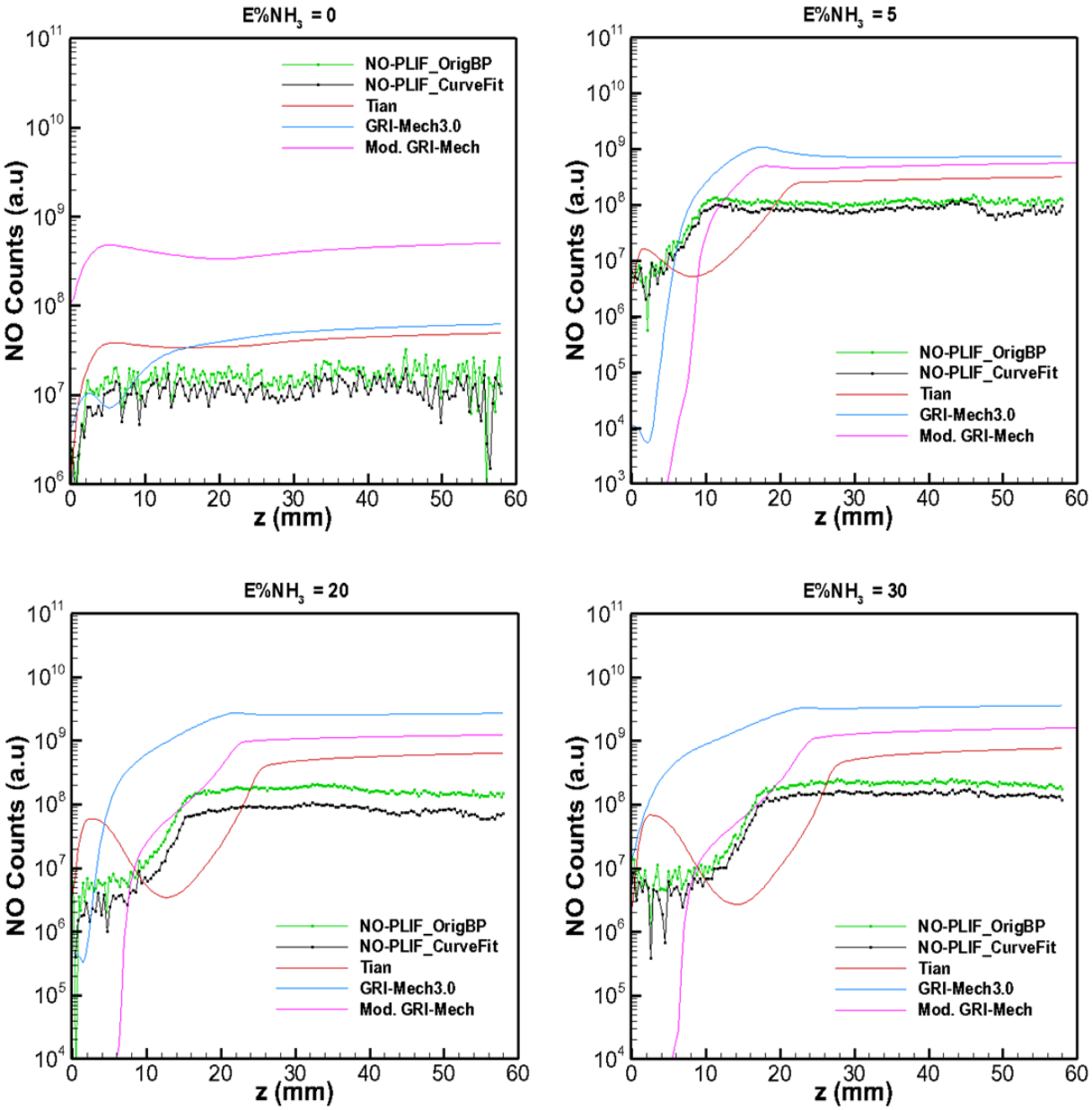

Fig. 5.15. Centerline quantitative comparison of *in-situ* NO profile with simulated NO-PLIF signals by the Tian, GRI-Mech3.0 and modified GRI-Mech mechanisms for lower range of NH_3 seeding level; (a) $E\%NH_3$ = 0, (b) $E\%NH_3$ = 5, (c) $E\%NH_3$ = 20 and (d) $E\%NH_3$ = 30.

For the ammonia-free flame ($E\%NH_3$ = 0), both the Tian and GRI-Mech3.0 mechanisms capture the *in-situ* NO trend along the centerline, as shown in Fig. 5.15a. In the proximity of tube exit (within 10 mm), the quantitative simulated NO-PLIF by GRI-Mech3.0 is in excellent

agreement with the experimental data, whereas the Tian mechanism overpredicts by almost ~3x times. Farther away from the tube exit, both the Tian and GRI-Mech3.0 mechanisms exhibited equivalent NO trends and overpredict the NO concentration compared to the experimental data. Unlike Tian and GRI-Mech3.0, the NO trend displayed by the modified GRI-Mech3.0 mechanism deviated from the experimental data by more than an order of magnitude.

For the lower range of ammonia seeding levels i.e., E%NH_3 = 5%, 20% and 30% (Figs. 5.15b, 5.15c and 5.15d), the *in-situ* NO profile exhibits a gradual linear increase in NO concentration near tube exit region and then displays approximately constant NO profile with minor fluctuations further downstream along the centerline. The increasing stretch of the linear NO growth region with increasing NH_3 seeding levels clearly indicates the shifting of reaction zone farther away from the tube exit, which can be attributed towards the higher moles of air requirements for NH_3 to reach stoichiometry.

The simulated NO-PLIF profile by the Tian mechanism is in fairly good agreement with the *in-situ* NO profiles in the high temperature and post flame regions for lower NH_3 seeding range (E%NH_3 = 5, 20 and 30). However, in the proximity of the tube exit region, the predicted NO by the Tian mechanism exhibits an interesting two-peak structure, in contrast to linear NO growth in experiments. For small NH_3 seeding (E%NH_3 = 5) in the fuel mixture, the simulated NO-PLIF by the Tian mechanism shows an onset of two-peak structure or a bell-shaped profile in near tube exit region (within 10 mm), with a sharp jump in NO concentration followed by gradual NO receding. The 1st peak magnitude is linearly increasing along with stretching of

NO receding region, as NH_3 content increases in the H_2/NH_3 fuel mixture ($E\%NH_3$ = 20 and 30).

As can be noticed from Fig. 5.15, for NH_3 seeding levels $E\%NH_3$ = 5, 20 and 30, the simulated NO-PLIF profiles by the GRI-Mech3.0 mechanism are in strong disagreement with the experimental *in-situ* NO in near tube exit region, where predicted NO increases steeply in comparison to experimental data (see Fig 5.15). In contrast to *in-situ* NO profiles, the simulated NO profiles by the GRI-Mech3.0 mechanism are noticed to be shifting towards the tube exit upstream with increasing NH_3 content in the H_2/NH_3 fuel mixture (refer Fig. 5.15). However, the GRI-Mech3.0 mechanism manages to capture the experimental NO trend in the post flame region with significant over prediction in magnitude compared to *in-situ* NO measurements. For example, for $E\%NH_3$ = 5, the difference between the experimental and simulated NO-PLIF by GRI-Mech3.0 is approximately more than one order of magnitude, which seems to grow larger by more than two orders of magnitude with increasing NH_3 level ($E\%NH_3$ = 20 and 30).

Surprisingly, the modified GRI-Mech3.0 (Mod. GRI-Mech) mechanism significantly under-predicts the NO concentration in the proximity of tube burner exit as noticed in Fig. 5.15, thus failing to capture the NO formation in low temperature regions of the flame for cases $E\%NH_3$ = 5, 20 and 30. However, the predicted NO trend by the modified GRI-Mech3.0 mechanism seems to improve significantly and found to approach towards the experimental NO-PLIF data in high temperature region and post flame zone, thus reducing the differences between the two mechanisms for all the three cases.

Similarly, for higher ammonia seeding ranges in H_2/NH_3 laminar diffusion flames from $E\%NH_3$ = 40 to 80 (Fig. 5.16), the *in-situ* NO profiles exhibit even more gradual linear

increase in NO concentration in near tube exit region and then display approximately constant NO profile.

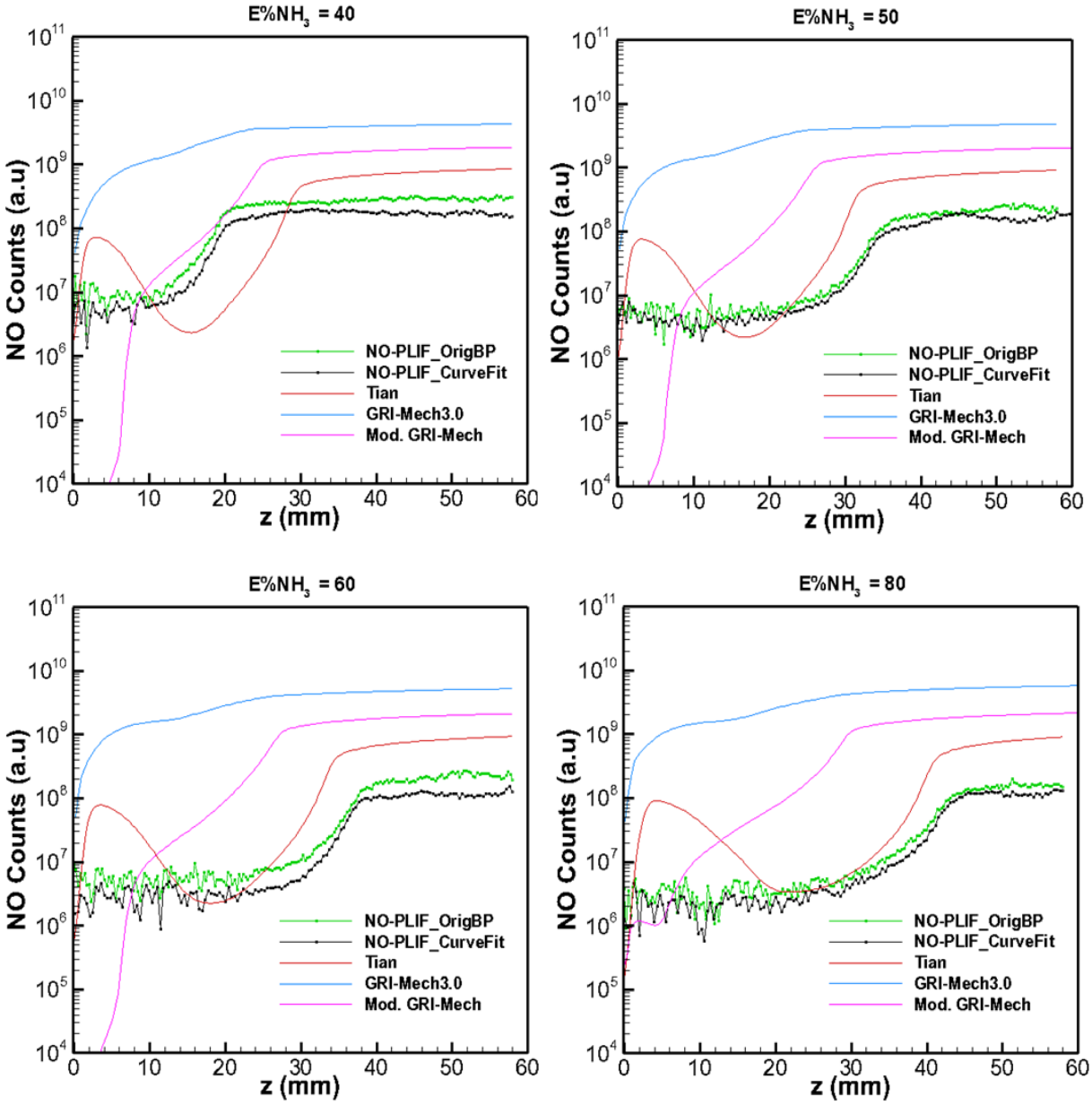

Fig. 5.16. Centerline quantitative comparison of *in-situ* NO profile with simulated NO-PLIF signals by the Tian, GRI-Mech3.0 and modified GRI-Mech mechanisms for higher range of NH_3 seeding level; (a) E%NH_3 = 40, (b) E%NH_3 = 50, (c) E%NH_3 = 60 and (d) E%NH_3 = 80.

For E%NH_3 = 40 to 80, the simulated NO-PLIF profiles by the Tian mechanism are in fairly good agreement with the *in-situ* NO profiles qualitatively in high temperature and post

flame regions. However, the magnitude of the 1st peak of the two-peak structure of predicted NO builds with the addition of ammonia.

In contrast, GRI-Mech3.0 shows greater disagreement when predicting flame structure, as well as quantitative NO, in comparison to experimental data (Fig. 5.16) for the higher range of NH_3 seeding ($E\%NH_3$ from 40 – 80). For example, in the near tube exit region, the simulated NO-PLIF signal magnitudes predicted by the GRI-Mech3.0 mechanism are two orders of magnitude higher, which are maintained further downstream along the centerline. For the modified GRI-Mech3.0 chemical mechanism, the NO trends for $E\%NH_3$ = 40, 50, and 60, in Fig. 5.16, repeated similar behaviors as observed for the lower NH_3 seeding levels i.e., $E\%NH_3$ = 5, 20 and 30. On the contrary, for $E\%NH_3$ = 80, the simulated NO-PLIF signal for the modified GRI-Mech3.0 showed fairly good agreement with the experimental NO-PLIF data within 10 mm, and the differences increased gradually in the post flame region along the centerline.

From the above discussions, the Tian mechanism is in reasonable agreement with the experimental *in-situ* NO data, and displays superior potential in predicting flame structure of NH_3 seeded H_2/NH_3 laminar diffusion flames and when compared to the GRI-Mech3.0 and modified GRI-Mech3.0 mechanisms. In comparison to standard GRI-Mech3.0 mechanisms, the NO trends for the modified GRI-Mech3.0 mechanism are observed to be in better agreement with the experimental NO profiles, especially in post flame region, for all the NH_3 seeding levels from $E\%NH_3$ = 5 to 80.

5.5.3 Radial NO profiles ($z = 20\ mm$)

In this section, comparisons of *in-situ* NO measurements are performed with the simulated NO-PLIF signals obtained by the three chemical mechanisms along the radial axis at an axial location of 20 mm for both lower and higher levels of NH_3 seeding. For ammonia-free flames ($E\%NH_3 = 0$), both the Tian and GRI-Mech3.0 mechanisms capture the *in-situ* NO trend along the radial axis, as shown in Fig. 5.17, with equivalent discrepancy in NO magnitudes in comparison to the experimental data. Farther away from the high flame temperature zone, both the Tian and GRI-Mech3.0 mechanisms exhibit less disagreement with the measured *in-situ* NO data. Unlike Tian and GRI-Mech3.0, the NO trend displayed by the modified GRI-Mech3.0 is over-predicting almost by an order of magnitude for pure H_2-air flame, as indicated along the centerline.

For the lower range of ammonia seeding levels, $E\%NH_3 = 5\%$, 20% and 30% (Fig. 5.17), the overall concentrations of *in-situ* NO are enhanced compared to the pure H_2-air case ($E\%NH_3 = 0$). Consistently for all the lower NH_3 seeding levels, the peak *in-situ* NO is identified at the center of the flame and then reduces gradually moving away from the center axis in the radial direction. Interestingly, the simulated NO-PLIF profile by the Tian mechanism is in disagreement with the experimental NO-PLIF data in the near centerline and high temperature regions. The profile broadens with increasing NH_3 seeding levels. Significant differences are observed at the onset of NO formation for the Tian mechanism, near the centerline region, with increasing under prediction as the seeding of NO as NH_3 in the flame rises.

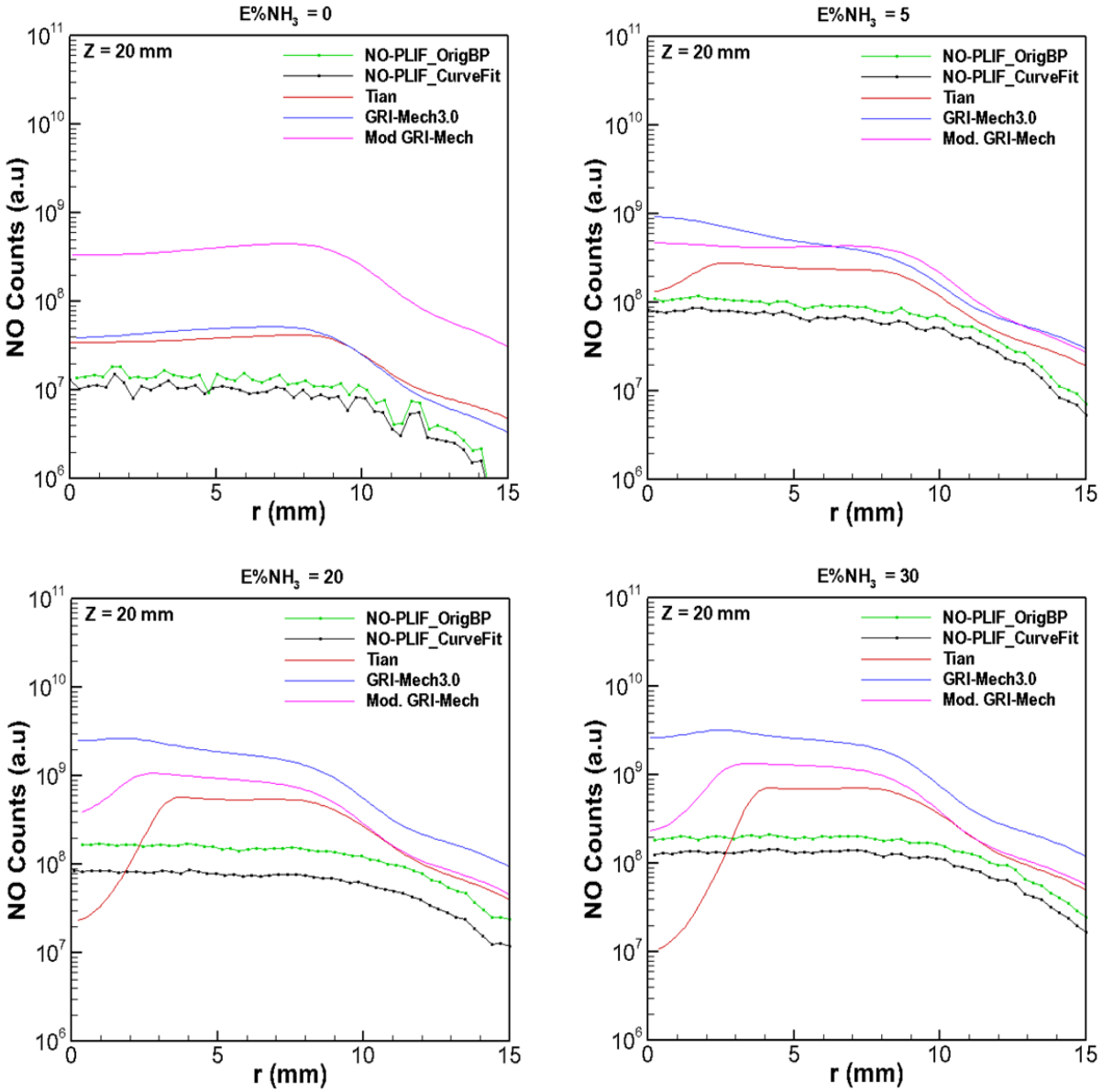

Fig. 5.17. Radial quantitative comparison of *in-situ* NO profile with simulated NO-PLIF signals by the Tian, GRI-Mech3.0 and modified GRI-Mech mechanisms at axial location 20 mm, for lower range of NH_3 seeding level; (a) $E\%NH_3 = 0$, (b) $E\%NH_3 = 5$, (c) $E\%NH_3 = 20$ and (d) $E\%NH_3 = 30$.

In contrast to the Tian mechanism, the NO trends for the GRI-Mech3.0 mechanism appear to significantly overpredict the experimental data (approximately by an order of magnitude) near the centerline region (Fig. 5.17). However, the agreement improved at the lean side of the flame (away from the centerline) for all $E\%NH_3$ cases (5-30). For example, for $E\%NH_3 = 5$,

the difference between the experimental and simulated NO-PLIF by GRI-Mech3.0 is approximately 5 times higher, and builds with increasing NH_3 level ($E\%NH_3$ = 20 and 30). The modified GRI-Mech3.0 (Mod. GRI-Mech) mechanism's NO profile deviates significantly from the experimental NO-PLIF data for the pure H_2-air diffusion flame, unlike the Tian and GRI-Mech3.0 mechanisms (Fig 5.17). However, for lower level NH_3 seeding cases ($E\%NH_3$ = 5, 20, 30), the Mod. GRI-Mech mechanism predicted better agreement of NO profiles with the *in-situ* NO compared to the GRI-Mech3.0 mechanism (Fig. 5.17).

Among higher NH_3 seeding level cases ($E\%NH_3$ 40 to 80), shown in Fig. 5.18, the experimental *in-situ* NO trends transitioned from a linear profile to a bell shaped curve due to significantly reduced NO concentration near the centerline region. The observed *in-situ* NO trend may indicate enhanced activation of the NO decomposition reactions in the near centerline region, resulting in reduced NO concentrations. As observed in Fig. 5.18, due to a reduction in *in-situ* NO measurements near the centerline region, the NO trends predicted by the Tian mechanism are in fairly good agreement with experimental NO-PLIF data within 5 mm on the radial axis for the higher ranges of NH_3 seeding levels ($E\%NH_3$ = 50, 60 and 80). Further along the radial axis, the Tian mechanism captured the NO concentration trend fairly well, with significant over-prediction of the NO magnitude in the high flame temperature region.

The simulated NO-PLIF signals by the GRI-Mech3.0 mechanism in Fig. 5.18 are observed to be similar in trend for higher NH_3 seeding cases ($E\%NH_3$ = 40 to 80) as noted for the lower ammonia seeding levels ($E\%NH_3$ = 5, 20 & 30). The NO is over-predicted in the

near centerline region by slightly more than two orders of magnitude with the agreement improving slightly on the lean side of the flame region.

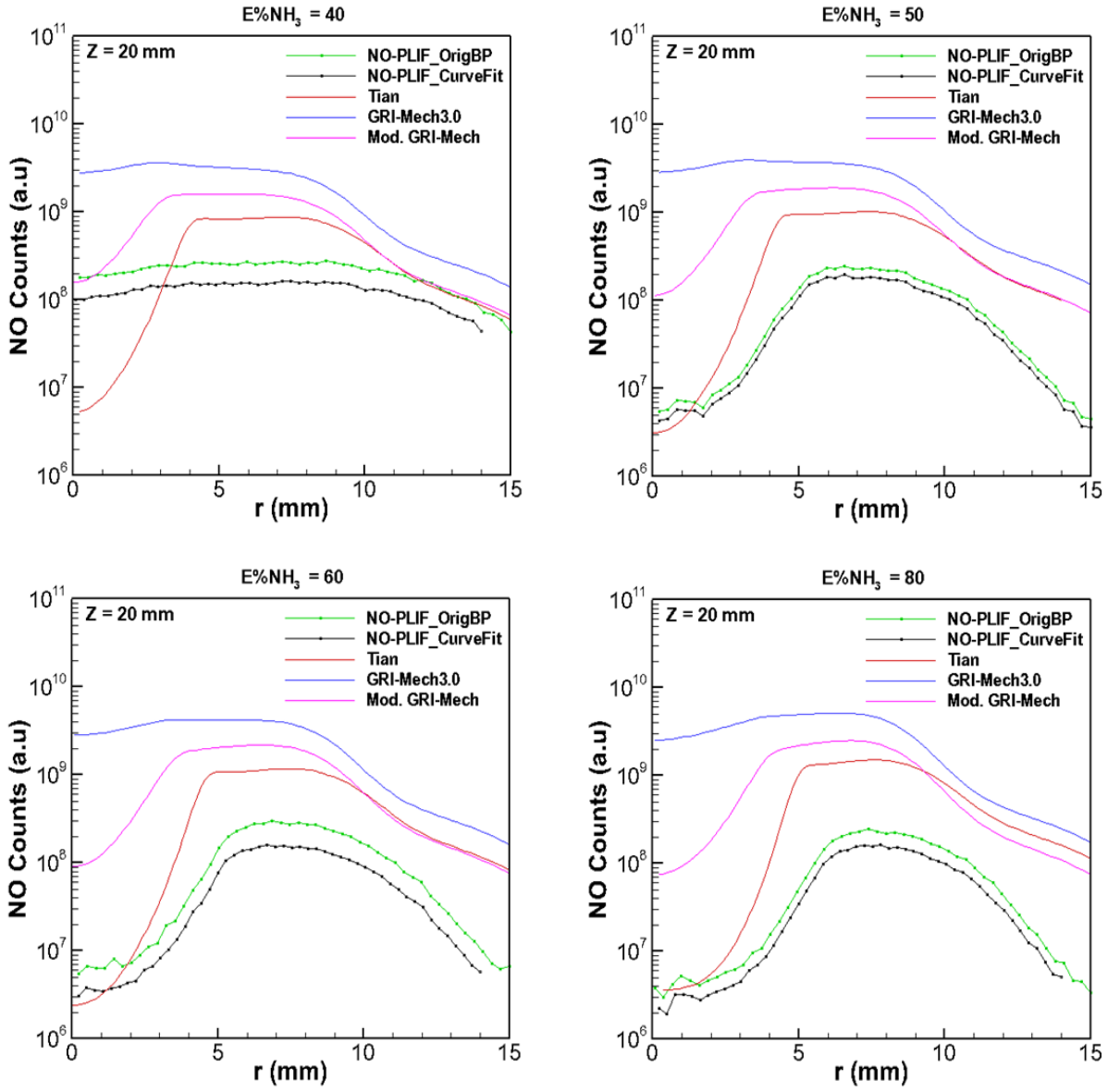

Fig. 5.18. Radial quantitative comparison of *in-situ* NO profile with simulated NO-PLIF signals by the Tian, GRI-Mech3.0 and modified GRI-Mech mechanisms at axial location 20 mm, for higher range of NH_3 seeding level; (a) $E\%NH_3 = 40$, (b) $E\%NH_3 = 50$, (c) $E\%NH_3 = 60$ and (d) $E\%NH_3 = 80$.

For the near centerline region along the radial axis, the NO trends recorded by the modified GRI-Mech3.0 mechanism differ significantly from the experimental NO trends. In

contrast, the Tian mechanism captured the NO concentrations profiles for all cases of higher ammonia seeding levels. The agreement between the modified GRI-Mech3.0 and the Tian mechanism was observed to be reasonable on the lean side of the higher level NH_3-seeded diffusion flames ($E\%NH_3$ = 40 to 80).

The Tian mechanism, is the most effective in capturing the fundamental flame characteristics, including flame length, in-flame NO distributions, etc., and is further analyzed to understand the NO kinetics. In order to investigate the cause of the first bell shaped curve of the simulated NO-PLIF, along the centerline by the Tian mechanism (Figs 5.15 and 5.16), the temperature and species profiles are investigated in detail. Figure 5.19 shows the predicted centerline flame temperature by the Tian mechanism with varying NH_3 content in fuel mixtures from $E\%NH_3$ = 0 to 80. The peak temperature magnitude and its location appeared to be drop and shift downstream with ammonia addition, as expected due to low adiabatic flame temperature and reactivity of ammonia.

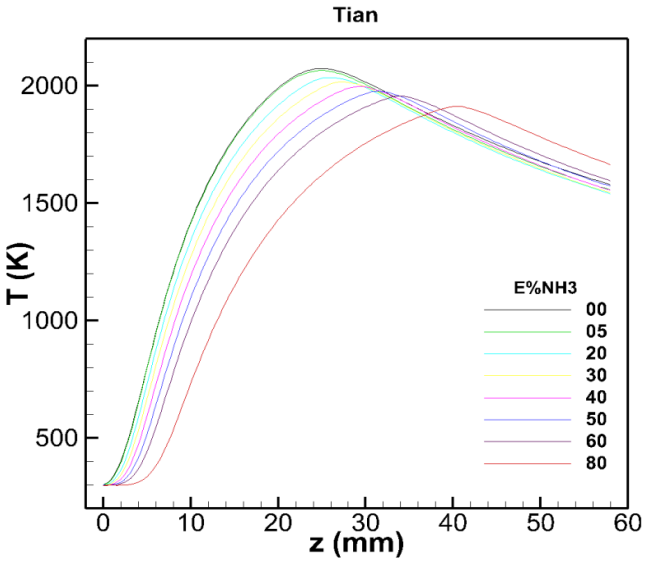

Fig. 5.19. Centerline flame temperature (K) profiles predicted by Tian mechanism with varying NH_3 levels; $E\%NH_3$ = 0 to 80.

The axial location and the temperature magnitudes of the first peak of simulated NO profiles by the Tian mechanism, with varying ammonia content in the H_2/NH_3 fuel mixture, are displayed in Table 5.2. The first peak location for all NH_3 seeding cases is well within 5 mm from the tube exit, and the local flame temperature is observed to be within 400 K. This indicates that the NO kinetics with very low activation energy impact the NO formations in this low temperature region (within 5 mm).

Table 5.2. Axial location and flame temperature of 1st peak of simulated NO-PLIF profiles for the Tian mechanism, with varying amounts of NH_3 in H_2/NH_3 fuel mixture.

	E%NH_3 (Tian Mechanism)							
	0	5	20	30	40	50	60	80
z (mm)	NA	1.3	2.4	2.6	2.65	2.95	3.1	4
T (K)	303	340	395	380	355	345	325	310

Effects of NH_3 seeding on the centerline species profiles, (a) H, (b) OH, (c) O and (d) O_2, predicted by the Tian mechanism are shown in Fig. 5.20. Peak concentration of the H radical within 5 mm is predicted to be in the order of ~ 10^{-3} for pure H_2-air (E%NH_3 = 0) diffusion flame, and monotonically decreases to ~ 10^{-6} with increasing NH_3 in the fuel mixture. On the contrary, concentrations of OH and O radicals are negligible for all cases of NH_3 seeding within 5 mm, playing a key role in determining ammonia oxidation in the flame zone.

Interestingly, the predicted mole fractions of O_2 along the centerline of the flame by the Tian mechanism is enhanced by orders of magnitude with increasing NH_3 within 5 mm of the tube exit region. In addition, the shapes of the O_2 profiles are comparable with the simulated NO-PLIF profiles for the Tian mechanisms, as observed in Figs. 5.15 and 5.16. Fig. 5.20 shows that the pathways associated with the O_2 production in the reaction zone, especially within 20 mm along the centerline, may also have significant impact on the NO formation pathways.

This association may be a potential cause for the first peak bell shape NO curve elicited by the Tian mechanism apart from contributions from the radicals H, O, and OH.

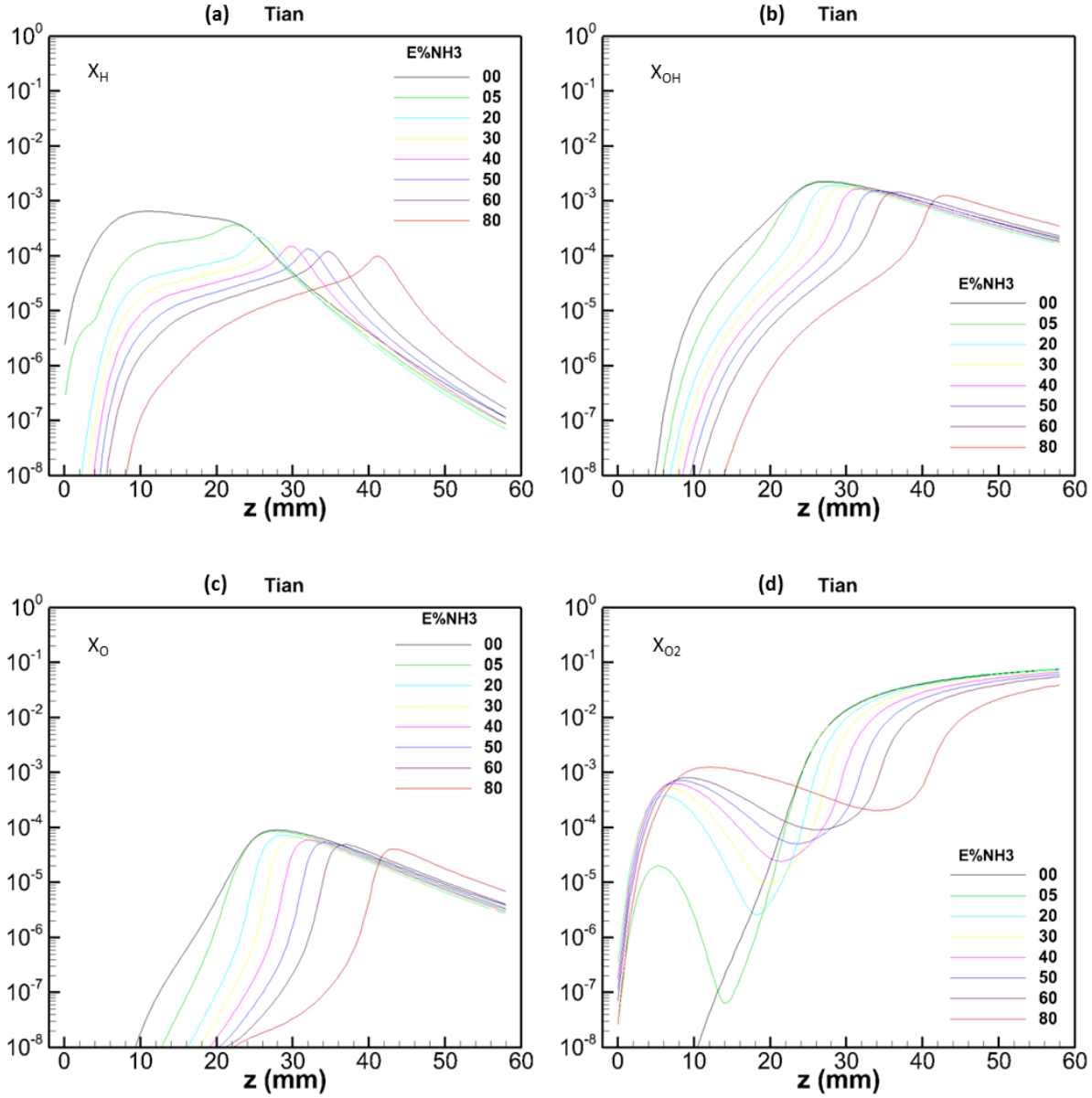

Fig. 5.20. Centerline profiles of predicted mole fractions of species like (a) H, (b) OH, (c) O and (d) O_2 with varying NH_3 seeding level from E%NH_3 = 0 to 80, for the Tian mechanism.

5.5.4 Reaction rate analyses

The NO production and decomposition pathways in the Tian mechanism are displayed in Tables 5.3 and 5.4 respectively, with corresponding rate parameters. The reaction rates of all the NO production and decomposition reactions for the Tian mechanism are estimated within the computational domain, based on the rate parameters shown in the following tables.

Table 5.3. NO production pathways for the Tian mechanism. A = pre-exponential factor, b = pre-factor and E_a = activation energy.

Rxn #	Reaction	Rate parameters		
		A	b	E_a
304	$HNO+H \leftrightarrow NO+H_2$	4.40E+11	0.72	650
305	$HNO+O \leftrightarrow NO+OH$	2.30E+13	0	0
306	$HNO+OH \leftrightarrow NO+H_2O$	3.60E+13	0	0
307	$HNO+O_2 \leftrightarrow HO_2+NO$	2.00E+13	0	16000
309	$HNO+NO_2 \leftrightarrow HONO+NO$	4.40E+04	2.64	4040
315	$NO_2+H \leftrightarrow NO+OH$	1.30E+14	0	362
316	$NO_2+O \leftrightarrow NO+O_2$	1.10E+14	-0.52	0
323	$2NO_2 \leftrightarrow NO+NO+O_2$	4.50E+12	0	27599
324	$2NO_2 \leftrightarrow NO3+NO$	9.60E+09	0.73	20900
326	$HONO+H \leftrightarrow NO+H_2O$	8.10E+06	1.89	3850
329	$HONO+NO_2 \leftrightarrow HONO_2+NO$	2.00E+11	0	32700
330	$2HONO \leftrightarrow NO+NO_2+H_2O$	3.50E-01	3.64	12140
338	$NO3+NO_2 \leftrightarrow NO+NO_2+O_2$	5.00E+10	0	2940
346	$N_2O+O \leftrightarrow NO+NO$	9.20E+13	0	27679
349	$N_2O+OH \leftrightarrow HNO+NO$	1.20E-04	4.33	25080
369	$NH_2+HNO \leftrightarrow NH_3+NO$	3.60E+06	1.63	-1250
374	$NH_2+NO_2 \leftrightarrow H_2NO+NO$	6.50E+16	-1.44	268
376	$NH+O \leftrightarrow NO+H$	9.20E+13	0	0
380	$NH+O_2 \leftrightarrow NO+OH$	1.30E+06	1.5	100
388	$N+OH \leftrightarrow NO+H$	3.80E+13	0	0
389	$N+O_2 \leftrightarrow NO+O$	6.40E+09	1	6280
395	$NNH+O \leftrightarrow NH+NO$	5.00E+13	0	0
413	$N_2H_3+O \leftrightarrow NH_2+NO+H$	3.00E+13	0	0
425	$N_2H_2+O \leftrightarrow NH_2+NO$	1.00E+13	0	0
435	$H_2NN+O \leftrightarrow NH_2+NO$	7.00E+13	0	0
437	$H_2NN+OH \leftrightarrow NH_2+NO+H$	2.00E+12	0	0
438	$H_2NN+HO_2 \leftrightarrow NH_2+NO+OH$	9.00E+12	0	0

Based on the reaction rate analyses, contributions of various pathways toward NO production within 10 mm region from the tube exit for cases E%NH_3 = 5 and 50 are displayed in Fig. 5.21. For example, for HNO pathways, only Rxns 304 (magnitude $\sim 10^{1.8}$) and 307 ($\sim 10^{0.4}$) are dominant. NO_2 pathways for Rxns 315 and 323 play a minor role in NO production. The contribution of NH_2, NH and N species via Rxns 380 and 389 are on the order of $\sim 10^{1.0}$ for NO production. In contrast, contributions towards NO production within the 10 mm region from the tube exit are negligible for pathways controlled by species such as HONO, NNH, N_2O, N_iH_i and H_2NN.

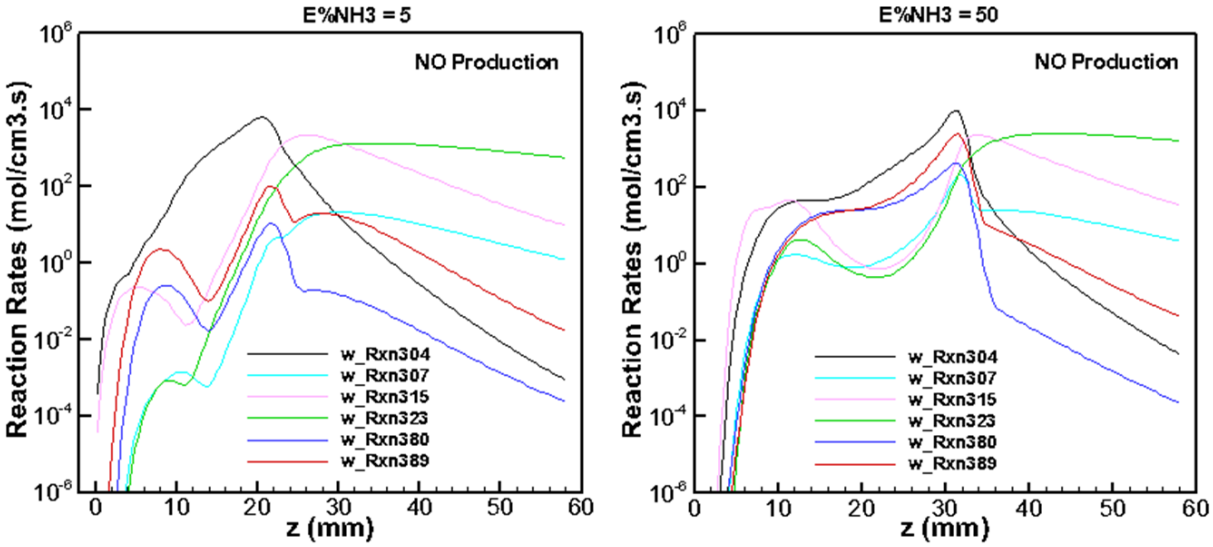

Fig. 5.21. Reaction rates for key NO production pathways for Tian mechanisms for NH_3 seeding level (a) E%NH_3 = 5 and (b) E%NH_3 = 50.

Table 5.4. NO decomposition pathways for the Tian mechanism. A = pre-exponential factor, b = pre-factor and E_a = activation energy.

Rxn #	Reaction	Rate parameters		
		A	b	E_a
310	$NO+H(+M)\leftrightarrow HNO(+M)$	1.50E+15	-0.41	0
311	$NO+O(+M)\leftrightarrow NO_2(+M)$	1.30E+15	-0.75	0
312	$NO+O(+AR)\leftrightarrow NO_2(+AR)$	1.30E+15	-0.75	0
313	$NO+OH(+M)\leftrightarrow HONO(+M)$	1.10E+14	-0.3	0
314	$NO+O_2\leftrightarrow NO_2+OH$	2.10E+12	0	497
350	$N_2O+NO\leftrightarrow NO_2+N_2$	5.30E+05	2.23	46280
370	$NH_2+NO\leftrightarrow N_2+H_2O$	2.80E+20	-2.654	1258
371	$NH_2+NO\leftrightarrow NNH+OH$	2.30E+10	0.425	814
383	$NH+NO\leftrightarrow N_2O+H$	2.90E+14	-0.4	0
385	$NH+NO\leftrightarrow N_2+OH$	2.20E+13	-0.23	0
390	$N+NO\leftrightarrow N_2+O$	2.10E+13	0	0
401	$NNH+NO\leftrightarrow N_2+HNO$	5.00E+13	0	0
429	$N_2H_2+NO\leftrightarrow N_2O+NH_2$	4.00E+12	0	11922
451	$H_2NO+NO\leftrightarrow HNO+HNO$	2.00E+04	2	13000

Similarly, the rate of reactions for NO decomposition pathways (Table 5.4) are estimated along the centerline axis for the Tian mechanism for both E%NH_3 = 5 and 50 cases. As shown in Fig. 5.22, several key reactions are identified as responsible for NO decomposition within a 10 mm region from the tube exit for both cases. For example, NO decompositions by H (Rxn 310) and OH (Rxn 313) radicals are the most dominant pathways with an order of magnitude $\sim 10^{2.5}$ and $10^{1.2}$, respectively, for both E%NH_3 = 5 and 50 (Fig. 5.22). Amine radicals (NH_2, NH) are observed to be significant contributors to NO decomposition via Rxns 370, 371, 383 and 385, with equivalent magnitude order in a range of $\sim 10^{1.2}$. On the contrary, contributions towards NO decomposition via other reaction pathways (Table 5.4) are negligible.

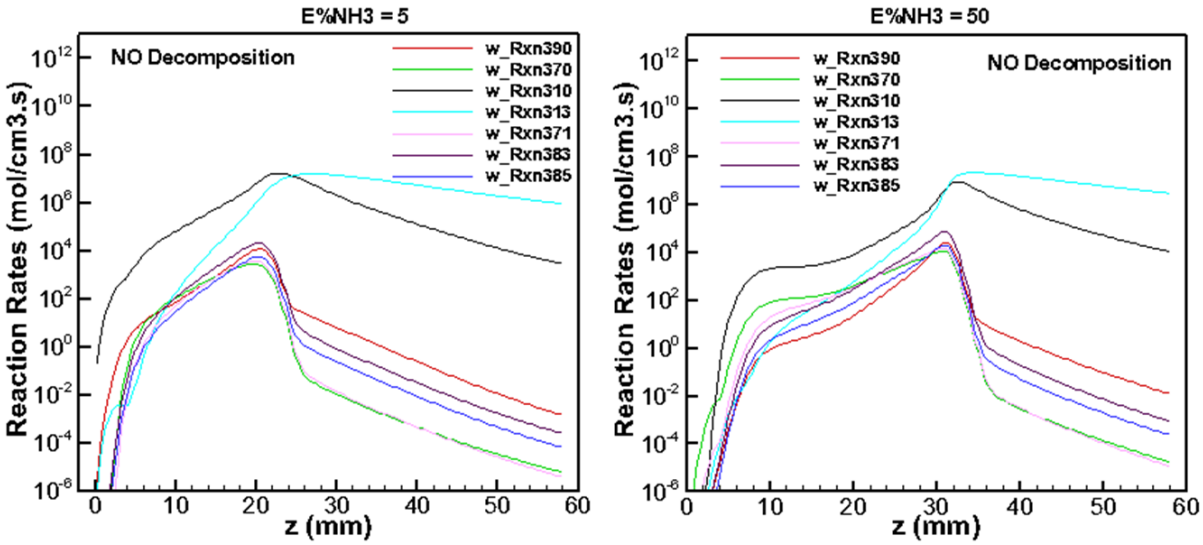

Fig. 5.22. Reaction rates for key NO decomposition pathways for Tian mechanisms for NH_3 seeding level (a) E%NH_3 = 5 and (b) E%NH_3 = 50.

5.5.5 Effects of key reactions on NO formation

Analysis of the reaction rates of all the NO production and decomposition reactions (Tables 5.3 and 5.4), indicates that major critical reactions have relatively higher reaction rates within the 10 mm region from the tube exit, as shown in Figs 5.21 and 5.22. The individual effects of each important NO production and decomposition pathway on the NO formation (or simulated NO PLIF) trend by the Tian mechanism are studied. For each individual NO pathway effects, simulated NO-PLIF counts are estimated by the CFD simulation using the Tian mechanism, by disabling the NO pathway. With this method, the effects of a total of 24 reaction pathways on the NO formation are investigated (Rxn 304 to 390), including three pathways of O_2 formations via Rxns 5.1, 5.2 and 5.3, due to their low activation energies. Reaction pathways of O_2 formation in the Tian mechanism are analyzed based on the observed trend of O_2 formation along the centerline, which is similar to simulated NO PLIF by the Tian mechanism.

$$H + O_2(+M) \Leftrightarrow HO_2(+M) \quad \text{(Rxn \# 5.1)}$$

$$HO_2 + O \Leftrightarrow OH + O_2 \quad \text{(Rxn \# 5.2)}$$

$$HO_2 + OH \Leftrightarrow H_2O + O_2 \quad \text{(Rxn \# 5.3)}$$

5.5.5.1 Axial direction

In Fig. 5.23, among all the NO production pathways via HNO, only Rxn 304 affected the NO trend, with relatively higher NO concentrations within 10 mm region from the exit for E%NH_3 = 5. As noted in Fig. 5.23, suppressing NO decomposition pathway Rxns 311 and 314 showed significant reduction in NO in the proximity of the tube burner and subdued NO magnitude in the post flame region. Pathways including NH_i, N_2O, H_2NN, thermal NO, and free radicals H and OH, have a relatively insignificant affect over NO formation for E%NH_3 = 5. Unexpectedly, reaction pathways of O_2 formation (Rxns 5.1, 5.2 and 5.3) have negligible effects on the NO trend as well as for E%NH_3 = 5.

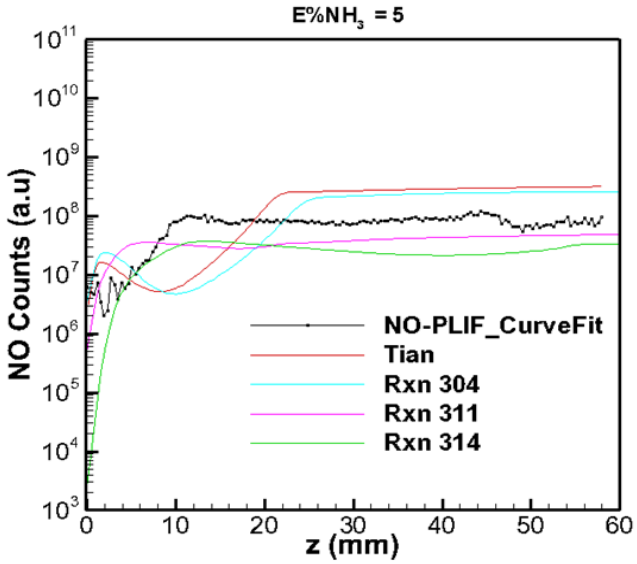

Fig. 5.23. Predicted NO counts profiles by suppressing Reactions 304, 311 and 314 for Tian mechanisms with predicted NO profile by original Tian mechanism and compared with experimental NO-PLIF counts for case E%NH_3 = 5.

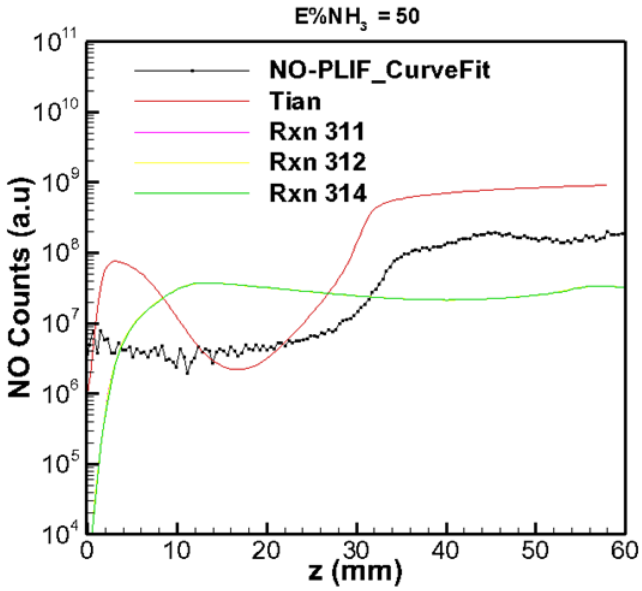

Fig. 5.24. Predicted NO counts profiles by suppressing Reactions 311, 312 and 314 for Tian mechanisms are shown along with predicted NO profile by original Tian mechanism and compared with experimental NO-PLIF counts for case E%NH_3 = 50.

Figure 5.24 shows the predicted NO count profiles created by suppressing Rxns 311, 312 and 314 for the Tian mechanism for E%NH_3 = 50, located along the centerline. For E%NH_3 = 50, most of the reaction pathways exhibited similar affects over NO formation as observed for case E%NH_3 = 5, with minor differences. Suppression of Rxns 311, 312 and 314 exhibits similar axial NO profiles and underpredicts NO by more than two orders of magnitude compared to the experimental data. The trends show significant deviation from the experimental NO-PLIF data. Similar to E%NH_3 =5, the effects of O_2 production pathways via Rxns 5.1, 5.2 and 5.3 are found negligible for E%NH_3 = 50.

5.5.5.2 Radial direction

The effects of suppression of critical NO kinetics pathways on NO profiles along the radial direction at an axial location of 20 mm away from the tube burner are illustrated and

compared with the original Tian mechanism and the experimental NO-PLIF data for both $E\%NH_3 = 5$ and 50.

As noted from Fig. 5.25, for $E\%NH_3 = 5$, the radial NO profile from the original Tian mechanism is in reasonable agreement with the experimental NO-PLIF data, and has significantly overpredicted values from 3-9 mm along the entire radial distance. Among the entire Tian NO chemistry set, Rxns 304, 311, 312 and 314 are the most influential for the NO chemistry as illustrated by the significant changes in radial NO profiles. With Rxn 304, the simulated NO signal closes toward the experimental NO-PLIF within 2 mm, but significantly overpredicts the rest of the radial distance, thus indicating no favorable NO agreement with the experimental data. However, deactivation of reactions 311, 312 and 314 displayed relatively better agreement of the NO trend with the NO-PLIF.

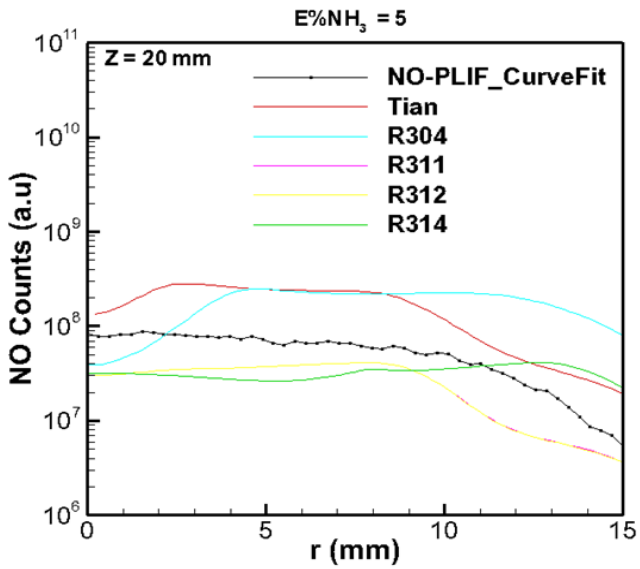

Fig. 5.25. Predicted radial NO counts profiles by suppressing Reactions 304, 311, 312 and 314 for Tian mechanisms are shown along with predicted NO profile by original Tian mechanism and compared with experimental NO-PLIF counts for case $E\%NH_3 = 5$ at 20 mm axial position.

Similar to centerline comparisons, the pathways involving NH_2, NH, N_2O and free radicals don't significantly affect the NO trend. O_2 generation pathways via Rxns 5.1, 5.2 and 5.3 exhibited negligible effects on NO production or decomposition.

Figure 5.26 shows the comparison of NO trends obtained by deactivating Rxns 304, 311, 312 and 314, with the original Tian mechanism, along the radial direction at 20 mm axial distance for $E\%NH_3 = 50$. The original Tian mechanism is in reasonable agreement with NO-PLIF in near centerline region and significantly overpredicts in the high flame temperature zone. Unlike $E\%NH_3 = 5$, many NO pathways are activated in the NO chemistry as observed by changes in radial NO profiles by deactivation of those chemical pathways in the original Tian mechanism. Reactions 304, 311, 312 and 314 have pronounced effects on the Tian's NO profile, however, comparable effects are noted for NO production via NH_2 pathways (315, 316, 323, 326). In contrast, to the case of $E\%NH_3 = 5$, O_2 production pathways 5.1, 5,2 and 5.3 have similar effects as Rxn 304, along the radial direction for $E\%NH_3 = 50$.

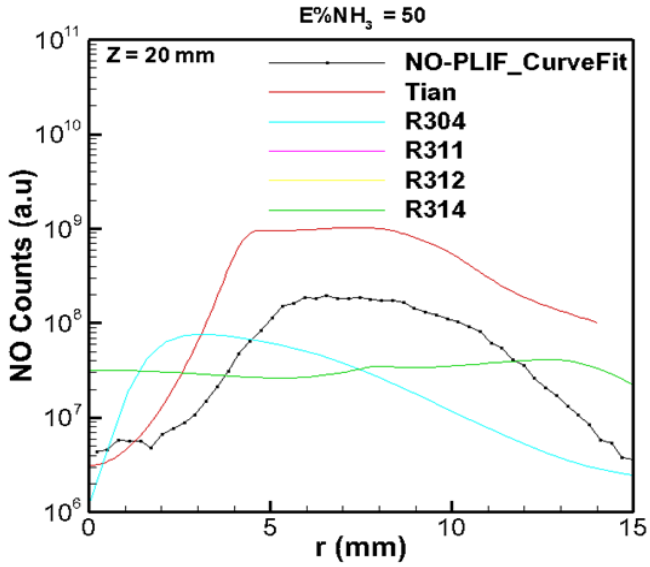

Fig. 5.26. Predicted radial NO counts profiles by suppressing Reactions 304, 311, 312 and 314 for Tian mechanisms are shown along with predicted NO profile by original Tian mechanism and compared with experimental NO-PLIF counts for case $E\%NH_3 = 50$ at 20 mm axial position.

5.6 Conclusions

Detailed study of NO chemistry is performed with various levels of ammonia seeding in H_2/NH_3 laminar diffusion flames by comparing the *in-situ* quantitative 2-D NO measurements via planar laser-induced fluorescence with predicted 2-D NO contours by CFD modeling with the UNICORN code using the Tian, GRI-Mech3.0, and new modified GRI-Mech3.0 (Mod. GRI-Mech) chemical mechanisms. A CH_4-air laminar premixed calibration flame seeded with NO range from 0 – 600 ppm at equivalence ratio 0.8, is used at identical experimental settings to obtain a relationship between *in-situ* signal intensity with NO concentrations in the flame. PLIF signals are corrected for background noise, laser energy, beam profile, Boltzmann fraction distribution and quenching of the NO signal by major species. From NO contour map comparisons, the flame length predictions and the qualitative distribution of NO in the entire flame domain is in relatively good correlation with the experimental NO-PLIF data for the Tian mechanism, followed by the modified GRI-Mech3.0 mechanism.

Comparison of *in-situ* NO measurements with the simulated NO-PLIF signals ($S_{f,Computational}$) for the three chemical mechanisms along the centerline and radial axes for the entire range of NH_3 seeding from E%NH_3 = 0 to 80 the predicted NO profiles as well as the flame structure by the Tian mechanism are in reasonable agreement with the experimental NO-PLIF data, followed by the he modified GRI-Mech3.0 mechanism. Along the centerline axis, the discrepancy is within 10 mm near the tube burner exit where the Tian mechanism is observed to produce a local NO peak (bell shape curve), in contrast to the more gradually increasing experimental NO-PLIF data. On the contrary, the GRI-Mech3.0 mechanism is in

poor overall agreement with the experimental flame length trend and NO concentration distribution along both the centerline and radial axis.

Interestingly, improved and reasonable agreement of simulated NO-PLIF data with the *in-situ* NO measurements, as well as flame length, are recorded for the modified GRI-Mech3.0 mechanism, which is proposed to simplify the chemistry for NH_3 seeded flames from previous studies (Chapter 4). Overall, the modified GRI-Mech3.0 failed to predict the accurate NO distribution in lower flame temperature zones. However, it is in reasonable agreement with the experimental data, as well as the Tian mechanism's NO predictions in the post-flame region and the lean side of the flame along the centerline and the radial axes, respectively, for all levels of ammonia seeding ($E\%NH_3$ = 0 to 80). Among the three chemical mechanisms, the Tian mechanism is superior in predicting NO trends.

The reaction kinetics studies, utilizing the Tian mechanism, are used to investigate the cause of the first peak in NO (bell shape curve) along the centerline axis. The most critical NO production and decomposition pathways are narrowed dfrom the Tian NO pathways. The effect of each critical NO pathway for the original Tian mechanism are analyzed for two cases, $E\%NH_3$ = 5 and 50. Reactions 304, 311, 312 and 314 have the most pronounced effects on NO chemistry compared to other reactions. However, none of the reactions contribute sufficiently to be identified as the cause of the local NO peak generation for the Tian mechanism for $E\%NH_3$ = 5 and 50. Based on the NO reaction path analysis, simultaneous deactivation of multiple pathways for NO production and decomposition is suggested as the cause of the local NO peak structure, rather than individual pathway deactivation. This is due to the inherent complexity involved in NO chemistry under ammonia seeding conditions.

5.7 References

[1] K. Kohse-Höinghaus. Laser techniques for the quantitative detection of reactive intermediates in combustion systems. Prog. Energy Combust. Sci. 1994;20:203–279.

[2] Eckbreth AC. Laser diagnostics for combustion temperature and species. Hartford, Connecticut: Gordon and Breach, 1996.

[3] Eckbreth AC, Bonczyk PA, Verdieck JF. Progress in Energy and Combustion Science 1979;15:253–322.

[4] Chraplyvy JH. Proc. IEEE 1982;70(658):253–322.

[5] Hirano A, Tsujishita M. The imaging diagnositics of flames by means of planar laser-induced fluorescence. In: 16th meeting on lightwave sensing technology, vol. 29. Osaka 554, Japan: 1997.

[6] Demory R, Crua C, Martin RG, Morgan RH. Measuring and processing in-cylinder distributions of NO and OH obtained by laser-induced fluorescence in a diesel rapid compressions machine. In: 13th international symposium on applications of laser techniques to fluid mechanics. 2006.

[7] Aoyagi Y, Kamimoto T, Matsui Y, Matsuoka S. A gas sampling study on the formation processes of soot and NO in a DI diesel engine. SAE Technical Paper 1980;(800254).

[8] Andresen P, Meijer G, Schlüter H, Voges H, Koch A, Hentschel, W, Oppermann W, Rothe E. Fluorescence imaging inside an internal combustion engine using tunable excimer lasers. Applied Optics 1990;29:2392-2404.

[9] Alatas B, Pinson JA, Litzinger TA, Santavicca DA. A study of NO and soot evolution in a DI diesel engine via planar imaging. SAE Paper 930973 1993.

[10] Arnold A, Dinkelacker F, Heitzmann T, Monkhouse P, Schäfer M, Sick V, Wolfrum J, Hentschel W, Schindler KP. DI diesel engine combustion visualized by combined laser techniques. 24th International Symposium on Combustion. 1992.

[11] Ravikrishna RV, Laurendeau NM. Laser-induced fluorescence measurements and modeling of nitric oxide in methane–air and ethane–air counterflow diffusion flames. Combustion and Flame 2000;120(3):372-382.

[12] Lutz AE, Kee RJ, Grcar JF. Oppdif: a fortran program for computing opposed-flow diffusion flames. 1996.

[13] GRI-Mech web site http://www.me.berkeley.edu/gri-mech.

[14] Thomsen DD, Laurendeau NM. LIF measurements and modeling of nitric oxide concentration in atmospheric counterflow premixed flames. Combustion and Flame 2001;124(3):350-369.

[15] Cooper CS, Laurendeau NM. Parametric study of NO production via quantitative laser-induced fluorescence in high-pressure, swirl-stabilized spray flames. Combustion 2000;28:287-293.

[16] Cooper CS, Laurendeau NM. Quantitative measurements of nitric oxide in high-pressure (2–5 atm), swirl-stabilized spray flames via laser-induced fluorescence. Combustion and Flame 2000;123(1):175-188.

[17] Hahn WA, Wendt JOL. NO_x formation in flat, laminar, opposed jet methane diffusion flames. Eighteenth Symposium (Int.) on Combustion, The Combustion Institute 1981;18(1):121-131.

[18] Battles BE, Hanson RK. Laser-induced fluorescence measurements of NO and OH mole fraction in fuel-lean, high-pressure (1-10atm) methane flames: fluorescence modeling and experimental validation. J. Quant. Spectrosc. Radiat. Transfer 1995;54:521-537.

[19] Paul PH, Gray JA, Durant JL, Thoman JW. Applied Physics 1993;57:249.

[20] Paul PH. JQSRR 1994;51:511.

[21] Ratner A, Pun W, Palm SL, Culick FEC. Phase-resolved NO planar laser-induced fluorescence of a jet flame in an acoustic chamber with excitation at frequencies 60 hz 2002;29:85-90.

[22] Barlow RS, Carter CD. Raman/Rayleigh/LIF measurements of nitric oxide formation in turbulent hydrogen jet flames. Combustion and Flame 1994;97(3-4):261-280.

[23] Barlow RS, Fiechtner GJ, Chen JY. Oxygen atom concentrations and NO production rates in a turbulent H_2/N_2 jet flame. Symposium (International) on Combustion 1996;26(2):2199-2205.

[24] Barlow RS, Karpetis AN, Frank JH, Chen JY. Scalar profiles and NO formation in laminar opposed-flow partially premixed methane/air flames. Combustion and Flame 2001;127(3):2102-2118.

[25] Miller JA. Sandia national laboratories, personal communication of electronic file for mechanism, (Sept, 2000).

[26] Cattolica RJ, Cavolowsky JA, Mataga TG. Laser-fluorescence measurements of nitric oxide in low-pressure H_2/O_2/NO flames. Symposium (International) on Combustion 1989;22(1):1165-1173.

[27] Driscoll JJ, Sick V, Schrader PE, Farrow RL. Measurements of NO distributions and fluorescence lifetimes in a non-premixed counterflow CH_4/air flame using picosecond time-resolved laser-induced fluorescence 2002;29:2719-2726.

[28] Bessler WG, Schulz C, Lee T, Jeffries JB, Hanson RK. Strategies for laser-induced fluorescence detection of nitric oxide in high-pressure flames. A-X (0, 0) excitation. Applied Optics, 2002;41(18):3547-3557.

[29] Hanson RK. Combustion diagnostics: planar imaging techniques. Twenty-first Symposium on Combustion 1986:1677-1691.

[30] Lee T, Jeffries JB, Hanson RK. Experimental evaluation of strategies for quantitative laser-induced-fluorescence imaging of nitric oxide in high-pressure flames (1–60bar). Proceedings of the Combustion Institute 2007;31(1):757-764.

[31] Powell OA, Papas P, Dreyer CB. Flame structure measurements of NO in premixed hydrogen–nitrous oxide flames. Proceedings of the Combustion Institute 2011;33(1):1053-1062.

[32] Bell JB, Day MS, Grcar JF, Bessler WG, Schulz C, Glarborg P, Jensen AD. Detailed modeling and laser-induced fluorescence imaging of nitric oxide in a NH_3-seeded non-premixed methane/air flame. Proceedings of the Combustion Institute 2002;29(2):2195–2202.

[33] Rahinov I, Goldman A, Cheskis S. Absorption spectroscopy diagnostics of amidogen in ammonia-doped methane/air flames. Combustion and Flame 2006;145(1-2):105-116.

[34] Venizelos DT, Sausa RC. Detailed chemical kinetics studies of an NH_3/N_2O/Ar flame by laser-induced fluorescence. Mass spectrometry and modeling 2000;28:2411-2418.

[35] Sick V, Hildenbrand F, Lindstedt P. Quantitative laser-based measurements and detailed chemical kinetic modeling of nitric oxide concentrations in methane-air counterflow diffusion flames. Symposium (International) on Combustion 1998;27(1):1401-1409.

[36] Katta VR, Roquemore WM. Role of flow visualization in the development of unicorn. In: Proceedings of vsj-spie98. 1998. p. 1-6.

[37] Katta VR, Forlines RA, Roquemore WM, Anderson WS, Zelina J, Gord JR, Stouffer SD, Roy S. Experimental and computational study on partially premixed flames in a centerbody burner. Combustion and Flame 2011;158(3):511-524.

[38] Katta VR, Goss L, Roquemore WM. Effect of non-unity Lewis number and finite-rate chemistry on the dynamics of a hydrogen-air jet diffusion flame. Systems research 1994;74:60-74.

[39] Carter CD, Barlow RS. Simultaneous measurements of NO, OH and the major species in turbulent flames. Optics Letters 1994;19(4):299-301.

[40] Luque J, Crosley DR. LIFBASE: database and spectral simulation (version 1.5). 1999.

[41] McDermid S, Laudenslager JB. J. Quant. Spectrosc. Radiat. Transf. 1982;27:483.

[42] Tamura M, Berg PA, Harrington JE, Luque J, Jeffries JB, Smith GP, Crosley DR. Collisional quenching of CH(a), OH(a), and NO(a) in low pressure hydrocarbon flames. Combustion and Flame 1998;114(3-4):502-514.

[43] Dagaut P, Lecomte F, Chevailler S, Cathonnet M. Experimental and detailed kinetic modeling of nitric oxide reduction by a natural gas blend in simulated reburning conditions. Combustion Science and Technology 1998;139(1):329-363.

[44] Sick V. Deriving quantitative concentration distributions from planar laser-induced fluorescence measurements in engines. J. Flow Visualization & Image Processing 1999;6(4):313-331.

[45] Mokhov AV, Levinsky HB, Van Der Meij CE. Temperature dependence of laser-induced fluorescence of nitric oxide in laminar premixed atmospheric-pressure flames. Applied Optics 1997;36(15):3233-3243.

[46] Berg PA, Smith GP, Jeffries JB, Crosley DR. Nitric oxide formation and reburn in low-pressure methane flames. Proc. 27th Int. Symp. Combust. 1998;1:1377-1384.

[47] Li M. A numerical and experimental study of *in-situ* NO formation in laminar NH_3-seeded syngas diffusion flames. Iowa State University, 2011.

[48] Burke SP, Schumann TEW. Diffusion flames. Industrial & Engineering Chemistry Research 1928;20(10):998-1004.

[49] Fay JA. The distributions of concentration and temperature in a laminar jet diffusion flame. Journal of Aeronautical Sciences 1954;21:681-689.

CHAPTER 6. GENERAL CONCLUSIONS

6.1 General discussions

Based on the potential for the use of ammonia (NH_3) as a zero-carbon fuel, it is considered as a potential sustainable energy resource. However, ammonia as a fuel poses severe challenges due to its low reactivity and tendency to produce significant amounts of NO_x in flames. In this dissertation, two major aspects of anhydrous ammonia combustion are explored. First is the development of strategies and burner designs to achieve pure ammonia combustion up to a heat rate of ~40 kW and with an ultra-low emissions in a swirl-stabilized turbulent flame. Second is the study of NO_x formation and decomposition pathways in NH_3 seeded H_2 flames. The fundamental flame studies are supported by the state-of-the-art tools and techniques, such as CHEMKIN flame speed, reaction path and sensitivity analyses; numerical simulations of 2-D flame structure by CFDC (Computational Fluid Dynamics with Chemistry) using the UNICORN (UNsteady Ignition and COmbustion with ReactioNs) code, and *in-situ* NO measurements by planar laser-induced fluorescence (PLIF) of NO, for H_2/NH_3 fuel mixtures.

In Chapter 2, an extensive parametric, application based study of combustion of ammonia (vapor NH_3) mixtures with contemporary fuels e.g., H_2 and CH_4, is detailed in a 40 kW, turbulent, swirl-stabilized domestic oil heating furnace. Parameters studied include (a) air temperature, (b) equivalence ratio, (c) heat-rate, (d) nozzle position, (e), swirl effects, and (f) burner geometry, which are varied to optimize the flame stability for both H_2/NH_3 and CH_4/NH_3 fuel. From these experiments, it is observed that the flame-holder burner geometry helps to achieve higher $E\%NH_3$ levels, lower NO_x emissions, and lower NH_3 slip.

Significantly greater mixing of fuel and air facilitates a reduction of NO created by remaining NH_3 in the mixing zone for the case with the flame-holder. In this case, near stoichiometric conditions are also superior to fuel-line conditions when using a flame holder… An optimized set of parameters is identified and along with a custom-designed fuel nozzle is used to achieve a pure NH_3 flame ($E\%NH_3 = 100$) with an ultra-low NO_x (3-5 ppm), although with significantly higher NH_3 slip (800-1300 ppm) without air preheating.

To understand the chemical kinetics of NO and NH_3 interactions in H_2/NH_3 flames, fundamental flame studies of the H_2/NH_3 fuel mixture are conducted under both premixed and diffusion flame conditions. In Chapter 3, flame speed measurements for H_2-NH_3-Air mixtures in a laminar jet flame configuration are compared with the flame speed predictions using the Tian, Konnov and GRI-Mech3.0 chemical mechanisms in a 1-D, laminar, freely propagating flame speed model in CHEMKIN PRO 4.0 for both adiabatic and non-adiabatic flame conditions. Cases include equivalence ratios of 0.5 to 1.1 and NH_3 as a percent of the energy in H_2 of $E\%NH_3 = 0$ (pure H_2-Air), 20, 50 and 80. The Tian and Konnov mechanisms are found to be in fairly good agreement for lower and higher range of $E\%NH_3$. Conversely, GRI-Mech3.0 consistently failed to capture the experimental flame speed trends for all ammonia doped flames. More importantly, the radical mole fractions have strong implications on the predicted flame speeds, inferring that it is critical for a chemical mechanism to predict accurate radical concentrations in order to predict an accurate flame structure.

After analysis of the effects of flame radicals on the flame speeds of the H_2/NH_3 laminar premixed flame, analysis of the effects of radical concentrations on NO chemistry via NO

production and decomposition pathways in NH_3 seeded flames is conducted. In Chapter 4, a numerical study of laminar premixed H_2-NH_3-air flames is conducted to compare the NO and NH_3 reaction kinetics among the (1) Tian, (2) Konnov and (3) GRI-Mech3.0 chemical mechanisms for the same flow conditions and to identify and resolve the key sources of disagreement among the chemical mechanisms. Both sensitivity and rate of production analyses are performed to determine the relative contributions of various precursors, radical species, and reaction pathways to NO and NH_3 production and destruction in the flame zone. Based on the sensitivity and rate of production analyses, significant differences in NO decomposition pathways are observed between the Tian and GRI-Mech3.0 mechanisms, which widen with increasing NH_3 seeding levels in H_2/NH_3 flames where disagreements are noted in both NO production and decomposition reactions. A modified GRI-Mech3.0 (Mod. GRI-Mech) mechanism with 328 reactions and 53 species is proposed. The new mechanism verifies the key role of these reactions in net NO production and displays improved agreement for lean and rich conditions.

Comprehensive validation of the contemporary chemical mechanisms, i.e., the Tian, GRI-Mech3.0 and the newly proposed modified GRI-Mech3.0 (Mod. GRI-Mech) chemical mechanism is performed using 2-D *in-situ* NO-PLIF measurements in laminar H_2/NH_3 diffusion flames with varying amounts of NH_3 content ($E\%NH_3$ = 0 to 80). The data are quantitatively compared with the corresponding computational 2-D NO concentration predictions from the UNICORN code by utilizing the above mentioned chemical mechanisms (Chapter 5). Overall, the predicted NO profiles as well as the flame structure predicted by the Tian mechanism are in fairly good agreement with the trends of the

experimental NO-PLIF data. A discrepancy is noted within 10 mm from the tube burner exit along the center line, where the Tian mechanism recorded a local NO peak (bell shape curve), in contrast to the gradually increasing experimental NO-PLIF data. On the other hand, the GRI-Mech3.0 mechanism is in significant disagreement in predicting flame length trends and NO concentration distributions with varying ammonia seeding in H_2-air diffusion flames. Interestingly, improved and reasonable agreement of 2-D NO mapping, as well as flame length, is recorded for the modified GRI-Mech3.0 mechanism with the experimental NO measurements along both the axial centerline and radial directions. These findings support the modifications made to the GRI-Mech3.0 chemical mechanism to build the new modified GRI-Mech3.0 chemical mechanism.

6.2 Future recommendations

From the swirl-stabilized turbulent flame studies in H_2/NH_3 mixtures, for an optimized burner design, 100% ammonia combustion is achieved for a heat rate range of 16 kW without requiring any air preheating with ultra-low levels of NO_x. However, NH_3 slip from the burner system is in a significantly higher range from 900 – 1300 ppm, and is considered a key remaining challenge in practical application of anhydrous ammonia as a fuel.

Continuing improvements in the burner performance include NH_3 preheating prior to injection, utilizing the available combustion heat to support the catalytic decomposition of NH_3 into H_2 and N_2. The NH_3 can be heated up to a sufficiently high temperature, where in the presence of Ni catalyst, partial decomposition of NH_3 would produce higher H_2 content along with N_2. From these experimental studies, H_2 enhances the combustion performance of

NH_3 due to its high reactivity and low ignition temperature. Hence, partial catalytic decomposition of NH_3 is expected to improve the heat-rate range, but more importantly significant abatement in NH_3 slip can be achieved even with NH_3 burning at higher heat rates.

From the flame speed validation method and NO chemistry analyses among the contemporary chemical mechanisms (Tian, Konnov, and GRI-Mech3.0) noted in Chapters 3 and 4 respectively, the sensitivity and reaction path analyses are performed at the peak heat release location of the 1-D premixed H_2/NH_3 flame structures. Effects of radical concentrations on NH_3 and NO decompositions are also investigated at this particular location by assuming that reaction rates would be highest at the peak heat release location. Further studies would provide support for the present assumption if the sensitivity and reaction path analysis can be performed at the other locations of the 1-D flame structures.

As an improved and accurate validation method, the predicted 2-D NO concentrations for the Tian, GRI-Mech3.0 and the modified GRI-Mech3.0 chemical mechanisms (a proposed chemical mechanism from previous work) are compared quantitatively with the *in-situ* NO measurements by using planar laser-induced fluorescence (PLIF). For appropriate comparison, predicted NO concentrations are converted from mole fractions to simulated NO-PLIF signals with arbitrary units in counts by incorporating corrections from the laser beam profile, Boltzmann fraction, optical efficiency and quenching corrections of NO signals by other major species. The quenching corrections for almost all of the major species such as O_2, CO_2, N_2, OH, CO are found from the literature except the NO self-quenching and NH_3 quenching parameters for the NO molecule. It would be of significant importance to measure

the quenching parameters of the NO molecule by NH_3 and NO self-quenching species as the concentrations of both NO and NH_3 are abundant in H_2/NH_3 diffusion flames.

APPENDIX A. UNCERTAINTY ANALYSES

A. 1 Flowrate uncertainty

As described in Chapter 5, experimental *in-situ* NO measurements by planar laser-induced fluorescence (PLIF) had many sources of uncertainty, including laser beam profile, Boltzmann fraction correction, optical efficiency and quenching corrections. Also included is the uncertainty in flow measurements from the mass flow controllers, which are given as $\pm$ 5% of the maximum range as suggested by the manufacturers. To estimate the effects of the mass flow controller uncertainty in simulated NO-PLIF signals, numerical results of the Tian mechanisms are re-run for two new flow rate cases; (1) Uncertainty +5, where the flow rates of each of the species is specified as 5% higher than the set H_2 and NH_3 flow rates for the Tian mechanism simulations and (2) Uncertainty -5, where the flow rates of both the species are set ~ 5% lower than the original set flow rates for simulations by the Tian mechanism.

Figure A.1 shows the simulated NO counts for the set flow rates of H_2 and NH_3 species comparison with both flow rate uncertainty cases; (1) Uncertainty +5 and (2) Uncertainty -5, along the centerline axis for a particular case of 5% NH_3 by energy in H_2 ($E\%NH_3 = 5$). Minor fluctuations within the range of $\pm$ 5% of the flow rates result in significant discrepancy in simulated NO signal by the Tian mechanism, within the region of 10 mm from the tube exit of the burner, along the central axis. Whereas, in the high temperature zone (after approximately 20 mm), no significant affects are observed on the NO concentrations by both plus and minus 5 uncertainty levels. Fig. A.2 shows the percent error for both cases of uncertainties estimated with respect to the Tian results. As noted earlier, the overprediction for both cases was up to 10 times higher in the region of 10 to 20 mm along the centerline axis. On the contrary, for the

high temperature flame zone and fuel lean region, the percentage error is negligible, indicating no effects.

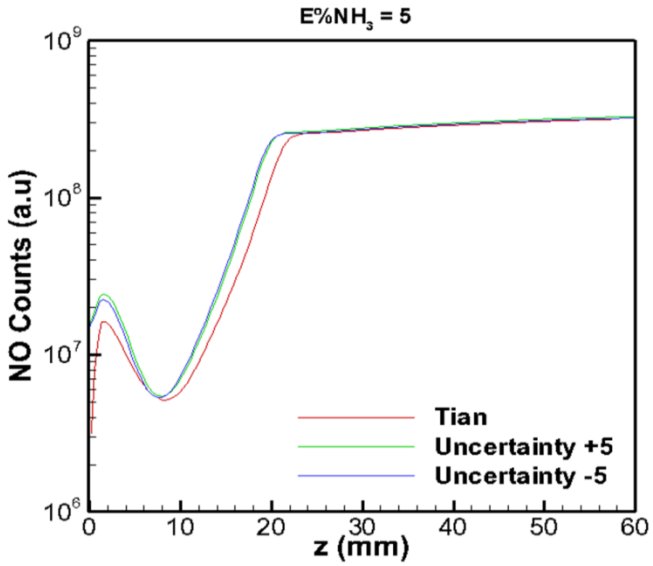

Fig. A.1. Comparison of simulated NO counts with ±5% uncertainty in the flowrates of H_2 and NH_3 along the centerline axis for case E%NH_3 = 5.

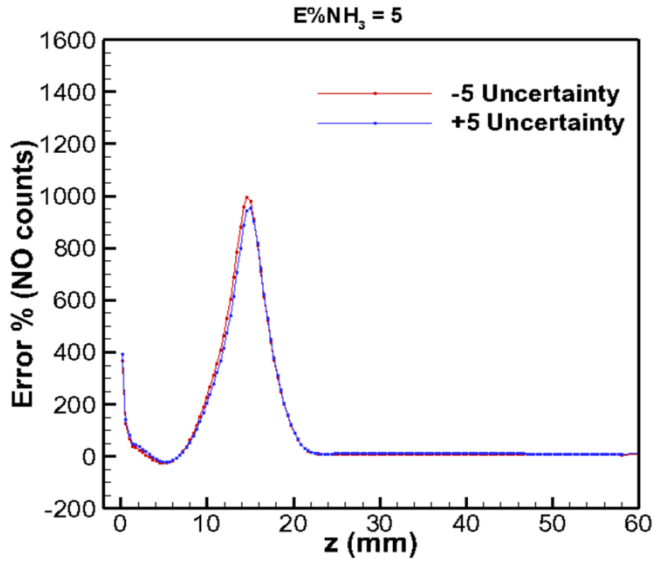

Fig. A.2. The percentage error in simulated NO counts estimated using the Tian mechanism and with ±5% uncertainty in the H_2 and NH_3 flowrates.

From the flow rate uncertainty analysis, the effects of flow rate uncertainties are more prevalent and dominant in the region close to the tube burner exit (within approximately 20

mm) where significant disagreement is observed between the Tian mechanism's simulated NO signal and the *in-situ* NO measurements (shown in Chapter 5). Comparison is made to the high temperature and post flame zone where the flow rate uncertainty effects are negligible for all the cases of NH_3 seeding in H_2/NH_3 laminar diffusion flames.

A. 2 Laser profile uncertainty

For the quantification comparison of *in-situ* NO measurements with simulated fluorescence signal ($S_{f,Computational}$), corrections of laser profiles are incorporated in the experimental *in-situ* NO data. Ideally, the laser profile should be a Gaussian distribution. However, in experimental measurements, the laser profiles were not precisely Gaussian for all the test runs. Thus, an additional curve fitting model was utilized to fit the laser profile for *in-situ* NO normalization ($\frac{S_{f,Experimental}}{E_{laser}}$), where E_{laser} is the laser pulse energy or laser irradiance.

In Fig. A.3, a measured laser profile for the case of E%NH_3 = 5 is plotted and compared with the curve fitting models using 5-Gaussian and 7-Gaussian fitted functions and is expressed in Matlab as:

$$I_{\mathrm{r}} \triangleq \sum_{n=1}^{5-7} a_n \exp\left[-\left(\frac{(x-b_n)}{c_n}\right)^2\right]. \qquad (A.1)$$

For all test runs, the range of Gaussian fitted functions were kept in the range of 5 to 7 for the curve fitting to maintain the R-square above 0.99, which captured the multiple peak or modes in the measured laser profile reasonably well. As seen in Fig. A.3, both 5-Gaussian and 7-Gaussian functions closely replicate the experimentally measured laser profile in the central

region of the domain (axial location from 4 mm to 50 mm) with minor discrepancies near the boundaries.

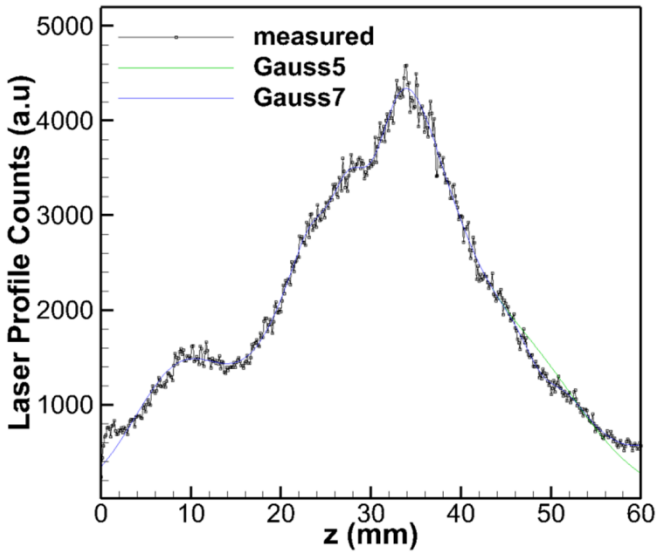

Fig. A.3. Measured laser profile, 5-Gaussian and 7-Gaussian curve fitted profiles.

The % errors in beam profile are plotted in Fig. A.4 for both 5-Gaussian and 7-Gaussian functions compared to the experimental data in Fig. A.3. Figure A.4. shows that both the Gaussian functions exhibit significant % error in range of 30% - 40% within 10 mm from the tube exit. However, the 7-Gaussian function stays fairly constant and within a 10% error. In contrast, the 5-Gaussian function error percent rises to approximately 30%. Overall, the 7-Gaussian curve was chosen for the curve fitting.

From PLIF theory, the laser induced fluorescence signal is directly proportional to the laser profile, as;

$$S_{f,Experimental} \sim E_{laser}$$

The relative uncertainty of $S_{f,Experimental}$ is observed to be directly related to the uncertainty of E_{laser} as expressed in the following;

$$\frac{u\left(S_{f,Experimental}\right)}{S_{f,Experimental}} \propto \frac{u(E_{laser})}{E_{laser}} \tag{A. 2}$$

where $u(\mathrm{z})$ is the uncertainty of quantity "z". The significant error percentage in laser profile curve fitting could possibly be attributed to the relatively large fluctuations of *in-situ* NO signal, $S_{f,Experimental}$ in the proximity of the tube exit.

The uncertainty caused due to temporal fluctuations of the laser profile was not estimated for any of the test runs, as the measured laser sheet profile is a temporal average of laser profiles images.

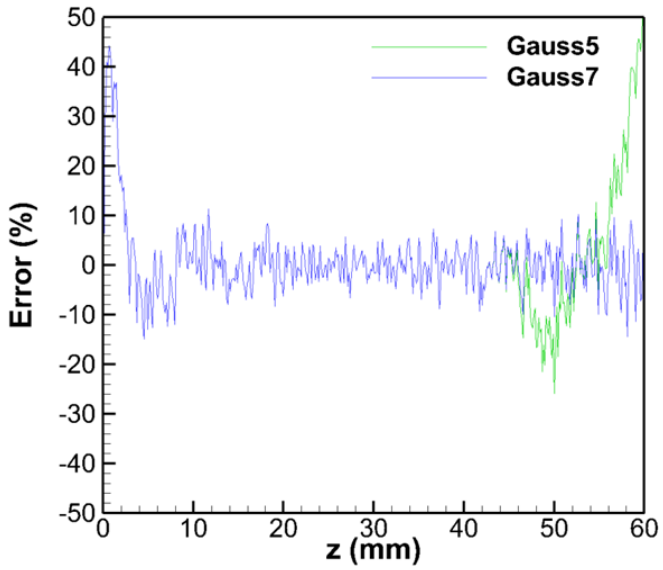

Fig. A.4. The relative spatial error introduced by multi-Gaussian curve fitting.

The relative spatial error introduced by multi-Gaussian curve fitting, with respect to the actual measured beam profile, is calculated and shown in Fig. A.4. This error is encountered within 5% for the entire range of the centerline axis, except in the near tube exit region, where the curve fit profiles overpredict up to 40% higher than the actual beam intensity profile.

A. 3 Boltzmann fraction uncertainty

To ascertain the uncertainty due to Boltzmann fraction corrections applied to convert the numerical 2-D NO mole fractions into NO counts (arbitrary units) for comparison with the experimental *in-situ* NO measurements, the curve fit Boltzmann fraction profile of the NO molecule, as a function of temperature is compared with the LIFBASE database for NO molecule transitions aligned with the 226 nm wavelengths.

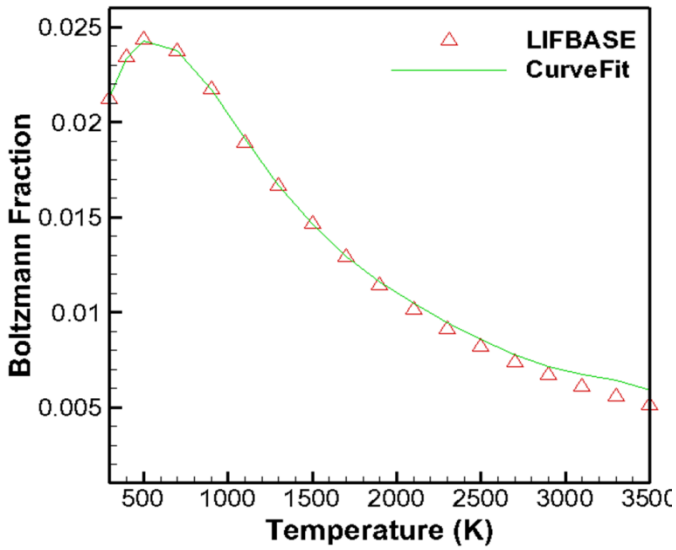

Fig. A.5. Curve fit and LIFBASE Boltzmann fraction profiles as a function of temperature for NO molecule.

It is evident from Fig. A.5 that up to 2500 °K, the curve fit and the LIFBASE data are aligned, with only a slight deviation toward the high temperature limit. Overall, the uncertainty introduced due to Boltzmann fraction approximation is small because the temperature range encountered in the H_2/NH_3 flames stayed well within 2500 °K.

A. 4 Laser power fluctuations

For each test run, laser pulse energy (E_{laser}) is recorded for a duration of five minutes, at the beginning and the end of the test run. For each power measurement recording, mean power

and the standard deviation are recorded. Given two sets of laser pulse energy measurements ($E_{laser,begin}$ & $E_{laser,end}$) for each test run, an overall averaged laser energy (E_{laser}) is estimated by the mean of the two laser energy measurements and the overall standard deviation calculated as;

$$\sigma^2{}_{overall} = \frac{N_1\sigma_1^2 + N_2\sigma_2^2 + N_1\left(E_{laser,begin} - E_{laser}\right)^2 + N_2\left(E_{laser,end} - E_{laser}\right)^2}{N_1 + N_2} \quad (A.3)$$

For example, for test run E%NH_3 = 5, the averaged laser pulse energy and the standard deviation recorded for five minutes duration at the beginning of the test run are shown in eq. A.4.

$$E_{laser,begin} = 0.028W \pm 2.83mW \quad (A.4)$$

Likewise, the averaged laser pulse energy and the standard deviation recorded for five minutes duration at the ending of the test run are shown in eq. A.5.

$$E_{laser,end} = 0.041W \pm 1.53mW \quad (A.5)$$

Hence, the laser pulse energy (E_{laser}) is determined as follows;

$$E_{laser} = \frac{E_{laser,begin} + E_{laser,end}}{2} = 0.0285 \text{ W} \quad (A.6)$$

The overall standard deviation ($\sigma_{overall}$) estimated using equation A.3;

$$\sigma_{overall} = 2.68891\ mW \quad (A.7)$$

For all NO-PLIF measurements of H_2/NH_3 laminar diffusion flames, the 95% accuracy intervals are estimated based on the standard deviations measured.

The averaged laser energy (E_{laser}) is plotted with respect to test runs, i.e. E%NH_3 range from 0% to 80% in Fig. A.6 along with the 95% confidence interval band. It is noticed that the fluctuation in laser energy stayed within 10% of the average energy for all the test runs. Hence,

the uncertainty in NO-PLIF measurements caused due to fluctuations in laser pulse energy is assumed to be negligible.

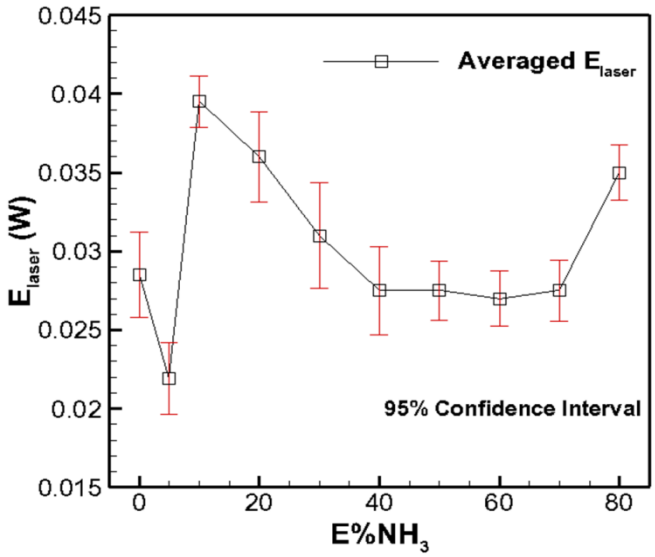

Fig. A.6. Measured average laser beam power for cases of NH_3 seeding ($E\%NH_3$) from 0 to 80s, with 95% confidence interval.

A. 5 NO sensor measurements corrections

To ascertain the uncertainty of NO analyzer in NO measurements for the premixed H_2/NH_3/air flames (Chapter 4) as well as the for the NH_3 seeded H_2/air diffusion flames (Chapter 5), several NO calibration tests are performed on a laminar $CH_4/O_2/N_2$/NO premixed flame at equivalence ratio 1.2 over an eight port tube burner with a total flowrate of 4.4 slpm. To keep the flame from the surrounding drifts, the flame is established in an enclosed aluminum duct and the sampling probe is fixed at a location of 120 mm downstream from the tube exit.

In the established methane-air premixed flames, NO is doped in the flame ranging from 0 – 3400 ppm, and for each doped NO flame, NO and NO_2 measurements are recorded by an IMR analyzer. Figure A.7 displays an $1x\ 1$ comparison of measured NO (X_{NO} measured)

with the doped NO concentration (X_{NO} seeded). The true measured NO mole fraction is considered as the sum of the NO and NO_2 sensor readings, due to a higher possibility of partial NO reburning into N_2/NO_2 for rich ($\emptyset = 1.2$) $CH_4/O_2/N_2/NO$ premixed flame.

From Fig. A.7, it can be observed that up to a 600 ppm NO seeding level, the measured NO by the analyzer is linearly increasing. However, for higher range of NO seeding e.g., 1000 – 3400 ppm, the measured NO is deviating farther away with increasing NO seeding level.

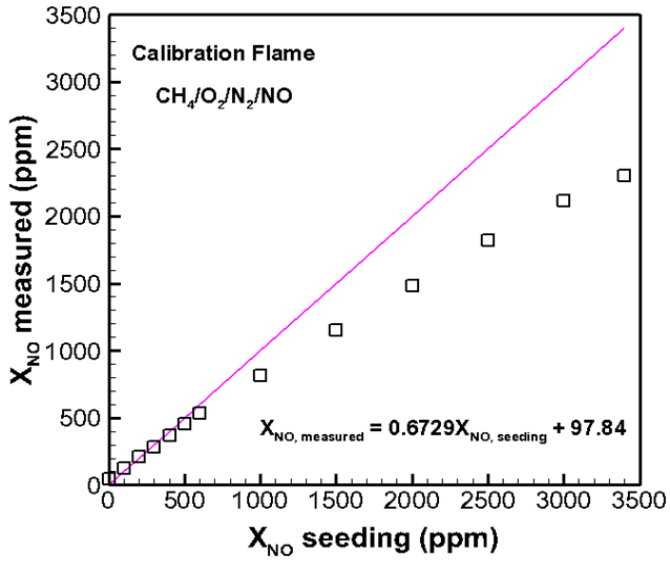

Fig. A.7. Measured NO mole fractions vs. seeded NO concentrations for NO analyzer, established with premixed $CH_4/O_2/N_2/O_2$ laminar flame.

The calibration curve for the NO sensor displayed in Fig. A.7 is later used for correcting the measured NO concentrations by the IMR analyzer for the premixed H_2/NH_3/air flames (Chapter 4). Whereas, NO measurements for the NH_3 seeded H_2/air diffusion flames are recorded to be in the linear region of the calibration curve, thus almost negligible correction factor is needed for the NO measurements.

The NO sensor calibration experiments for the IMR sensor are extended further by cold flow test runs of NO seeding from 0 to 3400 ppm by utilizing a 4906 ppm NO with balance N_2 and a separate N_2 gas bottle at a total flowrate ~ 6 slpm.

For each level of NO seeding, response of NO, NO_2 and O_2 sensors are recorded. Figure A.8 shows the recorded NO comparison to the linear trendline.

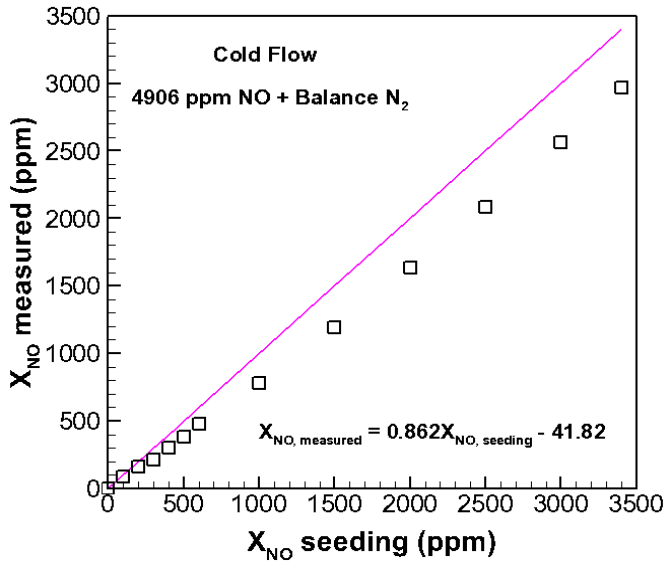

Fig. A.8. Measured NO mole fractions vs. seeded NO concentrations for NO analyzer, established with cold flow of 4906 ppm NO in N_2.

For each cold-flow test run, no dilution of NO and NO_2 is observed as the measured O_2 is recorded as zero from the sensor. Interestingly, the NO_2 sensor displayed readings in the range of one order of magnitude lower than the NO seeding levels throughout the NO seeding test runs. Due to the absence of NO_2 in the seeding mixture and minimal possibility of NO reburning into NO_2 at cold flow conditions, it is ascertained that the NO_2 sensor is sensitive to the NO molecule; however, the true NO measurements are taken from the NO sensor readings.

Overall, the linear trend exhibited by the NO sensor for the cold flow calibration tests (Fig.

A.8) showed improved agreement with the linear trendline compared to flame calibration tests (Fig. A7) for the higher NH_3 seeding range.

A. 6 Uncertainty estimation in X_{NO} (PLIF)

The uncertainty estimation of X_{NO}(PLIF) is obtained by starting from equation A.8 as follows;

$$S_{f,Experimental} = E_{laser} * \tau * B_{12} * n_{opt} * N_{NO} * f_B * n_f \quad (A.8)$$

$$S_{f,Experimental} = cc * E_{laser} * N_{NO} * f_B * n_f \quad (A.9)$$

Where cc is represented as following;

$$cc = \tau * B_{12} * n_{opt} \quad (A.10)$$

and estimated using calibration flame data via Eq. (5.10).

In order to estimate the uncertainty in the X_{NO}, first derivation of equation A.9 is evaluated in equation A.12, with substitution of N_{NO}derivative from equation A.11, as shown below;

$$N_{NO} = X_{NO} * \left(\frac{p}{kT}\right) \quad (A.11)$$

$$\frac{\Delta S_{f,Experimental}}{S_{f,Experimental}} = \frac{\Delta E_{laser}}{E_{laser}} + \left(\frac{\Delta X_{NO}}{X_{NO}} - \frac{\Delta T}{T}\right) + \frac{\Delta f_B}{f_B} + \frac{\Delta n_f}{n_f} \quad (A.12)$$

In equation A.12, $\Delta S_{f,Experimental}$, ΔE_{laser}, Δf_B, Δn_f and ΔT are denoted as uncertainties in the PLIF signal, laser beam profile, Boltzmann fraction, and temperature, respectively. The X_{NO} represents the NO mole fraction from the PLIF signal (see Fig. 5.14) as estimated by utilizing the Tian major species concentrations and temperature, and ΔX_{NO} represents the uncertainty in X_{NO}, which is an unknown in equation A.12.

The uncertainty fractions for each above listed parameter for each case of E%NH_3 are shown in Table A.1, along with calculated uncertainty in NO mole fraction from the PLIF signal (ΔX_{NO}).

Table A.1. Uncertainty contributions of relevant parameters in X_{NO} uncertainty (ΔX_{NO}).

E%NH_3	$\frac{\Delta T}{T}$	$\frac{\Delta f_B}{f_B}$	$\frac{\Delta n_f}{n_f}$	$\frac{\Delta E_{laser}}{E_{laser}}$	$\frac{\Delta S_{f,Experiment}}{S_{f,Experimenta}}$	X_{NO}	ΔX_{NO}
0	0.04	5.52E-03	2.94E-02	2.70E-01	2.10E-01	1.91E-05	1.06E-05
5	0.04	5.45E-03	1.47E-02	2.70E-01	1.30E-01	1.09E-04	5.02E-05
10	0.04	5.43E-03	1.47E-02	2.70E-01	1.10E-01	2.12E-04	9.34E-05
20	0.04	5.41E-03	2.94E-02	2.70E-01	1.40E-01	1.50E-04	7.29E-05
30	0.04	5.42E-03	2.94E-02	2.70E-01	1.10E-01	2.04E-04	9.29E-05
40	0.04	5.45E-03	2.94E-02	2.70E-01	1.00E-01	3.27E-04	1.45E-04
50	0.04	5.49E-03	2.94E-02	2.70E-01	8.00E-02	1.90E-04	8.09E-05
60	0.04	5.55E-03	2.94E-02	2.70E-01	8.00E-02	2.33E-04	9.92E-05
70	0.04	5.63E-03	2.99E-02	2.70E-01	1.70E-01	2.54E-04	1.31E-04
80	0.04	5.73E-03	2.99E-02	2.70E-01	1.20E-01	1.64E-04	7.64E-05

The uncertainty in temperature (ΔT) is estimated as 4% from the grid independence tests (Fig. 5.5) assumed to be same for major species concentrations and temperatures for all E%NH_3 cases. Then, the uncertainty in Boltzmann fraction (Δf_B) and fluorescence efficiency (Δn_f) is calculated from the uncertainties in species and temperature. The uncertainty in laser beam profile (ΔE_{laser}) is estimated from case E%NH_3 = 60, due mostly to the fluctuating beam profile. It is assumed that the beam profile fluctuation would be similar for each case of NH_3 seeding. The uncertainty in NO-PLIF signal for each case is estimated from the NO-PLIF signal values in the axial range of 55 – 60 mm and the radial range of 0 – 15 mm. The exhaust measurements are performed ~75 mm downstream of the flame. Thus by substituting the relevant parameters (shown in Table A.1) into equation A.12, the uncertainty in NO mole fraction from the PLIF signal (ΔX_{NO}) is estimated for each E%NH_3 case and presented in

Table A.1. The uncertainty of mass flow controllers (Alicat, ±5.0% full scale) is utilized to estimate the uncertainty in E%NH_3 for the case of NH_3 seeding, resulting in horizontal error bars for the NO mole fraction from the PLIF signal, as shown in Fig. 5.14.

APPENDIX B. UNICORN CFD MODEL

A time-dependent 2D computational fluid dynamics code with chemistry (CFDC), known as UNICORN (UNsteady Ignition and COmbustion with ReactioNs), has been used in the present numerical studies. The UNICORN code has been developed to better comprehend the flame dynamics of hydrocarbon flames like ignition, blow-out, instabilities and species compositions [1]. UNICORN solves full PDEs of continuity/mass, u- and v- momentum, species and enthalpy conservation equations in both radial (r) and axial (z) directions and has been one of the most methodically developed and validated CFDC codes. For numerous complex combustion phenomena, UNICORN has successfully predicted flame dynamics (mixing, velocity field) and species concentrations for major, minor and intermediate species when coupled with detailed chemical mechanisms. For example, predictions of flame, recirculation zone and soot structures for a laminar ethylene-air flame were confirmed by experimental measurements of flow-field and soot using Mie scattering and laser induced incandescence (LII)[2]. In another instance, for low-speed buoyant H_2/air non-premixed flames, the local temperature and NO concentration was predicted to be higher in the compressed region of the flame and lower in the stretch regions due to the effects of curvature and non-unity Lewis number [3]. Later, Cater and Barlow [4] made time-resolved measurements of NO and OH using PLIF and of temperature using thin-filament pyrometry. The time evolution of temperature, OH, and NO concentrations for both experiments and simulations seemed to be in an excellent agreement. Thus, it is confirmed that the UNICORN predictions combined with PLIF measurements is a powerful approach for studying flame structure in both laminar and turbulent flames.

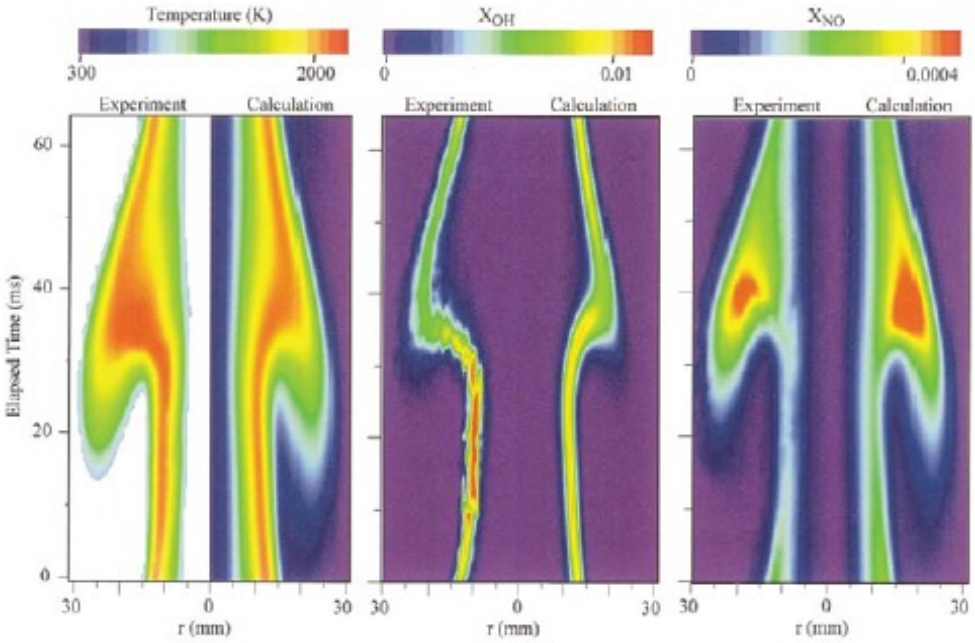

Fig. B.1. Evolution of temperature, OH concentration, and NO concentration in H_2/air jet diffusion flame at axial location 80 mm above nozzle exit. Contour table is given at the top[5].

For the formulation of a CFDC model to numerically integrate the fluid-dynamics with chemical kinetics, five key elements of the numerical model are identified; (1) governing equations with initial/boundary conditions, (2) discretization schemes, (3) computational domain, (4) chemical kinetics, and (5) thermodynamics and transport properties. Each of the key elements are elaborated further in the following sections.

B.1 Governing equations

The time-dependent governing equations for a 2-D axisymmetric reacting flow problem can be written in the cylindrical (z, r) coordinate system as follows;

$$\frac{\partial(\rho)}{\partial t} + \frac{1}{r}\frac{\partial(r\rho v)}{\partial r} + \frac{\partial(\rho u)}{\partial z} = 0 \qquad \text{(B. 1)}$$

[5] Comparison of predictions by Katta et al. [3] with experiments by Carter and Barlow [4]

$$\frac{\partial(\rho\phi)}{\partial t}+\frac{\partial(\rho v\phi)}{\partial r}+\frac{\partial(\rho u\phi)}{\partial z}$$

$$=\frac{\partial}{\partial r}\left(\Gamma^{\phi}\frac{\partial\phi}{\partial r}\right)+\frac{\partial}{\partial z}\left(\Gamma^{\phi}\frac{\partial\phi}{\partial z}\right)-\frac{\rho v\phi}{r}+\frac{\Gamma^{\phi}}{r}\frac{\partial\phi}{\partial r}+S^{\phi} \qquad \text{(B. 2)}$$

where ρ represents density, u and v are the axial and radial components of the velocity vector, respectively, and p is the pressure. The equation B.2 represents a generalized form of u and v momentum as well as species and enthalpy conservation, depending on the variable ϕ, transport coefficient Γ^{ϕ} and source term S^{ϕ}, for which the correlations are listed in Table B.1. Here μ, λ, and C_p are the viscosity, thermal conductivity, and specific heat of the mixture, respectively; Y_i is the mass fraction; and $\dot{\omega}_\iota$ is the mass-production rate of the ith species; ρ_0 is the density of air; and g is the gravitational acceleration.

Table B.1. Variable ϕ, transport coefficients, and source terms in governing equations.

Equations	ϕ	Γ^{ϕ}	S^{ϕ}
Axial Momentum (B.3)	u	μ	$-\frac{\partial \mathrm{P}}{\partial \mathrm{z}}+(\rho_0-\rho)g+\frac{\partial}{\partial z}\left(\mu\frac{\partial u}{\partial z}\right)+\frac{\partial}{\partial r}\left(\mu\frac{\partial v}{\partial z}\right)+\frac{\mu}{r}\frac{\partial v}{\partial z}$ $-\frac{2}{3}\left(\frac{\partial}{\partial z}\left(\mu\frac{\partial u}{\partial z}\right)+\frac{\partial}{\partial z}\left(\mu\frac{\partial v}{\partial r}\right)\right)+\frac{\partial}{\partial z}\left(\mu\frac{v}{r}\right)$
Radial Momentum (B.4)	v	μ	$-\frac{\partial \mathrm{P}}{\partial \mathrm{r}}+\frac{\partial}{\partial \mathrm{r}}\left(\mu\frac{\partial u}{\partial r}\right)+\frac{\partial}{\partial r}\left(\mu\frac{\partial v}{\partial r}\right)+\frac{\mu}{r}\frac{\partial v}{\partial r}-2\mu\frac{v}{r^2}$ $-\frac{2}{3}\left(\frac{\partial}{\partial r}\left(\mu\frac{\partial u}{\partial z}\right)+\frac{\partial}{\partial r}\left(\mu\frac{\partial v}{\partial r}\right)\right)+\frac{\partial}{\partial r}\left(\mu\frac{v}{r}\right)$
Species mass fraction (B.5)	Y_i	ρD_{i-mix}	$\dot{\omega}_i$
Enthalpy (B.6)	H	$\frac{\lambda}{c_p}$	$\nabla\left(\frac{\lambda}{c_p}\sum_{1}^{N_s}\left(\left(Le_i^{-1}-1\right)H_i\nabla Y_i\right)\right)-\sum_{1}^{N_s}\left(h_{f,i}^{0}\dot{\omega}_\iota\right)+q_{rad}$

The transport property D_{i-mix} represents the mixture-averaged diffusion coefficients of the i^{th} species in the gas mixture, where $i = 1, \dots, N_S$. N_S is the total number of chemical species in the chemical mechanism. The enthalpy H is defined as

$$\mathrm{H} = \sum_{i=1}^{N_s} Y_i H_i = \sum_{i=1}^{N_s} Y_i(h_i - h_{f,i}^0) = \int_{T_0}^{T} c_p dT \tag{B.3}$$

where h_i is the total enthalpy of the i-th species, $h_{f,i}^0$ is the i-th species heat of formation at standard temperature T_0. The Lewis number for each species is defined as;

$$Le_i = \frac{\lambda}{\rho c_{p,i} D_{i-mix}} \tag{B.4}$$

With N_S representing the total number of species, the remaining unknowns include species mass fraction ($Y_i, i\ 1, \dots N_S$), enthalpy (H), temperature (T), density (ρ), pressure (P), axial velocity (u) and radial velocity (v), adding up to a total number of unknowns as $N_S + 6$. To provide a closure to the problem set, two additional equations are used: (1) the sum of all mass fractions is unity (eq. B.5);

$$Y_{N_2} = 1.0 - \sum_{i=1}^{N_s - 1} Y_i, \tag{B.5}$$

and (2) equation of state (ideal gas law). By convention, the mass fraction of the largest major species is determined using eq. B.6.

$$P = \rho T R_u \sum_{i=1}^{N_s} \left(\frac{Y_i}{MW_i}\right), \tag{B.6}$$

For the energy equation, a sink term $q_{\text{rad}} = -4\sigma K_p(T^4 - T_0^4)$ is introduced by assuming optically thin gas properties to account for the thermal radiation heat losses from the flame.

Here, K_p is the total absorption and emission coefficient from participating media (H_2, CH_4, CO, CO_2 etc.) [5], defined as $K_p = P\sum_k X_i K_{p,i}$ and $K_{p,i}$ refers to the mean absorption coefficient of i-th species [6].

B.2 Boundary conditions

The boundary conditions applied for a 2-D axisymmetric laminar flame problem are shown in Fig. B.2. The entire domain is bounded by four different boundary conditions. The vertical line on the left-most corner represents the center of the physical flame and is imposed with an axisymmetric boundary condition, meaning that the flux of mass and momentum is zero across this boundary.

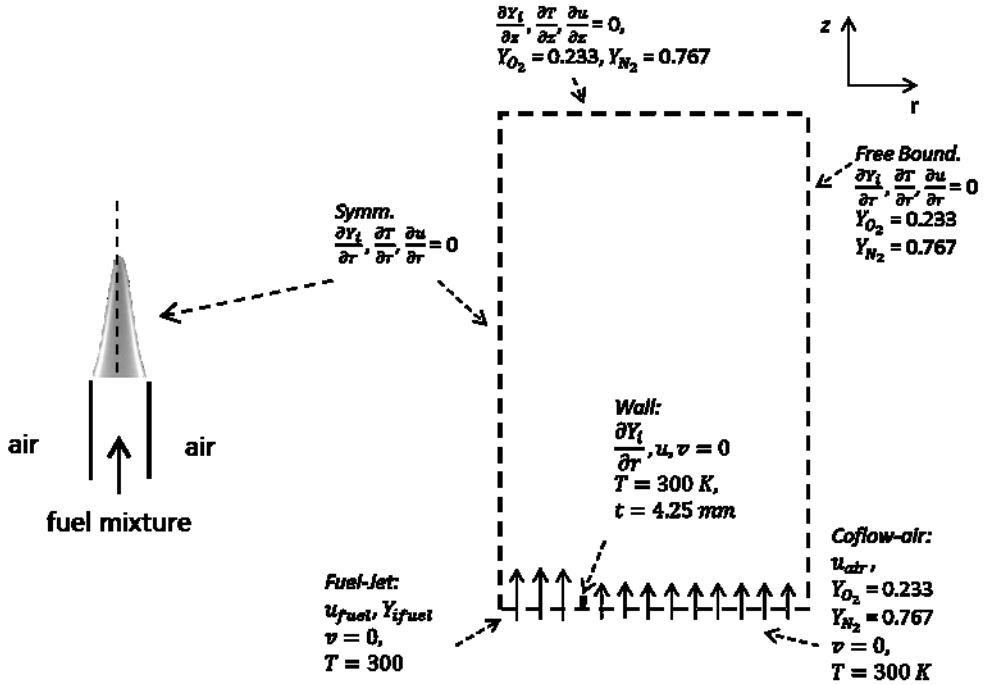

Fig. B.2. Schematic of boundary and initial conditions.

The bottom horizontal line represents the inlet boundary conditions, for both the fuel jet and co-flow. The inlet variables like u and v velocities, temperature, pressure, species mass

fractions (H_2, CH_4, NH_3, O_2, and N_2 etc.) are provided as inputs. The fuel jet inlet conditions are provided in the computational range $0 \leq r \leq R_0$, where R_0 is the ID of the tube, whereas the air coflow boundary conditions are assigned in the range $R_0 < r \leq R_{\text{domain}}$ with axial velocity ~0.001 m/s. The right-most vertical line represents the free flow boundary having the same boundary conditions as the coflow. The top horizontal line represents pressure outlet boundary, where the gradient of variables like $(Y_i, T, u, v\ etc.)$ are zero in the axial direction.

B.3 Chemical kinetics

For the present numerical modeling utilizes three detailed chemical mechanisms: (1) Tian [8] with 84 species and 706 reactions, (2) GRI-Mech3.0 [7] with 53 species and 325 reactions, and (3) Modified GRI-Mech with 53 species and 328 reactions. In the modeling, the net rate of production $\dot{\omega}_i$ of the ith species is obtained by summing up all the individual contributions from each reaction, as given in eq. B.7:

$$\dot{\omega}_i = \sum_{i=1}^{N_s} \nu_{i,k}\, q_j = \left(\nu''_{i,k} - \nu'_{i,k}\right)\left(k_{f,k} \prod_{i=1}^{N_s} [X_i]^{\nu''_{i,k}} - k_{b,k} \prod_{i=1}^{N_s} [X_i]^{\nu'_{i,k}} \right), \tag{B.7}$$

where $\nu''_{i,k}$ is the stoichiometric coefficient on the product side for the i-th species in the k-th reaction and $\nu'_{i,k}$ is the stoichiometric coefficient from the reactant side for the i-th species in the k-th reaction; $[X_i]$ is the molar concentration of the i-th species; and $k_{f,k}$ and $k_{b,k}$ are the forward and backward rate of k-th reaction, respectively. From Arrhenius rate law, the forward or backward rate of reaction $k_{f,k}$ or $k_{b,k}$ can be estimated as:

$$k_{f,k}\ or\ k_{b,k} = AT^n \exp\left(-\frac{E_a}{R_u T}\right), \tag{B.8}$$

where, A, n, and E_a are the pre-exponential factor, temperature exponent, and activation energy, respectively, for the chemical reaction. Subsequently, assuming equilibrium for the reaction, the other backward/forward rate of reaction can be estimated using following expressions

$$K_p = \frac{k_{f,k}}{k_{b,k}} = \exp\left(-\frac{\Delta G_T^0}{R_u T}\right) \tag{B.9}$$

where K_p is the equilibrium constant, ΔG_T^0 is the standard gibbs energy, and R_u is the universal gas constant.

B.4 Thermodynamics and transport properties

To determine the chemical kinetics and spatial distribution of the variables (e.g., species, temperature, etc.), it is imperative to provide thermodynamics and transport properties of the chemical species involved in the problem. Thermodynamic properties include specific enthalpy (h_i), constant specific heat $(c_{p,i})$, entropy (s_i), etc. for each species, whereas, transport properties include the binary diffusion coefficient (D_{i-j}), thermal conductivity (λ_i), and viscosity (μ_i), which are estimated by the correlations based on the Chapman-Enskog collision theory [9], as follows;

$$D_{i-j} = \left[0.2669 \times 10^{-6} \frac{T^{\frac{3}{2}}}{P \cdot \sigma_{ij}^2 \sqrt{MW_i}\,\Omega_D(T^*)}\right]. \tag{B.10}$$

$$\lambda_i = \left(0.115 + 0.354 \cdot \frac{c_{p,i}}{R_u}\right)\left[8.322 \times 10^{-2} \frac{\sqrt{T}}{\sqrt{MW_i}\,\sigma_i^2 \Omega_v(T^*)}\right] \tag{B.11}$$

$$\mu_i = \left[2.669 \frac{\sqrt{MW_i T}}{\sigma_i^2 \Omega_v(T^*)}\right], \tag{B.12}$$

For polyatomic gases, the thermal conductivity is corrected for internal energy storage and $\Omega_D(T^*)$ and $\Omega_v(T^*)$ are known as transport collision integrals provided by Neufeld et al. [10]. The transport properties of the gaseous mixture are determined using following empirical correlations [11]:

$$\mu = \sum_{i=1}^{N} \frac{\mu_i}{1 + \sum_{\substack{k=1 \\ k \neq i}}^{N} \left(\frac{X_j}{X_i}\right) \phi_{ij}}, \tag{B.13}$$

$$\lambda = \sum_{i=1}^{N} \frac{\lambda_i}{1 + \sum_{\substack{k=1 \\ k \neq i}}^{N} 1.065 \left(\frac{X_j}{X_i}\right) \phi_{ij}}, \tag{B.14}$$

$$D_{i-m} = \frac{1 - X_i}{\sum_{\substack{j=1 \\ j \neq i}}^{N} 1 \left(\frac{X_j}{D_{ij}}\right)}, \tag{B.15}$$

where, φ_{ij} is defined as:

$$\varphi_{ij} = \frac{1}{2\sqrt{2}} \left[1 + \frac{MW_i}{MW_j}\right]^{-\frac{1}{2}} \left[1 + \left(\frac{\mu_i}{\mu_j}\right)^{\frac{1}{4}} \left(\frac{MW_i}{MW_j}\right)^{\frac{1}{4}}\right]^2. \tag{B.16}$$

For thermal radiation from major species like H_2O, CO_2, CH_4, H_2, and CO, the Planck mean absorption coefficients are utilized from Grosshandler et al. [5].

B.5 Numerical schemes

A hybrid discretization scheme (combined form of finite volume and finite difference schemes) developed by Spalding [12] is used to solve the PDEs of the species and enthalpy equations on a non-uniform staggered grid. However, a finite difference form of u- and v-

momentum equations are implemented using the implicit QUICKEST (Quadratic Upstream Interpolation for Convective Kinematics with Estimated Streaming Terms) scheme, developed by Leonard [13]. This scheme is third order accurate in both space and time and has very low numerical dissipation, which is important in buoyancy driven flames.

In Fig. B.3, a schematic of the QUICKEST scheme is shown. The variables in the N+1th time step when proceeding from Nth time step with known variables can be calculated from eq. B.17:

$$A_P\Phi_P^{N+1} + A_{EE}\Phi_{EE}^{N+1} + A_E\Phi_E^{N+1} + A_W\Phi_W^{N+1} + A_{WW}\Phi_{WW}^{N+1} + A_{NN}\Phi_{NN}^{N+1} + A_N\Phi_N^{N+1} + A_S\Phi_S^{N+1} + A_{SS}\Phi_{SS}^{N+1} = \Delta t \cdot S_P^{\Phi} + \rho_P\Phi_{P.}^{N} \qquad (B.17)$$

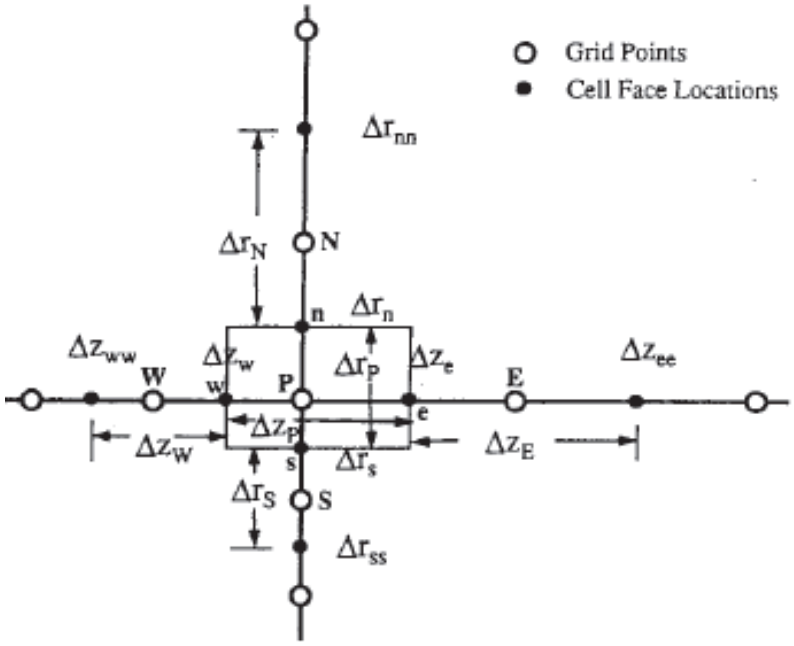

Fig. B.3. Schematic diagrams of the FVM/FDM schemes, courtesy of Katta et al. [14].

Here, Φ_P^{N+1} represents a variable at the N+1th time step. Subscripts P, denotes grid point "P" in the figure and E and W represent next neighboring grid points in the positive and negative z-direction, respectively; whereas grid points EE and WW represent two grid points

away from point P in the corresponding direction. A similar convention goes for the N, S, NN and SS grid points in r-direction.

The time step Δt is estimated from the CFL number by following correlation;

$$\Delta t = CFL \cdot \frac{\Delta l_{\min}}{|\vec{v}|_{\max}} \tag{B.18}$$

where $\Delta l_{\min}$ is the minimum distance between two grid points and $|\vec{v}|_{\max}$ is the maximum velocity magnitude. The A coefficients on the neighboring grid points of point P and parameters on the right hand side of eq. B.17 are estimated based on parameters at the Nth time step:

$$A_N = \frac{\Delta t}{\Delta r_p}\left[-(\rho_n v_n)\Delta r_n^2\left(\frac{1}{6} - \gamma_n - \frac{1}{6}C_n^2\right)c_1\right] \tag{B.19}$$

$$A_{NN} = \frac{\Delta t}{\Delta r_p}\left\{(\rho_n v_n)\left[\frac{1}{2} - \frac{C_n}{2} - \Delta r_n^2\left(\frac{1}{6} - \gamma_n - \frac{1}{6}C_n^2\right)c_2\right] + (\rho_s v_s)\Delta r_s^2\left(\frac{1}{6} - \gamma_s - \frac{1}{6}C_s^2\right)d_1 - \frac{\Gamma_n}{r_n}\right\} - \frac{\Delta t}{r_p}\frac{\Gamma_p}{2\Delta r_n} \tag{B.20}$$

$$A_S = \frac{\Delta t}{\Delta r_p}\left\{-(\rho_n v_n)\Delta r_n^2\left(\frac{1}{6} - \gamma_n - \frac{1}{6}C_n^2\right)c_4 - (\rho_s v_s)\left[\frac{1}{2} + \frac{C_s}{2} - \Delta r_s^2\left(\frac{1}{6} - \gamma_s - \frac{1}{6}C_s^2\right)d_3\right] - \frac{\Gamma_s}{r_s}\right\} + \frac{\Delta t}{r_p}\frac{\Gamma_p}{2\Delta r_s} \tag{B.21}$$

$$A_{SS} = \frac{\Delta t}{\Delta r_p}\left[(\rho_s v_s)\Delta r_s^2\left(\frac{1}{6} - \gamma_s - \frac{1}{6}C_s^2\right)d_4\right] \tag{B.22}$$

Likewise, the coefficients A_E, A_W, A_{EE}, A_{WW} can be expressed in terms of local Courant numbers. Here the local Courant numbers ($C_S,\ C_N$) and the diffusion parameters (γ_n, γ_s) are

$$C_n = v_n \frac{\Delta t}{\Delta r_n} \tag{B.23}$$

$$C_s = v_s \frac{\Delta t}{\Delta r_s} \tag{B.24}$$

$$\gamma_n = \Gamma_n \frac{\Delta t}{\Delta r_n^2} \tag{B.25}$$

$$\gamma_s = \Gamma_s \frac{\Delta t}{\Delta r_s^2} \tag{B.26}$$

Where, v_n, v_s are defined as follows:

$$v_n \geq 0 \begin{Bmatrix} c_1 = 0 \\ c_2 = \left(\frac{1}{\Delta r_p}\frac{1}{\Delta r_n}\right) \\ c_3 = -\left(\frac{1}{\Delta r_p}\frac{1}{\Delta r_n} + \frac{1}{\Delta r_p}\frac{1}{\Delta r_s}\right) \\ c_4 = \left(\frac{1}{\Delta r_p}\frac{1}{\Delta r_s}\right) \end{Bmatrix}, \tag{B.27}$$

$$v_n < 0 \begin{Bmatrix} c_1 = \left(\frac{1}{\Delta r_N}\frac{1}{\Delta r_{nn}}\right) \\ c_2 = -\left(\frac{1}{\Delta r_N}\frac{1}{\Delta r_{nn}} + \frac{1}{\Delta r_N}\frac{1}{\Delta r_n}\right) \\ c_3 = \left(\frac{1}{\Delta r_N}\frac{1}{\Delta r_n}\right) \\ c_4 = 0 \end{Bmatrix}, \tag{B.28}$$

$$v_s \geq 0 \begin{Bmatrix} d_1 = 0 \\ d_2 = \left(\frac{1}{\Delta r_S}\frac{1}{\Delta r_s}\right) \\ d_3 = -\left(\frac{1}{\Delta r_S}\frac{1}{\Delta r_s} + \frac{1}{\Delta r_S}\frac{1}{\Delta r_{ss}}\right) \\ d_4 = \left(\frac{1}{\Delta r_S}\frac{1}{\Delta r_{ss}}\right) \end{Bmatrix}, \tag{B.29}$$

$$v_s < 0 \begin{Bmatrix} d_1 = \left(\frac{1}{\Delta r_P}\frac{1}{\Delta r_n}\right) \\ d_2 = -\left(\frac{1}{\Delta r_P}\frac{1}{\Delta r_n} + \frac{1}{\Delta r_P}\frac{1}{\Delta r_s}\right) \\ d_3 = \left(\frac{1}{\Delta r_P}\frac{1}{\Delta r_s}\right) \\ d_4 = 0 \end{Bmatrix}. \tag{B.30}$$

then, the coefficient A_P is calculated as:

$$A_P = \rho_P^N - (A_{NN} + A_N + A_{SS} + A_S + A_{WW} + A_W + A_{EE} + A_E). \tag{B.31}$$

B.6 Numerical procedure

For the present work, a CFL number of 0.5 is used on a grid system of 201x64 with time step $\Delta t = 0.137\ msec$. The procedure for each time iteration is as follows:

1. Transport properties (ν, α, D_{ij}) for each species are estimated first, followed by the mixture.
2. Species and energy equations are solved next, to calculate Y_i and sensible enthalpy (h_{mix}).
3. Ideal gas is utilized to estimate the mixture temperature (T) and density (ρ).
4. Momentum equations in both x and y directions are solved.
5. The Poisson equation is solved for pressure (p).

$$\nabla(momentum\ eq)\ and\ apply\ \nabla.V = 0 \Rightarrow\ \nabla^2 p = f(\vartheta, V)$$

6. Velocity field, u- and v- velocity are corrected based on pressure gradients.

B.7 References

[1] Katta VR, Roquemore WM. Role of flow visualization in the development of unicorn. In: Proceedings of VSJ-SPIE98. 1998. p. 1-6.

[2] Katta VR, Forlines RA, Roquemore WM, Anderson WS, Zelina J, Gord JR, Stouffer SD, Roy S. Experimental and computational study on partially premixed flames in a center body burner. Combustion and Flame 2011;158(3):511-524.

[3] Katta VR, Goss L, Roquemore WM. Effect of non-unity Lewis number and finite-rate chemistry on the dynamics of a hydrogen-air jet diffusion flame. Systems Research 1994;74:60-74.

[4] Carter CD, Barlow RS. Simultaneous measurements of NO, OH and the major species in turbulent flames. Optics Letters 1994;19(4):299-301.

[5] Grosshandler WR. A narrow band model for radiation calculations in a combustion environment. Gaithersburg: 1993.

[6] Howell JR, Siegel R, Mengüç MP. Thermal radiation heat transfer. Boca Raton, Fla.: CRC Press, 2011.

[7] Smith GP, Golden DM, Frenklach M, Moriarty NW, Eiteneer B, Goldenberg M, Bowman CT, Hanson RK, Song S, Gardiner JWC, Lissianski VV, Qin Z. GRI-Mech 3.0 1999.

[8] Tian Z, Li Y, Zhang L, Glarborg P, Qi F. An experimental and kinetic modeling study of premixed $NH_3/CH_4/O_2$/Ar flames at low pressure. Combustion and Flame 2009;156(7):1413-1426.

[9] Poling BE, Prausnitz JM, Connell, JP. The properties of gases and liquids. McGraw-Hill New York, 2001.

[10] Neufeld PD, Janzen AR, Aziz RA. Empirical equations to calculate 16 of the transport collision integrals $\omega(1,s)^*$ for the lennard-jones (12-6) potential. J. Chem. Phys. 1972;57:1100-1102.

[11] Gardiner WC, Burcat A. Thermochemical data for combustion calculations. Springer-Verlag, Newark: 1984.

[12] Spalding DB. Int. J. Num. Meth. Eng. 1972:4:551.

[13] Leonard BP. Comp. meth. Appl. Mech. Eng. 1979:19:59.

[14] Katta VR, Goss PL, Roquemore WM. Numerical investigations of transitional H_2/N_2 jet diffusion flames. American Institute of Aeronautics and Astronautics 1994.

APPENDIX C. MODIFIED GRI-MECH3.0 MECHANISM

ELEMENTS CONSIDERED	ATOMIC WEIGHT
1. O	15.9994
2. H	1.00797
3. C	12.0112
4. N	14.0067
5. AR	39.9480

(k = A T**b exp(-E/RT))

REACTIONS CONSIDERED			A	b	E
1. 2O+M<=>O2+M			1.20E+17	-1.0	0.0
	H2	Enhanced by	2.400E+00		
	H2O	Enhanced by	1.540E+01		
	CH4	Enhanced by	2.000E+00		
	CO	Enhanced by	1.750E+00		
	CO2	Enhanced by	3.600E+00		
	C2H6	Enhanced by	3.000E+00		
	AR	Enhanced by	8.300E-01		
2. O+H+M<=>OH+M			5.00E+17	-1.0	0.0
	H2	Enhanced by	2.000E+00		
	H2O	Enhanced by	6.000E+00		
	CH4	Enhanced by	2.000E+00		
	CO	Enhanced by	1.500E+00		
	CO2	Enhanced by	2.000E+00		
	C2H6	Enhanced by	3.000E+00		
	AR	Enhanced by	7.000E-01		
3. O+H2<=>H+OH			3.87E+04	2.7	6260.0
4. O+HO2<=>OH+O2			2.00E+13	0.0	0.0
5. O+H2O2<=>OH+HO2			9.63E+06	2.0	4000.0
6. O+CH<=>H+CO			5.70E+13	0.0	0.0
7. O+CH2<=>H+HCO			8.00E+13	0.0	0.0
8. O+CH2(S)<=>H2+CO			1.50E+13	0.0	0.0
9. O+CH2(S)<=>H+HCO			1.50E+13	0.0	0.0
10. O+CH3<=>H+CH2O			5.06E+13	0.0	0.0
11. O+CH4<=>OH+CH3			1.02E+09	1.5	8600.0
12. O+CO(+M)<=>CO2(+M)			1.80E+10	0.0	2385.0
Low pressure limit:	0.60200E+15	0.00000E+00	0.30000E+04		
	H2	Enhanced by	2.000E+00		
	O2	Enhanced by	6.000E+00		
	H2O	Enhanced by	6.000E+00		
	CH4	Enhanced by	2.000E+00		
	CO	Enhanced by	1.500E+00		
	CO2	Enhanced by	3.500E+00		
	C2H6	Enhanced by	3.000E+00		
	AR	Enhanced by	5.000E-01		
13. O+HCO<=>OH+CO			3.00E+13	0.0	0.0

14.	O+HCO<=>H+CO2		3.00E+13	0.0	0.0
15.	O+CH2O<=>OH+HCO		3.90E+13	0.0	3540.0
16.	O+CH2OH<=>OH+CH2O		1.00E+13	0.0	0.0
17.	O+CH3O<=>OH+CH2O		1.00E+13	0.0	0.0
18.	O+CH3OH<=>OH+CH2OH		3.88E+05	2.5	3100.0
19.	O+CH3OH<=>OH+CH3O		1.30E+05	2.5	5000.0
20.	O+C2H<=>CH+CO		5.00E+13	0.0	0.0
21.	O+C2H2<=>H+HCCO		1.35E+07	2.0	1900.0
22.	O+C2H2<=>OH+C2H		4.60E+19	-1.4	28950.0
23.	O+C2H2<=>CO+CH2		6.94E+06	2.0	1900.0
24.	O+C2H3<=>H+CH2CO		3.00E+13	0.0	0.0
25.	O+C2H4<=>CH3+HCO		1.25E+07	1.8	220.0
26.	O+C2H5<=>CH3+CH2O		2.24E+13	0.0	0.0
27.	O+C2H6<=>OH+C2H5		8.98E+07	1.9	5690.0
28.	O+HCCO<=>H+2CO		1.00E+14	0.0	0.0
29.	O+CH2CO<=>OH+HCCO		1.00E+13	0.0	8000.0
30.	O+CH2CO<=>CH2+CO2		1.75E+12	0.0	1350.0
31.	O2+CO<=>O+CO2		2.50E+12	0.0	47800.0
32.	O2+CH2O<=>HO2+HCO		1.00E+14	0.0	40000.0
33.	H+O2+M<=>HO2+M		2.80E+18	-0.9	0.0
	O2	Enhanced by	0.000E+00		
	H2O	Enhanced by	0.000E+00		
	CO	Enhanced by	7.500E-01		
	CO2	Enhanced by	1.500E+00		
	C2H6	Enhanced by	1.500E+00		
	N2	Enhanced by	0.000E+00		
	AR	Enhanced by	0.000E+00		
34.	H+2O2<=>HO2+O2		2.08E+19	-1.2	0.0
35.	H+O2+H2O<=>HO2+H2O		1.13E+19	-0.8	0.0
36.	H+O2+N2<=>HO2+N2		2.60E+19	-1.2	0.0
37.	H+O2+AR<=>HO2+AR		7.00E+17	-0.8	0.0
38.	H+O2<=>O+OH		2.65E+16	-0.7	17041.0
39.	2H+M<=>H2+M		1.00E+18	-1.0	0.0
	H2	Enhanced by	0.000E+00		
	H2O	Enhanced by	0.000E+00		
	CH4	Enhanced by	2.000E+00		
	CO2	Enhanced by	0.000E+00		
	C2H6	Enhanced by	3.000E+00		
	AR	Enhanced by	6.300E-01		
40.	2H+H2<=>2H2		9.00E+16	-0.6	0.0
41.	2H+H2O<=>H2+H2O		6.00E+19	-1.2	0.0
42.	2H+CO2<=>H2+CO2		5.50E+20	-2.0	0.0
43.	H+OH+M<=>H2O+M		2.20E+22	-2.0	0.0
	H2	Enhanced by	7.300E-01		
	H2O	Enhanced by	3.650E+00		
	CH4	Enhanced by	2.000E+00		
	C2H6	Enhanced by	3.000E+00		
	AR	Enhanced by	3.800E-01		
44.	H+HO2<=>O+H2O		3.97E+12	0.0	671.0
45.	H+HO2<=>O2+H2		4.48E+13	0.0	1068.0
46.	H+HO2<=>2OH		8.40E+13	0.0	635.0
47.	H+H2O2<=>HO2+H2		1.21E+07	2.0	5200.0
48.	H+H2O2<=>OH+H2O		1.00E+13	0.0	3600.0
49.	H+CH<=>C+H2		1.65E+14	0.0	0.0

```
50. H+CH2(+M)<=>CH3(+M)                           6.00E+14    0.0        0.0
        Low pressure limit:  0.10400E+27 -0.27600E+01 0.16000E+04
  TROE centering:      0.56200E+00  0.91000E+02 0.58360E+04  0.85520E+04
                 H2              Enhanced by    2.000E+00
                 H2O             Enhanced by    6.000E+00
                 CH4             Enhanced by    2.000E+00
                 CO              Enhanced by    1.500E+00
                 CO2             Enhanced by    2.000E+00
                 C2H6            Enhanced by    3.000E+00
                 AR              Enhanced by    7.000E-01
51. H+CH2(S)<=>CH+H2                              3.00E+13    0.0        0.0
52. H+CH3(+M)<=>CH4(+M)                           1.39E+16   -0.5      536.0
        Low pressure limit:  0.26200E+34 -0.47600E+01 0.24400E+04
  TROE centering:      0.78300E+00  0.74000E+02 0.29410E+04  0.69640E+04
                 H2              Enhanced by    2.000E+00
                 H2O             Enhanced by    6.000E+00
                 CH4             Enhanced by    3.000E+00
                 CO              Enhanced by    1.500E+00
                 CO2             Enhanced by    2.000E+00
                 C2H6            Enhanced by    3.000E+00
                 AR              Enhanced by    7.000E-01
53. H+CH4<=>CH3+H2                                6.60E+08    1.6    10840.0
54. H+HCO(+M)<=>CH2O(+M)                          1.09E+12    0.5     -260.0
        Low pressure limit:  0.24700E+25 -0.25700E+01 0.42500E+03
  TROE centering:      0.78240E+00  0.27100E+03 0.27550E+04  0.65700E+04
                 H2              Enhanced by    2.000E+00
                 H2O             Enhanced by    6.000E+00
                 CH4             Enhanced by    2.000E+00
                 CO              Enhanced by    1.500E+00
                 CO2             Enhanced by    2.000E+00
                 C2H6            Enhanced by    3.000E+00
                 AR              Enhanced by    7.000E-01
55. H+HCO<=>H2+CO                                 7.34E+13    0.0        0.0
56. H+CH2O(+M)<=>CH2OH(+M)                        5.40E+11    0.5     3600.0
        Low pressure limit:  0.12700E+33 -0.48200E+01  0.65300E+04
  TROE centering:      0.71870E+00  0.10300E+03 0.12910E+04  0.41600E+04
                 H2              Enhanced by    2.000E+00
                 H2O             Enhanced by    6.000E+00
                 CH4             Enhanced by    2.000E+00
                 CO              Enhanced by    1.500E+00
                 CO2             Enhanced by    2.000E+00
                 C2H6            Enhanced by    3.000E+00
57. H+CH2O(+M)<=>CH3O(+M)                         5.40E+11    0.5     2600.0
        Low pressure limit:  0.22000E+31 -0.48000E+01  0.55600E+04
  TROE centering:      0.75800E+00  0.94000E+02 0.15550E+04  0.42000E+04
                 H2              Enhanced by    2.000E+00
                 H2O             Enhanced by    6.000E+00
                 CH4             Enhanced by    2.000E+00
                 CO              Enhanced by    1.500E+00
                 CO2             Enhanced by    2.000E+00
                 C2H6            Enhanced by    3.000E+00
58. H+CH2O<=>HCO+H2                               5.74E+07    1.9     2742.0
59. H+CH2OH(+M)<=>CH3OH(+M)                       1.06E+12    0.5       86.0
        Low pressure limit:  0.43600E+32 -0.46500E+01  0.50800E+04
```

```
  TROE centering:      0.60000E+00  0.10000E+03 0.90000E+05  0.10000E+05
                H2              Enhanced by    2.000E+00
                H2O             Enhanced by    6.000E+00
                CH4             Enhanced by    2.000E+00
                CO              Enhanced by    1.500E+00
                CO2             Enhanced by    2.000E+00
                C2H6            Enhanced by    3.000E+00
60. H+CH2OH<=>H2+CH2O                          2.00E+13    0.0        0.0
61. H+CH2OH<=>OH+CH3                           1.65E+11    0.7     -284.0
62. H+CH2OH<=>CH2(S)+H2O                       3.28E+13   -0.1      610.0
63. H+CH3O(+M)<=>CH3OH(+M)                     2.43E+12    0.5       50.0
        Low pressure limit:  0.46600E+42 -0.74400E+01  0.14080E+05
  TROE centering:      0.70000E+00  0.10000E+03 0.90000E+05  0.10000E+05
                H2              Enhanced by    2.000E+00
                H2O             Enhanced by    6.000E+00
                CH4             Enhanced by    2.000E+00
                CO              Enhanced by    1.500E+00
                CO2             Enhanced by    2.000E+00
                C2H6            Enhanced by    3.000E+00
64. H+CH3O<=>H+CH2OH                           4.15E+07    1.6     1924.0
65. H+CH3O<=>H2+CH2O                           2.00E+13    0.0        0.0
66. H+CH3O<=>OH+CH3                            1.50E+12    0.5     -110.0
67. H+CH3O<=>CH2(S)+H2O                        2.62E+14   -0.2     1070.0
68. H+CH3OH<=>CH2OH+H2                         1.70E+07    2.1     4870.0
69. H+CH3OH<=>CH3O+H2                          4.20E+06    2.1     4870.0
70. H+C2H(+M)<=>C2H2(+M)                       1.00E+17   -1.0        0.0
        Low pressure limit:  0.37500E+34 -0.48000E+01  0.19000E+04
  TROE centering:      0.64640E+00  0.13200E+03 0.13150E+04  0.55660E+04
                H2              Enhanced by    2.000E+00
                H2O             Enhanced by    6.000E+00
                CH4             Enhanced by    2.000E+00
                CO              Enhanced by    1.500E+00
                CO2             Enhanced by    2.000E+00
                C2H6            Enhanced by    3.000E+00
                AR              Enhanced by    7.000E-01
71. H+C2H2(+M)<=>C2H3(+M)                      5.60E+12    0.0     2400.0
        Low pressure limit:  0.38000E+41 -0.72700E+01  0.72200E+04
  TROE centering:      0.75070E+00  0.98500E+02 0.13020E+04  0.41670E+04
                H2              Enhanced by    2.000E+00
                H2O             Enhanced by    6.000E+00
                CH4             Enhanced by    2.000E+00
                CO              Enhanced by    1.500E+00
                CO2             Enhanced by    2.000E+00
                C2H6            Enhanced by    3.000E+00
                AR              Enhanced by    7.000E-01
72. H+C2H3(+M)<=>C2H4(+M)                      6.08E+12    0.3      280.0
        Low pressure limit:  0.14000E+31 -0.38600E+01  0.33200E+04
  TROE centering:      0.78200E+00  0.20750E+03 0.26630E+04  0.60950E+04
                H2              Enhanced by    2.000E+00
                H2O             Enhanced by    6.000E+00
                CH4             Enhanced by    2.000E+00
                CO              Enhanced by    1.500E+00
                CO2             Enhanced by    2.000E+00
                C2H6            Enhanced by    3.000E+00
```

```
                AR              Enhanced by    7.000E-01
73. H+C2H3<=>H2+C2H2                           3.00E+13    0.0        0.0
74. H+C2H4(+M)<=>C2H5(+M)                      5.40E+11    0.5     1820.0
        Low pressure limit:  0.60000E+42 -0.76200E+01  0.69700E+04
  TROE centering:      0.97530E+00  0.21000E+03 0.98400E+03  0.43740E+04
                H2              Enhanced by    2.000E+00
                H2O             Enhanced by    6.000E+00
                CH4             Enhanced by    2.000E+00
                CO              Enhanced by    1.500E+00
                CO2             Enhanced by    2.000E+00
                C2H6            Enhanced by    3.000E+00
                AR              Enhanced by    7.000E-01
75. H+C2H4<=>C2H3+H2                           1.32E+06    2.5    12240.0
76. H+C2H5(+M)<=>C2H6(+M)                      5.21E+17   -1.0     1580.0
        Low pressure limit:  0.19900E+42 -0.70800E+01  0.66850E+04
  TROE centering:      0.84220E+00  0.12500E+03 0.22190E+04  0.68820E+04
                H2              Enhanced by    2.000E+00
                H2O             Enhanced by    6.000E+00
                CH4             Enhanced by    2.000E+00
                CO              Enhanced by    1.500E+00
                CO2             Enhanced by    2.000E+00
                C2H6            Enhanced by    3.000E+00
                AR              Enhanced by    7.000E-01
77. H+C2H5<=>H2+C2H4                           2.00E+12    0.0        0.0
78. H+C2H6<=>C2H5+H2                           1.15E+08    1.9     7530.0
79. H+HCCO<=>CH2(S)+CO                         1.00E+14    0.0        0.0
80. H+CH2CO<=>HCCO+H2                          5.00E+13    0.0     8000.0
81. H+CH2CO<=>CH3+CO                           1.13E+13    0.0     3428.0
82. H+HCCOH<=>H+CH2CO                          1.00E+13    0.0        0.0
83. H2+CO(+M)<=>CH2O(+M)                       4.30E+07    1.5    79600.0
        Low pressure limit:  0.50700E+28 -0.34200E+01  0.84350E+05
  TROE centering:      0.93200E+00  0.19700E+03 0.15400E+04  0.10300E+05
                H2              Enhanced by    2.000E+00
                H2O             Enhanced by    6.000E+00
                CH4             Enhanced by    2.000E+00
                CO              Enhanced by    1.500E+00
                CO2             Enhanced by    2.000E+00
                C2H6            Enhanced by    3.000E+00
                AR              Enhanced by    7.000E-01
84. OH+H2<=>H+H2O                              2.16E+08    1.5     3430.0
85. 2OH(+M)<=>H2O2(+M)                         7.40E+13   -0.4        0.0
        Low pressure limit:  0.23000E+19 -0.90000E+00 -0.17000E+04
  TROE centering:      0.73460E+00  0.94000E+02 0.17560E+04  0.51820E+04
                H2              Enhanced by    2.000E+00
                H2O             Enhanced by    6.000E+00
                CH4             Enhanced by    2.000E+00
                CO              Enhanced by    1.500E+00
                CO2             Enhanced by    2.000E+00
                C2H6            Enhanced by    3.000E+00
                AR              Enhanced by    7.000E-01
86. 2OH<=>O+H2O                                3.57E+04    2.4    -2110.0
87. OH+HO2<=>O2+H2O                            1.45E+13    0.0     -500.0
                    Declared duplicate reaction...
88. OH+H2O2<=>HO2+H2O                          2.00E+12    0.0      427.0
```

```
                    Declared duplicate reaction...
89. OH+H2O2<=>HO2+H2O                           1.70E+18    0.0    29410.0
                    Declared duplicate reaction...
90. OH+C<=>H+CO                                 5.00E+13    0.0        0.0
91. OH+CH<=>H+HCO                               3.00E+13    0.0        0.0
92. OH+CH2<=>H+CH2O                             2.00E+13    0.0        0.0
93. OH+CH2<=>CH+H2O                             1.13E+07    2.0     3000.0
94. OH+CH2(S)<=>H+CH2O                          3.00E+13    0.0        0.0
95. OH+CH3(+M)<=>CH3OH(+M)                      2.79E+18   -1.4     1330.0
        Low pressure limit:  0.40000E+37 -0.59200E+01  0.31400E+04
  TROE centering:      0.41200E+00  0.19500E+03 0.59000E+04  0.63940E+04
                 H2              Enhanced by    2.000E+00
                 H2O             Enhanced by    6.000E+00
                 CH4             Enhanced by    2.000E+00
                 CO              Enhanced by    1.500E+00
                 CO2             Enhanced by    2.000E+00
                 C2H6            Enhanced by    3.000E+00
96. OH+CH3<=>CH2+H2O                            5.60E+07    1.6     5420.0
97. OH+CH3<=>CH2(S)+H2O                         6.44E+17   -1.3     1417.0
98. OH+CH4<=>CH3+H2O                            1.00E+08    1.6     3120.0
99. OH+CO<=>H+CO2                               4.76E+07    1.2       70.0
100. OH+HCO<=>H2O+CO                            5.00E+13    0.0        0.0
101. OH+CH2O<=>HCO+H2O                          3.43E+09    1.2     -447.0
102. OH+CH2OH<=>H2O+CH2O                        5.00E+12    0.0        0.0
103. OH+CH3O<=>H2O+CH2O                         5.00E+12    0.0        0.0
104. OH+CH3OH<=>CH2OH+H2O                       1.44E+06    2.0     -840.0
105. OH+CH3OH<=>CH3O+H2O                        6.30E+06    2.0     1500.0
106. OH+C2H<=>H+HCCO                            2.00E+13    0.0        0.0
107. OH+C2H2<=>H+CH2CO                          2.18E-04    4.5    -1000.0
108. OH+C2H2<=>H+HCCOH                          5.04E+05    2.3    13500.0
109. OH+C2H2<=>C2H+H2O                          3.37E+07    2.0    14000.0
110. OH+C2H2<=>CH3+CO                           4.83E-04    4.0    -2000.0
111. OH+C2H3<=>H2O+C2H2                         5.00E+12    0.0        0.0
112. OH+C2H4<=>C2H3+H2O                         3.60E+06    2.0     2500.0
113. OH+C2H6<=>C2H5+H2O                         3.54E+06    2.1      870.0
114. OH+CH2CO<=>HCCO+H2O                        7.50E+12    0.0     2000.0
115. 2HO2<=>O2+H2O2                             1.30E+11    0.0    -1630.0
                    Declared duplicate reaction...
116. 2HO2<=>O2+H2O2                             4.20E+14    0.0    12000.0
                    Declared duplicate reaction...
117. HO2+CH2<=>OH+CH2O                          2.00E+13    0.0        0.0
118. HO2+CH3<=>O2+CH4                           1.00E+12    0.0        0.0
119. HO2+CH3<=>OH+CH3O                          3.78E+13    0.0        0.0
120. HO2+CO<=>OH+CO2                            1.50E+14    0.0    23600.0
121. HO2+CH2O<=>HCO+H2O2                        5.60E+06    2.0    12000.0
122. C+O2<=>O+CO                                5.80E+13    0.0      576.0
123. C+CH2<=>H+C2H                              5.00E+13    0.0        0.0
124. C+CH3<=>H+C2H2                             5.00E+13    0.0        0.0
125. CH+O2<=>O+HCO                              6.71E+13    0.0        0.0
126. CH+H2<=>H+CH2                              1.08E+14    0.0     3110.0
127. CH+H2O<=>H+CH2O                            5.71E+12    0.0     -755.0
128. CH+CH2<=>H+C2H2                            4.00E+13    0.0        0.0
129. CH+CH3<=>H+C2H3                            3.00E+13    0.0        0.0
130. CH+CH4<=>H+C2H4                            6.00E+13    0.0        0.0
```

```
131. CH+CO(+M)<=>HCCO(+M)                         5.00E+13    0.0        0.0
        Low pressure limit:  0.26900E+29 -0.37400E+01  0.19360E+04
  TROE centering:      0.57570E+00  0.23700E+03 0.16520E+04  0.50690E+04
                 H2              Enhanced by    2.000E+00
                 H2O             Enhanced by    6.000E+00
                 CH4             Enhanced by    2.000E+00
                 CO              Enhanced by    1.500E+00
                 CO2             Enhanced by    2.000E+00
                 C2H6            Enhanced by    3.000E+00
                 AR              Enhanced by    7.000E-01
132. CH+CO2<=>HCO+CO                              1.90E+14    0.0    15792.0
133. CH+CH2O<=>H+CH2CO                            9.46E+13    0.0     -515.0
134. CH+HCCO<=>CO+C2H2                            5.00E+13    0.0        0.0
135. CH2+O2=>OH+H+CO                              5.00E+12    0.0     1500.0
136. CH2+H2<=>H+CH3                               5.00E+05    2.0     7230.0
137. 2CH2<=>H2+C2H2                               1.60E+15    0.0    11944.0
138. CH2+CH3<=>H+C2H4                             4.00E+13    0.0        0.0
139. CH2+CH4<=>2CH3                               2.46E+06    2.0     8270.0
140. CH2+CO(+M)<=>CH2CO(+M)                       8.10E+11    0.5     4510.0
        Low pressure limit:  0.26900E+34 -0.51100E+01  0.70950E+04
  TROE centering:      0.59070E+00  0.27500E+03 0.12260E+04  0.51850E+04
                 H2              Enhanced by    2.000E+00
                 H2O             Enhanced by    6.000E+00
                 CH4             Enhanced by    2.000E+00
                 CO              Enhanced by    1.500E+00
                 CO2             Enhanced by    2.000E+00
                 C2H6            Enhanced by    3.000E+00
                 AR              Enhanced by    7.000E-01
141. CH2+HCCO<=>C2H3+CO                           3.00E+13    0.0        0.0
142. CH2(S)+N2<=>CH2+N2                           1.50E+13    0.0      600.0
143. CH2(S)+AR<=>CH2+AR                           9.00E+12    0.0      600.0
144. CH2(S)+O2<=>H+OH+CO                          2.80E+13    0.0        0.0
145. CH2(S)+O2<=>CO+H2O                           1.20E+13    0.0        0.0
146. CH2(S)+H2<=>CH3+H                            7.00E+13    0.0        0.0
147. CH2(S)+H2O(+M)<=>CH3OH(+M)                   4.82E+17   -1.2     1145.0
        Low pressure limit:  0.18800E+39 -0.63600E+01  0.50400E+04
  TROE centering:      0.60270E+00  0.20800E+03 0.39220E+04  0.10180E+05
                 H2              Enhanced by    2.000E+00
                 H2O             Enhanced by    6.000E+00
                 CH4             Enhanced by    2.000E+00
                 CO              Enhanced by    1.500E+00
                 CO2             Enhanced by    2.000E+00
                 C2H6            Enhanced by    3.000E+00
148. CH2(S)+H2O<=>CH2+H2O                         3.00E+13    0.0        0.0
149. CH2(S)+CH3<=>H+C2H4                          1.20E+13    0.0     -570.0
150. CH2(S)+CH4<=>2CH3                            1.60E+13    0.0     -570.0
151. CH2(S)+CO<=>CH2+CO                           9.00E+12    0.0        0.0
152. CH2(S)+CO2<=>CH2+CO2                         7.00E+12    0.0        0.0
153. CH2(S)+CO2<=>CO+CH2O                         1.40E+13    0.0        0.0
154. CH2(S)+C2H6<=>CH3+C2H5                       4.00E+13    0.0     -550.0
155. CH3+O2<=>O+CH3O                              3.56E+13    0.0    30480.0
156. CH3+O2<=>OH+CH2O                             2.31E+12    0.0    20315.0
157. CH3+H2O2<=>HO2+CH4                           2.45E+04    2.5     5180.0
158. 2CH3(+M)<=>C2H6(+M)                          6.77E+16   -1.2      654.0
```

```
        Low pressure limit:  0.34000E+42 -0.70300E+01  0.27620E+04
   TROE centering:      0.61900E+00  0.73200E+02 0.11800E+04  0.99990E+04
                  H2              Enhanced by    2.000E+00
                  H2O             Enhanced by    6.000E+00
                  CH4             Enhanced by    2.000E+00
                  CO              Enhanced by    1.500E+00
                  CO2             Enhanced by    2.000E+00
                  C2H6            Enhanced by    3.000E+00
                  AR              Enhanced by    7.000E-01
159. 2CH3<=>H+C2H5                                6.84E+12    0.1    10600.0
160. CH3+HCO<=>CH4+CO                             2.65E+13    0.0        0.0
161. CH3+CH2O<=>HCO+CH4                           3.32E+03    2.8     5860.0
162. CH3+CH3OH<=>CH2OH+CH4                        3.00E+07    1.5     9940.0
163. CH3+CH3OH<=>CH3O+CH4                         1.00E+07    1.5     9940.0
164. CH3+C2H4<=>C2H3+CH4                          2.27E+05    2.0     9200.0
165. CH3+C2H6<=>C2H5+CH4                          6.14E+06    1.7    10450.0
166. HCO+H2O<=>H+CO+H2O                           1.50E+18   -1.0    17000.0
167. HCO+M<=>H+CO+M                               1.87E+17   -1.0    17000.0
                  H2              Enhanced by    2.000E+00
                  H2O             Enhanced by    0.000E+00
                  CH4             Enhanced by    2.000E+00
                  CO              Enhanced by    1.500E+00
                  CO2             Enhanced by    2.000E+00
                  C2H6            Enhanced by    3.000E+00
168. HCO+O2<=>HO2+CO                              1.34E+13    0.0      400.0
169. CH2OH+O2<=>HO2+CH2O                          1.80E+13    0.0      900.0
170. CH3O+O2<=>HO2+CH2O                           4.28E-13    7.6    -3530.0
171. C2H+O2<=>HCO+CO                              1.00E+13    0.0     -755.0
172. C2H+H2<=>H+C2H2                              5.68E+10    0.9     1993.0
173. C2H3+O2<=>HCO+CH2O                           4.58E+16   -1.4     1015.0
174. C2H4(+M)<=>H2+C2H2(+M)                       8.00E+12    0.4    86770.0
        Low pressure limit:  0.15800E+52 -0.93000E+01  0.97800E+05
   TROE centering:      0.73450E+00  0.18000E+03 0.10350E+04  0.54170E+04
                  H2              Enhanced by    2.000E+00
                  H2O             Enhanced by    6.000E+00
                  CH4             Enhanced by    2.000E+00
                  CO              Enhanced by    1.500E+00
                  CO2             Enhanced by    2.000E+00
                  C2H6            Enhanced by    3.000E+00
                  AR              Enhanced by    7.000E-01
175. C2H5+O2<=>HO2+C2H4                           8.40E+11    0.0     3875.0
176. HCCO+O2<=>OH+2CO                             3.20E+12    0.0      854.0
177. 2HCCO<=>2CO+C2H2                             1.00E+13    0.0        0.0
178. N2O+O<=>N2+O2                                1.40E+12    0.0    10810.0
179. N2O+O<=>2NO                                  2.90E+13    0.0    23150.0
180. N2O+H<=>N2+OH                                3.87E+14    0.0    18880.0
181. N2O+OH<=>N2+HO2                              2.00E+12    0.0    21060.0
182. N2O(+M)<=>N2+O(+M)                           7.91E+10    0.0    56020.0
        Low pressure limit:  0.63700E+15  0.00000E+00  0.56640E+05
                  H2              Enhanced by    2.000E+00
                  H2O             Enhanced by    6.000E+00
                  CH4             Enhanced by    2.000E+00
                  CO              Enhanced by    1.500E+00
                  CO2             Enhanced by    2.000E+00
```

	C2H6	Enhanced by	3.000E+00		
	AR	Enhanced by	6.250E-01		
183.	HO2+NO<=>NO2+OH		2.11E+12	0.0	-480.0
184.	NO+O+M<=>NO2+M		1.06E+20	-1.4	0.0
	H2	Enhanced by	2.000E+00		
	H2O	Enhanced by	6.000E+00		
	CH4	Enhanced by	2.000E+00		
	CO	Enhanced by	1.500E+00		
	CO2	Enhanced by	2.000E+00		
	C2H6	Enhanced by	3.000E+00		
	AR	Enhanced by	7.000E-01		
185.	NO2+O<=>NO+O2		3.90E+12	0.0	-240.0
186.	NH+H<=>N+H2		3.20E+13	0.0	330.0
187.	NH+OH<=>HNO+H		2.00E+13	0.0	0.0
188.	NH+OH<=>N+H2O		2.00E+09	1.2	0.0
189.	NH+O2<=>HNO+O		4.61E+05	2.0	6500.0
190.	NH+O2<=>NO+OH		1.28E+06	1.5	100.0
191.	NH+N<=>N2+H		1.50E+13	0.0	0.0
192.	NH+H2O<=>HNO+H2		2.00E+13	0.0	13850.0
193.	NH2+O<=>OH+NH		3.00E+12	0.0	0.0
194.	NH2+O<=>H+HNO		3.90E+13	0.0	0.0
195.	NH2+H<=>NH+H2		4.00E+13	0.0	3650.0
196.	NH2+OH<=>NH+H2O		9.00E+07	1.5	-460.0
197.	NNH<=>N2+H		3.30E+08	0.0	0.0
198.	NNH+M<=>N2+H+M		1.30E+14	-0.1	4980.0
	H2	Enhanced by	2.000E+00		
	H2O	Enhanced by	6.000E+00		
	CH4	Enhanced by	2.000E+00		
	CO	Enhanced by	1.500E+00		
	CO2	Enhanced by	2.000E+00		
	C2H6	Enhanced by	3.000E+00		
	AR	Enhanced by	7.000E-01		
199.	NNH+O2<=>HO2+N2		5.00E+12	0.0	0.0
200.	NNH+O<=>OH+N2		2.50E+13	0.0	0.0
201.	NNH+O<=>NH+NO		7.00E+13	0.0	0.0
202.	NNH+H<=>H2+N2		5.00E+13	0.0	0.0
203.	NNH+OH<=>H2O+N2		2.00E+13	0.0	0.0
204.	NNH+CH3<=>CH4+N2		2.50E+13	0.0	0.0
205.	HNO+O<=>NO+OH		2.50E+13	0.0	0.0
206.	CN+O<=>CO+N		7.70E+13	0.0	0.0
207.	CN+OH<=>NCO+H		4.00E+13	0.0	0.0
208.	CN+H2O<=>HCN+OH		8.00E+12	0.0	7460.0
209.	CN+O2<=>NCO+O		6.14E+12	0.0	-440.0
210.	CN+H2<=>HCN+H		2.95E+05	2.5	2240.0
211.	NCO+O<=>NO+CO		2.35E+13	0.0	0.0
212.	NCO+H<=>NH+CO		5.40E+13	0.0	0.0
213.	NCO+OH<=>NO+H+CO		2.50E+12	0.0	0.0
214.	NCO+N<=>N2+CO		2.00E+13	0.0	0.0
215.	NCO+O2<=>NO+CO2		2.00E+12	0.0	20000.0
216.	NCO+M<=>N+CO+M		3.10E+14	0.0	54050.0
	H2	Enhanced by	2.000E+00		
	H2O	Enhanced by	6.000E+00		
	CH4	Enhanced by	2.000E+00		
	CO	Enhanced by	1.500E+00		

```
                CO2             Enhanced by    2.000E+00
                C2H6            Enhanced by    3.000E+00
                AR              Enhanced by    7.000E-01
217. NCO+NO<=>N2O+CO                            1.90E+17   -1.5      740.0
218. NCO+NO<=>N2+CO2                            3.80E+18   -2.0      800.0
219. HCN+M<=>H+CN+M                             1.04E+29   -3.3   126600.0
                H2              Enhanced by    2.000E+00
                H2O             Enhanced by    6.000E+00
                CH4             Enhanced by    2.000E+00
                CO              Enhanced by    1.500E+00
                CO2             Enhanced by    2.000E+00
                C2H6            Enhanced by    3.000E+00
                AR              Enhanced by    7.000E-01
220. HCN+O<=>NCO+H                              2.03E+04    2.6     4980.0
221. HCN+O<=>NH+CO                              5.07E+03    2.6     4980.0
222. HCN+O<=>CN+OH                              3.91E+09    1.6    26600.0
223. HCN+OH<=>HOCN+H                            1.10E+06    2.0    13370.0
224. HCN+OH<=>HNCO+H                            4.40E+03    2.3     6400.0
225. HCN+OH<=>NH2+CO                            1.60E+02    2.6     9000.0
226. H+HCN(+M)<=>H2CN(+M)                       3.30E+13    0.0        0.0
        Low pressure limit:  0.14000E+27 -0.34000E+01  0.19000E+04
                H2              Enhanced by    2.000E+00
                H2O             Enhanced by    6.000E+00
                CH4             Enhanced by    2.000E+00
                CO              Enhanced by    1.500E+00
                CO2             Enhanced by    2.000E+00
                C2H6            Enhanced by    3.000E+00
                AR              Enhanced by    7.000E-01
227. H2CN+N<=>N2+CH2                            6.00E+13    0.0      400.0
228. C+N2<=>CN+N                                6.30E+13    0.0    46020.0
229. CH+N2<=>HCN+N                              3.12E+09    0.9    20130.0
230. CH+N2(+M)<=>HCNN(+M)                       3.10E+12    0.1        0.0
        Low pressure limit:  0.13000E+26 -0.31600E+01  0.74000E+03
  TROE centering:      0.66700E+00  0.23500E+03  0.21170E+04  0.45360E+04
                H2              Enhanced by    2.000E+00
                H2O             Enhanced by    6.000E+00
                CH4             Enhanced by    2.000E+00
                CO              Enhanced by    1.500E+00
                CO2             Enhanced by    2.000E+00
                C2H6            Enhanced by    3.000E+00
                AR              Enhanced by    1.000E+00
231. CH2+N2<=>HCN+NH                            1.00E+13    0.0    74000.0
232. CH2(S)+N2<=>NH+HCN                         1.00E+11    0.0    65000.0
233. C+NO<=>CN+O                                1.90E+13    0.0        0.0
234. C+NO<=>CO+N                                2.90E+13    0.0        0.0
235. CH+NO<=>HCN+O                              4.10E+13    0.0        0.0
236. CH+NO<=>H+NCO                              1.62E+13    0.0        0.0
237. CH+NO<=>N+HCO                              2.46E+13    0.0        0.0
238. CH2+NO<=>H+HNCO                            3.10E+17   -1.4     1270.0
239. CH2+NO<=>OH+HCN                            2.90E+14   -0.7      760.0
240. CH2+NO<=>H+HCNO                            3.80E+13   -0.4      580.0
241. CH2(S)+NO<=>H+HNCO                         3.10E+17   -1.4     1270.0
242. CH2(S)+NO<=>OH+HCN                         2.90E+14   -0.7      760.0
243. CH2(S)+NO<=>H+HCNO                         3.80E+13   -0.4      580.0
```

```
244. CH3+NO<=>HCN+H2O                                 9.60E+13    0.0    28800.0
245. CH3+NO<=>H2CN+OH                                 1.00E+12    0.0    21750.0
246. HCNN+O<=>CO+H+N2                                 2.20E+13    0.0        0.0
247. HCNN+O<=>HCN+NO                                  2.00E+12    0.0        0.0
248. HCNN+O2<=>O+HCO+N2                               1.20E+13    0.0        0.0
249. HCNN+OH<=>H+HCO+N2                               1.20E+13    0.0        0.0
250. HCNN+H<=>CH2+N2                                  1.00E+14    0.0        0.0
251. HNCO+O<=>NH+CO2                                  9.80E+07    1.4     8500.0
252. HNCO+O<=>HNO+CO                                  1.50E+08    1.6    44000.0
253. HNCO+O<=>NCO+OH                                  2.20E+06    2.1    11400.0
254. HNCO+H<=>NH2+CO                                  2.25E+07    1.7     3800.0
255. HNCO+H<=>H2+NCO                                  1.05E+05    2.5    13300.0
256. HNCO+OH<=>NCO+H2O                                3.30E+07    1.5     3600.0
257. HNCO+OH<=>NH2+CO2                                3.30E+06    1.5     3600.0
258. HNCO+M<=>NH+CO+M                                 1.18E+16    0.0    84720.0
                  H2              Enhanced by    2.000E+00
                  H2O             Enhanced by    6.000E+00
                  CH4             Enhanced by    2.000E+00
                  CO              Enhanced by    1.500E+00
                  CO2             Enhanced by    2.000E+00
                  C2H6            Enhanced by    3.000E+00
                  AR              Enhanced by    7.000E-01
259. HCNO+H<=>H+HNCO                                  2.10E+15   -0.7     2850.0
260. HCNO+H<=>OH+HCN                                  2.70E+11    0.2     2120.0
261. HCNO+H<=>NH2+CO                                  1.70E+14   -0.8     2890.0
262. HOCN+H<=>H+HNCO                                  2.00E+07    2.0     2000.0
263. HCCO+NO<=>HCNO+CO                                9.00E+12    0.0        0.0
264. CH3+N<=>H2CN+H                                   6.10E+14   -0.3      290.0
265. CH3+N<=>HCN+H2                                   3.70E+12    0.1      -90.0
266. NH3+H<=>NH2+H2                                   5.40E+05    2.4     9915.0
267. NH3+OH<=>NH2+H2O                                 5.00E+07    1.6      955.0
268. NH3+O<=>NH2+OH                                   9.40E+06    1.9     6460.0
269. NH+CO2<=>HNO+CO                                  1.00E+13    0.0    14350.0
270. CN+NO2<=>NCO+NO                                  6.16E+15   -0.8      345.0
271. NCO+NO2<=>N2O+CO2                                3.25E+12    0.0     -705.0
272. N+CO2<=>NO+CO                                    3.00E+12    0.0    11300.0
273. O+CH3=>H+H2+CO                                   3.37E+13    0.0        0.0
274. O+C2H4<=>H+CH2CHO                                6.70E+06    1.8      220.0
275. O+C2H5<=>H+CH3CHO                                1.10E+14    0.0        0.0
276. OH+HO2<=>O2+H2O                                  5.00E+15    0.0    17330.0
                     Declared duplicate reaction...
277. OH+CH3=>H2+CH2O                                  8.00E+09    0.5    -1755.0
278. CH+H2(+M)<=>CH3(+M)                              1.97E+12    0.4     -370.0
         Low pressure limit:  0.48200E+26 -0.28000E+01  0.59000E+03
   TROE centering:      0.57800E+00  0.12200E+03  0.25350E+04  0.93650E+04
                  H2              Enhanced by    2.000E+00
                  H2O             Enhanced by    6.000E+00
                  CH4             Enhanced by    2.000E+00
                  CO              Enhanced by    1.500E+00
                  CO2             Enhanced by    2.000E+00
                  C2H6            Enhanced by    3.000E+00
                  AR              Enhanced by    7.000E-01
279. CH2+O2=>2H+CO2                                   5.80E+12    0.0     1500.0
280. CH2+O2<=>O+CH2O                                  2.40E+12    0.0     1500.0
```

```
281. CH2+CH2=>2H+C2H2                                 2.00E+14    0.0    10989.0
282. CH2(S)+H2O=>H2+CH2O                              6.82E+10    0.2     -935.0
283. C2H3+O2<=>O+CH2CHO                               3.03E+11    0.3       11.0
284. C2H3+O2<=>HO2+C2H2                               1.34E+06    1.6     -384.0
285. O+CH3CHO<=>OH+CH2CHO                             2.92E+12    0.0     1808.0
286. O+CH3CHO=>OH+CH3+CO                              2.92E+12    0.0     1808.0
287. O2+CH3CHO=>HO2+CH3+CO                            3.01E+13    0.0    39150.0
288. H+CH3CHO<=>CH2CHO+H2                             2.05E+09    1.2     2405.0
289. H+CH3CHO=>CH3+H2+CO                              2.05E+09    1.2     2405.0
290. OH+CH3CHO=>CH3+H2O+CO                            2.34E+10    0.7    -1113.0
291. HO2+CH3CHO=>CH3+H2O2+CO                          3.01E+12    0.0    11923.0
292. CH3+CH3CHO=>CH3+CH4+CO                           2.72E+06    1.8     5920.0
293. H+CH2CO(+M)<=>CH2CHO(+M)                         4.86E+11    0.4    -1755.0
         Low pressure limit:  0.10120E+43 -0.76300E+01  0.38540E+04
   TROE centering:      0.46500E+00  0.20100E+03 0.17730E+04  0.53330E+04
                  H2              Enhanced by    2.000E+00
                  H2O             Enhanced by    6.000E+00
                  CH4             Enhanced by    2.000E+00
                  CO              Enhanced by    1.500E+00
                  CO2             Enhanced by    2.000E+00
                  C2H6            Enhanced by    3.000E+00
                  AR              Enhanced by    7.000E-01
294. O+CH2CHO=>H+CH2+CO2                              1.50E+14    0.0        0.0
295. O2+CH2CHO=>OH+CO+CH2O                            1.81E+10    0.0        0.0
296. O2+CH2CHO=>OH+2HCO                               2.35E+10    0.0        0.0
297. H+CH2CHO<=>CH3+HCO                               2.20E+13    0.0        0.0
298. H+CH2CHO<=>CH2CO+H2                              1.10E+13    0.0        0.0
299. OH+CH2CHO<=>H2O+CH2CO                            1.20E+13    0.0        0.0
300. OH+CH2CHO<=>HCO+CH2OH                            3.01E+13    0.0        0.0
301. CH3+C2H5(+M)<=>C3H8(+M)                          9.43E+12    0.0        0.0
         Low pressure limit:  0.27100E+75 -0.16820E+02  0.13065E+05
   TROE centering:      0.15270E+00  0.29100E+03 0.27420E+04  0.77480E+04
                  H2              Enhanced by    2.000E+00
                  H2O             Enhanced by    6.000E+00
                  CH4             Enhanced by    2.000E+00
                  CO              Enhanced by    1.500E+00
                  CO2             Enhanced by    2.000E+00
                  C2H6            Enhanced by    3.000E+00
                  AR              Enhanced by    7.000E-01
302. O+C3H8<=>OH+C3H7                                 1.93E+05    2.7     3716.0
303. H+C3H8<=>C3H7+H2                                 1.32E+06    2.5     6756.0
304. OH+C3H8<=>C3H7+H2O                               3.16E+07    1.8      934.0
305. C3H7+H2O2<=>HO2+C3H8                             3.78E+02    2.7     1500.0
306. CH3+C3H8<=>C3H7+CH4                              9.03E-01    3.6     7154.0
307. CH3+C2H4(+M)<=>C3H7(+M)                          2.55E+06    1.6     5700.0
         Low pressure limit:  0.30000E+64 -0.14600E+02  0.18170E+05
   TROE centering:      0.18940E+00  0.27700E+03 0.87480E+04  0.78910E+04
                  H2              Enhanced by    2.000E+00
                  H2O             Enhanced by    6.000E+00
                  CH4             Enhanced by    2.000E+00
                  CO              Enhanced by    1.500E+00
                  CO2             Enhanced by    2.000E+00
                  C2H6            Enhanced by    3.000E+00
                  AR              Enhanced by    7.000E-01
```

```
308. O+C3H7<=>C2H5+CH2O                              9.64E+13    0.0        0.0
309. H+C3H7(+M)<=>C3H8(+M)                           3.61E+13    0.0        0.0
         Low pressure limit:  0.44200E+62 -0.13545E+02  0.11357E+05
   TROE centering:      0.31500E+00  0.36900E+03 0.32850E+04  0.66670E+04
                  H2              Enhanced by    2.000E+00
                  H2O             Enhanced by    6.000E+00
                  CH4             Enhanced by    2.000E+00
                  CO              Enhanced by    1.500E+00
                  CO2             Enhanced by    2.000E+00
                  C2H6            Enhanced by    3.000E+00
                  AR              Enhanced by    7.000E-01
310. H+C3H7<=>CH3+C2H5                               4.06E+06    2.2      890.0
311. OH+C3H7<=>C2H5+CH2OH                            2.41E+13    0.0        0.0
312. HO2+C3H7<=>O2+C3H8                              2.55E+10    0.3     -943.0
313. HO2+C3H7=>OH+C2H5+CH2O                          2.41E+13    0.0        0.0
314. CH3+C3H7<=>2C2H5                                1.93E+13   -0.3        0.0
315. HNO+H=NO+H2                                     8.80E+11    0.7      650.0
316. NO2+H=NO+OH                                     1.30E+14    0.0      362.0
317. HNO+OH=NO+H2O                                   3.60E+13    0.0        0.0
318. NH+O=NO+H                                       3.68E+14    0.0        0.0
319. HNO+O2=HO2+NO                                   2.00E+13    0.0    16000.0
320. N+O2=NO+O                                       6.40E+09    1.0     6280.0
321. N+OH=NO+H                                       3.80E+13    0.0        0.0
322. NH+NO=N2O+H                                     2.90E+14   -0.4        0.0
                     Declared duplicate reaction...
323. NH+NO=N2O+H                                    -2.20E+13   -0.2        0.0
                     Declared duplicate reaction...
324. N+NO=N2+O                                       1.05E+12    1.5        0.0
325. NH2+NO<=>N2+H2O                                 2.80E+20   -2.7     1258.0
326. NH2+NO<=>NNH+OH                                 2.30E+10    0.4     -814.0
327. NO+H(+M)=HNO(+M)                                1.50E+15   -1.4        0.0
         Low pressure limit:  0.24000E+15  0.20600E+00 -0.15500E+04
   TROE centering:      0.82000E+00  0.10000E-29 0.10000E+31  0.10000E+31
                  N2              Enhanced by    1.600E+00
328. NH+NO=N2+OH                                     2.20E+13   -0.2        0.0

        UNITS for the preceding reactions (unless otherwise noted):
                  A units mole-cm-sec-K, E units cal/mole
```